



**HAL**  
open science

## Fracture analysis of advanced ceramics

Sara Jiménez Alfaro

► **To cite this version:**

Sara Jiménez Alfaro. Fracture analysis of advanced ceramics. Mechanics [physics]. Sorbonne Université, 2023. English. NNT : 2023SORUS751 . tel-04694320v2

**HAL Id: tel-04694320**

**<https://theses.hal.science/tel-04694320v2>**

Submitted on 11 Sep 2024

**HAL** is a multi-disciplinary open access archive for the deposit and dissemination of scientific research documents, whether they are published or not. The documents may come from teaching and research institutions in France or abroad, or from public or private research centers.

L'archive ouverte pluridisciplinaire **HAL**, est destinée au dépôt et à la diffusion de documents scientifiques de niveau recherche, publiés ou non, émanant des établissements d'enseignement et de recherche français ou étrangers, des laboratoires publics ou privés.

# Sorbonne Université

École doctorale Sciences Mécaniques, Acoustique, Électronique et Robotique

THÈSE DE DOCTORAT  
SPECIALITÉ: MÉCANIQUE DES SOLIDES

---

## Fracture analysis of advanced ceramics

---

Présentée par  
**Sara Jiménez Alfaro**  
pour obtenir le grade de  
**Docteur de Sorbonne Université**

Sous la direction de  
**Prof. Corrado Maurini and Prof. Dominique Leguillon**

à l'Institut Jean Le Rond d'Alembert, Sorbonne Université, CNRS, UMR 7190

Soutenue le 16/10/2023, devant le jury composé de :

---

M. Pietro Cornetti	Professore Associato, Politecnico di Torino	<i>Rapporteur</i>
M. Rafael Estevez	Professeur, Université de Grenoble	<i>Rapporteur</i>
Mme. Veronique Lazarus	Professeur, Institut Polytechnique de Paris	<i>Examineur</i>
M. Djimedo Kondo	Professeur, Sorbonne Université	<i>Examineur</i>
M. Luis Tavera	Profesor Titular, Universidad de Sevilla	<i>Examineur</i>
M. Hyung-Jun Chang	Ingénieur de recherche, Safran	<i>Examineur</i>
M. Corrado Maurini	Professeur, Sorbonne Université	<i>Directeur de thèse</i>
M. Dominique Leguillon	Directeur de Recherche CNRS	<i>Co-directeur de thèse</i>



*"J'ai appris que la voie du progrès n'était ni rapide ni facile"*  
Marie Curie



# Abstract

Ceramic materials are widely used in the industry owing to their countless advantages, such as the resistance to corrosion or oxidation. However, they have a very low fracture toughness, which is related to the spontaneous brittle failure of the component. In this context, the main objective of this thesis is the consistent extension of numerical modelling tools in fracture mechanics for predicting crack nucleation and growth in advanced ceramics, with a special emphasis in the relationship between the micro and macro-scale characteristics within these materials. Two approaches are followed: the Coupled Criterion (CC) within the Finite Fracture Mechanics (FFM) framework and the Phase Field (PF) model for fracture.

Two parts are distinguished in this thesis. The first one is dedicated to the study of ceramics fracture properties at the micro-scale. In the second part we focus on the fracture analysis of brittle materials reinforced by a second constituent in the form of micro-platelets or short fibers, a kind of structure of high technological interest for advanced ceramics.



# Résumé

Les matériaux céramiques sont largement utilisés dans l'industrie en raison de leurs innombrables avantages, tels que leur résistance à la corrosion ou à l'oxydation. Cependant, ils ont une ténacité à la rupture très faible, ce qui est lié à la défaillance fragile spontanée du composant. Dans ce contexte, l'objectif principal de cette thèse est l'extension cohérente des outils de modélisation numérique en mécanique de la rupture pour prédire la formation et la croissance des fissures dans les céramiques avancées, en mettant l'accent sur la relation entre les caractéristiques micro et macroscales de ces matériaux. Deux approches sont suivies : le critère couplé (CC) dans le cadre de la mécanique de la rupture finie (FFM) et le modèle du champ de phase (PF) pour la rupture.

Deux parties sont distinguées dans cette thèse. La première est dédiée à l'étude des propriétés de rupture des céramiques à l'échelle microscopique. Dans la deuxième partie, nous nous concentrons sur l'analyse de la rupture des matériaux fragiles renforcés par un second constituant sous forme de microplaquettes ou de fibres courtes, une structure d'un grand intérêt technologique pour les céramiques avancées.



# Remerciements

It is amazing how quickly time goes by when you are happy. I think this perfectly defines my PhD experience, that has been intense and short, but which I have enjoyed very much, not only for doing what I am passionate about, but also for being surrounded by wonderful people to whom I would like to make a special mention in this document.

I would first of all like to thank my two supervisors for their participation and constant support. Prof. Leguillon, thank you for all the invaluable help and for guiding me through this thesis. It has been an honour to work and learn from you. Prof. Maurini, thank you for the fantastic management of my PhD, for all the support I received to teach at Sorbonne and thus fulfil one of my dreams, and for all the help I received with Phase Field. I would also like to add a special thanks to the two supervisors I have had during my two secondments, Dr. Reinoso and Dr. Chang, for all their advice and support.

I could not forget to mention also my big NewFrac family. It has been incredible to do a PhD within this network. Without a doubt, what fracture joins never breaks and we are and will be the example of that. Thanks also to my singularities group in Seville, for giving me the opportunity to continue collaborating with them during my PhD.

Je voudrais également remercier mes collègues de l'Institut Jean Le Rond d'Alembert. Je n'exagère pas si je nous définis comme un groupe d'amis qui font de la science, car l'atmosphère ouverte et amicale qui règne dans le laboratoire est merveilleuse. Je voudrais tout particulièrement mentionner mes collègues du bureau 313, où j'ai passé de nombreuses heures, et mes amis de "Samedi Soir", pour avoir fait de Paris un endroit amusant et pas seulement un lieu de travail. La première année du doctorat, nous étions tous confinés, ce qui m'a d'abord effrayé. Cependant, c'était une expérience unique à la Cité Universitaire, et de ces moments sont nées des amitiés qui, je le sais, dureront toute une vie. A ma petite famille en cité... merci pour tout.

Quisiera mencionar también a mis amigos en España. Gracias por aguantarme siempre y por todo el cariño y apoyo que tengo de vosotros. Siempre me hacéis sentir que no estoy lejos, y que siempre tendré un hogar en Sevilla.

Mamá, Papá, gracias por ser mi ejemplo a seguir en todo, por ser los mejores científicos que yo podía conocer, y por estar siempre a mi lado pase lo que pase. Andrea, gracias por ser mi mayor confidente, así te hable de ecuaciones o de relaciones. Abuelita, gracias por ser mi alegría y mi ejemplo. Gracias también al resto de mi familia por vuestro constante apoyo. Esta tesis no hubiera sido posible sin vosotros.

Finalmente, gracias a ti, Juan, por ser mi mayor apoyo y motivación para todo. Has estado siempre, en los momentos malos y buenos. Esta tesis te la dedico muy especialmente a ti, porque sin ti no hubiera salido adelante. Aunque ya te lo voy a decir muy pronto... te amo y quiero pasar contigo todos los días de mi vida.



# Acknowledgements

The funding received from the European Union's Horizon 2020 research and innovation programme under Marie Skłodowska-Curie grant agreement No. 861061- NEWFRAC is gratefully acknowledged.





# Contents

<b>1</b>	<b>Introduction</b>	<b>1</b>
1.1	Introduction to advanced ceramics . . . . .	2
1.1.1	Mechanical testing at the micro-scale . . . . .	5
1.1.2	Glass ceramics . . . . .	6
1.2	Numerical tools for predicting fracture . . . . .	7
1.2.1	The Coupled Criterion . . . . .	7
1.2.2	Matched asymptotic expansions . . . . .	14
1.2.3	Phase Field model for brittle fracture . . . . .	18
1.3	Aims and objectives . . . . .	25
<b>2</b>	<b>Ceramic fracture properties at the micro-scale</b>	<b>27</b>
2.1	Introduction . . . . .	28
2.2	FFM of brittle materials at the micro-scale . . . . .	29
2.2.1	A preliminary remark . . . . .	29
2.2.2	Bending tests . . . . .	30
2.2.3	Comparison with experiments found in the literature . . . . .	43
2.3	PF model of brittle materials at the micro-scale . . . . .	51
2.3.1	Preliminary remark . . . . .	51
2.3.2	Apparent strengthening effect in an unnotched specimen . . . . .	52
2.3.3	Scale effect in a V-notched specimen . . . . .	57
2.3.4	Influence of the fracture properties . . . . .	61
2.4	Conclusions . . . . .	64
<b>3</b>	<b>A design tool for advanced ceramics with reinforcements</b>	<b>67</b>
3.1	Description of the computational tool . . . . .	68
3.1.1	Description of the reference problem . . . . .	68
3.1.2	Matched Asymptotic approach . . . . .	69
3.1.3	The Coupled Criterion . . . . .	72
3.2	Application example: borosilicate glass reinforced by alumina platelets . . . . .	75
3.2.1	Description of the material . . . . .	75
3.2.2	The role of a single platelet . . . . .	77
3.2.3	Influence of residual stresses . . . . .	96

*Contents*

3.2.4	Influence of the volume fraction . . . . .	101
3.2.5	Comparison to experiments . . . . .	109
3.2.6	Conclusions . . . . .	111
3.3	Industrial application: Ceramic matrix composites with short fibers . . . . .	115
3.3.1	Introduction and general description . . . . .	115
3.3.2	Considerations in the problem . . . . .	117
3.3.3	The influence of the size of the fiber . . . . .	119
3.3.4	Influence of other design parameters . . . . .	124
3.3.5	Mutiple fibers vs single fiber model . . . . .	127
3.3.6	Conclusions . . . . .	128
<b>4</b>	<b>Conclusions and further studies</b>	<b>131</b>
<b>5</b>	<b>Appendices</b>	<b>135</b>
5.1	Terms in Williams' expansion . . . . .	136
5.2	Generalized stress intensity factors (GSIFs) . . . . .	136
5.3	Calculation of the dimensionless coefficient $A^*$ . . . . .	137
5.4	Codes developed . . . . .	138
5.4.1	Automatic algorithms for the application of the CC . . . . .	138
5.4.2	A code for the application of the PF model for brittle fracture . . . . .	146

# Introduction

## Contents

---

<b>1.1</b>	<b>Introduction to advanced ceramics . . . . .</b>	<b>2</b>
<b>1.2</b>	<b>Numerical tools for predicting fracture . . . . .</b>	<b>7</b>
<b>1.3</b>	<b>Aims and objectives . . . . .</b>	<b>25</b>

---

More than 15,000 years of history have demonstrated the industrial applicability of ceramics, although their use has always been limited by their natural disadvantages, such as their brittleness. For this reason, around 200 years ago, a great deal of research was undertaken to improve them and further enhance their industrial applications. The concept of advanced ceramics [1] was therefore introduced to designate new materials with ceramic components that have been improved by various technologies to overcome the aforementioned disadvantages. Since then, advanced ceramics are expected to be present in countless industries and sectors ranging from biomedicine, automotive, aerospace, electronics and renewable energy systems. In this chapter we describe the main characteristics of advanced ceramics, and we carefully explain the objectives of this PhD thesis.

One of the most important goals in advanced ceramics is to avoid the inherent brittleness commonly associated with classical ceramics. To that aim, the micro-scale structure of classical ceramics is modified through processing techniques or addition of additives. A fracture analysis of these new materials is therefore an essential design component, combining experimental investigations with numerical studies. In this context, this thesis focuses on the consistent extension of numerical modelling tools in fracture mechanics for the prediction of crack nucleation and growth in advanced ceramics. Notably, a crucial aspect of the analysis revolves around establishing the relationship between the micro and macro-scale characteristics within these materials. To accomplish this, two approaches are followed: the Coupled Criterion (CC) within the Finite Fracture Mechanics (FFM) framework and the Phase Field (PF) model for fracture.

## 1.1 Introduction to advanced ceramics

Although the term ceramics is derived from the Greek word *keramikos*, which means, *made of clay* [2], nowadays the concept of ceramics moves away from this initial definition. They are inorganic and nonmetallic materials having high melting points [3], which are formed by interconnected atoms, held together by ionic, covalent, and sometimes metallic bonds. Examples of ceramic materials are alumina, zirconia, mullite...

Ceramics have many advantages. They are in general chemically stable, which means that their resistance to corrosion or oxidation is very high. They have high thermal conductivity, due to the high presence of phonons, and can also have high electrical conductivity, depending on the constituents. As shown in Table 1.1, they can have higher Young's modulus ( $E$ ) and tensile strength ( $\sigma_c$ ) than metals or polymers, whereas the thermal expansion coefficient ( $\alpha_T$ ) and the fracture toughness ( $K_c$ ) are typically smaller.

Material	$E$ [GPa]	$\sigma_c$ [MPa]	$\alpha_T \cdot 10^{-6}$ [K <sup>-1</sup> ]	$K_c$ [MPa m <sup>1/2</sup> ]	$G_c$ [MPa m]
<b>Alumina</b>	250-400	350-500	7-9	3.5-4	0.031-0.064
<b>Zirconia</b>	150-250	200-1400	6-12	4.5-5	0.081-0.167
<b>Silicon carbide</b>	410-450	410-650	4.95-5.8	4-4.7	0.036-0.054
<b>Glasses</b>	40-80	20-150	3-5	0.6-0.7	0.005-0.012
<b>Aluminum</b>	60-90	60-550	20-30	22-35	5.38-20.42
<b>Steels</b>	180-250	300-2000	3-4	> 50	> 10
<b>Polyethylene</b>	0.1-0.9	20-45	130-250	1.5	2.5-22.5
<b>Epoxies</b>	1-3	45-90	60-100	0.4-2	0.053-4

Table 1.1: Mechanical properties of some materials at room temperature [1, 4]. Materials are classified by colours. Ceramic materials are highlighted in orange, glasses in green, metals in yellow and finally polymers in red.

Another advantage of ceramics is their refractory behaviour, which means that their properties do not degrade at high temperatures. Moreover, they have very good specific properties, as shown in the Ashby's diagrams<sup>1</sup> in Fig. 1.1 and 1.2, which plots Young's modulus and tensile

<sup>1</sup>Images obtained from <https://www.grantadesign.com/education/students/charts/>

strength as a function of the material density [5]. It can be observed that ceramics are located on the diagrams top right side, especially technical ceramic materials (also called advanced ceramic materials) that can exhibit even better properties, as it is explained below. All these characteristics make ceramics particularly suitable for high-technological purposes.

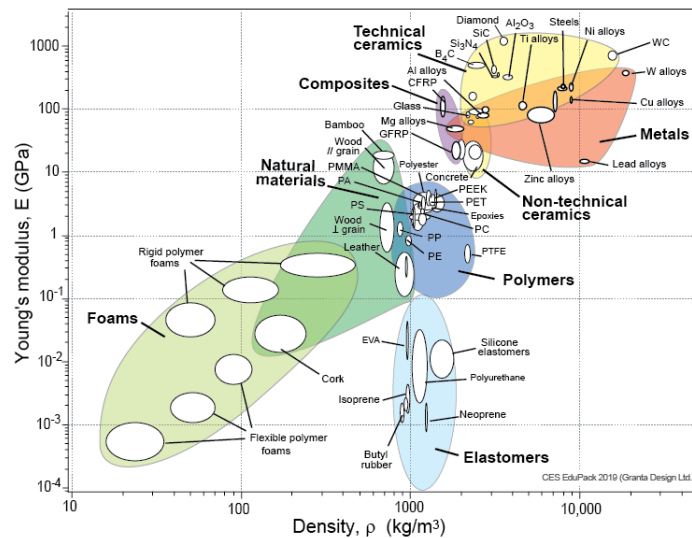


Figure 1.1: Ashby's diagram representing Young's modulus as a function of the material density.

Fracture in ceramic materials is generally brittle, especially under tensile loading. In ceramics, ionic/covalent bonds and electrons are immobile and plastic deformation caused by dislocation movement requires too much energy. Table 1.1 shows the fracture properties typically used to characterize a material,  $K_C$  and  $\sigma_c$ . The latter is very controversial in ceramics as it is highly dependent on the number and size of defects in the microstructure. If we look at  $K_C$ , we can see that it is much smaller than in metals. This is the main drawback of ceramics, which severely limits their industrial applications.

The increasingly demanding technological requirements in many sectors (electronics, biomedicine, chemical industries...) together with the remarkable advantages of ceramics, led science to enhance them through technological advancements. The objective is to create novel materials that surpass the limitations associated with classical ceramics. These high-tech materials were designated as advanced ceramics in the 70s [6].

Describing the properties of advanced ceramics is difficult, as it entirely depends on the technological process and the design objectives. In general, advanced ceramics have high temperature stability (up to 2500°C), high hardness and corrosion resistance, and totally variable electrical properties, ranging from insulators to highly conductive materials [4]. In comparison to metals, fracture toughness is still low, but high-tech processes are now under

development to achieve reinforced advanced ceramics with greater toughness.

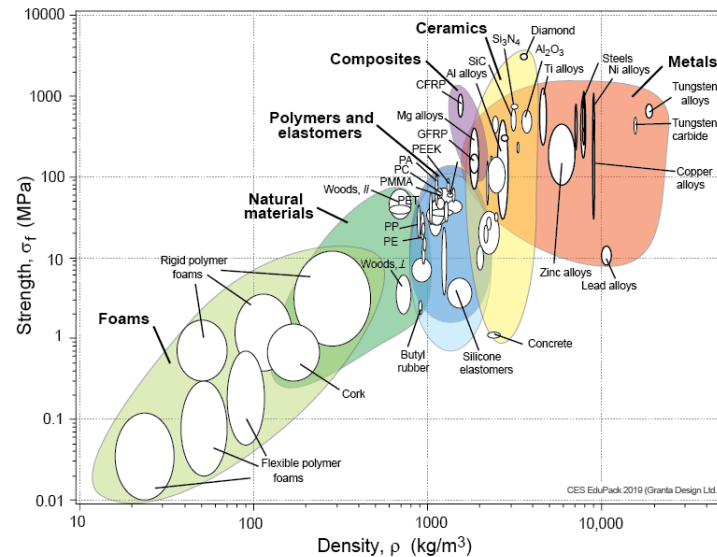


Figure 1.2: Ashby's diagram representing tensile strength as a function of the material density.

An example is shown in Table 1.2 where the alumina-zirconia composite is compared to its constituents alumina ( $\text{Al}_2\text{O}_3$ ) and zirconia ( $\text{ZrO}_2$ ) (previously shown in Table 1.1). Zirconia and alumina are used as structural materials because they have good strength, moderate fracture toughness and high corrosion resistance, among others [7]. Zirconia-based ceramics have a higher fracture toughness than alumina-based ceramics, but they can suffer low-temperature degradation. The  $\text{Al}_2\text{O}_3/\text{ZrO}_2$  composite combines the good properties of both components. Notice that an intermediate density ( $d$ ) is achieved in the composite.

Material	$d$ [g/cm <sup>3</sup> ]	$E$ [GPa]	$K_c$ [MPa m <sup>1/2</sup> ]	$\sigma_c$ [MPa]
Alumina-zirconia	4.28-5.46	205-370	3.72-6.39	277-888
Alumina ( $\text{Al}_2\text{O}_3$ )	3.95	250-400	3.5-4	350-500
Zirconia ( $\text{ZrO}_2$ )	6.03	150-250	4.5-5	200-1400

Table 1.2: Mechanical properties at room temperature of alumina-zirconia composite [7] and its constituents [1].

A classification of advanced ceramics was made in [4], depending on their applications:

- Structural advanced ceramics: They are used in components of engineering systems that are subject to high mechanical, tribological, thermal or chemical stresses. An example is the alumina-zirconia composite shown above.
- Functional advanced ceramics: They are used to create microstructural effects to obtain conductive or isolated materials, for example in fuel cells.
- Bioceramics: They are used to create biocompatible materials for biomedical purposes.

A large part of the improved properties of advanced ceramic materials can be explained by their microstructure. For example, in advanced ceramics with a heterogeneous microstructure, where there is a mismatch in the thermal expansion coefficients  $\alpha_T$  of the constituents, the change in temperature after manufacture generates residual stresses that can contribute to improve the mechanical behaviour of the material. For such cases, a simple rule of mixtures can correctly define the equivalent homogenized material, according to [1]. Therefore, they might be studied at the micro-scale for their characterization, although standard techniques at the macro-scale are still being used. The following section summarizes the most common experimental techniques currently available for micro-scale testing.

### 1.1.1 Mechanical testing at the micro-scale

Advances in micro-technology over the past century have highlighted the need to understand the mechanical behaviour of materials at the micro-scale. Among the latest developments is the evolution of the microelectronics industry, with the manufacture of small size components [8], such as inter-layer dielectric and chip passivation films [9]. Furthermore, the nuclear industry is also in demand for a better knowledge of the behaviour of fuels, such as the uranium dioxide  $UO_2$  in pressurized water reactors [10, 11]. It is also important to highlight the tendency to mimic natural materials, like mother-of-pearl to create nacre-like inorganic materials [12, 13].

Experiments at the microscale were developed from advances in microscopy during the last century. In 1937, Manfred von Ardenne [14] invented the Scanning Electron Microscope (SEM), a type of electron microscope capable of producing high-resolution images of the surface of a sample using electron-matter interactions. Then, in 1981 a new type of microscopy appeared, based on the application of a probe that travels over the surface of the specimen to capture images. It was called Scanning Probe Microscopy (SPM), and started with the invention of the Scanning Tunneling Microscopy (STM) [15], which is a microscope able to image surfaces at the atomic level, whose principle is based on the tunnel effect. Although these techniques revolutionized the field of ceramics experimentation, some more traditional techniques are still used today. One of these is reflected light microscopy, based on the optical principles of light passing through the curved surface of a typically glass lens [16].

Another important development that appeared at that time was the nano-indentation, a type of experiment in which an indenter (whose tip is typically made of diamond) applies a prescribed force or displacement into the material surface. The output of the test is the

load-displacement curve [17].

On the other hand, MEMS (Micro-Electro-Mechanical System) technology can be used to fabricate, using lithography techniques, structures in which the sensors, the specimen and sometimes the actuator are all integrated [18]. These structures are called lab on chip. According to [19], Kahn et al. [20] and Ballarini et al [21] were pioneers on the fracture mechanical analysis using a MEMS with sharp cracks to measure the fracture toughness. Both performed the tests on polysilicon MEMS devices, using indentation to generate pre-existing defects on the specimens and measure the fracture toughness. Another example considering MEMS technology can be found in [22].

Furthermore, the FIB (Focused Ion Beam) [23] technique is used to fabricate micro-specimens. Since the application of this technology on micro-compression testing by Uchic et al. [24], it has been deeply applied in many studies, e.g. bending of notched and chevron notched micro-cantilever beams in [25, 26, 27], and compression on micro-pillars in [18, 28].

From an experimental point of view, many things change when we move from the macro- to the micro-scale. For example, tensile testing, so well-known in the scientific community at the macro-scale due to the uniformity of stresses during its application, is a challenge at the micro-scale. They are much more expensive and it is difficult to obtain reliable quantitative results in terms of displacement force, since the load application point is too close to the measurement regions [18]. On the contrary, micro-bending experiments are much more reliable, since the application of a point load far away from the area where the damage occurs allows the Saint-Venant principle to be taken into account.

### 1.1.2 Glass ceramics

Glass is increasingly used in structural applications, especially in architecture [29], owing to its numerous advantages: oxidation and corrosion resistance, hardness, and wear resistance. However, the main drawback of glass is its very low fracture toughness. New glass ceramic composites have been developed to face this problem, adding a second constituent, with either higher Young's modulus, higher strength, or higher ductility, under the form of platelets, powders, or whiskers. In this context, when the second constituent is a ceramic material we name this kind of structures as glass ceramics.

In particular, ceramic platelets can be used as a reinforcing constituent in glass matrices [30]. One example is the borosilicate glass  $\text{Al}_2\text{O}_3$  platelet composite, which can be really interesting for industrial applications due to its low production cost and environmental safety [31]. It was first introduced in 1996 by Boccaccini et al. [32]. Since then, multiple studies have been made about this material to explore its capabilities, numerically and experimentally. First, in [32] a characterization of the material was presented using SEM. The fracture surface of the composite was investigated through reflected light microscopy, whereas a single-edge notched beam (SENB) was used to measure the fracture toughness. On the other hand, in [30] and [33] a characterization of the material by means of the roughness in the fracture surface was

proposed. In particular, in [30] the fracture surface was correlated with the fracture toughness applying SEM.

The borosilicate glass  $\text{Al}_2\text{O}_3$  platelet composite is fabricated via powder technology, one of the most used techniques to fabricate ceramics [34]. In [32] the composite is fabricated using uniaxial hot-pressing, and therefore glass powders are uniaxially compacted with platelets at high temperatures. However, in [35] and [36] a cold-pressing was proposed.

As it was mentioned above, the potential advantage of these composites is the enhancement of fracture toughness with respect to the one in the matrix. The different ways by which this fracture property is increased are called toughening mechanisms. Some of them were experimentally observed in [30] and [33], such as the penetration of a crack into the platelet, a crack deflection or a decohesion at the end of the platelet.

Furthermore, one of the most important characteristics of this composite is the thermal expansion mismatch between alumina and glass [37]. The thermal coefficient in alumina is higher than the one in glass, and consequently, compressive residual stresses will appear in the matrix after cooling, as well as tensile residual stresses in the platelet. This effect has been studied experimentally and numerically. In 1999, Todd et al. [37] measured residual stresses and their toughening effect in experiments using fluorescence microscopy to relate the change in the luminescence spectrum of alumina to stresses. They also justified the consideration of isotropic thermal properties in the platelet, since results do not differ from the anisotropic measurements. The results were compared to some theoretical models [38] and [39], based on the aspect ratio of the platelet. Then, in 2001 Cannillo et al. [40] performed numerical simulations using the finite element method (FEM) to quantify residual stresses. Calculations were made using a map image micro-structure onto the finite element mesh.

## 1.2 Numerical tools for predicting fracture

In this section we describe the two numerical tools that have been applied in this thesis for predicting crack nucleation and propagation: the Coupled Criterion (CC), in the framework of Finite Fracture Mechanics (FFM), and the Phase Field (PF) model for brittle fracture. Moreover, the Matched Asymptotics Expansion (MAE) is also explained, as a mathematical theory used to predict the elastic solution in the neighbourhood of perturbations. It will be applied in this thesis to reduce computational complexity in simulations when studying some heterogeneous structures at the micro-scale of advanced ceramics.

### 1.2.1 The Coupled Criterion

The CC allows predicting crack nucleation in brittle materials. It has been successfully applied in several problems at the macroscale, such as notched specimens, laminates, adhesive joints or embedded inclusions [41]. This criterion is corroborated by previous experiments on

transverse cracking in cross-ply laminates [42].

According to the CC, two necessary conditions are together sufficient to predict crack nucleation, since fracture occurs when both are simultaneously fulfilled: (i) an energy condition, based on an energy balance, and (ii) a stress condition.

(i) The energy balance is obtained considering two states of the loaded structure, prior to and following a crack onset. The potential and kinetic energy are characterized by  $\Pi_p^{(i)}$  and  $\Pi_k^{(i)}$  respectively, where the superscript  $i = 0, 1$  is related to the state we are referring to. The initial one,  $i = 0$ , elasto-static, is characterized by a potential energy  $\Pi_p^{(0)}$  and a zero kinetic energy  $\Pi_k^{(0)}$ , whereas the final state,  $i = 1$ , is defined after the onset of a new crack or the growth of a preexisting one. Hence, considering a homogeneous material in which an expected crack path is predicted (see Fig. 1.3), we have

$$\Pi_p^{(0)} = \Pi_p^{(1)} + \Pi_k^{(1)} + G_c \delta S, \quad (1.1)$$

where  $\Pi_p^{(1)}$  and  $\Pi_k^{(1)}$  are the potential and kinetic energy related to the final state, respectively,  $G_c$  is the fracture energy per unit surface, and  $\delta S$  is the newly created crack surface. Both the final potential and kinetic energy can be defined as  $\Pi_p^{(1)} = \Pi_p^{(0)} + \delta \Pi_p$  and  $\Pi_k^{(1)} = \Pi_k^{(0)} + \delta \Pi_k$ . Therefore,

$$\delta \Pi_p + \delta \Pi_k + G_c \delta S = 0, \quad (1.2)$$

Since  $\delta \Pi_k \geq 0$ , we have

$$\delta \Pi_p + G_c \delta S \leq 0, \quad (1.3)$$

which is a necessary energy condition for crack nucleation since it derives from the unquestionable energy balance (1.1).

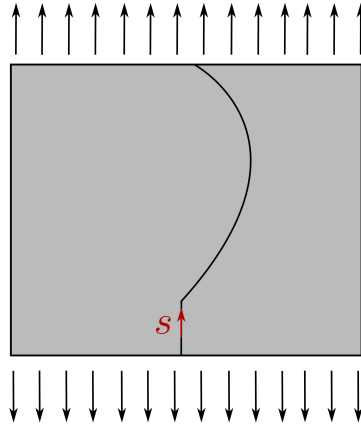


Figure 1.3: Expected crack path in a specimen.

In the following, equations will be defined in the 2D domain. It means that the condition can be rewritten considering the admissible crack extension  $\delta l$  (also called the newly created

crack length)

$$\delta\Pi_p + G_c\delta l \leq 0, \quad (1.4)$$

Being understood that  $\delta\Pi_p$  is now defined per unit thickness of the specimen. This is commonly written, introducing the Incremental Energy Release Rate (IERR) [43], as

$$-\frac{\delta\Pi_p}{\delta l} = G_{\text{inc}}(\delta l) \geq G_c, \quad (1.5)$$

In this relationship,  $\delta l$  is unknown. Griffith (1921) [44] considered the limit  $\delta l \rightarrow 0$

$$-\frac{\partial\Pi_p}{\partial l} = G \geq G_c, \quad (1.6)$$

where  $G$  is the Energy Release Rate (ERR). However, it is well-known that if there is no pre-existing crack  $G = 0$ , hence, the onset of a crack at a stress concentration point which is not a crack tip cannot be predicted using (1.6).

(ii) On the other hand, the stress condition is based on a maximum tension that a material can undergo, known as the tensile strength  $\sigma_c$ . According to the CC, the tensile stress in the initial state must be higher than the tensile strength all along the presupposed crack path to allow crack onset

$$\sigma(s) \geq \sigma_c \quad \text{for} \quad 0 \leq s \leq \delta l, \quad (1.7)$$

where  $s$  is the coordinate along the expected crack path (see Fig. 1.3). As a consequence of the two inequalities (1.5) and (1.7), it can be shown that the crack nucleation occurs abruptly from 0 to  $\delta l$ . It is important to highlight that this incremental form is the foundation of FFM, since it assumes the instantaneous formation of cracks of finite size [41], [43],[45] and [46]. Moreover, in the case of the CC this instantaneous crack onset is not an assumption but a consequence of the two inequalities (1.5) and (1.7), as shown in [43].

To sum up, the crack nucleation in a homogeneous structure is predicted by the CC using two necessary and together sufficient conditions

$$\bar{G}_{\text{inc}} = \frac{G_{\text{inc}}(\delta l)}{G_c} \geq 1, \quad (1.8)$$

$$\bar{\sigma} = \frac{\sigma(s)}{\sigma_c} \geq 1, \quad \text{for} \quad 0 \leq s \leq \delta l, \quad (1.9)$$

where the stress condition (1.9) is expressed as a non-local condition. Note that, in general,  $\sigma(s)$  is a decreasing function of  $s$  and the second inequality reduces to

$$\bar{\sigma} = \frac{\sigma(\delta l)}{\sigma_c} \geq 1, \quad (1.10)$$

which is called the Point Method, see [47] and [48]. According to [41], the stress condition can also be defined following the so-called Line-Method, based on the average stress along the prescribed crack path proposed by Cornetti et al. [49],

$$\frac{1}{\delta l} \int_0^{\delta l} \sigma(z) dz \geq \sigma_c. \quad (1.11)$$

Both the Point Method and Line Method are good approximations to experiments, giving very close results to each other. Note that when  $\sigma(s)$  is a decreasing function the non-local condition is the Point Method.

**Remark 1:** We denote the crack initiation length as  $\delta l_c$ . The crack initiation length corresponds to the admissible crack extension  $\delta l$  associated with the minimum load applied in the structure fulfilling the two conditions (1.8) and (1.9).

**Remark 2:** In this approach, the exact amount of kinetic energy that can be produced during the initiation process is ignored. It is simply considered as positive (see (1.2) and (1.3)). Its influence on the CC was studied by Laschuetza et al. [50], who explained that the load at initiation is well captured by the CC (at least in the case they study). Only the transient process following initiation is not described by the CC.

### 1.2.1.1 The CC in a heterogeneous structure

A special care must be brought when the crack is nucleated in a heterogeneous material. Hence, considering a structure with  $N$  different materials, the stress condition is written as a function of the tensile stress  $\sigma(s)$  along the expected crack path (i.e. prior to any crack extension), using  $s$  as a coordinate,

$$\bar{\sigma} = \frac{\sigma(s)}{\sigma_c(s)} \geq 1, \quad \text{for } 0 \leq s \leq \delta l. \quad (1.12)$$

being  $\delta l$  the newly created crack length. The tensile strength  $\sigma_c(s)$  is defined as

$$\sigma_c(s) = \sum_{i=1}^N \sigma_c^i [H(s - \delta l_{i-1}) - H(s - \delta l_i)], \quad (1.13)$$

where  $H$  is the Heaviside function and  $\delta l_0 = 0$ . In this PhD thesis we will work with two different heterogeneous structures, one with  $N = 2$  and another with  $N = 3$ . An example of a heterogeneous structure with  $N = 2$  is shown in Fig. 1.4.

In the energy condition the fracture energy is now considered for each material  $i$ ,  $G_c^i S_i$ ,

$$\Delta \Pi_p + \Delta \Pi_k + \sum_{i=1}^N G_c^i S_i = 0, \quad (1.14)$$

where  $S_i$  is the newly created crack surface and  $G_c^i$  is the critical energy release rate in each material  $i$ . In a bidimensional case, this balance holds per unit thickness of the specimen,

$$\Delta \Pi_p + \Delta \Pi_k + \sum_{i=1}^N G_c^i \delta l_i = 0, \quad (1.15)$$

and  $\delta l_i$  denotes the newly created crack length within each material  $i$ . Assuming the initial state to be quasi-static,  $\Delta \Pi_k \geq 0$ , the energy condition can be written as

$$\bar{G}_{\text{inc}} = -\frac{\Delta \Pi_p(\delta l)}{\delta l} \cdot \frac{1}{G_c(\delta l)} \geq 1, \quad (1.16)$$

where the parameter  $G_c(\delta l)$  is

$$G_c(\delta l) = \frac{\sum_{i=1}^N G_c^i \delta l_i}{\delta l}, \quad (1.17)$$

in which  $\delta l = \sum_{i=1}^N \delta l_i$ .

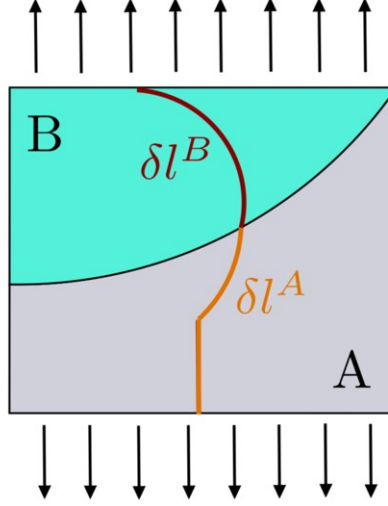


Figure 1.4: Expected crack path in a specimen with a heterogeneous structure.

As an example, if  $N = 2$  it means that the expected crack is formed by two segments (see Fig. 1.4), one in material A and the other in material B, with different material properties. Hence, the energy and stress condition are expressed as a function of the fracture properties of the two materials  $G_c^{A,B}$  and  $\sigma_c^{A,B}$ . In that context, (1.9) is splitted into two conditions, described as

$$\sigma(s) \geq \sigma_c^A, \quad \text{for } 0 \leq s \leq \delta l^A, \quad (1.18)$$

$$\sigma(s) \geq \sigma_c^B, \quad \text{for } \delta l^A \leq s \leq \delta l^A + \delta l^B. \quad (1.19)$$

On the other hand, the energy balance given in (1.4) is rewritten as

$$\delta \Pi_p + G_c^A \delta l^A + G_c^B \delta l^B \leq 0, \quad (1.20)$$

where  $\delta l^A$  and  $\delta l^B$  are the newly created crack lengths in materials A and B. Then the energy condition can be written

$$\frac{-\Delta \Pi_p}{\delta l^A + \delta l^B} = G_{\text{inc}}(\delta l^A, \delta l^B) \geq \frac{G_c^A \delta l^A + G_c^B \delta l^B}{\delta l^A + \delta l^B}. \quad (1.21)$$

### 1.2.1.2 Asymptotic approach

The Matched Asymptotics Expansion (MAE) procedure, is a quasi-analytical formulation that allows to find the elastic solution for applying the CC with low computational complexity.

It is particularly suitable to predict crack nucleation at the tip of sharp V-notches, under the assumption that the admissible crack extension  $\delta l$  is small compared to any dimension of the structure (in this case,  $\delta l$  is compared to the notch depth as a reference). It is based on the Williams' expansion [51], whose terms are described in the Annex 5.1. Before crack nucleation, the tensile stress at a distance  $\delta l$  is described as

$$\sigma(\delta l) = K\delta l^{\lambda-1} + \dots \quad (1.22)$$

where  $\lambda$  represents the singularity exponent and  $K$  the Generalized Stress Intensity Factor (GSIF). The IERR (see (1.5)) at a distance  $\delta l$  can be expanded as

$$G_{\text{inc}} = AK^2\delta l^{2\lambda-1} + \dots, \quad \text{with} \quad A = \frac{(1-\nu^2)A^*}{E} \quad (1.23)$$

with an appropriate normalization of  $s_{\theta\theta} = 1$ , see (5.6). The coefficient  $1-\nu^2$  relies on the plane strain assumption. In (1.23),  $A$  is a scaling coefficient calculated through a path-independent integral, see Annex 5.3, and  $A^*$  is a dimensionless scaling coefficient depending only on the opening angle  $\omega$ .

Following [43], the energy condition provides a lower bound for  $\delta l$  while the stress condition gives an upper bound. Then, using the Irwin length ( $l_{\text{Irwin}}$ ) [52], compatibility between the two conditions provides the crack initiation length  $\delta l_c$

$$\delta l_c = \frac{l_{\text{Irwin}}}{A^*}, \quad \text{with} \quad l_{\text{Irwin}} = \frac{EG_c}{(1-\nu^2)\sigma_c^2}. \quad (1.24)$$

To ensure the validity of the asymptotic expansions, its smallness is checked afterwards, i.e., we check that the initiation length is much smaller than the dimensions of the specimen. Finally, the CC takes the following form, involving the critical value  $K_c$  of the GSIF

$$K \geq K_c = \left( \frac{EG_c}{(1-\nu^2)A^*} \right) \sigma_c^{2\lambda-1}. \quad (1.25)$$

This holds true disregarding the way of loading.

As an example, Table 1.3 reports the crack length at initiation  $\delta l_c$  and the critical GSIF  $K_c$  for various opening angles. Material data are for alumina-zirconia ceramic, in which Young's modulus, Poisson's ratio, tensile strength and fracture energy are reported in [53] to be:  $E = 380$  GPa,  $\nu = 0.22$ ,  $\sigma_c = 400$  MPa and  $G_c = 0.023$  MPa mm ( $23$  J m<sup>-2</sup>).

Let us recall that for a crack ( $\omega = 0^\circ$ ) the parameter  $K$  is called Stress Intensity Factor (SIF) and  $K_c = K_{\text{IC}} = 38.23$  MPa mm<sup>1/2</sup>, derived from  $G_c$  using Irwin's formula. Moreover, note that no length is given for a crack ( $\omega = 0^\circ$ ), since Griffith's criterion [44] (with which coincides for a crack) does not involve any length. Indeed, observe that  $2\lambda - 1 = 0$  in (1.23) so that no lower bound exists for admissible crack extension lengths. Thus, any infinitely small extension can be considered, which justifies the use of derivative in (1.8) in case of a preexisting crack.

$\omega$	0°	30°	60°	90°	120°	150°
$\lambda$	0.5	0.502	0.512	0.545	0.616	0.752
$A^*$	6.28	6.16	5.82	5.18	4.25	3.03
$\delta l_c$ ( $\mu\text{m}$ )		9.3	9.7	11.1	13.5	18.9
$K_c$ ( $\text{MPa mm}^{1-\lambda}$ )	38.23	38.98	41.99	51.57	76.59	149.58

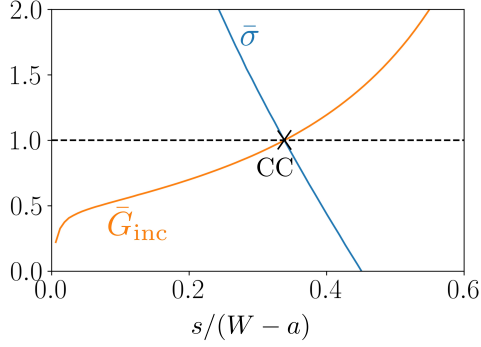
Table 1.3: CC parameters extracted from the asymptotic approach.

### 1.2.1.3 Full Finite Element approach

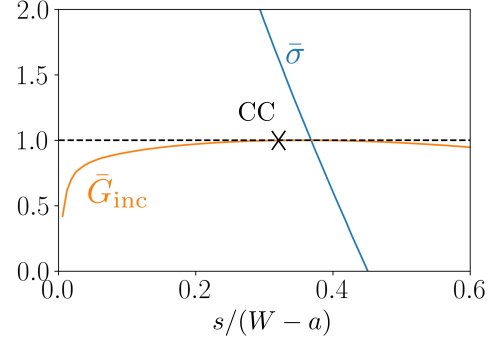
In some cases where the assumption of smallness of  $\delta l_c$  may not be verified, the Full Finite Element (FFE) approach [54] gets rid of this limitation. The whole structure under consideration is modelled by FE either under a prescribed displacement (DC) or a prescribed force (FC).

In a first step an undamaged configuration is considered, i.e. with no new crack in the structure. The tensile stress  $\sigma(s)$  along the expected crack path is computed together with the potential energy  $\Pi_p(0)$ . Then, nodes along the crack path are released one after the other, generating a virtual crack with an increasing length  $\delta l$ , and therefore  $\Pi_p(\delta l)$  is computed, which allows to calculate  $G_{\text{inc}}(\delta l)$ . Notice that several linear calculations are required to build the function  $G_{\text{inc}}(\delta l)$  in the FFE approach. We look for the minimum load at which the CC is fulfilled, where a crack with a length  $\delta l_c$  is nucleated. Obviously, the computational cost is higher than in the MAE approach. But, of course, this procedure is valid without restrictions, whereas the MAE approach needs a smallness assumption. In any case, whatever the approach, the numerical effort remains small compared to other approaches involving the resolution of nonlinear problems like cohesive zone models [55] or phase field method [56] and [57]. Notice that in the horizontal axis in Fig. 1.5 the coordinate  $s$  is normalized by the width of the specimen  $W - a$ , as it will be explained later.

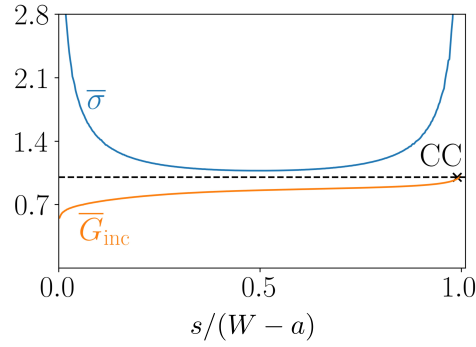
Different cases that could be met when implementing the CC are illustrated in Fig. 1.5 and refer to coming examples in Section 2.2. The load is gradually increased so that a first point fulfilling the two conditions of the CC appears (black cross). Fig. 1.5a is the classically encountered situation where  $\bar{\sigma}$  is a decreasing function while  $\bar{G}_{\text{inc}}$  is monotonically increasing. In Fig. 1.5b,  $\bar{\sigma}$  is still decreasing but  $\bar{G}_{\text{inc}}$  is no longer monotonically increasing, it goes through a maximum and then decreases. On the contrary, in Fig. 1.5c, it is  $\bar{\sigma}$  which is no longer monotonically decreasing while  $\bar{G}_{\text{inc}}$  is increasing. These situations were already discussed in [41] and [58].



(a) The U-notched specimen at the micro-scale under FC loading (Section 2.2.2.3)



(b) The U-notched specimen at the micro-scale under DC loading (Section 2.2.2.3)



(c) The double edge notched specimen at the nano-scale under DC loading (Section 2.2.3.2)

Figure 1.5: Examples of implementation of the CC. Stress condition (1.9): blue solid line, energy condition (1.8): orange solid line. The cross shows the CC point, defined by the minimum load that meets the two conditions.

## 1.2.2 Matched asymptotic expansions

The matched asymptotic expansion [59] can be used to predict the mechanical behaviour of a structure in the vicinity of an inclusion, a crack, or a cavity, see Fig. 1.6. The size of the perturbation, denoted as  $l$  in this PhD thesis, is assumed to be small compared to any dimension of the structure.

Some numerical difficulties are found when solving an elasticity problem in the actual domain  $\Omega_l$ , due to the small size of the perturbation. The use of very small elements in the vicinity of the perturbation increases the computational complexity of the problem, and leads to numerical errors that could be produced by strong gradients in the mesh size. For this reason, the matched asymptotic expansion is proposed to approximate the actual solution  $\underline{U}_l(x_1, x_2)$  in the neighbourhood of the perturbation. To that aim, a twofold representation of  $\underline{U}_l(x_1, x_2)$

is proposed, in the form of an outer and an inner expansion. The set of equations that defines the actual problem is

$$-\nabla_x \cdot \underline{\underline{\sigma}}_l = 0 \quad \text{in } \Omega_l, \quad (1.26)$$

$$\underline{\underline{\sigma}}_l = \mathbf{C} : \nabla_x \underline{U}_l \quad (1.27)$$

$$\underline{\underline{\sigma}}_l \cdot \underline{n} = \underline{h} \quad \text{on } \Gamma_N \quad (1.28)$$

$$\underline{\underline{\sigma}}_l \cdot \underline{n} = 0 \quad \text{on } \Gamma_V \cup \Gamma_l \quad (1.29)$$

$$\underline{U}_l = \bar{U} \quad \text{on } \Gamma_D \quad (1.30)$$

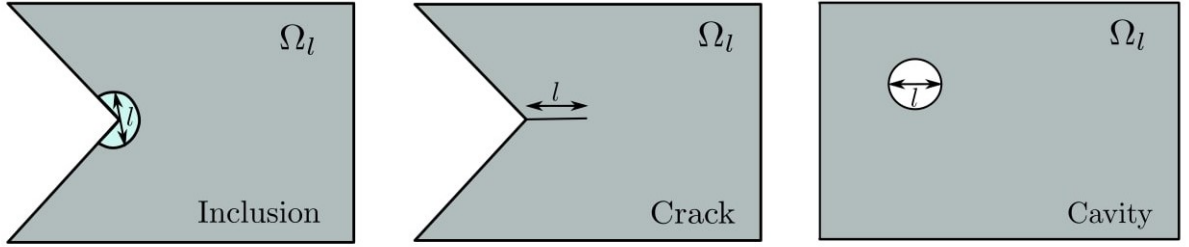


Figure 1.6: Examples of cases that can be studied applying the MAE. For display purposes in the representation  $l$  is not small compared to any dimension of the structure.

It is assumed that only homogeneous Neumann boundary conditions are set in the vicinity of the perturbation, whose contour is denoted as  $\Gamma_l$ . This notation can be observed in the example of a cavity that is shown in Fig. 1.7a, where  $\underline{h} = 0$ .

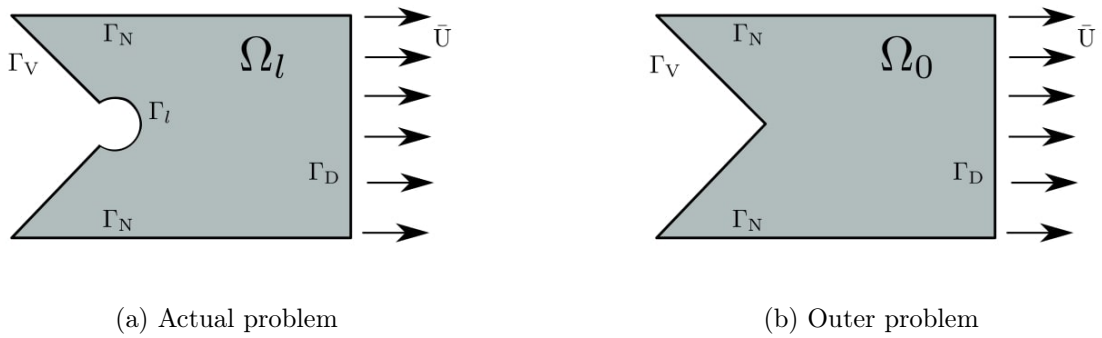


Figure 1.7: Examples of a cavity. Representation of the notation.

First, the actual solution  $\underline{U}_l(x_1, x_2)$  can be approximated by an outer expansion, represented as

$$\underline{U}_l(x_1, x_2) = \underline{U}_0(x_1, x_2) + \dots \quad (1.31)$$

where  $\underline{U}_0(x_1, x_2)$  is the solution of the same elasticity problem considering that the perturbation is not observable in the domain, i.e., solved in an unperturbed domain  $\Omega_0$ , see Fig. 1.7b as an example for a cavity. The second term in (1.31) denoted with an ellipsis is a "small correction" that decreases to 0 as  $l \rightarrow 0$ . The solution  $\underline{U}_0(x_1, x_2)$  is a good approximation of  $\underline{U}_l(x_1, x_2)$  far away from the perturbation. For this reason, it is called the outer field. The set of equations that defines the outer field is

$$-\nabla_x \cdot \underline{\underline{\sigma}}_0 = 0 \quad \text{in } \Omega_0, \quad (1.32)$$

$$\underline{\underline{\sigma}}_0 = \mathbf{C} : \nabla_x \underline{U}_0 \quad (1.33)$$

$$\underline{\underline{\sigma}}_0 \cdot \underline{n} = \underline{h} \quad \text{on } \Gamma_N \quad (1.34)$$

$$\underline{\underline{\sigma}}_0 \cdot \underline{n} = 0 \quad \text{on } \Gamma_V \quad (1.35)$$

$$\underline{U}_0 = \bar{U} \quad \text{on } \Gamma_D \quad (1.36)$$

A second expansion can be used to approximate the actual solution by introducing the change of variables  $y_i = x_i/l$  and  $\rho = r/l$ . In the limit when  $l \rightarrow 0$  we obtain an unbounded domain  $\Omega_{\text{in}}$  in which the characteristic length of the perturbation is now equal to 1, see Fig. 1.8 as an example, where the chosen characteristic length is the diameter of the cavity. The inner expansion is therefore expressed as

$$\underline{U}_l(x_1, x_2) = \underline{U}_l(l y_1, l y_2) = F_0(l) \underline{V}_0(y_1, y_2) + F_1(l) \underline{V}_1(y_1, y_2) + \dots \quad (1.37)$$

The set of equations related to the two terms  $\underline{V}_0(y_1, y_2)$  and  $\underline{V}_1(y_1, y_2)$  are

$$-\nabla_y \cdot \underline{\underline{\tilde{\sigma}}}_0 = 0 \quad \text{in } \Omega_{\text{in}}, \quad -\nabla_y \cdot \underline{\underline{\tilde{\sigma}}}_1 = 0 \quad \text{in } \Omega_{\text{in}},$$

$$\underline{\underline{\tilde{\sigma}}}_0 = \mathbf{C} : \nabla_y \underline{V}_0 \quad \underline{\underline{\tilde{\sigma}}}_1 = \mathbf{C} : \nabla_y \underline{V}_1$$

$$\underline{\underline{\tilde{\sigma}}}_0 \cdot \underline{n} = 0 \quad \text{on } \Gamma_V \cup \Gamma_l \quad \underline{\underline{\tilde{\sigma}}}_1 \cdot \underline{n} = 0 \quad \text{on } \Gamma_V \cup \Gamma_l$$

The inner problem is well-posed when the so-called matching conditions are added to these sets of equations. The inner expansion is a good approximation of the actual solution  $\underline{U}_l(x_1, x_2)$  in the neighbourhood of the perturbation, whereas the outer expansion properly approximates  $\underline{U}_l(x_1, x_2)$  far away from the perturbation. Hence, there must exist an intermediate region where both expansions are valid. In that region the matching conditions are defined.

The behaviour of the far field near the origin can be described by an expansion in powers of  $r$ , that can be the Taylor's expansion in the case of a smooth stress field or the Williams' expansion (see Annex 5.1) in case of a singularity. The latter can be expressed in polar coordinates as

$$\underline{U}(r, \theta) = \underline{U}(0, 0) + K r^\lambda \underline{u}(\theta) + \dots \quad (1.38)$$

assuming that the dominant term is real and have multiplicity one. The matching conditions can be expressed as

$$F_0(l) \underline{V}_0(y_1, y_2) \approx \underline{U}(0, 0), \quad \text{when } \rho \rightarrow \infty \quad (1.39)$$

$$F_1(l) \underline{V}_1(y_1, y_2) \approx K l^\lambda \rho^\lambda \underline{u}(\theta), \quad \text{when } \rho \rightarrow \infty \quad (1.40)$$

where the term  $\approx$  means "behaves like". It can be set

$$F_0(l) = 1 \quad \text{and} \quad \underline{V}^0(y_1, y_2) \approx \underline{U}(0, 0), \quad \text{when } \rho \rightarrow \infty \quad (1.41)$$

$$F_1(l) = Kl^\lambda \quad \text{and} \quad \underline{V}^1(y_1, y_2) \approx \rho^\lambda \underline{u}(\theta). \quad \text{when } \rho \rightarrow \infty \quad (1.42)$$

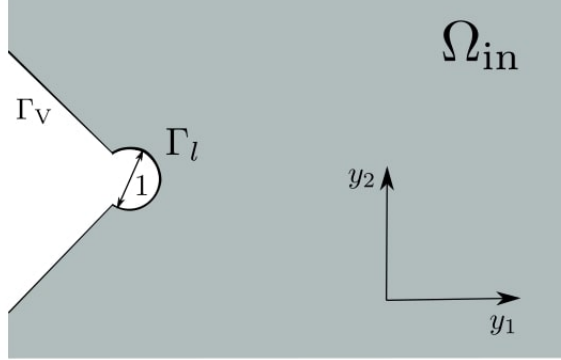


Figure 1.8: Scheme of the inner problem.

However, it can be shown that the matching condition over  $\underline{V}_1(y_1, y_2)$  does not fulfill the Lax-Milgram theorem, since it has an infinite energy in the unbounded domain  $\Omega_{\text{in}}$ , while it should decrease to 0 at infinity to have a finite energy. For this reason, the superposition principle is applied,

$$\underline{V}_1(y_1, y_2) = \rho^\lambda \underline{u}(\theta) + \hat{\underline{V}}_1(y_1, y_2) \quad (1.43)$$

where  $\hat{\underline{V}}_1(y_1, y_2)$  is the solution to a well-posed problem. The set of equations that defines the new term  $\hat{\underline{V}}_1(y_1, y_2)$  is

$$\begin{aligned} -\nabla_y \cdot \underline{\hat{\sigma}}_1 &= 0 && \text{in } \Omega_{\text{in}}, \\ \underline{\hat{\sigma}}_1 &= \mathbf{C} : \nabla_y \hat{\underline{V}}_1 \\ \underline{\hat{\sigma}}_1 \cdot \underline{n} &= 0 && \text{on } \Gamma_l \\ \hat{\underline{V}}_1 &\approx 0 && \text{as } \rho \rightarrow \infty \\ \underline{\hat{\sigma}}_1 \cdot \underline{n} &= -\mathbf{C} : \nabla_y (\rho^\lambda \underline{u}(\theta)) \cdot \underline{n} && \text{on } \Gamma_V \end{aligned}$$

where matching conditions have already been included in the formulation. Finally, it is obtained that

$$\underline{U}_l(x_1, x_2) = \underline{U}_l(l y_1, l y_2) = F_0(l) \underline{U}(0, 0) + Kl^\lambda \left[ \rho^\lambda \underline{u}(\theta) + \hat{\underline{V}}_1(y_1, y_2) \right] + \dots \quad (1.44)$$

The solution  $\hat{\underline{V}}_1(y_1, y_2)$  has finite energy at infinity.

### 1.2.3 Phase Field model for brittle fracture

**Initial Remark:** although a variety of PF models can be found in the literature, the one applied in this PhD thesis is also a gradient damage model, as explained below, and therefore we will refer to it using both terms depending on the context.

Fracture in brittle materials can be modelled as the nucleation and propagation of cracks, generating a decrease in the stiffness of the structure [60]. There are two methods for modeling such phenomena: discrete and continuous models. In discrete models, such as the very well-known Griffith model [44] or the Coupled Criterion [43], the crack is treated as a discontinuity in the material. On the other hand, continuous models define the crack as a damaged zone where the stiffness is degraded. Generally, discrete models are simpler than continuous models, but they can not be applied when the crack path is unknown a priori.

Damage models [60] are a type of continuous models where an internal variable named as damage variable is used to define the stiffness degradation. In standard damage models a variational formulation is used, based on the local minimization of the total energy in the system [61], that is defined as the sum of the elastic and dissipated energy. Moreover, in local damage models the failure is primarily governed by local conditions, f.e., when the damage variable reaches a certain value at a material point. These models are commonly applied to stress hardening structures (after failure the stress is increased, a common phenomenon given for example in plasticity), but their applicability is limited in case of stress softening systems, since the evolution problem becomes ill-posed [60], and results obtained are very mesh dependent. In such systems, gradient damage models, where a non-local term is included in the formulation, are a good alternative. The non-local term depends on the gradient of the damage variable, leading to the introduction of an internal length scale.

A gradient damage model for brittle fracture was introduced in [62], inspired by the variational formulation for brittle fracture [56]. In this formulation the mechanical behaviour of a cracked solid (Fig. 1.9) is defined using the minimization of the functional

$$\Psi(\Gamma, \underline{u}) = \int_{\Omega/\Gamma} \psi_{\text{el}}(\underline{u}) dx + \int_{\Gamma} \psi_{\text{d}}(\Gamma, \underline{u}) ds, \quad (1.45)$$

where  $\psi_{\text{el}}(\underline{u})$  is the elastic energy density and  $\psi_{\text{d}}(\Gamma, \underline{u})$  is the fracture energy density dissipated in the crack. The second term of (1.45) represents the total dissipated energy in the solid, expressed as an integral in the crack surface  $\Gamma$ , see Fig. 1.9. An essential irreversibility condition is included to avoid healing: at time step  $i$   $\Gamma_i \supset \Gamma_{i-1}$ .

The numerical implementation of the problem was achieved approximating the functional  $\Psi(\Gamma, \underline{u})$  by a regularized elliptical functional [63], named as  $\Psi_{l_{\text{PF}}}(s_{\text{d}}, \underline{u})$ . This regularization is based on the theory of image segmentation in [64] and the regularization made in [65]. In this approximation, the dissipated energy is expressed as a domain integral, and therefore the regularized functional is defined as

$$\Psi_{l_{\text{PF}}}(s_{\text{d}}, \underline{u}) = \int_{\Omega} \psi_{\text{el}}(s_{\text{d}}, \underline{u}) dx + \frac{G_{\text{c}}}{l_{\text{PF}}} \int_{\Omega} \left( \frac{1}{4}(1 - s_{\text{d}}^2) + l_{\text{PF}}^2 |\nabla s_{\text{d}}|^2 \right) dx. \quad (1.46)$$

The variable  $s_d$  denotes if the material is completely damaged  $s_d = 0$  or not damaged  $s_d = 1$ . Moreover,  $l_{PF}$  is a length parameter obtained when including the gradient in the integral, defined as the width of the regularized crack. Based on  $\Gamma$ -convergence [65], it can be shown that the global minimizer of (1.46) tends to the global minimizer of (1.45) when  $l_{PF} \rightarrow 0$ . This was also explained using Matched Asymptotics Expansion in [66].

The damage variable  $s_d$  used in [63] is frequently substituted by  $\alpha$ , where  $\alpha = 0$  means no damage and  $\alpha = 1$  complete failure. Moreover,  $\alpha$  is usually named as the phase field parameter, since the formulation introduced in [63] can be interpreted as a degenerated Phase Field model. Using this notation, the regularized version of the irreversibility condition is defined as  $\dot{\alpha} \geq 0$  [67].

In the regularized model proposed in [63] there was no distinction between tension and compression, which can lead to unrealistic crack patterns [68]. For this reason, a modified regularized formulation including a decomposition of the elastic energy is proposed in [67] (see Section 1.2.3.2 for more details).

A thermodynamically consistent formulation of the Phase Field model for brittle fracture was presented in [57]. In this formulation viscous effects were also considered, as well as a new spectral decomposition of the elastic energy to include stress degradation only in tension, slightly different from the one introduced in [67]. The irreversibility condition is included using a history-field variable  $H(\underline{x}, \tau)$  [69] evaluated at each material point  $\underline{x}$  and time  $\tau$ ,

$$H(\underline{x}, \tau) = \max_{s \in \tau} \psi_{el}^+(\underline{x}, s). \quad (1.47)$$

where  $\psi_{el}^+(\underline{x}, \tau)$  is the elastic energy density related to tension. Therefore, the fracture phase field model is presented as a set of two equations

$$\nabla \cdot \underline{\sigma} + \underline{f} = 0, \quad (1.48)$$

$$\frac{G_c}{l_{PF}} (\alpha - l_{PF}^2 \Delta \alpha) - 2(1 - \alpha)H = 0, \quad (1.49)$$

where  $\underline{f}$  is the vector of volumetric forces. The proposed formulation allowed the numerical implementation of the PF model in some commercial codes, such as ABAQUS [70].

When the parameter  $l_{PF}$  is interpreted as an internal length of the material the model can be considered as a gradient damage model [61, 62].

**Remark:** throughout this document  $\alpha$  will be used to denote the damage variable.

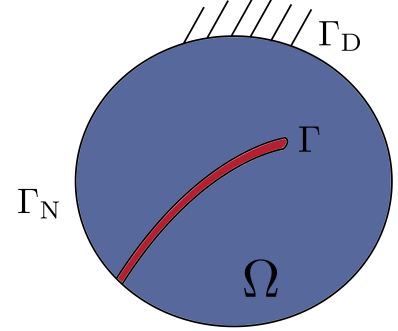


Figure 1.9: Scheme of the cracked solid

### 1.2.3.1 Definition of an isotropic gradient damage model for brittle fracture

The mechanical behaviour of a damaged solid made of a brittle material [60] is characterized by:

- A damage variable  $\alpha$  which fulfills  $0 \leq \alpha \leq 1$  ( $\alpha = 0$  denotes no damage and  $\alpha = 1$  complete damage).
- A state:  $(\alpha, \nabla\alpha, \underline{\underline{\varepsilon}}(\underline{u}))$ .
- An energy density  $\psi_{l_{\text{PF}}}(\alpha, \nabla\alpha, \underline{\underline{\varepsilon}}(\underline{u}))$
- The so-called dual quantities of  $\psi_{l_{\text{PF}}}$ :  $\underline{\underline{\sigma}}$  (the stress tensor),  $Y$  (the energy release rate density) and  $\underline{q}$  (the damage vector flux):

$$\underline{\underline{\sigma}} = \frac{\partial\psi_{l_{\text{PF}}}}{\partial\underline{\underline{\varepsilon}}}, \quad Y = -\frac{\partial\psi_{l_{\text{PF}}}}{\partial\alpha}, \quad \underline{q} = \frac{\partial\psi_{l_{\text{PF}}}}{\partial\nabla\alpha}, \quad (1.50)$$

The total energy density in the system  $\psi_{l_{\text{PF}}}$  is defined as

$$\psi_{l_{\text{PF}}}(\alpha, \nabla\alpha, \underline{\underline{\varepsilon}}(\underline{u})) = \psi_{el}(\alpha, \underline{\underline{\varepsilon}}(\underline{u})) + w(\alpha) + \frac{1}{2}w_1 l_{\text{PF}}^2 \nabla\alpha \cdot \nabla\alpha. \quad (1.51)$$

The elastic energy density  $\psi_{el}(\alpha, \underline{\underline{\varepsilon}}(\underline{u}))$  is:

$$\psi_{el}(\alpha, \underline{\underline{\varepsilon}}(\underline{u})) = \frac{1}{2} \left( A(\alpha) : \underline{\underline{\varepsilon}}(\underline{u}) \right) : \underline{\underline{\varepsilon}}(\underline{u}), \quad (1.52)$$

being the stiffness tensor  $A(\alpha)$  characterized by  $A(0) = A_0$ , the stiffness tensor of the pristine material, and  $A(1) = 0$ . Moreover, the dissipated energy is made by a local term  $w(\alpha)$  and a non-local term depending on the damage gradient. Notice that  $w(1) = w_1$  corresponds to the total energy dissipated in a damage process in a solid volume element. An internal length parameter  $l_{\text{PF}}$  appears in the formulation.

The total energy in the system can be defined as

$$P_\tau(\underline{v}, \beta) = \int_{\Omega} \psi_{l_{\text{PF}}}(\beta, \nabla\beta, \underline{\underline{\varepsilon}}(\underline{v})) dx - \Psi_f(\underline{v}) \quad \underline{v} \in \mathcal{W}_v \text{ and } \beta \in \mathcal{W}_\beta \quad (1.53)$$

where  $\Psi_f(\underline{v})$  is the work of external forces at a certain time  $\tau$ ,

$$\Psi_f(\underline{v}) = \int_{\Omega} \underline{f}_\tau \cdot \underline{v} dx + \int_{\Gamma_N} \underline{F}_\tau \cdot \underline{v} ds, \quad \underline{v} \in \mathcal{W}_v \quad (1.54)$$

and

$$\mathcal{W}_v = \{ \underline{v} : \underline{v} = \underline{U} \text{ on } \Gamma_D \}, \quad (1.55)$$

$$\mathcal{W}_\beta = \{ \beta : 0 \leq \beta \leq 1 \text{ in } \Omega \}, \quad (1.56)$$

where  $\Gamma_D$  and  $\Gamma_N$  are the Dirichlet and Neumann boundaries of the solid, see Fig. 1.9. The solution  $(\underline{u}_\tau, \alpha_\tau)$  at a certain time  $\tau$  fulfills the damage evolution law:

- Principle of irreversibility  $\dot{\alpha} \geq 0 \forall \tau \geq 0$
- Principle of stability: the solution  $(\underline{u}_\tau, \alpha_\tau)$  must be stable  $\forall \tau$  and therefore

$$\exists \bar{h} > 0 : \forall h \in [0, \bar{h}] \quad P_\tau(\underline{u}_\tau, \alpha_\tau) \leq P_\tau(\underline{u}_\tau + h(\underline{v} - \underline{u}_\tau), \alpha_\tau + h(\beta - \alpha_\tau)), \quad (1.57)$$

$\forall \underline{v} \in \mathcal{W}_v$  and  $\beta \in \mathcal{W}_\beta$ .

- Principle of balanced energy: the energy must always be conserved.

$$P_\tau(\underline{u}_\tau, \alpha_\tau) = P_0(\underline{u}_0, \alpha_0) + \int_0^\tau \left( \int_\Omega \underline{\sigma}_s : \underline{\varepsilon}_s dx - \Psi_f(\dot{\underline{u}}_s) - \dot{\Psi}_f(\underline{u}_s) \right) ds. \quad (1.58)$$

According to [60], these conditions are fulfilled if the equilibrium equation of the elastic problem and the Kuhn-Tucker conditions are simultaneously fulfilled. This is true only for the first order of stability conditions, but it is not sufficient for the second order of stability. The Kuhn-Tucker conditions applied on the solution  $(\underline{u}_\tau, \alpha_\tau)$  at time  $\tau$  are:

- Irreversibility:  $\dot{\alpha}_\tau \geq 0$
- Damage criterion:  $\nabla \cdot \underline{q}_\tau + Y_\tau \leq 0$  in  $\Omega$
- Energy balance:  $(\nabla \cdot \underline{q}_\tau + Y_\tau) \dot{\alpha}_\tau = 0$  in  $\Omega$
- Boundary conditions:  $\underline{q}_\tau \cdot \underline{n}_\tau \cdot \dot{\alpha}_\tau \geq 0$  and  $\underline{q}_\tau \cdot \underline{n}_\tau \geq 0$  on  $\Gamma_N \cup \Gamma_D$ , the outer contour of the solid.

### 1.2.3.2 Implementation of the gradient damage model

In the previous section, the concept of a gradient damage model was introduced. However, it was not specified for any particular damage law or stiffness evolution. In this section, the previous model is specialized for numerical implementation, providing an expression for the damage law as well as the evolution of stiffness, based on explanations found in [60] and [71]. At a certain time  $\tau$  we can describe  $\psi_{l_{\text{PF}}}(\alpha_\tau, \underline{\varepsilon}(\underline{u}_\tau), \nabla \alpha_\tau)$  as

$$\psi_{l_{\text{PF}}}(\alpha_\tau, \underline{\varepsilon}(\underline{u}_\tau), \nabla \alpha_\tau) = \psi_{el}(\alpha_\tau, \underline{\varepsilon}(\underline{u}_\tau)) + \frac{G_c}{l_{\text{PF}} c_w} (w(\alpha_\tau) + l_{\text{PF}}^2 \|\nabla \alpha_\tau\|^2). \quad (1.59)$$

The function  $w(\alpha_\tau)$  and the coefficient  $c_w$  can be defined

$$w(\alpha_\tau) = \alpha_\tau \quad \text{and} \quad c_w = 8/3, \quad (1.60)$$

if an elastic phase with no damage ( $\alpha_\tau = 0$ ) is considered, after which there is a damaged phase where the damage variable evolves until the complete damage  $\alpha_\tau = 1$ . This model is known as the AT1 model [71]. If, on the contrary, no elastic phase is included, the following functions can be used

$$w(\alpha_\tau) = \alpha_\tau^2 \quad \text{and} \quad c_w = 2, \quad (1.61)$$

which is known as AT2 model [71].

The elastic energy density given in (1.52) is split into  $\psi_{el}^+(\alpha_\tau, \underline{\underline{\varepsilon}}(\underline{u}_\tau))$  and  $\psi_{el}^-(\alpha_\tau, \underline{\underline{\varepsilon}}(\underline{u}_\tau))$ , being respectively related to traction and compression strain components:

$$\psi_{el}(\alpha_\tau, \underline{\underline{\varepsilon}}(\underline{u})) = ((1 - \alpha_\tau)^2 + k_{\text{res}}) \psi_{el}^+(\alpha_\tau, \underline{\underline{\varepsilon}}(\underline{u}_\tau)) + \psi_{el}^-(\underline{\underline{\varepsilon}}(\underline{u}_\tau)), \quad (1.62)$$

where  $k_{\text{res}}$  is a residual parameter artificially included to prevent the stiffness from being completely zero in numerical computations when the damage is complete in the structure. This parameter is typically very small, around  $10^{-6}$ . In this work, the strain energy split is based on the volumetric-deviatoric decomposition presented in [67].

$$\psi_{el}^+(\alpha_\tau, \underline{\underline{\varepsilon}}(\underline{u}_\tau)) = \frac{B}{2} \langle \text{tr}(\underline{\underline{\varepsilon}}(\underline{u}_\tau)) \rangle_+^2 + A_0 : \underline{\underline{\varepsilon}}'(\underline{u}_\tau) : \underline{\underline{\varepsilon}}'(\underline{u}_\tau), \quad (1.63)$$

$$\psi_{el}^-(\underline{\underline{\varepsilon}}(\underline{u}_\tau)) = \frac{B}{2} \langle \text{tr}(\underline{\underline{\varepsilon}}(\underline{u}_\tau)) \rangle_-^2, \quad (1.64)$$

being  $\langle \text{tr}(\underline{\underline{\varepsilon}}) \rangle_{\pm} = \frac{\text{tr}(\underline{\underline{\varepsilon}}) \pm |\text{tr}(\underline{\underline{\varepsilon}})|}{2}$  and  $B$  the bulk modulus of the material.

For its application on 2D or 3D structures, the FEM is used, applying either a monolithic or a staggered scheme. Monolithic schemes are more efficient, because the solution is obtained with only one loop of iterations [68]. In this work, however, we use a staggered scheme, since they have more robustness. For each time  $\tau$ , an iterative process starts. First, the displacement field  $\underline{u}_\tau^i$  at iteration  $i$  is obtained while keeping constant the damage variable  $\alpha_\tau^i = \alpha_t^{i-1}$ . Then, the damage variable at iteration  $i$  denoted as  $\alpha_\tau^i$  is calculated keeping constant  $\underline{u}_\tau^i$ . The process is iterated until the algorithm finds a convergence, based on  $|\alpha_\tau^i - \alpha_\tau^{i-1}| < \text{Tol}$ , where Tol is a tolerance. Note that the first iteration  $i = 1$  uses the damage variable from the previous step  $\alpha_{t-1}$ . More information on this process can be found in Annex 5.4.2.

### 1.2.3.3 A simple case: 1D solution

Many authors have used the 1D solution of the PF model for brittle fracture to explain in a simple way how this model work. The key advantage is that analytic developments can be obtained. In [57] an infinite long bar with the following boundary conditions:  $\alpha(0) = 1$  and  $\alpha(\pm\infty) = 0$  is introduced, characterized by the damage evolution (represented in Fig. 1.10)

$$\alpha(x) = e^{-|x|/l_{\text{PF}}}. \quad (1.65)$$

The damage law in (1.65) is the Euler equation of the variational principle

$$\alpha = \text{Arg} \left\{ \inf_{\alpha \in \mathcal{W}_\alpha} \Gamma_{l_{\text{PF}}}(\alpha) \right\}. \quad (1.66)$$

where  $\mathcal{W}_\alpha = \{\alpha | \alpha(0) = 1, \alpha(\pm\infty) = 0\}$  and the functional  $\Gamma_{l_{\text{PF}}}(\alpha)$  is

$$\Gamma_{l_{\text{PF}}}(\alpha) = \frac{1}{2l_{\text{PF}}} \int_{\Omega} \left( \alpha^2 + l_{\text{PF}}^2 \alpha'^2 \right) dx. \quad (1.67)$$

This analytical development was generalized for a 2D/3D model, defining the dissipated energy in the system in [69]. Moreover, it clearly illustrates the physical meaning of the phase

field length scale, since it defines the width of the regularized damage region (Fig. 1.10).

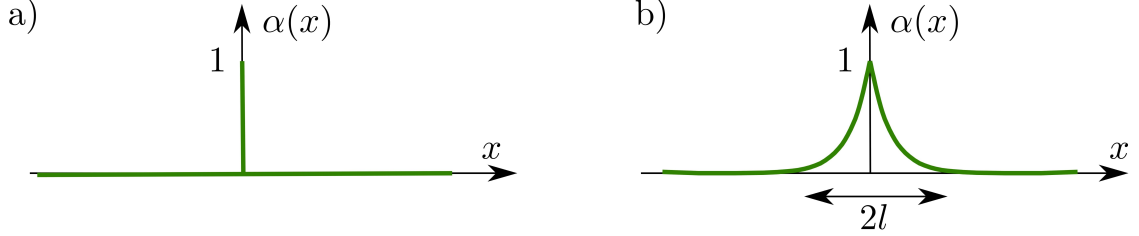


Figure 1.10: Scheme of the infinite long bar and the damage evolution  $\alpha(x)$ . In (a) the discrete evolution is represented, whereas in (b) the continuous evolution given by (1.65) is shown.

In [60], the damage gradient model can be applied in the traction test of a one-dimensional bar of length  $L$  made of homogeneous material with stress softening. This simple study is the basis for the definition of the internal length  $l_{PF}$  as a function of the Irwin length  $l_{Irwin}$ . Only the axial displacement is defined in the 1D problem, see Fig. 1.11, and therefore the boundary conditions are written as

$$u_\tau(x=0) = 0, \quad u_\tau(x=L) = U_\tau \quad \text{and} \quad U_0 = 0. \quad (1.68)$$

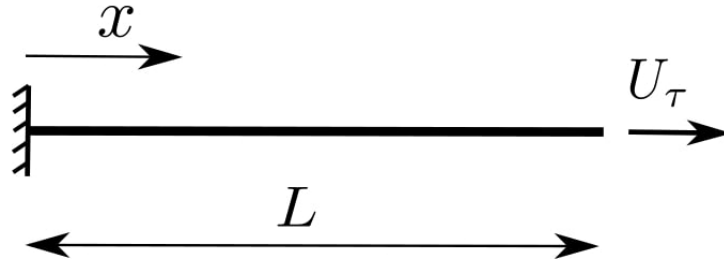


Figure 1.11: Scheme of the 1D tensile test

As it was mentioned above, the solution to this problem  $(u_\tau, \alpha_\tau)$  at a certain time  $\tau$  is obtained applying the equilibrium together with the Kuhn-Tucker conditions. In this case after the equilibrium condition we obtain that the stress is constant along the bar

$$\sigma'_\tau = 0 \rightarrow \sigma_\tau = A(\alpha_\tau(x))\varepsilon_\tau = A(\alpha_\tau(x))u'_\tau, \quad (1.69)$$

where  $(\cdot)' = \partial(\cdot)/\partial x$ . After applying the boundary conditions the tensile stress in the bar

$$\sigma_\tau = u_\tau \int_0^L A(\alpha_\tau(x)) dx. \quad (1.70)$$

The following conditions are obtained from the application of the Kuhn-Tucker conditions using the energy density presented in (1.59),

- Irreversibility:  $\dot{\alpha}_\tau \geq 0$ . Initially there is no damage  $\alpha_0 = 0$
- Damage criterion:  $-\frac{2l_{\text{PF}}G_c}{c_w}\alpha_\tau'' - A_0(1 - \alpha_\tau)u_\tau'^2 + \frac{G_c}{l_{\text{PF}}c_w}\frac{\partial w}{\partial \alpha_\tau} \geq 0$
- Energy balance:  $\dot{\alpha}_\tau \left( -\frac{2l_{\text{PF}}G_c}{c_w}\alpha_\tau'' - A_0(1 - \alpha_\tau)u_\tau'^2 + \frac{G_c}{l_{\text{PF}}c_w}\frac{\partial w}{\partial \alpha_\tau} \right) = 0$
- Boundary conditions:  $\alpha_\tau'(0) \leq 0$  and  $\alpha_\tau'(L) \geq 0$ .

We now assume that the damage variable at a certain time  $\tau$  is constant along the bar  $\alpha_\tau(x) = \alpha_\tau$ . The solution derived from this hypothesis is called homogeneous solution, and it always fulfills the boundary conditions described in the last item of the list above. In the homogeneous solution the tensile stress is also constant along the bar and therefore the displacement is  $u_\tau(x) = \tau x$ .

Two models are defined. In the first one an initial elastic phase is considered, followed by a damaged phase. In the elastic phase there is no damage in the bar, and therefore  $\alpha_\tau = \dot{\alpha}_\tau = 0$ . The solution corresponds to the one of the elastic problem. Notice that during the elastic phase the irreversibility and the energy balance are verified, but not the damage criterion.

The last point of the elastic phase corresponds to the critical point where the damaged phase is initiated. At that point, all the Kuhn-Tucker conditions are together fulfilled. Starting from an undamaged configuration of the solid,  $\alpha_\tau = 0$ , the damage starts growing only if  $\dot{\alpha}_\tau > 0$  at a certain time  $\tau$ . Hence, the energy balance and the damage criterion are fulfilled only if

$$A_0(1 - \alpha_\tau)u_\tau'^2 - \frac{G_c}{l_{\text{PF}}c_w}\frac{\partial w}{\partial \alpha_\tau} = 0. \quad (1.71)$$

Notice that  $\alpha_\tau' = 0$ , since we are considering the homogeneous solution. Applying (1.60), the damage evolution is now written as a function of the tensile strain as

$$\alpha_\tau(t) = 1 - \frac{3G_c}{8l_{\text{PF}}A_0\tau^2}, \quad (1.72)$$

and therefore the tensile stress

$$\sigma_\tau = A_0\frac{\tau_c^4}{\tau^3} \quad (1.73)$$

where  $\tau_c = \sigma_c/A_0$  is the critical tensile strain. Notice that prior to the damaged phase the stress increases with growing  $\tau$ , whereas it decreases in the damaged phase. Hence, there is a peak stress at the end of the elastic phase, where  $\sigma_\tau = \sigma_c$ , a critical value that is the tensile strength. This model is called AT1 model [71], and the phase field length scale in (1.59) is therefore described as

$$l_{\text{PF}} = \frac{3G_cA_0}{8\sigma_c^2} = \frac{3}{8}l_{\text{Irwin}}, \quad (1.74)$$

On the other hand, a different model can be studied without the elastic phase. In that case,  $\dot{\alpha}_0 > 0$  and the Kuhn-Tucker conditions must always be fulfilled from the beginning of the

loading. From (1.71) the damage evolution is now written as a function of the tensile strain as

$$\alpha_\tau(\tau) = \frac{A_0\tau^2}{A_0\tau^2 + \frac{G_c}{l_{PF}}} \quad (1.75)$$

and therefore the tensile stress

$$\sigma_\tau = \frac{A_0\tau}{\left(1 + \frac{t^2}{2\tau_c^2}\right)^2}. \quad (1.76)$$

Again, it is a stress softening system after a certain peak stress, since the tensile stress is reduced with growing  $\tau$  for  $\tau > \tau_c$ . Notice that this critical value of the tensile strain is not the same as in the AT1 model. This model is called AT2 model, and the phase field length scale is written

$$l_{PF} = \frac{27G_c A_0}{256\sigma_c^2} = \frac{27}{256} l_{Irwin}. \quad (1.77)$$

In Fig. 1.12 the evolution of  $\sigma/\sigma_c$  is represented as a function of  $\tau/\tau_c$  for the AT1 and the AT2 model. The slope in the damage phase of the AT1 model is much higher than in the AT2 model. It means that the damage evolves faster in the AT1.

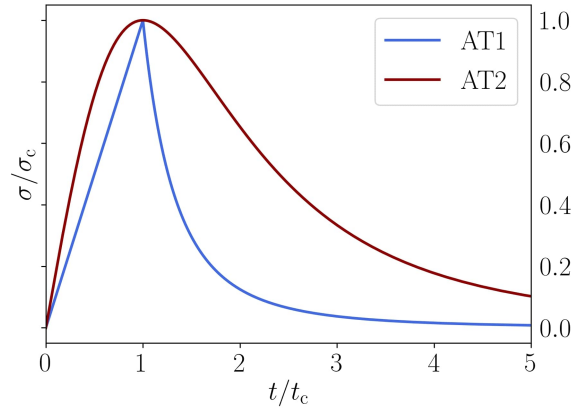


Figure 1.12: Evolution of the tensile stress with respect to the tensile strain in the 1D test according to the AT1 and the AT2 models.

### 1.3 Aims and objectives

As it was explained in previous sections, ceramic materials are widely used in the industry owing to their countless advantages, such as the resistance to corrosion or oxidation. However, they have a very low fracture toughness, which is related to the spontaneous brittle failure of the component. In this context, the main objective of this thesis is the consistent extension of numerical modelling tools in fracture mechanics for predicting crack nucleation and growth in advanced ceramics, with a special emphasis in the relationship between the micro and macro-scale characteristics within these materials. Two approaches are followed:

---

the Coupled Criterion (CC) within the Finite Fracture Mechanics (FFM) framework and the Phase Field (PF) model for fracture.

An inherent property of materials is an internal length frequently named as the Irwin length, that depends on the fracture properties. At the macro-scale, this length is small compared to the dimensions of the specimen. However, at the micro-scale it is of the same order of magnitude or even larger and can interact with the dimensions of the structure. In Chapter 2, this phenomenon is studied considering two different numerical tools. First, in the framework of FFM, a crack is assumed to jump a given finite length at onset, and the CC estimates that this length is proportional to the internal length of the material. On the other hand, in the PF model for brittle fracture there is a length related to the size of the damaged region, called the phase field length scale, that is also proportional to the internal length of the material.

In Chapter 2 we study the answer brought by both the CC and the PF model when descending the scales from the cm-scale to the  $\mu\text{m}$ -scale and even nm-scale. This would help to better describe ceramic materials at the micro-scale, and therefore to enhance the design of advanced ceramics, which is commonly based on changing the micro-structure of classical ceramics to generate new materials with improved mechanical properties. One type of these new structures is deeply studied in Chapter 3, made of brittle matrices reinforced by short fibers or platelets. They are analyzed using numerical techniques that avoid the controversial conclusions obtained about fracture properties when descending the scales in ceramics.

Thus, in Chapter 3 we develop a computational tool to study the fracture behaviour of such composites, based on the connection between the micro- and the macro-scale. The aim of this tool is to provide an insight into the changes generated in the crack propagation when it encounters the reinforcing element, estimating the apparent fracture toughness of the composite as a function of design parameters.

To sum up, two parts are distinguished in this thesis. The first one (Chapter 2) is dedicated to the study of ceramics fracture properties at the micro-scale. In the second part (Chapter 3) we focus on the fracture analysis of brittle materials reinforced by a second constituent in the form of micro-platelets or short fibers, a kind of structure of high technological interest for advanced ceramics.

# Chapter 2

## Ceramic fracture properties at the micro-scale

### Contents

---

<b>2.1</b>	<b>Introduction</b>	<b>28</b>
<b>2.2</b>	<b>FFM of brittle materials at the micro-scale</b>	<b>29</b>
<b>2.3</b>	<b>PF model of brittle materials at the micro-scale</b>	<b>51</b>
<b>2.4</b>	<b>Conclusions</b>	<b>64</b>

---

At the macro-scale, the Irwin length is small compared to any dimension of the structure, whereas at the micro-scale it is of the same order of magnitude or even larger and can interact with the dimensions of the specimen. This could strongly affect two important methodologies to predict crack nucleation in brittle materials, the Coupled Criterion (CC) and the Phase Field (PF) model, that depends on a length parameter proportional to the Irwin length. Then, the question that arises is: can fracture mechanics theories be extended to small scales? The main objective of this chapter is to analyse the applicability of the CC and the PF at the micro-scale through case studies and comparisons to experiments. In particular, it discusses the reliability of experiments made at the micro- and nano-scale to obtain fracture properties, since an apparent strengthening of the material due to its smallness is observed, disregarding any statistical consideration on the presence and size of defects. It is important to highlight that a part of the work presented in this chapter is published in [72] and [73] and the other part will be sent to a journal in the following months.

## 2.1 Introduction

One of the fundamental ingredients of the recent methodology FFM for the prediction of crack events in materials and structures, is that a crack is assumed to jump a given finite length at onset. This can be formulated through the invocation of the CC presented in [43], stating that this length depends on the material toughness, the tensile strength but also the geometry. Complying with a different vision, according to [67] and [63], in the PF model for brittle fracture, there exists a material related length that describes the size of the damaged region, called the phase field length scale. Both the PF length scale and the nucleation length obtained by the CC are proportional to the Irwin length defined by the material toughness and the tensile strength. At the macro-scale, they are small compared to any dimension of the structure, whereas at the micro-scale both lengths have the same order of magnitude or even larger and can interact with the dimensions of the structure.

In the first part of this chapter the issue is examined via the CC when descending the scales from the macro-scale to the micro-scale. FFM [45, 46, 43, 41], and more precisely the CC [43, 41] has been successfully used to predict the crack onset at the macro-scale. Attempts to use the CC at the micro-scale have been made in [8, 10] and have brought into evidence how important a good knowledge of the fracture parameters (strength and fracture energy or toughness) is at this scale.

The analysis made with the CC is dedicated to case studies and comparison with experiments. In particular, it starts by a preliminary remark in which a bar in tension is analysed to bring into evidence the interpretation of the CC depending on the scale and to raise questions about the tensile strength parameter. Then, three-point bending tests on V-notched, U-notched and unnotched specimens are analyzed at different scales, enlightening the different influences of the fracture energy and the tensile strength parameters according to the scale. They also show that there is an increasing difference between force and displacement controlled loading modes when descending the scales. Finally, comparisons with experiments found in the literature are carried out. They highlight again the need but also the difficulty to identify the parameters of rupture and especially the tensile strength.

In the second part of the chapter, the same controversy is studied using the PF model, and therefore the influence of the phase field length scale in the crack nucleation at the micro-scale is examined. The PF model has been successfully applied in many applications, not only in crack nucleation [71, 74], but also in other damage phenomena, such as corrosion [75]. In this analysis we aim to demonstrate its applicability also when descending the scales, considering the tests made in the first part of the chapter. Moreover, a reflective comparison is made with the conclusions previously presented with the CC.

In the following mm-scale (resp.  $\mu\text{m}$ -scale) means that units for the dimensions of the specimens are mm (resp.  $\mu\text{m}$ ). These two scales are the most relevant to ceramic testing. However, side studies to the cm- or nm-scale will also be made as well as to intermediate scales.

## 2.2 FFM of brittle materials at the micro-scale

### 2.2.1 A preliminary remark

An elastic bar in tension with length  $L$  and cross-section surface  $S$  is submitted to a tensile load  $F$ , see Fig. 2.1a. The bar is made of alumina zirconia, whose mechanical properties [53] were mentioned in Section 1.2.1, and are given in Table 2.1.

$E$ [GPa]	$\nu$	$\sigma_c$ [MPa]	$G_c$ [MPa mm]
380	0.22	400	0.023

Table 2.1: Mechanical properties of the alumina zirconia [53].

Provided a brittle fracture of the bar, there is no longer any potential energy once the bar is broken, and the change in potential energy  $\Pi_p$  between the unbroken and the broken state is

$$\Pi_p(0) - \Pi_p(S) = \frac{1}{2} \frac{\sigma^2 LS}{E}, \quad (2.1)$$

where  $\sigma$  is the tensile stress. The energy dissipated during failure is  $G_c S$  and the energy condition (1.8) gives

$$\frac{1}{2} \frac{\sigma^2}{E} LS \geq G_c S, \quad \rightarrow \quad \sigma \geq \sqrt{2 \frac{EG_c}{L}}. \quad (2.2)$$

According to the CC, the stress condition (1.9) must be added. The application of the two conditions arises to the definition of a failure stress  $\sigma_{\text{fail}}$ , i.e., the minimum tensile stress  $\sigma$  at which the failure occurs for a certain material according to the Coupled Criterion. A governing parameter can be defined

$$L_c = 2 \frac{EG_c}{\sigma_c^2}, \quad (2.3)$$

being  $L_c = 109 \mu\text{m}$  with the material properties considered in Table 2.1. Based on the idea that both conditions are together necessary and sufficient to predict fracture, if  $L > L_c$ , then  $\sigma_{\text{fail}} = \sigma_c$  and it is the stress condition that governs failure. On the other hand, if  $L < L_c$ , then  $\sigma_{\text{fail}}$  is determined by the energy condition. This is due to the lack of elastic energy in the solid due to its small dimensions. In that case, the property  $\sigma_c$  does not play a role in brittle failure. Note that the surface of the cross-section  $S$  plays no role in this calculation, whereas the relation between the length of the bar and the Irwin length  $l_{\text{Irwin}}$  does. As an example, Fig. 2.1b shows  $\sigma_{\text{fail}}/\sigma_c$  with respect to  $L/L_c$ .

For example, for a  $500\ \mu\text{m}$  long bar, the coefficient  $\frac{L}{L_c} = 4.58$  and therefore  $\sigma_{\text{fail}} = \sigma_c$ . However, a small bar of  $10\ \mu\text{m}$  will break in tension for  $\sigma_{\text{fail}} = 1322\ \text{MPa} > \sigma_c$ , which should not be confused with the tensile strength set here at  $\sigma_c = 400\ \text{MPa}$ . Note that this result would remain unchanged as long as  $\sigma_c \leq 1322\ \text{MPa}$ .

In conclusion, this kind of experiments seems poorly appropriate to determine a tensile strength (by the way, Dehm et al. [18] use the word strength in quotation marks) when  $L < L_c$ . This reasoning is also valid for compression tests on micro-pillars [18], [28] although the configuration is not in general used to test fracture properties.

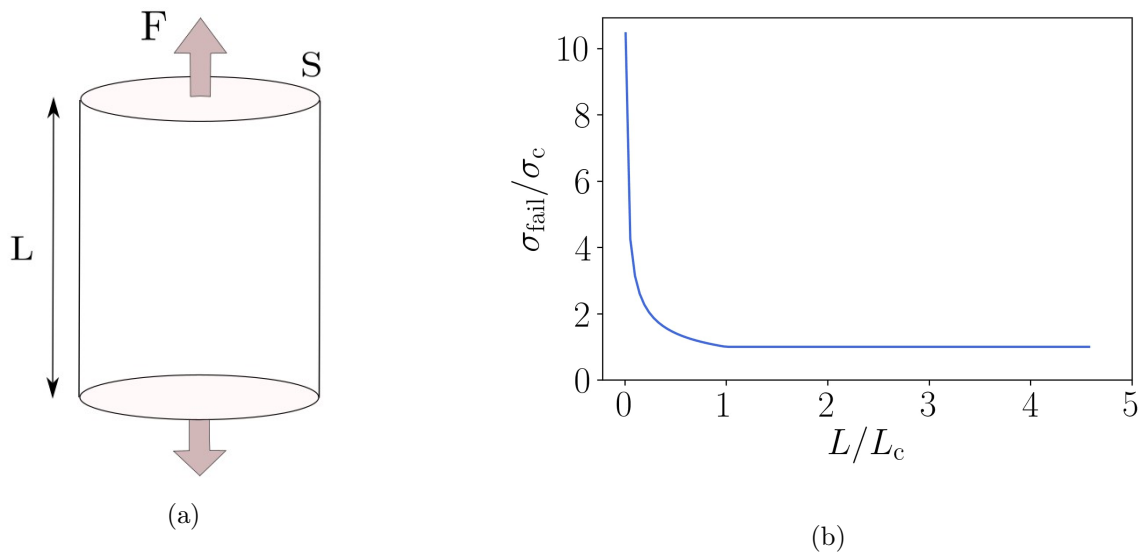


Figure 2.1: Solution of the Coupled Criterion for a bar in tension.

### 2.2.2 Bending tests

From the CC perspective, bending tests, see Fig. 2.2, differ significantly from tensile tests because a part of the specimen is under tension while the other one is in compression; thus, the stress condition cannot be fulfilled throughout the specimen. Failure occurs in two stages: crack initiation followed by crack growth, leading or not to the complete failure.

In this section, a possible size effect in bending tests is deeply studied from the point of view of the Coupled Criterion. To that aim, a FEM computation is performed in 2D plane strain elasticity, considering the material is alumina-zirconia ceramic, whose mechanical properties are given in Table 2.1.

The dimensions of the specimen in Fig. 2.2 are  $L = 8$ ,  $W = 2$ ,  $t = 2$ ,  $a = 0.4$ . Units are not specified, they vary depending on the selected scale. To set the scale of the analysis ( $-\mu\text{m}$  or  $-\text{mm}$  for example) the only change to bring during the post-processing is to modify the value of  $G_c$  (e.g.  $0.023\ \text{MPa mm} = 23\ \text{MPa } \mu\text{m}$ ), which reduces significantly the numerical effort.

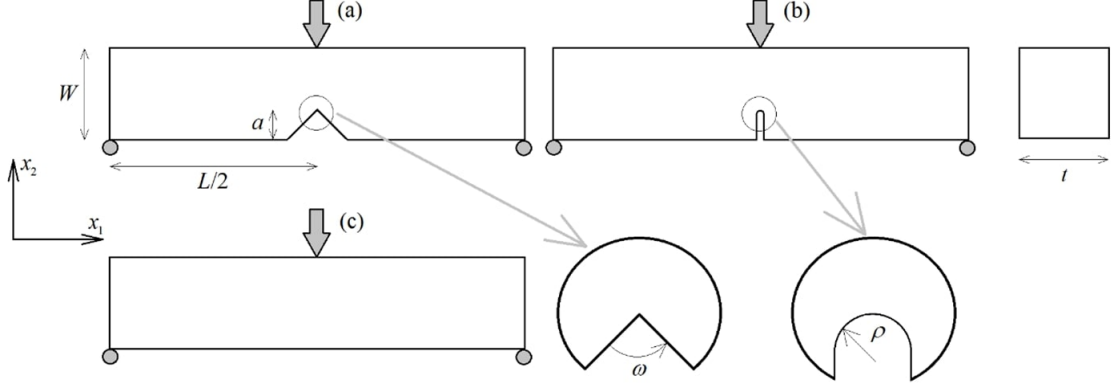


Figure 2.2: 3-point bending tests. (a) V-notched specimen, (b) U-notched specimen, (c) plain specimen

The analysis is made under displacement controlled loading mode (DC) for a unitary displacement  $U = 1$ , from which we obtain  $G_{\text{inc}}(\delta l)$  and  $\sigma(s)$  along the expected crack path, as explained in Section 1.2.1. The CC is applied to obtain the critical load, defined as the minimum load for which the energy and the stress conditions are simultaneously fulfilled. Under DC, the critical load is named as  $U_{\text{crit}}$ , and the system of inequations we need to solve is expressed as

$$\bar{G}_{\text{inc}} = U_{\text{crit}}^2 \frac{G_{\text{inc}}(\delta l)}{G_c} \geq 1, \quad (2.4)$$

$$\bar{\sigma} = U_{\text{crit}} \frac{\sigma(s)}{\sigma_c} \geq 1, \quad \text{for } 0 \leq s \leq \delta l. \quad (2.5)$$

Under force controlled loading mode (FC) an additional post-processing after FEM computation is needed. Based on the idea that the stiffness of the structure is the same for both DC and FC,

$$\frac{U^{\text{FC}}}{F^{\text{FC}}} = \frac{U^{\text{DC}}}{F^{\text{DC}}}, \quad (2.6)$$

where  $U^{\text{FC}}$ ,  $F^{\text{FC}}$  and  $U^{\text{DC}}$ ,  $F^{\text{DC}}$  are the displacement and the force under FC and DC respectively. Assuming a constant unitary force for FC, and a constant unitary displacement for DC, the elastic solution needed for the CC under FC is

$$\Pi_{\text{p}}^{\text{FC}}(\delta l) = \frac{\Pi_{\text{p}}^{\text{DC}}(\delta l)}{(F^{\text{DC}}(\delta l))^2}, \quad (2.7)$$

$$\sigma^{\text{FC}}(s) = \frac{\sigma^{\text{DC}}(s)}{F^{\text{DC}}(\delta l)}. \quad (2.8)$$

The force under DC is calculated using the potential energy as

$$F^{\text{DC}}(\delta l) = 2\Pi_{\text{p}}^{\text{DC}}(\delta l). \quad (2.9)$$

Notice that  $F^{\text{DC}}(\delta l)$  has to be calculated at each FEM calculation that is made, i.e., in the undamaged configuration for obtaining  $\sigma^{\text{FC}}(s)$  and each time one node is released for  $\Pi_{\text{p}}^{\text{FC}}(\delta l)$ .

In addition, we introduce a physically significant parameter  $\sigma_{\text{f}}$ , baptized flexural stress, that is the tensile stress in the middle of the bottom face of the unnotched specimen (Fig. 2.2c). In order to compare between the various cases, we define the equivalent flexural stress  $\sigma_{\text{f}}$  when the V-notched and the U-notched specimens are analyzed. It is defined as the flexural stress in an equivalent unnotched specimen of the same width undergoing the same bending load. At the moment of failure the flexural stress is denoted  $\sigma_{\text{fcrit}}$ .

### 2.2.2.1 Bending tests on an unnotched specimen

In Fig. 2.3, the schematic diagram of an unnotched specimen in a 3-point bending test specimen is shown, where the expected crack path is highlighted in red. Along this path, the stress  $\sigma(s)$  changes from tension at the bottom to compression at the top.

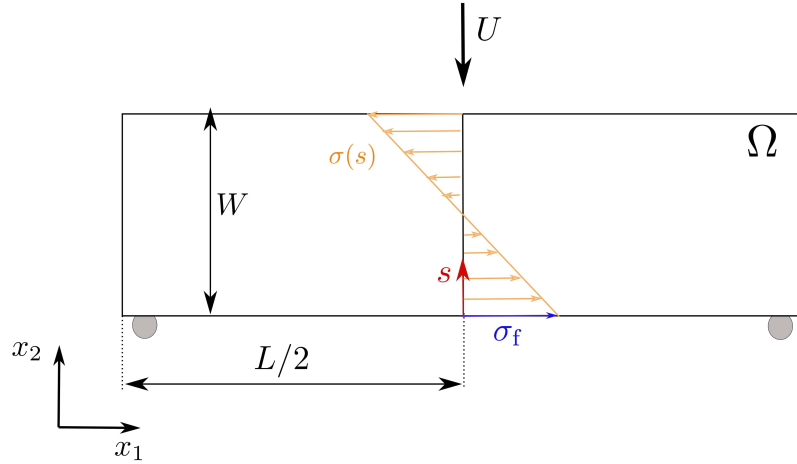


Figure 2.3: Schematic view of the stress gradient in the bending test of an unnotched specimen. The orange solid line is the tensile component of the stress tensor along the middle axis. It is positive on the bottom face and negative above. The red solid line is the expected crack path. The flexural stress is highlighted in blue.

The critical load (force or displacement) at which a crack appears in the specimen is determined applying the CC. An example is shown in Fig. 2.4 for DC, considering the specimen has dimensions of  $\mu\text{m}$ , i.e.,  $G_c = 23 \text{ MPa } \mu\text{m}$ . It can be observed that the energy condition represented by  $\bar{G}_{\text{inc}}$  is an increasing function, while the stress condition  $\bar{\sigma}$  is a decreasing function. At the CC point  $s = 0.9 \mu\text{m}$ , both conditions intersect and are equal to 1, that is,  $\sigma(s = 0.9 \mu\text{m}) = \sigma_c$  and  $G_{\text{inc}}(\delta l = 0.9 \mu\text{m}) = G_c$ . This point defines the critical nucleation length  $\delta l_c = 0.9 \mu\text{m}$ . Looking at  $s = 0 \mu\text{m}$ , which corresponds to the point located the middle of the lower part of the specimen,  $\sigma(s = 0) > \sigma_c$ . The tensile stress  $\sigma(s = 0)$  is denoted here

as  $\sigma_f$ , the flexural stress. Notice that to move from one scale to other only  $G_c$  is changed, thus, the stress field is unchanged whatever the units but the stress gradient through the specimen increases drastically when descending the scales.

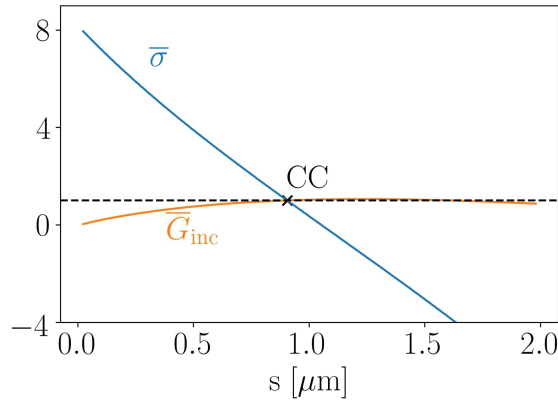


Figure 2.4: Example of the application of the CC in a bending test of an unnotched specimen at the micro-scale, considering DC loading mode.

Therefore, without any statistical consideration on the presence and size of defects [76], we can observe in Table 2.2 an apparent strengthening of the material when descending the scales. Moreover, FC and DC loading modes differ more and more significantly. The strengthening effect observed here is explained by the stress gradient of the bending test. Looking at Table 2.2, it is difficult to interpret these values as representative of a material bending strength, as it was similarly concluded in Section 2.2.1.

It is important to highlight that this is the configuration where the effects of the stress gradient are most noticeable, although in the other configurations important observations are also made, as it is shown below.

Scale (mm)	10	1	0.1	0.01	0.001
$\sigma_{\text{fcrit}}$ (MPa) FC	401.4	414.0	518.6	980.5	2375.1
$\sigma_{\text{fcrit}}$ (MPa) DC	401.5	413.9	522.9	1122.7	3909.9

Table 2.2: The flexural stress that prevails at failure  $\sigma_{\text{fcrit}}$  of the plain specimen in the middle of the bottom face.

### 2.2.2.2 Bending tests on a V-notched specimen

The case of a V-notched specimen is represented in Fig. 2.5, where the angle  $\omega$  is varied to study its influence on crack nucleation, considering the values  $\omega = 0^\circ$  (the crack case) 30, 60, 90, 120 and  $150^\circ$ .

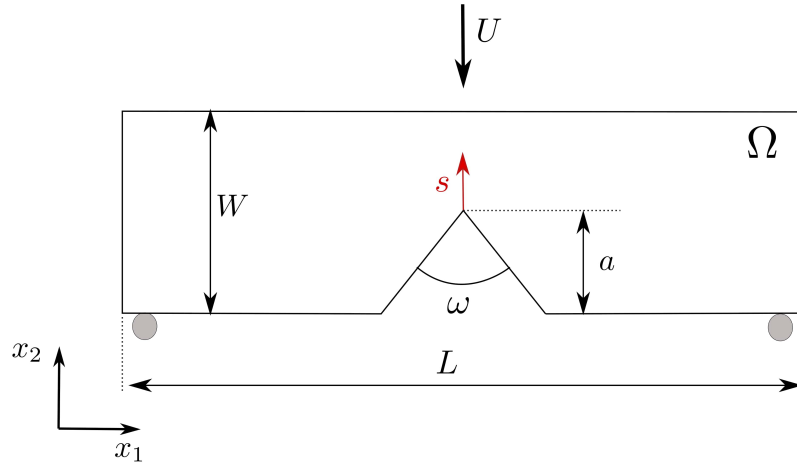


Figure 2.5: Scheme of the 3-point bending tests in a V-notched specimen. The red solid line represents the expected crack path.

As it is mentioned in Section 1.2.1, there are two approaches that can be used to predict the crack onset in the case of a V-notched specimen: Matched Asymptotic Expansion (MAE) and Full Finite Element (FFE) computations. Although the first one is related to less computational complexity, its application is limited to the fact that either  $a$  (the notch depth) or  $\delta l$  (the nucleation length) must be much lower than the dimensions of the specimen. Clearly,  $a = 0.4$  does not fulfill this requirement and the nucleation length  $\delta l$  is the only characteristic length that can be used to apply MAE (see Section 1.2.2). However, since the scale of the specimen will be reduced until the micro- and the nano-scale, the nucleation length, unknown a priori, could be of the order of the dimensions of the specimen as well, and therefore MAE approach might not be applied. To illustrate this, both MAE and FFE are compared in Fig. 2.6, where the ratio between the GSIF ( $K$ ) at failure computed by FFE approach (FC loading mode) and its critical value  $K_c$  derived from the asymptotic procedure, is represented.

The GSIF is calculated using the finite element solution obtained at the critical load, which is derived from the CC. As shown in Annex 5.2, it is computed applying a path independent integral. On the other hand,  $K_c$  was calculated in Table 1.3.

Not surprisingly, in Fig. 2.6 the two curves  $\omega = 0^\circ$  and  $\omega = 30^\circ$  merge because the singularity exponents are very close to each other (Table 1.3). Clearly, the asymptotic approach works well for any opening angle  $\omega$  at the cm- and mm-scale. This is because the crack increment length at initiation  $\delta l$  remains smaller than 1% of the ligament width  $W - a$  and thus satisfies the smallness condition which validates the asymptotic expansions, see Fig. 2.7. Notice that

in the estimation of the nucleation length  $\delta l$  there can be an error related to the mesh size, which is in this case of the order of  $10^{-3}$  x selected units.

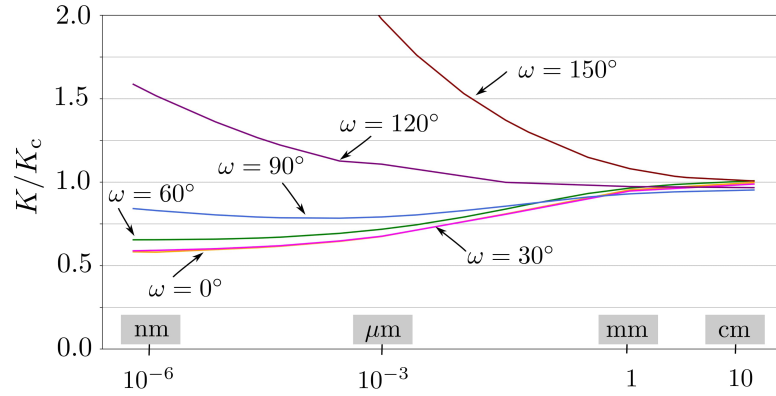


Figure 2.6: The ratio  $K/K_c$  between the GSIF at failure computed by FE (FC loading) and its asymptotic value for various opening angles.

For scales below the mm-scale,  $K$  deviates more and more significantly from  $K_c$ , because the ratio of the initiation length to the ligament width  $\delta l/(W - a)$  no longer meets the condition of smallness. Indeed, the FFE approach considers the whole elastic solution, thus, higher terms in Williams' expansion (see Annex 5.1), ignored in the asymptotic approach which retains only the leading term, become predominant as  $\delta l$  becomes bigger. This is also true for a crack  $\omega = 0^\circ$ , and, as a consequence, using formulas derived from Griffith's criterion to determine the material fracture toughness at the  $\mu\text{m}$ -scale risks to be unreliable, since only the first term in the Williams' expansion is used.

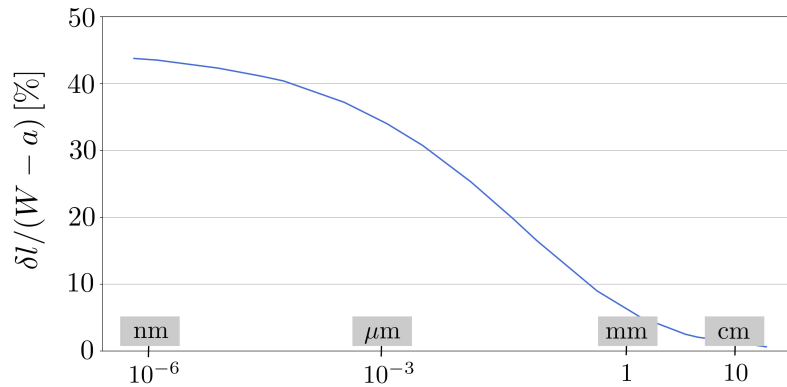


Figure 2.7: The ratio  $\delta l/(W - a)$  at various scales for  $\omega = 90^\circ$  (FC loading).

The previous study has been carried out under FC loading mode, but the same analysis can be made for DC. In Fig. 2.8  $K/K_c$  is represented for DC and FC for  $\omega = 90^\circ$ . Notice that not only in both cases  $K$  deviates more and more significantly from  $K_c$  when descending the

scales, but also the results of DC and FC loading modes differ more and more one from each other.

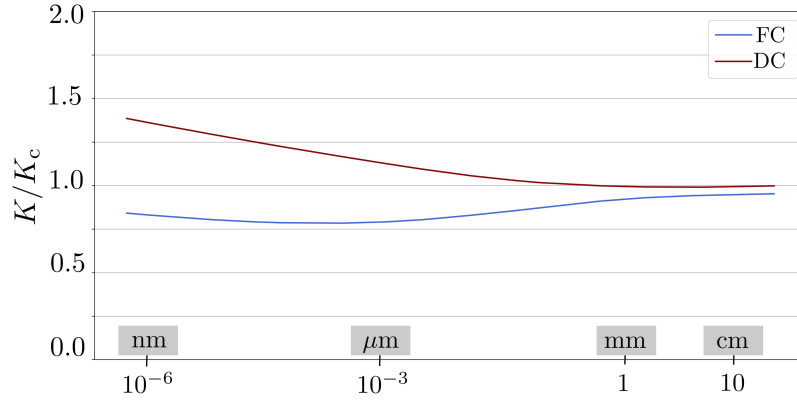


Figure 2.8: The ratio  $K/K_c$  for FC and DC loading, in the case of  $\omega = 90^\circ$ .

Finally, two examples of the application of the CC are shown in Fig. 2.9, for FC and DC controls, at the micro-scale and for  $\omega = 90^\circ$ . In both cases the CC point (which designates the newly created crack length  $\delta l_c$ ) corresponds to the point where  $\sigma = \sigma_c$ . Hence, for  $s < \delta l_c$  the tensile stress  $\sigma(s) > \sigma_c$  provided the stress gradient in the bending test, and the stress singularity of the V-notch.

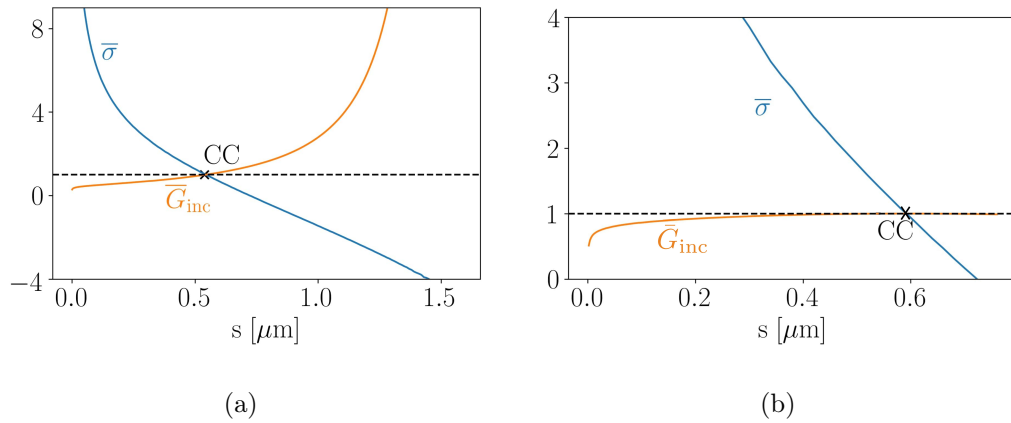


Figure 2.9: Example of the application of the Coupled Criterion in the bending test of a V-notched specimen under FC and DC at the micro-scale for  $\omega = 90^\circ$ .

The strengthening effect is summarized in Table 2.3, where the results obtained with a sharp V-notched specimen under FC loading mode are shown. The parameter used to represent the strengthening effect is the equivalent flexural stress  $\sigma_f$  (defined at the beginning of this section). As already observed in Fig. 2.6, the two cases  $0^\circ$  and  $30^\circ$  merge. Obviously, the

smaller the scale the smaller the influence of the geometry (this is more and more true when descending to the nm-scale although it is not shown here).

Scale (mm)	10	1	0.1	0.01	0.001
$\sigma_{\text{fcrit}}$ (MPa) $\omega = 0^\circ$	26.6	83.5	252.3	675.5	1786.7
$\sigma_{\text{fcrit}}$ (MPa) $\omega = 30^\circ$	26.6	83.7	252.3	675.5	1786.7
$\sigma_{\text{fcrit}}$ (MPa) $\omega = 60^\circ$	28.1	85.3	253.4	675.5	1786.7
$\sigma_{\text{fcrit}}$ (MPa) $\omega = 90^\circ$	32.7	92.4	258.2	677.7	1786.7
$\sigma_{\text{fcrit}}$ (MPa) $\omega = 120^\circ$	46.8	111.3	272.4	675.5	1786.7
$\sigma_{\text{fcrit}}$ (MPa) $\omega = 150^\circ$	82.6	145.6	283.3	675.5	1765.0

Table 2.3: The equivalent flexural stress at failure  $\sigma_{\text{fcrit}}$  for the V-notched specimen under FC loading mode for different opening angles.

### 2.2.2.3 Bending of a U-notched specimen

We will now focus on U-notched specimens (Fig. 2.10) which is the geometrical configuration closest to the fracture test conditions on ceramic specimens at both mm and  $\mu\text{m}$  scales.

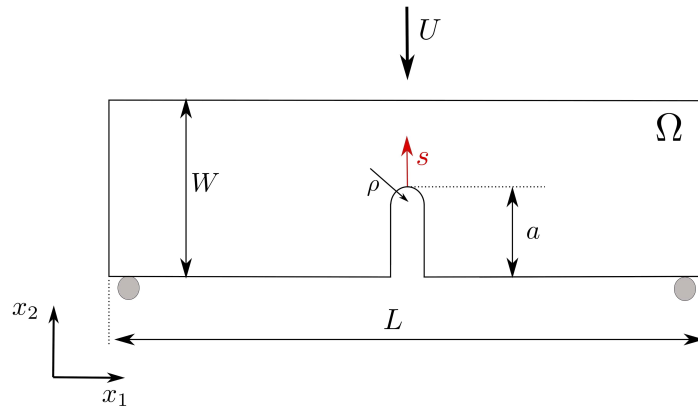


Figure 2.10: Scheme of the 3-point bending tests in a U-notched specimen. The red solid line represents the expected crack path.

Fig. 2.11 shows the equivalent flexural stress at the moment of failure  $\sigma_{\text{fcrit}}$  for U-notched specimens with  $\rho = 0.02$  (i.e. 0.02 mm at the mm-scale and 0.02  $\mu\text{m}$  at the  $\mu\text{m}$ -scale). Results

do not depend on how the load is applied at the cm- and mm-scale but the gap widens at smaller scales as already observed in Table 2.2.

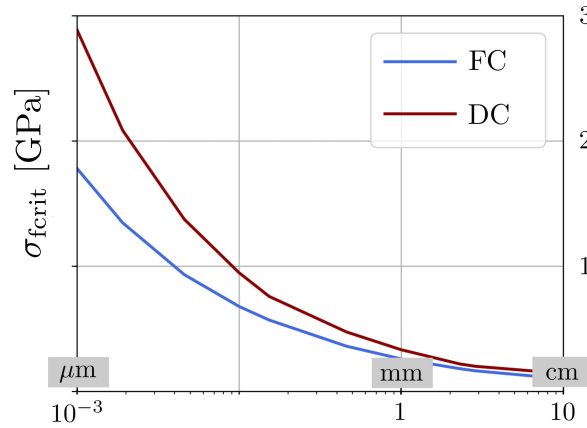


Figure 2.11: The equivalent flexural stress at failure  $\sigma_{\text{ferit}}$  for the U-notched specimen with  $\rho = 0.02$  at different scales.

This result that could surprise can be explained by two different failure mechanisms. In the DC case, as shown in Fig. 2.12a for the micro-scale, the energy curve grows slowly and even pass through a maximum before decreasing. In that case, there is initiation followed by a possible crack arrest at a shorter and shorter distance when descending the scales because there is less and less energy to be released. On the other hand, under FC loading mode, represented in Fig. 2.12b at the micro-scale, the energy curve grows rapidly. There is initiation followed by unstable crack growth until complete failure.

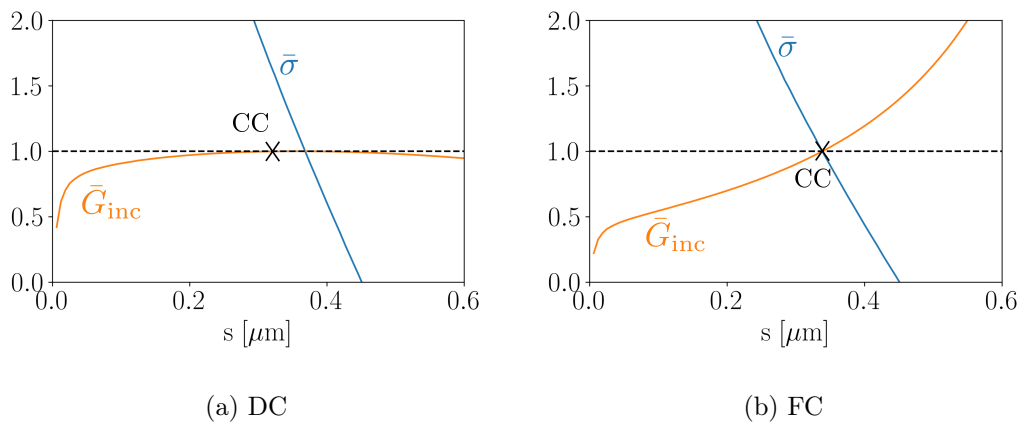


Figure 2.12: Example of the application of the Coupled Criterion in the bending test of a U-notched specimen under DC and DC at the micro-scale for  $\rho = 0.02 \mu\text{m}$ .

However, this is strongly related to the value of  $\sigma_c$ . If  $\sigma_c$  is higher, the energy curve moves to the left in Fig. 2.12a, and the conventional configuration of the CC can be observed, in which the CC point corresponds to the crossing point of an increasing energy curve and a decreasing stress curve. In those cases, there is no difference between DC and FC. Let us add that this difference between DC and FC loading modes is not only observed at the microscopic scale, the same phenomenon can be observed at the macroscopic scale if  $\sigma_c$  is small and consequently the initiation length is large.

Table 2.4 summarizes the results for two different notch blunting ( $\rho = 0.25 \times a = 0.1$  and  $\rho = 0.05 \times a = 0.02$ ). Obviously, the influence of the blunting is more prominent at larger scales. At the  $\mu\text{m}$ -scale the results almost merge with those of the V-notched specimens (see Table 2.3).

One conclusion to be drawn from Table 2.4 is that at the  $\mu\text{m}$ -scale the exact shape of the U-notch plays a minor role. Only its depth  $a$  or more precisely the width of the remaining ligament  $W - a$  is decisive. This conclusion is reinforced by a computation on an unnotched specimen whose width is  $W - a$  instead of  $W$ , under FC loading mode. After applying the CC to obtain the critical load in such plain specimen, the comparative parameter  $\sigma_f$  is calculated at the moment of failure in the thick unnotched specimen whose width is  $W$ , to be consistent. We obtain  $\sigma_{\text{fcrit}} = 1660.4$  MPa at the micro-scale, which is not far from the above values (Table 2.4).

Scale (mm)	10	1	0.1	0.01	0.001
$\sigma_{\text{fcrit}}$ (MPa) $\rho = 0.1$	88.6	122	268.0	675.5	1765.0
$\sigma_{\text{fcrit}}$ (MPa) $\rho = 0.02$	49.9	97.0	257.1	679.8	1786.7

Table 2.4: The equivalent flexural stress at failure  $\sigma_{\text{fcrit}}$  for the U-notched specimen under FC loading mode with  $\rho = 0.1$  and  $\rho = 0.02$  (units depend on the scale).

This remarkable feature is also visible in the followig section, where the influence of fracture properties is analysed. Such a phenomenon was already observed in [77] where it is noted that below a length scale the material (nacre) becomes insensitive to pre-existing flaws. It is concluded that Griffith criterion becomes inoperative and failure is governed by the theoretical strength. However, we disagree with this conclusion, the energy is still governing fracture and it is the small available amount that forces to increase the load.

### 2.2.2.4 Effect of fracture properties in the bending test

In this section we mainly focus on the U-notched specimen with  $\rho = 0.02$  and the plain specimen because the next sections will be dedicated to comparison with experiments found in the literature which refer to this type of samples. Fig. 2.13 compares the equivalent flexural stress at failure  $\sigma_{\text{fcrit}}$  as a function of the fracture energy at the mm-scale and Fig. 2.14 at the  $\mu\text{m}$ -scale. In case of plain specimens, we have considered two different widths. The first one has the width  $W$  and the second one the width  $W - a$ . To be consistent,  $\sigma_{\text{fcrit}}$  in the latter has been calculated using an equivalent plain specimen of width  $W$ .

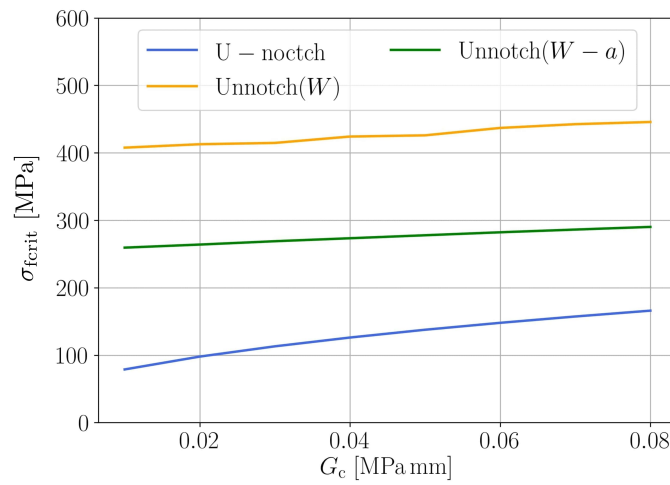


Figure 2.13: The equivalent flexural stress at failure  $\sigma_{\text{fcrit}}$  as a function of the fracture energy  $G_c$  at the mm-scale for the U-notched specimen with  $\rho = 0.02$ , and the plain specimens with the width  $W = 2$  and  $W - a = 1.6$ . Computations are carried out under FC loading.

As already noticed, the influence of the fracture energy is more pronounced at the  $\mu\text{m}$ -scale. However, at the mm-scale, the fracture energy still has some influence on the U-notched specimens while it is weaker for the plain specimens. Computations have been carried out under FC loading, expecting similar conclusions in the DC loading mode. Moreover,  $\sigma_{\text{fcrit}}$  in the U-notch is closer to the unnotch plain specimen of width  $W - a$  at the micro-scale, which means that results when descending scales depend less and less on the notch shape.

With the data shown in Table 2.1, the fracture toughness obtained is

$$K_{\text{IC}} = \sqrt{\frac{G_c E}{1 - \nu^2}} = 3.03 \text{ MPa m}^{0.5}. \quad (2.10)$$

Usually, the notch is considered, whatever its acuity, as a crack and the toughness is derived

from the load at failure  $U_{\text{crit}}$  using the following analytical formulas [78]

$$K_{\text{IC}} = \frac{6U_{\text{crit}}L}{4W^2} \sqrt{\pi a} f(a/W), \quad (2.11)$$

where

$$f(a/W) = \frac{1}{\sqrt{\pi}} \frac{1.99 - a/W(1 - a/W)(2.15 - 3.93a/W + 2.7(a/W)^2)}{(1 + 2a/W)(1 - a/W)^{3/2}}. \quad (2.12)$$

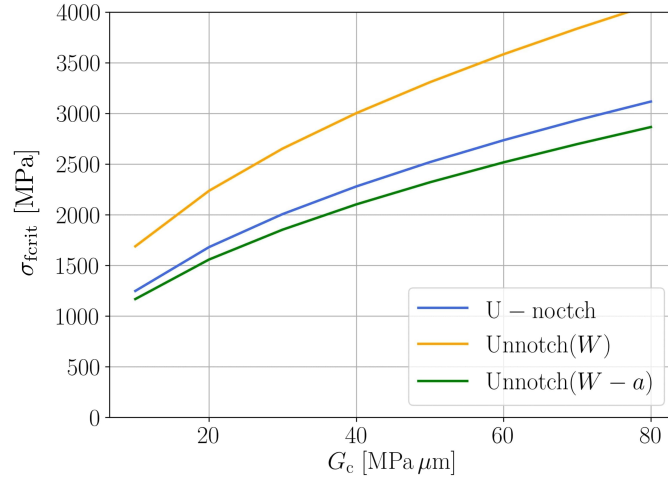


Figure 2.14: The equivalent flexural stress at failure  $\sigma_{\text{fcrit}}$  as a function of the fracture energy  $G_c$  at the  $\mu\text{m}$ -scale for the U-notched specimen with  $\rho = 0.02$ , and the plain specimens with the width  $W = 2$  and  $W - a = 1.6$ . Computations are carried out under FC loading.

Table 2.5 shows the toughness  $K_{\text{IC}}$  (MPa m<sup>0.5</sup>) calculated using (2.11) and the load at failure predicted by the CC for various specimens under FC loading mode. Obviously, at the macro-scale (i.e. cm-scale and mm-scale), Tada's formula and CC predictions of failure lead to an error not exceeding 2% for sharp notches with  $\omega \leq 30^\circ$ . The result is getting worse for larger opening angles and even becomes completely wrong for a strongly blunted U-notch with  $\rho = 0.02$  at the cm-scale (i.e.  $\rho = 0.02$  cm).

At the macro-scale the calculation tends to overestimate the actual value. This trend is reversed at smaller scales, the actual value is now underestimated by 32% at the  $\mu\text{m}$ -scale. Moreover, as already mentioned, the exact shape of the notch no longer plays any role, since the difference between the different angles selected for the V-notch and the U-notch is less and less noticeable, see the third and the fourth rows of Table 2.5. This conclusion is consistent with that of Section 2.2.2.3.

Scale (mm)	$\omega = 0^\circ$	$\omega = 30^\circ$	$\omega = 60^\circ$	$\omega = 90^\circ$	$\rho = 0.02$	Actual value
10	3.08	3.08	3.26	3.79	5.78	3.03
1	3.06	3.07	3.13	3.39	3.55	3.03
0.1	2.92	2.92	2.94	2.99	2.98	3.03
0.01	2.48	2.48	2.48	2.48	2.49	3.03
0.001	2.07	2.07	2.07	2.07	2.07	3.03

Table 2.5: The equivalent flexural stress at failure  $\sigma_{\text{fcrit}}$  for the U-notch specimen under FC loading mode with  $\rho = 0.1$  and  $\rho = 0.02$  (units depend on the scale).

Fig. 2.16 and 2.15 show the equivalent flexural stress at failure  $\sigma_{\text{fcrit}}$  as a function of the tensile strength  $\sigma_c$  at the mm-scale and the  $\mu\text{m}$ -scale. It can be observed that the tensile strength has a higher influence on the plain specimens, whereas it has a lower influence at the micro-scale, specially for the U-notched specimen. The reason for that phenomenon is a change in the governing condition of the CC. At the micro-scale, it is the energy condition that governs the failure, and therefore  $G_c$  has greater influence than  $\sigma_c$ .

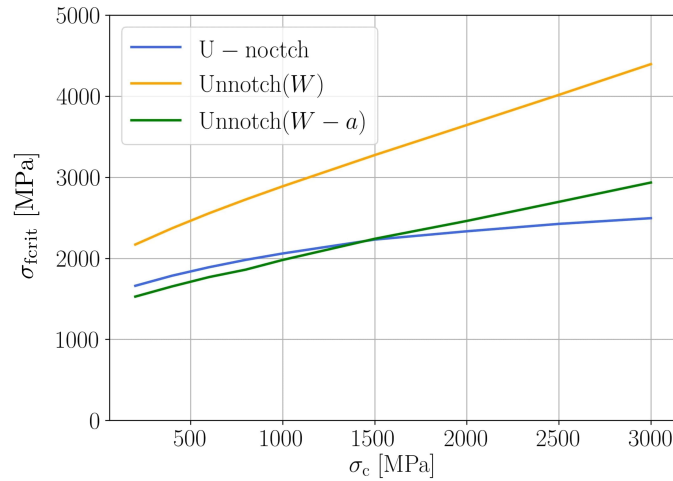


Figure 2.15: The equivalent flexural stress at failure  $\sigma_{\text{fcrit}}$  as a function of the tensile strength  $\sigma_c$  at the  $\mu\text{m}$ -scale for the U-notched specimen with  $\rho = 0.02$ , and the plain specimens with the width  $W = 2$  and  $W - a = 1.6$ . Computations are carried out under FC loading.

The opposite situation is observed at the macro-scale. Moreover,  $\sigma_{\text{fcrit}}$  in the U-notched specimen and the unnotched specimen with a width  $W$  are very similar, as it was observed when studying the influence of  $G_c$ , and therefore the shape of the notch has less and less influence when descending the scales.

Furthermore, looking at the plain specimens at the mm-scale,  $\sigma_{\text{fcrit}} \approx \sigma_c$  in the one with the width  $W$ , whereas this is no longer true at the micro-scale, being  $\sigma_{\text{fcrit}} > \sigma_c$ .

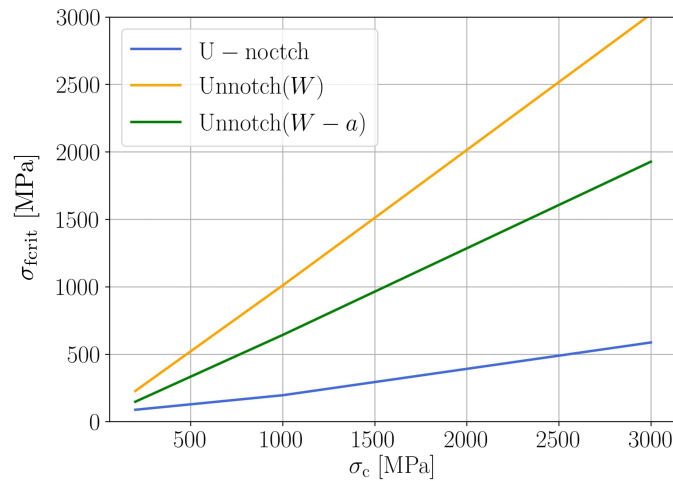


Figure 2.16: The equivalent flexural stress at failure  $\sigma_{\text{fcrit}}$  as a function of the tensile strength  $\sigma_c$  at the mm-scale for the U-notched specimen with  $\rho = 0.02$ , and the plain specimens with the width  $W = 2$  and  $W - a = 1.6$ . Computations are carried out under FC loading.

## 2.2.3 Comparison with experiments found in the literature

### 2.2.3.1 Bending tests of micro-cantilever beams

Using a micro-indenter, Henry et al. [79] carried out bending tests on notched micro-cantilever beams (Fig. 2.17) made of a ceramic material 8Y-FSZ cubic zirconia ( $E = 216$  GPa,  $\nu = 0.22$ ). Beams were milled with a FIB and remained clamped to a part of the bulk material. On micrographs, the specimen appears smooth and free of surface defects.

In this section an equivalent 2D model, see Fig. 2.18, is deeply studied and compared with experimental results. Some simplifications are made when the 3D model is transformed into a 2D model. First, the geometry of the beam cross section has a pentagonal shape, since it can be more easily milled, and such geometry cannot be reproduced in a 2D model. However, according to [80] results are very similar to the ones obtained by a rectangular cross section, that is the one assumed in the 2D simplification. Thus, the height of the specimen  $W$  in the numerical simulations is set as  $W = \hat{W} + C/2$ , see Fig. 2.17. Another important point to consider is the presence or not of the bulk material. After having noted the very small

difference between the case of a beam clamped at its end and a more complete simulation including a part of the bulk material, the first case was retained in the computations for simplicity.

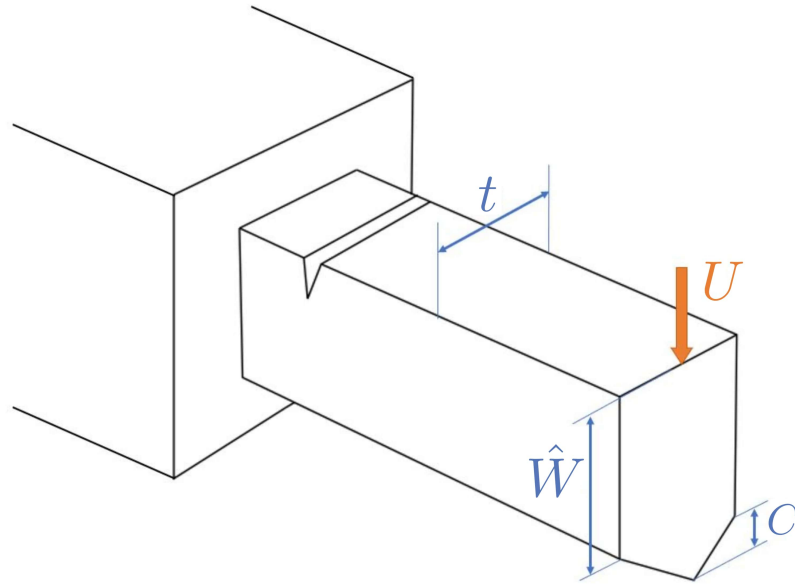


Figure 2.17: Sketch of the micro-cantilever bending test with associated dimensions

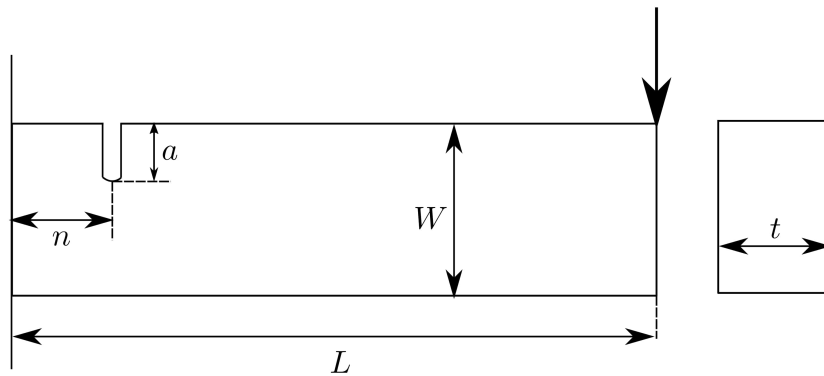


Figure 2.18: The U-notched micro-cantilever beam

The U-notch radius in Fig. 2.18 is  $0.01\mu\text{m}$ . Actual dimensions related to the 14 specimens are given in Table 2.6. It can be noted that the difficulty of milling specimens leads to a certain dispersion of the geometry.

Index	$L$	$W$	$t$	$n$	$a$	Index	$L$	$W$	$t$	$n$	$a$
1	9.20	4.34	5.98	0.920	1.32	8	8.76	4.30	4.99	0.876	0.50
2	9.97	4.04	4.99	0.997	0.64	9	8.13	4.57	5.34	0.813	0.42
3	9.74	5.01	6.27	0.974	0.70	10	7.19	4.12	3.45	0.719	0.84
4	9.10	4.66	6.21	0.910	0.61	11	7.33	4.60	4.18	0.733	0.56
5	8.03	4.20	4.57	0.803	0.56	12	9.40	4.13	4.56	0.940	0.70
6*	8.76	4.26	4.42	0.876	0.91	13	7.08	4.35	5.25	0.708	0.83
7*	12.11	3.32	4.40	1.211	0.64	14*	9.96	3.50	3.94	0.996	0.63

Table 2.6: Geometrical parameters of the 14 different specimens tested in [79]. All the parameters are in  $\mu\text{m}$ . Tests are carried out under FC loading mode except those with a\* done under DC loading mode.

A global least square method allows computing the best fit pair  $(\tilde{G}_c, \tilde{\sigma}_c)$

$$\tilde{G}_c, \tilde{\sigma}_c = \operatorname{argmin} \sum_{i=1}^{14} (F_i^{\text{sim}}(\sigma_c, G_c) - F_i^{\text{exp}})^2 \quad (2.13)$$

where  $F_i^{\text{sim}}(\sigma_c, G_c)$  is the applied load at which the CC is fulfilled according to the simulations and  $F_i^{\text{exp}}$  is the measured fracture load, for the  $i$ -th specimen. The range for  $G_c$  is 2 to 20  $\text{J m}^{-2}$  (step 0.5) and for  $\sigma_c$  0.4 to 8 GPa (step 0.2). It gives  $\tilde{G}_c = 10.5 \text{ J m}^{-2}$  and  $\tilde{\sigma}_c = 5600 \text{ MPa}$  under DC loading mode and  $\tilde{G}_c = 9.5 \text{ J m}^{-2}$  and  $\tilde{\sigma}_c = 7400 \text{ MPa}$  under FC loading mode. Obviously, there is an important difference in the evaluation of  $\sigma_c$  and the search for an optimal pair  $(\tilde{G}_c, \tilde{\sigma}_c)$  case by case can be carried out allowing a better perception of the scattering

$$\tilde{G}_{ic}, \tilde{\sigma}_{ic} = \operatorname{argmin} (F_i^{\text{sim}}(\sigma_c, G_c) - F_i^{\text{exp}})^2 \quad \text{for } i = 1, 14. \quad (2.14)$$

Results are given in Table 2.7 under FC loading mode, except specimens 6, 7 and 14 (marked with a\*) under DC loading mode like in experiments. Clearly, there is a wider scattering in the determination of the tensile strength than in that of the fracture energy, leading to the average values  $10.3 \text{ J m}^{-2}$  and  $4000 \text{ MPa}$ , excluding or not specimens 4 and 8 which does not make a big difference. In this regard, a comparison between Henry et al. estimations [79] of the material toughness  $K_{IC}$  and the present analysis shows that, precisely as in our identification of  $G_c$ , the minimum is found for sample 4 and the maximum for sample 8 (see Fig. 2.19). Thus, these extreme values seems not to be an inconsistency of the CC.

Index	$\tilde{G}_{ic}$	$\tilde{\sigma}_{ic}$									
1	8.5	5.0	5	12.0	4.0	9	13.5	4.4	13	8.5	1.6
2	11.0	3.8	6*	10.0	3.0	10	7.0	5.4	14*	7.5	4.4
3	11.5	4.6	7*	12.5	7.4	11	9.0	1.0			
4	4.0	7.8	8	18.5	18.5	12	10.5	1.6			

Table 2.7: Estimation of the fracture energy  $\tilde{G}_{ic}$  and tensile strength  $\tilde{\sigma}_{ic}$  for each specimen. Specimens 4 and 8 seem to be a bit out of the general trend.

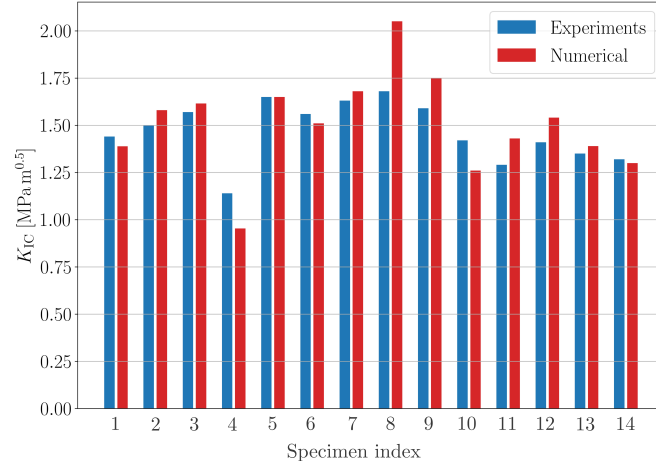


Figure 2.19: Comparison on the identification of the material toughness  $K_{IC}$  between the present analysis and Henry et al. [79] estimations for the 14 specimens.

Note that the minimization of the relative error

$$\tilde{G}_c, \tilde{\sigma}_c = \operatorname{argmin} \sum_{i=1}^{14} \left( \frac{F_i^{\text{sim}}(\sigma_c, G_c) - F_i^{\text{exp}}}{F_i^{\text{exp}}} \right)^2 \quad (2.15)$$

gives a close result to (2.13) in terms of fracture energy:  $\tilde{G}_c = 9 \text{ J } m^{-2}$ , but a significant difference in term of tensile strength:  $\tilde{\sigma}_i = 7000 \text{ MPa}$ , emphasizing the difficulty to determine the tensile strength with this kind of experiment. Of course, in the local minimization (2.14), the absolute and relative errors make no difference in terms of the optimized values  $(\tilde{G}_{ic}, \tilde{\sigma}_{ic})$ , since they will look for the pair of values that gives a load  $F_i^{\text{sim}}$  is closest to a certain experimental value  $F_i^{\text{exp}}$ , looking in a certain data base generated using the CC.

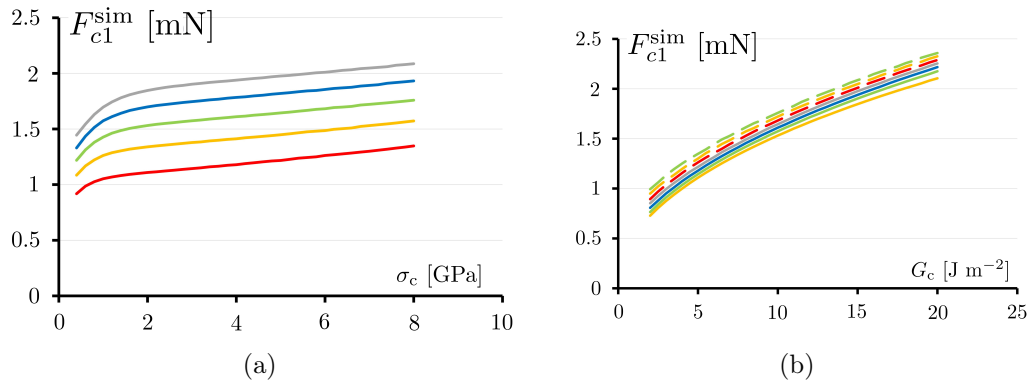


Figure 2.20: The critical applied force at failure on specimen 1 under FC loading mode using the CC, (a): function of the tensile strength for various values of the fracture energy from 2 to 15  $J m^{-2}$  step 2.5 (bottom to top); (b): function of the fracture energy for various tensile strength from 1 to 8 GPa step 1 (bottom to top).

To conclude, there is a good agreement with the global minimization on the fracture energy but a poor one on the tensile strength. This can be explained, as already mentioned, by a low sensitivity of the CC to  $\sigma_c$  at the micro-scale. This is visible in Fig. 2.20b (specimen 1 under FC loading mode) where the different fracture energies result in curves that are quite distinct one from each other, while different tensile strengths give curves that have a clear tendency to overlap, see Fig. 2.20a. This trend is even more pronounced in the case of DC loading mode. On the contrary, a fracture energy around 10  $J m^{-2}$  seems to be confirmed by the different approaches.

### 2.2.3.2 Traction tests on double-notched nano-tablets

Even if they are invoked in [18], tests at the nano-scale are likely to be very difficult to perform. Patil et al. [81] propose only simulations of traction tests on double-notched nano-tablets of aragonite, as represented in Fig. 2.21, where a 2D scheme of the specimen is shown. Two simulations techniques were applied in [81], PF and molecular dynamics (MD). The latter is used in molecular systems, since they are based on numerical solutions of Newton's equations for an interacting set of particles.

The reported material properties for aragonite are  $E = 126$  GPa,  $\nu = 0.44$ ,  $G_c = 2.091$   $J m^{-2}$ . In order to avoid non-linear elasticity and to carry out simplified linear elastic computations, the Young's modulus has been readjusted to  $E = 96$  GPa to have a similar global stiffness, as it is shown in Fig. 2.23, where a force-displacement diagram is represented, for DC and FC, considering  $u_d$  as the distributed displacement along  $\Gamma$ , see Fig. 2.21.

Moreover, this analysis is carried out in a different manner with respect to the ones in the bending test, since symmetry conditions can be applied, solving the problem shown in Fig. 2.22. Instead of releasing the nodes one by one in the expected crack path, the symmetric boundary condition on  $\Gamma_H$  is changed when a new value of the newly created crack length is

considered.

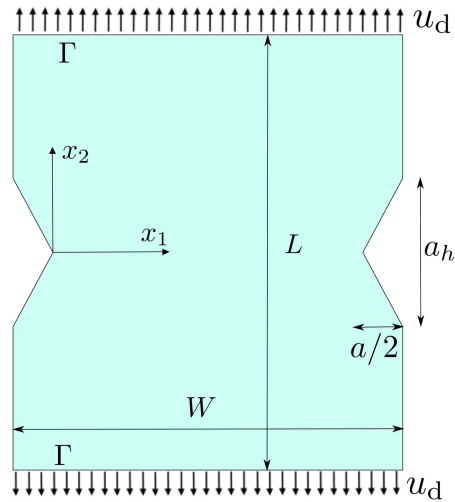


Figure 2.21: Double edge notched specimen of aragonite.  $L = 15.3$  nm,  $W = 11.2$  nm,  $a_h = 3.08$  nm and  $a = 3.68$  nm.

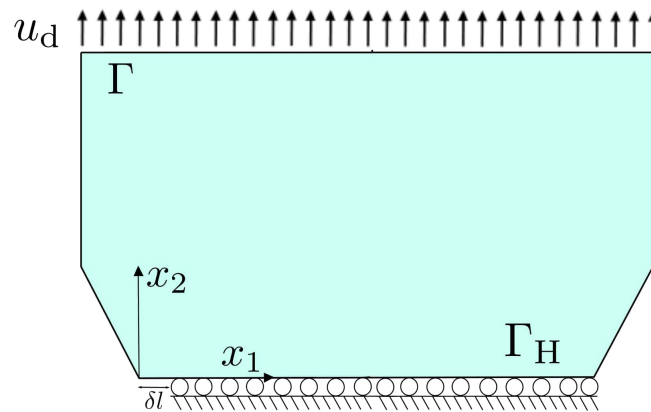


Figure 2.22: Double edge notched specimen of aragonite with symmetry conditions.

MD simulations tend to show that a crack initiates non-symmetrically at the tip of one of the notches and grows toward the other notch. It is this mechanism that is reproduced in the PF and CC simulations to obtain the critical failure load in Fig. 2.23. Notice that in this case PF results were provided by [81].

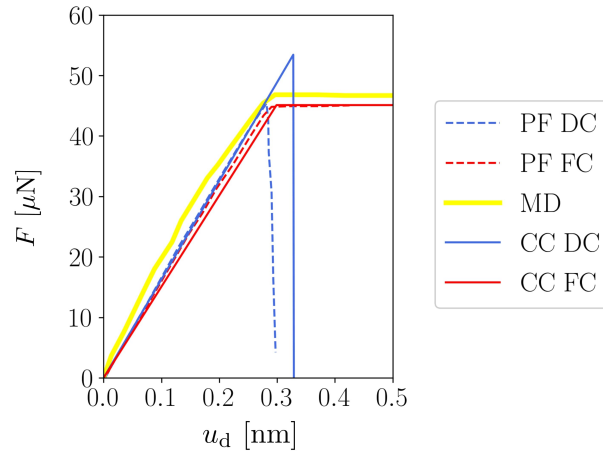


Figure 2.23: Simulation of failure of the nano-platelet of aragonite, using MD, PF and CC. Results applying PF and CC are shown under DC (dashed line) and FC loading (solid line). In this case  $\sigma_c = 5$  GPa. For MD and PF simulations the tool ORIGIN Pro (v0.8.0 OriginLab) has been used to obtain the values of the curves from [81].

The resultant critical force under DC is obtained as  $F_{\text{crit}} = 2\Psi_{\text{el}}/u_{\text{dc}}$ , where  $u_{\text{dc}}$  is the critical distributed displacement predicted by the CC and  $\Psi_{\text{el}}$  is the elastic strain energy. In a similar way, the critical distributed displacement under FC is calculated applying the postprocessing explained in (2.6). As it is shown in Fig. 2.23, results exhibit a satisfying agreement between MD, PF and CC simulations. For the CC, they are obtained after having adjusted  $\sigma_c = 5$  GPa. The CC predictions under DC and FC loading modes differ because of different modes of failure. This is due to the special shape of the stress curve, decreasing then increasing because of the two symmetric notches, and to a slowly increasing energy curve in case of the DC loading mode as shown in Fig. 2.24a. The energy condition is fulfilled for a crack jump corresponding to the whole width of the ligament between the two notches and the stress condition is then  $\sigma \geq \sigma_c$  through the whole ligament. There is only an initiation stage and the specimen is fully broken. In case of FC loading mode, the energy curve increases more rapidly and the situation is that of Fig. 2.24b. There is a first stage of initiation where  $\sigma$  is not needed to be larger than  $\sigma_c$  through the whole ligament but only along the initiation length, followed by an unstable crack growth due to the FC loading mode.

In Fig. 2.25 the predicted failure force is represented, according to the CC, as a function of the tensile strength, under DC and FC loading modes. Under DC loading mode, on the left side of the grey zone is entirely governed by the energy, inside the grey zone it is stress driven and on the right it is a mixed of the two conditions. Under FC loading mode the mixed conditions govern for the whole range of the parameter  $\sigma_c$ . It clearly appears that, according to the CC, in case of DC loading mode, the test is weakly sensitive to the tensile strength. It even becomes completely insensitive if  $\sigma_c < 5$  GPa, while it remains sensitive under FC loading mode.

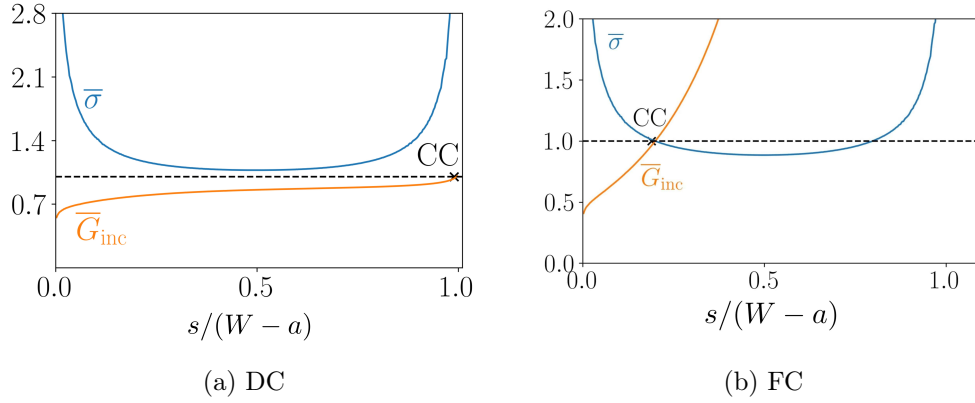


Figure 2.24: Application of the CC in the double-notched nano-tablets of aragonite, for  $\sigma_c = 5$  GPa, under DC and FC.

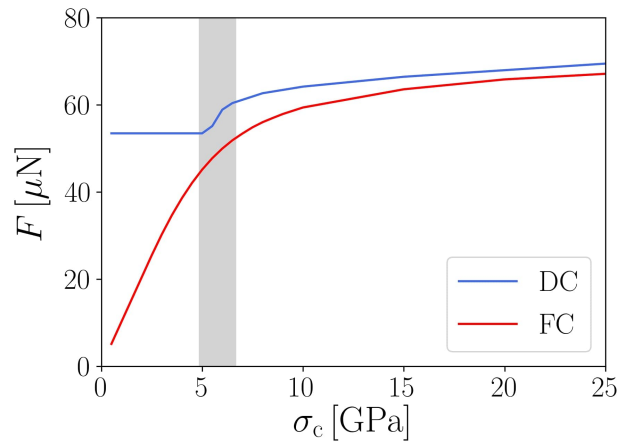


Figure 2.25: Predicted failure load, according to the CC, as a function of the tensile strength.

An interesting point to emphasize is that, under DC loading mode, the CC moves from a criterion entirely governed by the energy for  $\sigma_c < 5$  GPa (Fig. 2.24a), to a stress driven criterion for  $5 \text{ GPa} < \sigma_c < 6 \text{ GPa}$  (Fig. 2.26a) and to a classical mixed stress and energy condition for  $\sigma_c > 6 \text{ GPa}$  (Fig. 2.26b). Notice that for  $\sigma_c = 6.5 \text{ GPa}$  the initiation length is lower than the width of the ligament, since  $\delta l = 1.65 \text{ nm}$ . After the crack initiation, a stable crack growth due to the DC loading mode is followed.

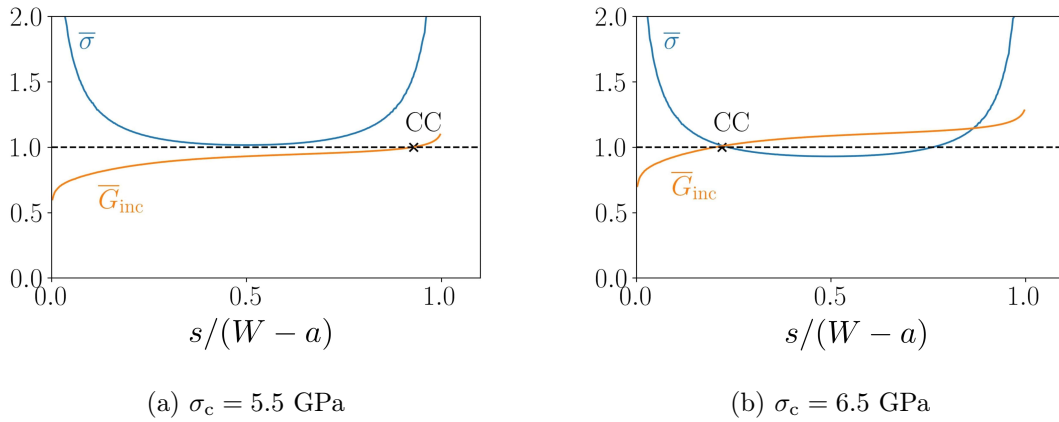


Figure 2.26: Two different applications of the CC under DC loading mode.

This test recalls the example of the bar in tension (Subsection 2.2.1) but with some differences due to the presence of the two notches. As a consequence, this test, especially under DC loading mode, seems again unsuitable for measuring any tensile strength.

## 2.3 PF model of brittle materials at the micro-scale

As it was mentioned at the beginning of this chapter both the CC and the PF model for fracture have a length parameter that is proportional to the Irwin length,  $l_{\text{Irwin}}$ . Hence, the aim of this section is to analyse the answer brought by both methodologies when  $l_{\text{Irwin}}$  is too close to the dimensions of the specimen, a situation observed at the micro-scale in brittle materials.

In the previous section the application of the CC at the micro-scale was deeply studied. In this section, the PF model for brittle fracture is applied, comparing the conclusions obtained with this methodology to the ones obtained with the CC. Note that the intention is not to determine whether one methodology is correct or not, but to compare both in a reasoned manner and explain the differences and similarities obtained. For the completion of this work, in addition to the collaboration with their supervisors, the author conducted a secondment during 5 months at University of Seville (Spain).

### 2.3.1 Preliminary remark

The previous section started with a preliminary remark where the case of a homogeneous bar under uniform tension was studied. This simple example was analytically solved by introducing a critical length,  $L_c$ , whose value is proportional to  $l_{\text{Irwin}}$ ,  $L_c = 2l_{\text{Irwin}}$ . When the length of the bar is less than  $L_c$ , the failure stress is entirely governed by the energy condition and its value is no longer dependent on the tensile strength,  $\sigma_c$ . An apparent strengthening effect

for  $L < L_c$  is therefore observed due to the smallness of the bar at the micro-scale.

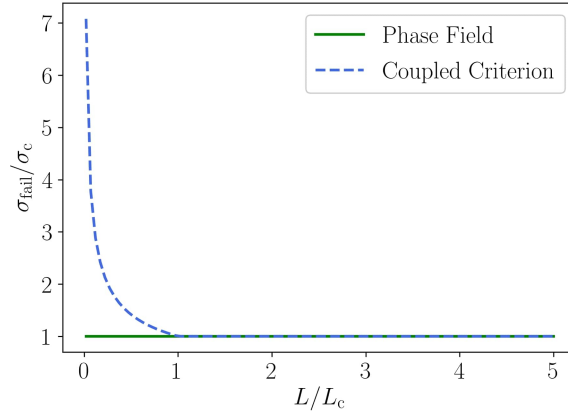


Figure 2.27: Evolution of the stress at failure  $\sigma_{\text{fail}}$  with respect to the length of the bar in the tensile test of a homogeneous bar, according to the CC and the PF model.

In the PF model considered in this PhD thesis the tensile strength is not directly included in the PF formulation. It is implicitly considered through the definition of the phase field length scale  $l_{\text{PF}}$ , that depends on  $\sigma_c$ , see (1.74) for the AT1 model. The definition of  $l_{\text{PF}}$  is based on the homogeneous solution of the 1D tensile test, where the peak stress at the end of the elastic phase is set as the tensile strength, see Fig. 1.12 as an example. Interestingly, this means that no strengthening effect would be observed in this problem regardless the length of the bar, and the CC and the PF predictions would be different for  $L < L_c$ , as it is shown in Fig. 2.27, where the tensile stress at failure  $\sigma_{\text{fail}}$  is represented as a function of the length of the bar  $L$ , considering material properties in Table 2.1. This example illustrates a general conclusion that will be observed throughout this section: different results are obtained in the PF model and the CC when the characteristic length of the material is of the order of the dimensions of the specimen.

### 2.3.2 Apparent strengthening effect in an unnotched specimen

When there is a stress gradient in the structure there is a strengthening effect, as it is mentioned in Section 2.2.2. One example is the bending test of an unnotched specimen, see Fig. 2.28, where compression is located in the upper part and tension in the lower part of the structure. The specimen has the following dimensions:  $L = 8 \mu\text{m}$  and  $W = 1 \mu\text{m}$ . A brittle material alumina-zirconia is selected, being the mechanical properties  $E = 380 \text{ GPa}$  and  $\nu = 0.22$ . The entire test is performed under displacement control.

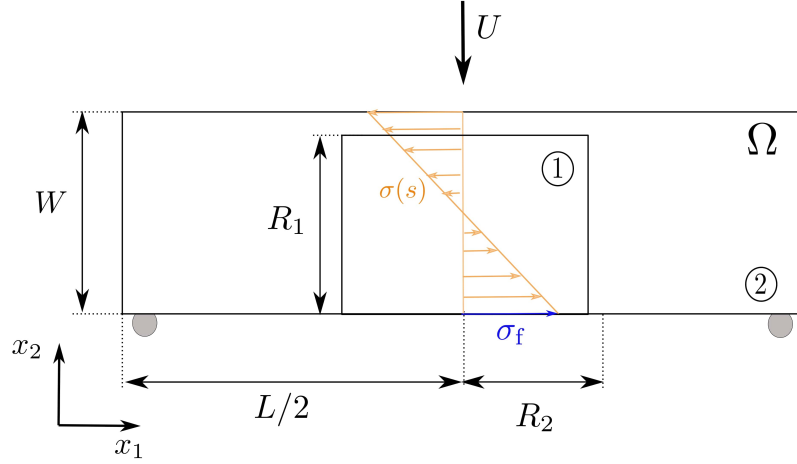


Figure 2.28: Schematic view of an unnotched specimen in a bending test. The orange solid line is the tensile component of the stress tensor along the middle axis. It is positive on the bottom face and negative above. In blue the flexural stress has been highlighted.

As it is shown in Fig. 2.28, a pointwise displacement is applied in the bending test, a simplification that is theoretically forbidden in the FE simulation, since it leads to an infinite energy that is incompatible with the Lax-Milgram theorem. In the PF model, this simplification can lead to local damage nucleation near the pointwise boundary conditions. As a result, the crack nucleation can deviate from the expected location (in the middle of the bottom part of the specimen). To avoid this effect, two subdomains are defined, as shown in Fig. 2.28. Subdomain 2 contains the pointwise boundary conditions, and  $\alpha = 0$  is imposed. In subdomain 1, the evolution of the damage variable is allowed. Notice that in the CC this problem is overcome imposing the expected crack path in the structure.

The dimensions of subdomains 1 and 2 are highly sensitive to the choice of the phase field length scale. For large values of  $l_{\text{PF}}$ , a large value of  $R_2$  is required, since the width of the damage region is greater (it is  $2l_{\text{PF}}$ ), but at the same time, the maximum mesh size is not extremely small. Notice that in subdomain 1 a maximum mesh size is imposed, considering that  $l_{\text{mesh}} = l_{\text{PF}}/5$  in the damaged initiation zone [70]. Hence, when  $l_{\text{PF}}$  is very small,  $R_2$  is also small to reduce computational complexity. The other magnitude to determine is  $R_1$ , which is set here as  $R_1 = 97\% W$ .

The strengthening effect is studied as a function of a control parameter, that is

$$\frac{l_{\text{PF}}}{W} \quad (2.16)$$

where  $W$  is a characteristic length of the specimen. When studying this problem considering the CC, see Section 2.3.2, the scale of the problem (mm,  $\mu\text{m}$ ...) was varied changing  $G_c$ . However, in this analysis only  $l_{\text{PF}}$  is varied to modify the control parameter and consequently,

the scale of the problem is not relevant and  $G_c = 23 \text{ MPa } \mu\text{m}$  is set in the whole analysis. Moreover, in the PF model considered in this analysis,  $l_{\text{PF}}$  is a characteristic length of the material proportional to  $l_{\text{Irwin}}$  and therefore to  $\sigma_c$ . The range of  $l_{\text{PF}}$  studied is  $l_{\text{PF}} = 0.005 - 1 \mu\text{m}$ , which means that the tensile strength varies as  $\sigma_c = 1845 - 26245 \text{ MPa}$ , according to the AT1 model.

Two quantities are determined: the critical displacement at which the structure fails  $U_{\text{crit}}$  and the critical flexural stress  $\sigma_{\text{fcrit}}$ , defined in Section 2.2.2 as the tensile stress at the moment of failure located in the middle of the bottom part in the unnotched specimen.

Table 2.8 shows  $U_{\text{crit}}$  according to the PF model and the CC. The nucleation length, the phase field length scale, and the Irwin length are also given. A good agreement between the two methods is observed, especially when reducing the ratio  $l_{\text{Irwin}}/W$ . The biggest difference (around 10%) is found when  $l_{\text{PF}} = W$  and  $l_{\text{Irwin}} \approx 2W$ , where there is a change in the decreasing tendency of  $U_{\text{crit}}$  with  $l_{\text{Irwin}}$  according to the PF model, but not according to the CC.

The critical displacement  $U_{\text{crit}}$  is determined when there is a significant force drop in the force-displacement (F-U) diagram, as shown in Fig. 2.29 for  $l_{\text{PF}} = 0.007 \mu\text{m}$  and  $l_{\text{PF}} = 0.5 \mu\text{m}$ . It is worth noting that the drop in force is greater for the case of  $l_{\text{PF}} = 0.007 \mu\text{m}$ , where  $F \approx 0$  after crack nucleation, meaning that the specimen is almost split into two parts at the critical load. On the contrary, for  $l_{\text{PF}} = 0.5 \mu\text{m}$  a smaller crack is nucleated because  $F$  is greater after the force drop. This means that our model is limited by  $l_{\text{PF}}$ . For a certain minimum value of  $l_{\text{PF}}$ , it is expected to obtain a specimen divided into two parts after crack nucleation, and this is not possible with our simplified model, where  $\alpha$  grows only in a region limited by  $R_1 = 97\%W$ . Convergence problems in the numerical simulations are obtained for this kind of cases.

$l_{\text{PF}}/W$	0.005	0.007	0.01	0.05	0.1	0.2	0.5	1
$l_{\text{Irwin}}/W$	0.0133	0.019	0.027	0.133	0.267	0.533	1.333	2.667
$l_{\text{nuc}}/W$	0.008	0.01	0.017	0.058	0.1	0.156	0.242	0.304
$U_{\text{crit}} [\mu\text{m}]$ (CC)	0.775	0.662	0.557	0.276	0.217	0.179	0.151	0.14
$U_{\text{crit}} [\mu\text{m}]$ (PF)	0.799	0.67	0.575	0.278	0.218	0.17	0.148	0.16

Table 2.8: Critical displacement obtained in the bending test of an unnotched specimen according to the CC and the PF model, as a function of  $l_{\text{PF}}/W$ .

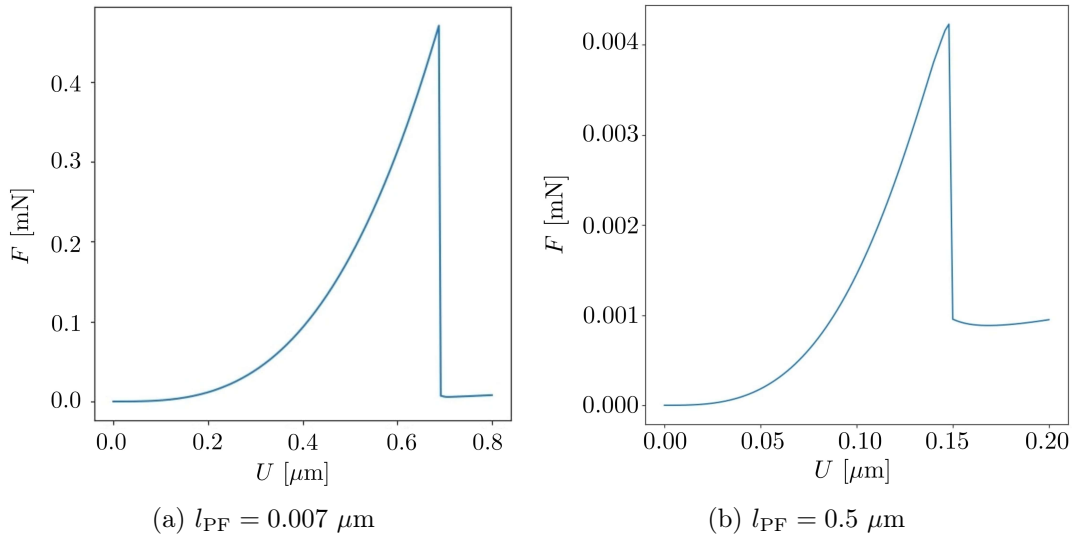


Figure 2.29: Force-Displacement curve in the bending test of an unnotched specimen for two different values of the phase field length scale.

Fig. 2.30 shows the flexural stress  $\sigma_f/\sigma_c$  as a function of the displacement applied  $U$  for  $l_{PF}/W = 0.007 \mu\text{m}$  and  $l_{PF}/W = 0.5 \mu\text{m}$ . If  $l_{PF}/W = 0.007$  a Griffith-like crack appears (see Fig. 2.32), and the damage variable abruptly evolves from  $\alpha = 0$  to 1. In that case,  $\sigma_f$  starts decreasing when it reaches the tensile strength  $\sigma_c$ . However, as  $l_{PF}/W$  increases, the damage variable does not abruptly change but evolves progressively. The damaged zone is no longer a small region in the material, and therefore there is not a crack in the sense of Griffith (see Fig. 2.33). The stress  $\sigma_f$  increases, surpassing  $\sigma_c$ , and this phenomenon is known as structural stress hardening.

In Fig. 2.31  $\sigma_{f,crit}/\sigma_c$  as a function of  $l_{PF}/W$  is represented, the latter on a logarithmic scale, according to the PF model and the CC. Notice that  $\sigma_{f,crit}$  considering the CC has been obtained applying the corresponding  $\sigma_c, G_c$  for each value of  $l_{PF}$  (assuming AT1 model). It can be observed that  $\sigma_{f,crit} \approx \sigma_c$  when  $l_{PF}/W \ll 1$  for both the CC and the PF model, whereas as  $l_{PF}$  increases,  $\sigma_{f,crit} > \sigma_c$  and the two curves diverge more and more. This is because the strengthening effect represented by the PF model, generated by damage dissipation, is not equal to the one predicted by the CC. First, in the CC a sharp crack (discontinuous model) is studied, and no dissipation of damage is considered. Moreover, a non-local stress condition is applied, which is highly affected by the stress gradient in the specimen. In conclusion, both estimations would never coincide for high values of  $l_{PF}/W$ , which is the common situation when descending the scales.

Furthermore, as an example of the damage region, Fig. 2.32 - 2.34 shows the damage variable for  $l_{PF} = 0.007, 0.05$  and  $1 \mu\text{m}$  when  $U = U_{crit}$ . In the last case the width of the damage region is, as mentioned before, much larger than in the first case. Clearly, the case of  $l_{PF} = 0.007 \mu\text{m}$  represents a narrow Griffith-like crack, whereas the case of  $l_{PF} = 1 \mu\text{m}$  shows

a damage dissipation model. The crack for  $l_{PF} = 0.007 \mu\text{m}$  is also longer, since more energy is dissipated as the moment of failure.

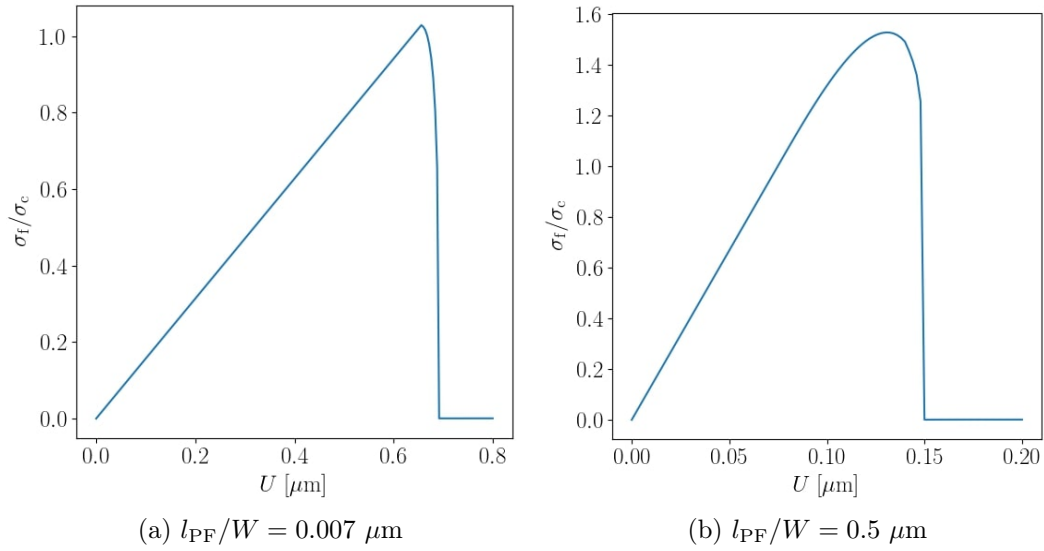


Figure 2.30: Evolution of  $\sigma_f/\sigma_c$  with respect to  $U$  in the bending test of an unnotched specimen for two values of the phase field length scale.

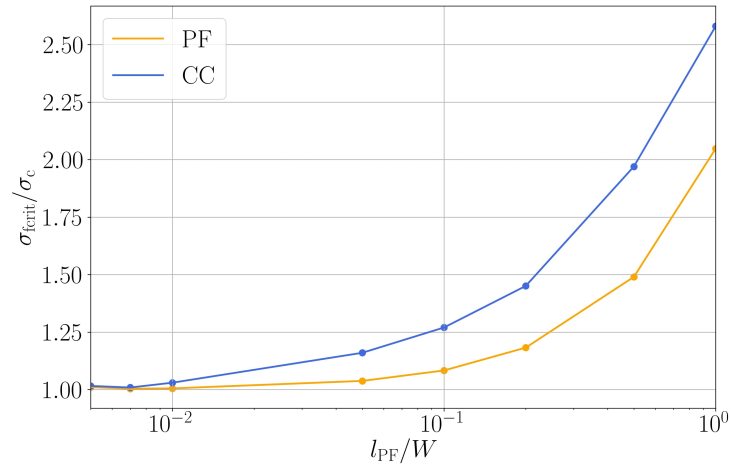
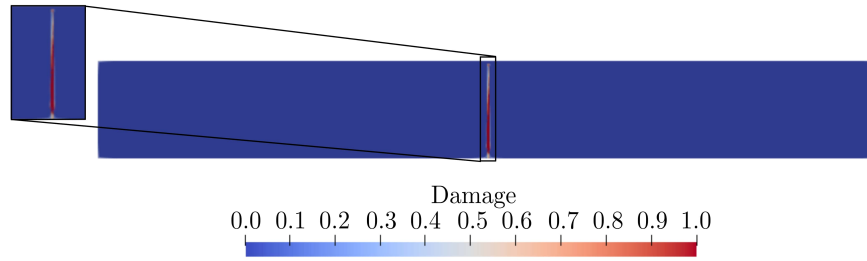
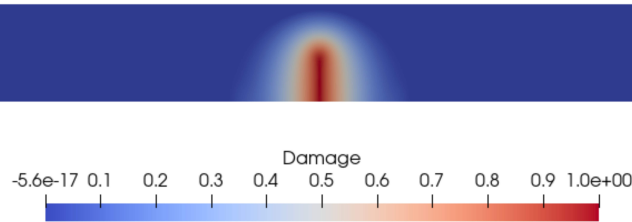
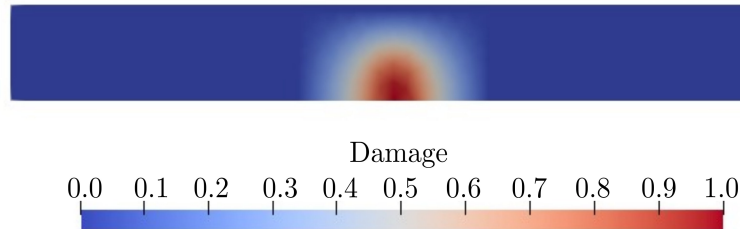


Figure 2.31: Evolution of  $\sigma_{\text{crit}}/\sigma_c$  as a function of  $l_{PF}/W$  in the bending test of an unnotched specimen. Two methods have been applied: the CC and the PF model.

Figure 2.32: Damage variable when  $U = U_{\text{crit}}$  for  $l_{\text{PF}} = 0.007 \mu\text{m}$ .Figure 2.33: Damage variable when  $U = U_{\text{crit}}$  for  $l_{\text{PF}} = 0.5 \mu\text{m}$ .Figure 2.34: Damage variable when  $U = U_{\text{crit}}$  for  $l_{\text{PF}} = 1 \mu\text{m}$ .

### 2.3.3 Scale effect in a V-notched specimen

A V-notched specimen with  $\omega = 90^\circ$  is considered in this section, represented in Fig. 2.35. As it was explained in [71] we impose the damage notch conditions, i.e., the condition  $\alpha = 1$  at the free edges of the notch, since undamaged notch conditions tend to overestimate the critical load. Moreover, two subdomains are defined in the specimen (see Fig. 2.35). Only in subdomain 1 the evolution of damage is allowed, and therefore the condition  $\alpha = 0$  is set out of subdomain 1. This is done to avoid local damage nucleation in the vicinity of the point-wise boundary conditions. The mesh size in subdomain 1 is again defined considering that the maximum mesh size should be 5 times lower than  $l_{\text{PF}}$ . The radius  $R$  is set

as  $97\%W$ . The general dimensions of the specimen are  $L = 8 \mu\text{m}$ ,  $W = 1 \mu\text{m}$  and  $a = 0.2 \mu\text{m}$ .

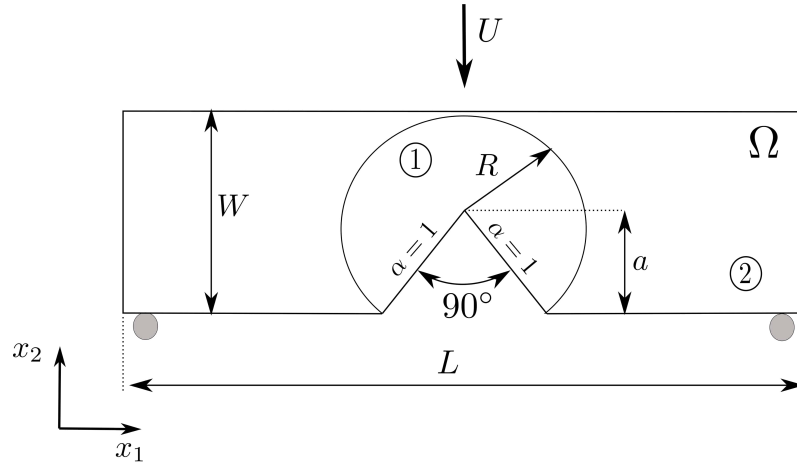


Figure 2.35: Scheme of a 3-point bending test in a V-notched specimen.

As in the previous section,  $U_{\text{crit}}$  is obtained using the PF model. However, estimating  $U_{\text{crit}}$  in this problem is not an easy task and might be deeply analysed. When  $l_{\text{PF}}/(W - a) \rightarrow 0$ , the force drop observed in the diagram  $F - U$  occurs for a critical displacement higher than the drop in the diagram  $K - U$ , where  $K$  is the stiffness of the structure, defined as the derivative of the force with respect to the displacement. One example is shown in Fig. 2.36 for  $l_{\text{PF}}/(W - a) = 0.0025$ . It is important to highlight that in the unnotched specimen analyzed in the previous section it was verified that both criteria conducted to the same result in the range of  $\sigma_c$  studied, and therefore only the  $F - U$  diagram was represented.

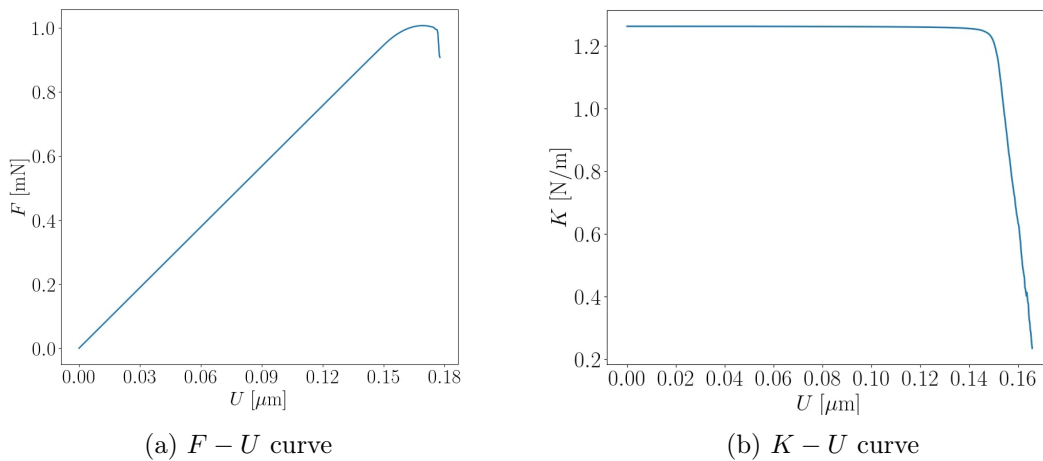


Figure 2.36: Application of the PF model in the V-notched specimen for  $l_{\text{PF}}/(W - a) = 0.0025$ .

Fig. 2.37 shows the damage variable at the moment of failure according to these two different criteria (the force and stiffness), for  $l_{PF}/(W - a) = 0.0025$ . When there is a drop in the  $K - U$  curve, a small crack is observed, whereas a much longer crack is shown when considering a drop in the  $F - U$  curve, related to a higher critical displacement.

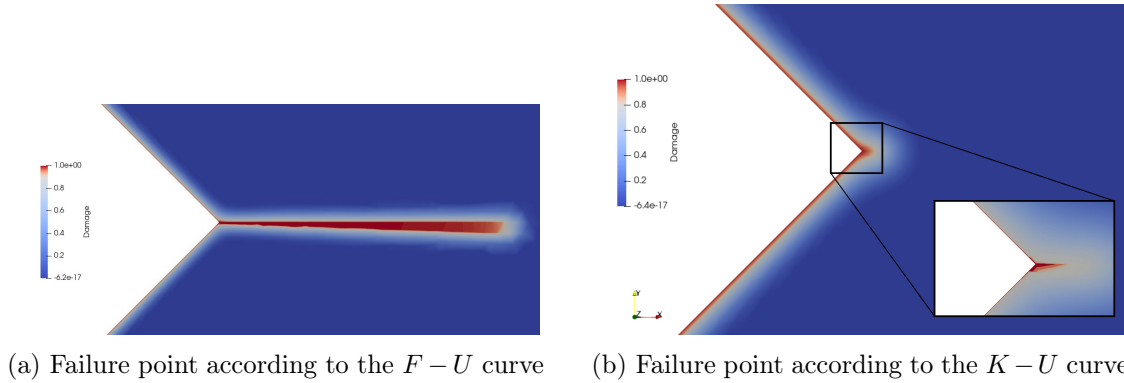


Figure 2.37: Damage variable at the moment of failure for  $l_{PF}/(W - a) = 0.0025$  according to different criteria.

Fig. 2.38 shows the critical displacement with respect to  $l_{PF}/(W - a)$  in the V-notched specimen, using the PF model with the two criteria (force and stiffness) and the CC. First, although for small and high values of  $l_{PF}/(W - a)$  there is a bias in the two PF predictions, the difference is smaller for intermediate values of  $l_{PF}/(W - a)$  in the range chosen. Moreover, there is a clear agreement in the predictions of the CC and the PF with the stiffness criterion for low values of  $l_{PF}/(W - a)$ , whereas the two curves diverge when increasing  $l_{PF}/(W - a)$ . The latter is explained by the dissipation of damage. If  $l_{PF}/(W - a)$  is high the PF model no longer predicts a Griffith-like crack, but a damage region in the structure.

Moreover, a change in the tendency is observed for great values of the phase field length scale with respect to the specimen. This is more clearly represented in Fig. 2.39, that represents the evolution of the critical displacement with respect to  $l_{Irwin}/(W - a)$  for the CC and the PF model (considering the two criteria explained above). The tendency change in the PF model is located at  $l_{Irwin} = W - a$ .

Although there is not any FFM assumption in the PF model, at the failure moment (understanding the failure point as the point where there is a drop in the stiffness or in the force), there is a certain crack of finite length, as it was shown in Fig. 2.37. This idea is also illustrated in Fig. 2.40, where a new criterion has been used to predict the critical displacement using the PF model. In this case, it is assumed that the critical displacement occurs when the damage variable reaches to 1 at a certain distance from the singularity point, equal to the nucleation length predicted by the Coupled Criterion. A good agreement of this prediction with respect to the others ( $F - U$  and  $K - U$ ) is observed for low values of the Irwin length, since the nucleation length obtained by the Coupled Criterion is small. On the contrary, a bigger bias is appreciated when increasing the Irwin length, since the nucle-

ation length estimated by the CC is much higher than the damage evolution predicted by the PF model. However, there is still a good agreement between this new criterion and the force criterion. Notice that the stiffness always predicts the lowest value of the critical displacement.

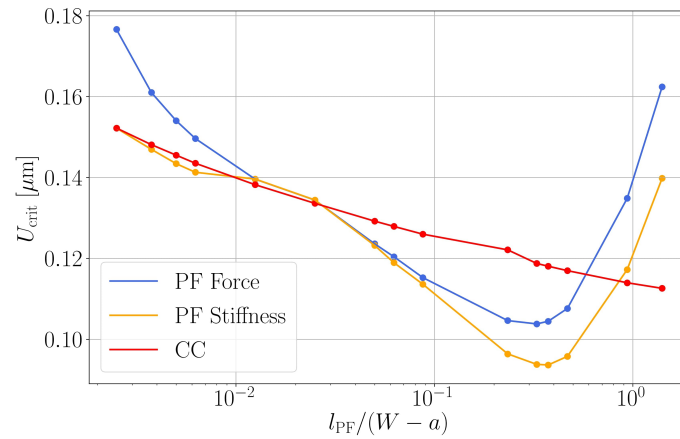


Figure 2.38: Evolution of the critical displacement  $U_{crit}$  with respect to  $l_{PF}/(W - a)$  considering the stiffness and the force criteria.

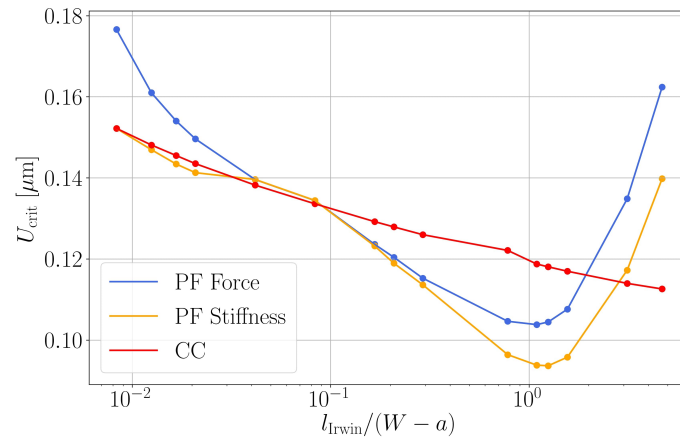


Figure 2.39: Evolution of the critical displacement  $U_{crit}$  with respect to  $l_{Irwin}/(W - a)$  considering the stiffness and the force criteria.

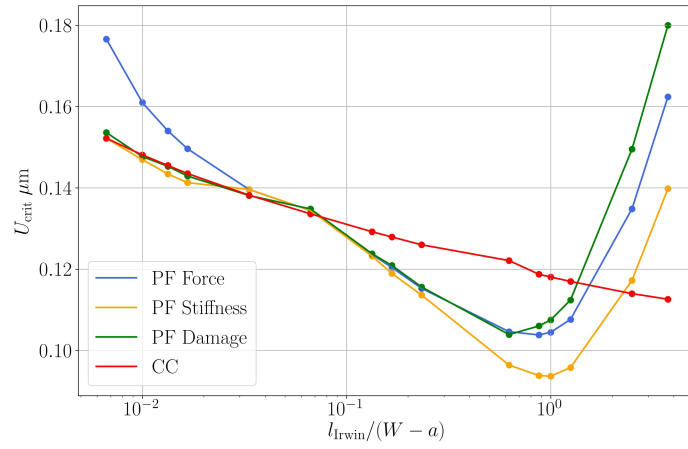


Figure 2.40: Evolution of the critical displacement  $U_{crit}$  with respect to  $l_{irwin}/(W-a)$  when including the damage criterion.

### 2.3.4 Influence of the fracture properties

In this section, we study the influence of  $\sigma_c$  and  $G_c$  at the micro-scale considering the bending tests of micro-cantilever beams made by Henry et al [10] and the PF model for brittle fracture. In particular, the first specimen whose dimensions were shown in Table 2.6 is used. Several values of  $\sigma_c$  and  $G_c$  are considered, while keeping constant  $E$  and  $\nu$  indicated in Section 2.2.3.1. A scheme of the problem is represented in Fig. 2.41. Notice that in this case a distributed displacement  $u_d$  (Displacement control is assumed in this study) at the tip of the micro-beam has been used to avoid nucleation of local damage in the vicinity of the point load that was applied in the original test of Fig. 2.18. Moreover, the CC has been used to determine a first estimation of the critical displacement in the simulations.

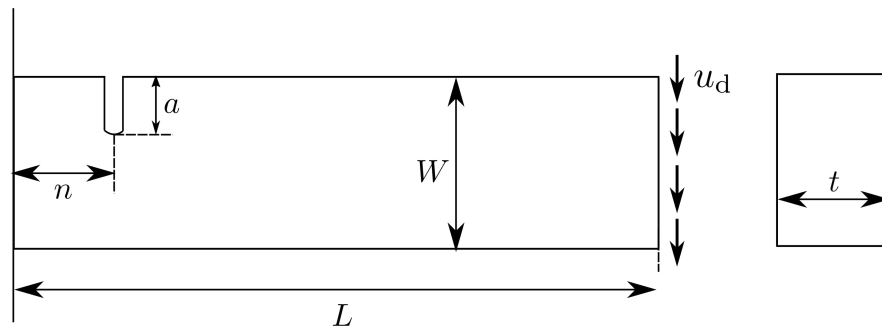


Figure 2.41: The U-notched micro-cantilever beam in the bending test analyzed using the PF model.

The parameter calculated to compare among the different values of  $\sigma_c$  and  $G_c$  is the critical

displacement  $U_{\text{crit}}$ , defined as the displacement  $u_d$  given when a crack is nucleated in the structure. As it was explained in previous section, this parameter is quite tricky to obtain when there is a notch in the specimen, since a conventional  $F - U$  curve might diverge from the  $K - U$  curve when reducing the phase field length scale. As an example, the difference between the force and the stiffness criterion is illustrated for the case of  $\sigma_c = 5$  GPa and  $G_c = 10$  MPa  $\mu\text{m}$ . The force drop corresponds to a critical displacement  $U_{\text{crit}} = 0.1343$   $\mu\text{m}$ , whereas the stiffness drop is produced at  $U_{\text{crit}} = 0.1286$   $\mu\text{m}$  (close to the estimation of the CC, which gives  $U_{\text{crit}} = 0.1301$   $\mu\text{m}$ ).

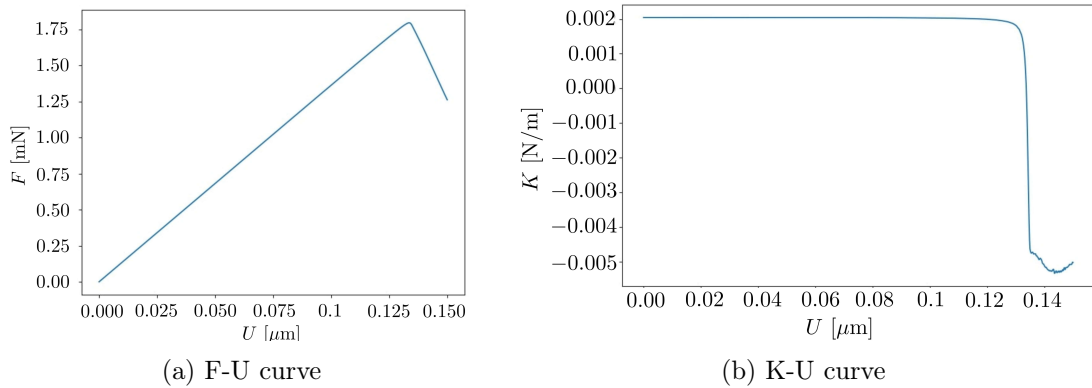


Figure 2.42: Result of the PF model. The example represented is for  $\sigma_c = 5000$  MPa and  $G_c = 10$  MPa  $\mu\text{m}$

As an example, in Fig. 2.42a the damage variable is represented at the moment of failure for  $\sigma_c = 5$  GPa and  $G_c = 10$  MPa  $\mu\text{m}$ . A very small crack is generated, increasing when the load is increased.

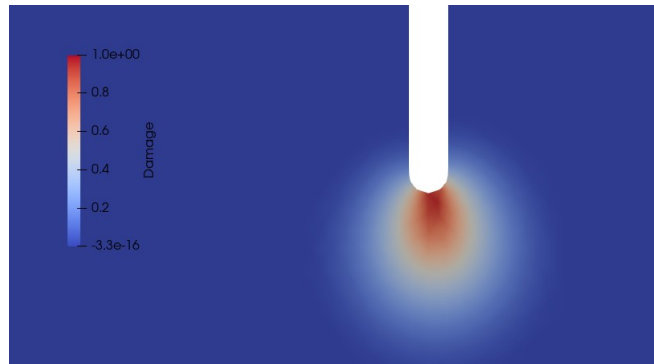


Figure 2.43: Damage variable at the moment of failure for  $\sigma_c = 5$  GPa and  $G_c = 10$  MPa  $\mu\text{m}$ .

In Fig. 2.44 the influence of  $\sigma_c$  is obtained when applying the PF model. It can be observed that high values of  $\sigma_c$  has much more influence, which are related to lower values of the Irwin length. In that situation, according to the CC, it is the stress condition that is governing the

failure. On the other hand, when lower values of  $\sigma_c$  are considered the critical displacement has a little dependance on the tensile strength. However, when  $\sigma_c$  is very small ( $\sigma_c = 1$  GPa) an increment of the critical displacement is observed. This was also shown in Fig. 2.40 in the V-notched specimen, and it happens when the Irwin length is of the order of the dimensions of the specimen.

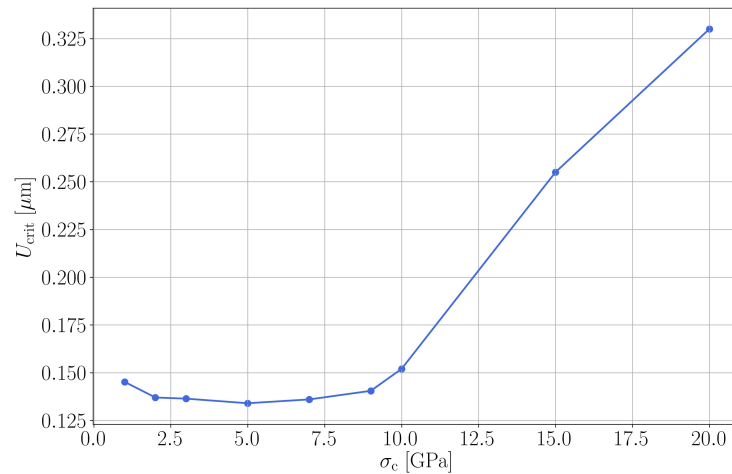


Figure 2.44: Influence of the tensile strength  $\sigma_c$  for  $G_c = 10 \text{ MPa} \mu\text{m}$  when considering the PF model.

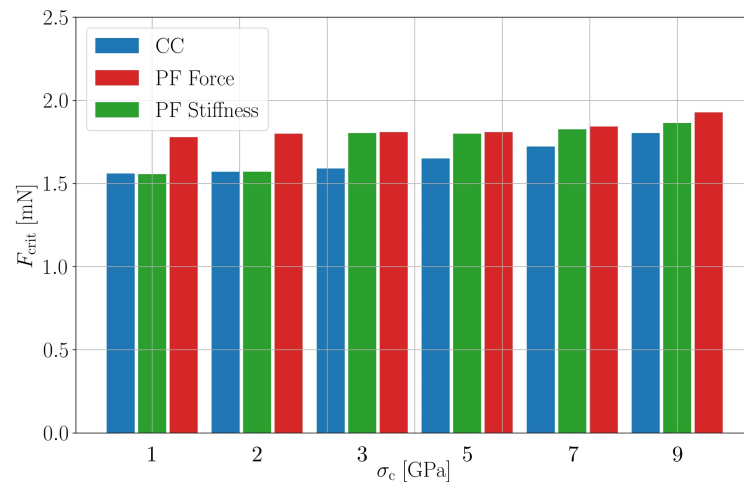


Figure 2.45: Influence of the tensile strength  $\sigma_c$  in the specimen 1 considering the PF model and the CC.

The CC and the PF model are compared in Fig. 2.45, where the value of the critical force  $F_{crit}$  is calculated for a certain range of  $\sigma_c$ . For the PF model, two criteria have been used, the

$F - U$  curve and the  $K - U$  curve, to obtain a value of the critical displacement. Then, the corresponding critical force has been obtained. It can be observed that the stiffness criterion agrees better with the Coupled Criterion. In general there are no big differences among the three options, and clearly in this range there is a little influence of  $\sigma_c$  in the crack nucleation.

Finally, the influence of  $G_c$  is shown in Fig. 2.46 predicted by the CC and the PF model. Notice that this fracture property has a bigger influence than  $\sigma_c$  in the range studied. When comparing to the experimental value,  $F_{\text{crit}} = 1.53 \text{ mN}$ , in Fig. 2.45 there is a good agreement between numerical results and this experimental measurement. However, only for  $G_c = 10 \text{ MPa } \mu\text{m}$  numerical results are closed to the experiment in Fig. 2.46. It is important to highlight that numerical results in this section are obtained under DC, but the real experiment was carried out under FC for specimen 1.

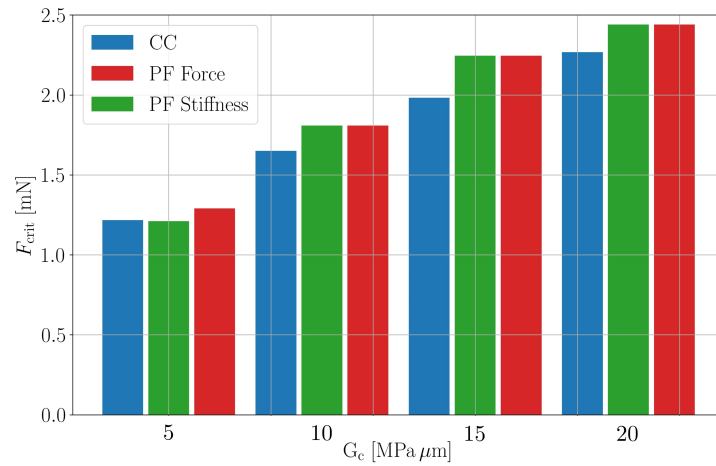


Figure 2.46: Influence of the critical energy release rate  $G_c$  in the specimen 1 considering the PF model and the CC.

## 2.4 Conclusions

From CC perspective there is a nucleation length proportional to the Irwin length. From the point of view of the PF model for brittle fracture, there is a phase field length scale. Both length parameters depend on the Irwin length, an intrinsic mechanical property of the material. At the macro-scale, this length is small compared to any dimension of the structure while at the micro-scale, it is of the same order of magnitude or even larger and can interact with the dimensions of the structure. Therefore, it is the relation between the Irwin length and the dimensions of the specimen that plays an important role in the predictions made by both the CC and the PF model. Throughout this chapter, the answer brought by these two methodologies widely well-known to predict fracture in brittle materials have been analysed and reasonably compared in ceramics at the micro-scale, to determine their similarities and differences.

First, the Coupled Criterion at the micro-scale must be used in its FFE form because the necessary condition of the asymptotic approach is no longer fulfilled. This prevents to use analytical formulas based on Williams' expansion. Moreover, the CC allows to show that the apparent strengthening observed in experiments conducted at the micro-scale is due to a lack of available energy as a consequence of the small size of the samples. In addition, in bending tests, the smaller the samples, the larger the stress gradient, leads to a similar apparent strengthening. It is often misinterpreted as an actual strengthening, although it has been shown in thin films, by varying the thickness of the film, that the tensile strength does not reach such high values [82, 83]. Accordingly, tests are often weakly or even totally insensitive to the tensile strength whereas they are sensitive to the fracture energy. Moreover, the smaller the samples, the more insensitive they are to notches. It can be also noted that the effect of force and displacement controlled loading modes differs more and more descending the scales.

On the other hand, using the PF model for brittle fracture it is possible to observe a strengthening effect in bending tests of ceramics at the micro-scale, explained by the dissipation of damage when descending the scales. As it was mentioned above, the control parameter in this study is the relation between the Irwin length and the dimensions of the specimen. To reinforce this idea, the analysis was conducted changing the Irwin length and keeping constant the scale of the specimen.

Differences and similarities were found when comparing the results obtained by the CC and the PF model. When the Irwin length is much smaller than the dimensions of the specimen, there is a good agreement between both methodologies. However, when the Irwin length can interact with the dimensions of the specimen the PF model no longer predicts a Griffith-like fracture, and the dissipation of damage increases the difference between results brought by the CC and the PF model for brittle fracture. A particular case is the homogeneous solution of the tensile test, where it is shown that both methodologies give different results when descending the scales.

Although both methodologies can differ when increasing the Irwin length or descending the scales in the specimen, the same qualitative conclusions can be obtained about the influence of the fracture properties. At the micro-scale, i.e., when the Irwin length is of the order of the dimensions of the specimen, the tensile strength has almost no influence on fracture and the critical energy release rate is governing crack nucleation.



# Chapter 3

## A design tool for advanced ceramics with reinforcements

### Contents

---

<b>3.1</b>	<b>Description of the computational tool . . . . .</b>	<b>68</b>
<b>3.2</b>	<b>Application example: borosilicate glass reinforced by alumina platelets . . . . .</b>	<b>75</b>
<b>3.3</b>	<b>Industrial application: Ceramic matrix composites with short fibers . . . . .</b>	<b>115</b>

---

One way of increasing the fracture toughness of brittle materials is to introduce a reinforcing component in the form of platelets or short fibres. In this chapter, we develop a computational tool to study the fracture behaviour of such composites, considered a type of advanced ceramics. The aim of this tool is to provide an insight into the changes generated in the crack propagation when it encounters the reinforcing element, estimating the apparent fracture toughness of the composite as a function of design parameters. Throughout this chapter, two materials are studied. The first one is used to explain the calculation tool and the second to illustrate its industrial applicability, since it was proposed by the company Safran.

The work presented in this chapter was published in [84] and [85].

### 3.1 Description of the computational tool

The computational tool developed is based on the numerical resolution of a reference problem, under the assumption of plane strain 2D elasticity, applying the Coupled Criterion (CC) together with the Matched Asymptotics (MA) approach.

#### 3.1.1 Description of the reference problem

Assuming that the dimensions of the reinforcing component are much smaller than the dimensions of the specimen, a symmetric 3-point bending test, see Fig. 3.1, with a pre-existing crack  $\Gamma_c$  under Mode I loading conditions, is considered as a reference problem to estimate the apparent fracture toughness of the composite. At the tip of the pre-existing crack there is a reinforcing element with a rectangular shape oriented a certain angle  $\alpha_r$ . This element is immersed in a volume of matrix according to the volume fraction of the reinforcement  $V_r$ , the whole being itself immersed in a homogenized material called in the following the composite. The length and thickness of the matrix envelope are  $a_l$  and  $a_t$  and fulfill

$$a_l = \frac{l}{\sqrt{V_r}} \quad \text{and} \quad a_t = \frac{t}{\sqrt{V_r}}. \quad (3.1)$$

The interface between the reinforcing element and the matrix can be weak or strong, depending on the materials. Notice that the reinforcing element could have a different shape, although in this chapter we assume that it is rectangular. In this reference problem we include a cooling change in temperature  $\Delta\theta$  to take into account the effect of residual stresses generated due to the mismatch between the matrix and the reinforcing element, a common phenomenon in this kind of composites.

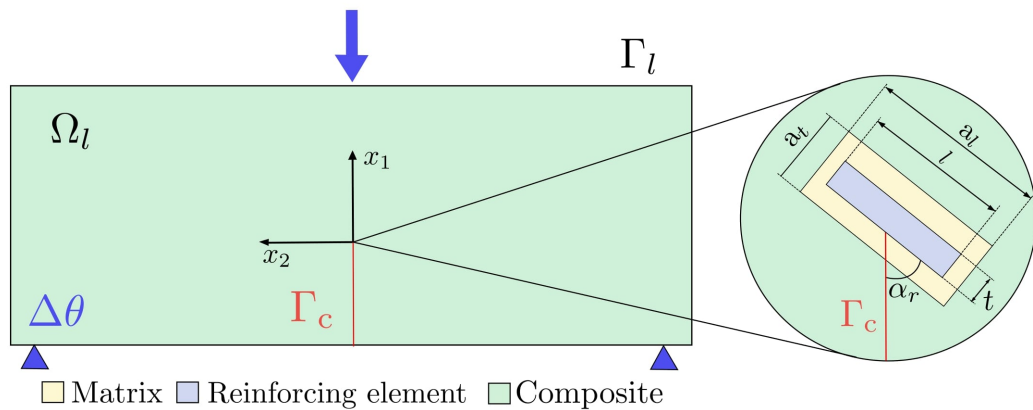


Figure 3.1: Scheme of a symmetric 3-point bending test on a cracked specimen after cooling. A rectangular reinforcing element (blue) and its environment (matrix in yellow and homogenized material in green) is located at the tip of the crack.

The problem illustrated in Fig. 3.1 is a thermomechanical one. A superposition principle can be applied to describe the solution  $\underline{U}(x_1, x_2)$  as the sum of the solution to a pure mechanical

problem  $\underline{U}^{\text{cr}}$  and the solution to a thermoelastic problem  $\underline{U}^{\text{te}}$

$$\underline{U}(x_1, x_2) = \underline{U}^{\text{cr}}(x_1, x_2) + \underline{U}^{\text{te}}(x_1, x_2). \quad (3.2)$$

The pure mechanical displacement,  $\underline{U}^{\text{cr}}$  is the solution to the following elastic problem

$$\text{Find } \underline{U}^{\text{cr}} \in \mathcal{W}^{\text{cr}} \text{ such that } \int_{\Omega_l} \mathbf{C} : \nabla \underline{U}^{\text{cr}} : \nabla \underline{\phi} dx_1 dx_2 = 0, \quad \forall \underline{\phi} \in \mathcal{W}_0^{\text{cr}}, \quad (3.3)$$

in which  $\underline{\phi}$  and  $\underline{U}^{\text{cr}}$  are the test and trial functions, respectively. The functional spaces of smooth functions  $\mathcal{W}^{\text{cr}}$  and  $\mathcal{W}_0^{\text{cr}}$  are defined as

$$\mathcal{W}^{\text{cr}} = \{ \underline{w}, \quad \underline{w} = \bar{U} \quad \text{on } \Gamma_{ld} \}, \quad \mathcal{W}_0^{\text{cr}} = \{ \underline{w}, \quad \underline{w} = 0 \quad \text{on } \Gamma_{ld} \}, \quad (3.4)$$

where  $\Gamma_{ld}$  is the contour where Dirichlet boundary conditions are sent. The variational formulation of the thermoelastic problem is

$$\text{Find } \underline{U}^{\text{te}} \in \mathcal{W}^{\text{te}} \text{ such that} \\ \int_{\Omega_l} \mathbf{C} : \nabla \underline{U}^{\text{te}} : \nabla \underline{\phi} dx_1 dx_2 = \int_{\Omega_l} \mathbf{C} : \underline{\underline{\varepsilon}}^{\text{in}} : \nabla \underline{\phi} dx_1 dx_2, \quad \forall \underline{\phi} \in H^1(\Omega_l), \quad (3.5)$$

where  $H^1(\Omega_l)$  is the first Sobolev space in the domain  $\Omega_l$ . Note that only the smoothness condition is required for the space of admissible solution since the cooling occurs without any constraint on the boundaries of the specimen. The inelastic strain tensor appearing in (3.5) is

$$\underline{\underline{\varepsilon}}^{\text{in}} = -\alpha_{\text{T}} \Delta \theta \underline{\underline{I}}, \quad (3.6)$$

where  $\underline{\underline{I}}$  is the identity matrix and the temperature change during cooling  $\Delta \theta = \theta_0 - \theta_f$  is the difference between the initial temperature  $\theta_0$ , and the final one  $\theta_f$ .

The analysis made in this chapter focuses on the role of the size effect due to the smallness of the reinforcing element. To that aim, and for simplicity, the analysis is conducted under the assumption of plane strain 2D elasticity. Moreover, due to the smallness of the reinforcing element, the elastic solution in the vicinity of the crack tip is estimated using the Matched Asymptotic approach, as explained in the following section.

### 3.1.2 Matched Asymptotic approach

The MA approach [86] provides a two-scale analysis of an elastic problem including a small perturbation in the domain where the problem is posed. This method, as mentioned in Section 1.2.2, can be applied if the size of the perturbation is much smaller than the specimen dimensions. In the present case, see Fig. 3.1, where  $\Omega_l$  is the actual perturbed domain, the reinforcing component is assumed to be the perturbation, and therefore the initial hypothesis of this methodology is fulfilled. The corresponding elastic displacement is denoted as  $\underline{U}_l(x_1, x_2)$ . The index  $l$  recalls the dependence of the solution to the perturbation. Following (3.2),

$$\underline{U}_l(x_1, x_2) = \underline{U}_l^{\text{cr}}(x_1, x_2) + \underline{U}_l^{\text{te}}(x_1, x_2) \quad (3.7)$$

In the framework of MA,  $\underline{U}_l(x_1, x_2)$  can be approximated by an outer and an inner expansions. Starting by the pure mechanical solution  $\underline{U}_l^{\text{cr}}(x_1, x_2)$  the outer expansion can be written as

$$\underline{U}_l^{\text{cr}}(x_1, x_2) = \underline{U}_0^{\text{cr}}(x_1, x_2) + \dots, \quad (3.8)$$

where the leading term  $\underline{U}_0^{\text{cr}}(x_1, x_2)$  corresponds to the solution of the same elastic problem settled in the so-called outer domain  $\Omega_0$ , i.e., assuming the perturbation (the reinforcing element) is too small to be visible in the specimen, and thus, is neglected. This approximation is expected to be relevant far away from the location of the perturbation, but becomes meaningless close to it.

In the neighbourhood of the crack tip in  $\Omega_0$ , the behaviour of  $\underline{U}_0^{\text{cr}}(x_1, x_2)$  is described by Williams' expansion [51], in this case for a crack under Mode I. It is expressed in the polar coordinates system  $(r, \theta)$  with origin at the crack tip as

$$\underline{U}_0^{\text{cr}}(r, \theta) = \underline{U}_0(0, 0) + K_{\text{I}}\sqrt{r}\underline{u}(\theta) + \dots, \quad (3.9)$$

where  $K_{\text{I}}$  is the stress intensity factor and  $\underline{u}(\theta)$  is the opening shape function.

On the other hand, the inner expansion is obtained by a change of variables  $x_i = ly_i$  ( $i = 1, 2$ ) and  $r = l\rho$ . The assumption of smallness brings us to consider the limit as  $l \rightarrow 0$ , it defines an unbounded domain, called inner domain  $\Omega_{\text{in}}$ , represented in Fig. 3.2, where parameters  $\hat{a}_l$ ,  $\hat{a}_t$ ,  $\hat{t}$  and  $\hat{l}$  are used to represent the dimensions of the heterogeneous region defined in Fig. 3.1 divided by the length of the reinforcing element,  $l$ . Obviously,  $\hat{l} = 1$ . The inner expansion for the pure mechanical solution  $\underline{U}_l^{\text{cr}}(x_1, x_2)$  is written as

$$\underline{U}_l^{\text{cr}}(x_1, x_2) = \underline{U}_l^{\text{cr}}(ly_1, ly_2) = F_0^{\text{cr}}(l)\underline{V}_0^{\text{cr}}(y_1, y_2) + F_1^{\text{cr}}(l)\underline{V}_1^{\text{cr}}(y_1, y_2) + \dots \quad (3.10)$$

Contrary to the outer expansion, this expression approximates  $\underline{U}_l^{\text{cr}}(x_1, x_2)$  in the neighbourhood of the perturbation.

Since both the inner and the outer expansions are representations of  $\underline{U}_l^{\text{cr}}(x_1, x_2)$ , there must be an intermediate region where both solutions coexist, i.e., the solution close to the crack tip in the outer domain must match with the solution far away from the reinforcing element in the inner domain. These are the so-called matching conditions,

$$F_0^{\text{cr}}(l) = 1, \quad \underline{V}_0^{\text{cr}}(y_1, y_2) \sim \underline{U}_0(0, 0) \quad \text{when} \quad \rho \rightarrow \infty, \quad (3.11)$$

$$F_1^{\text{cr}}(l) = K_{\text{I}}\sqrt{l}, \quad \underline{V}_1^{\text{cr}}(y_1, y_2) \sim \sqrt{\rho}\underline{u}(\theta) \quad \text{when} \quad \rho \rightarrow \infty, \quad (3.12)$$

where  $\sim$  means "behaves like". From (3.11) it is easily seen that  $\underline{V}_0^{\text{cr}}(y_1, y_2) = \underline{U}_0(0, 0)$ . On the other hand, the solution  $\underline{V}_1^{\text{cr}}(y_1, y_2)$  must be numerically calculated in an artificially bounded domain imposing the condition (3.12) at a very large distance from the perturbation. To that aim, a Finite Element (FE) simulation is performed using the software FEniCS [87] to numerically obtain the term  $\underline{V}_1^{\text{cr}}(y_1, y_2)$  in the inner problem. Notice that, from the theoretical point of view,  $\underline{V}_1^{\text{cr}}(y_1, y_2)$  has not a finite energy when  $\rho \rightarrow \infty$ , which means that the solution is not properly determined according to Lax-Milgram theorem. To establish the existence of

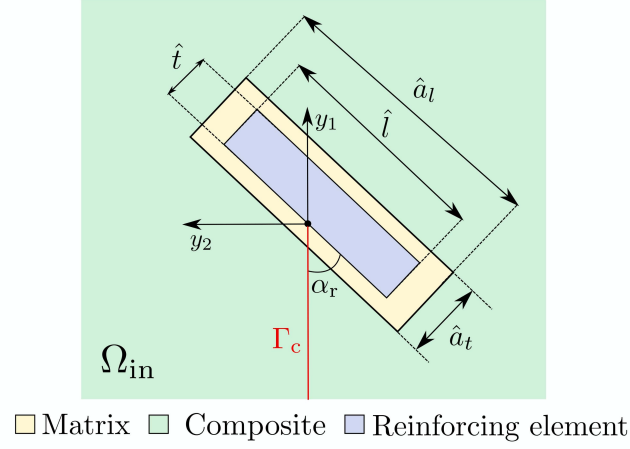


Figure 3.2: Schematic view of the inner domain.

the solution, a superposition procedure can be followed [86], as it was explained in Section 1.2.2. The final expression of the inner solution after applying the matching conditions is

$$\underline{U}_l^{\text{cr}}(x_1, x_2) = \underline{U}_0^{\text{cr}}(0, 0) + \sqrt{l}K_1 \underline{V}_1^{\text{cr}}(y_1, y_2) + \dots \quad (3.13)$$

In the thermoelastic problem, the outer expansion is written as

$$\underline{U}_l^{\text{te}}(x_1, x_2) = \underline{U}_0^{\text{te}}(x_1, x_2) + \dots, \quad (3.14)$$

where  $\underline{U}_0^{\text{te}}(x_1, x_2)$  is the solution of the same thermoelastic problem defined in the unperturbed domain  $\Omega_0$ . The outer solution  $\underline{U}_0^{\text{te}}(x_1, x_2)$  can be easily integrated from

$$\underline{\underline{\varepsilon}}_0^{\text{te}}(x_1, x_2) = \underline{\underline{\varepsilon}}^{\text{in}}; \quad \underline{\underline{\sigma}}_0^{\text{te}}(x_1, x_2) = \underline{\underline{0}} \quad (3.15)$$

obtaining that

$$\underline{U}_0^{\text{te}}(x_1, x_2) = \underline{U}_0^{\text{te}}(0, 0) + \underline{\underline{\varepsilon}}^{\text{in}} [x_1, x_2]^T. \quad (3.16)$$

This approximation correctly represents  $\underline{U}_l^{\text{te}}(x_1, x_2)$  far away from the perturbation. Notice that we should theoretically include the T-stress in the expansion (3.9) to be consistent with (3.16), but, after trying, it turns out that its influence is negligible in all cases.

On the other hand, the inner expansion, defined in the unbounded domain  $\Omega_{\text{in}}$ , see Fig. 3.2, is expressed as

$$\underline{U}_l^{\text{te}}(x_1, x_2) = \underline{U}_l^{\text{te}}(ly_1, ly_2) = F_0^{\text{te}}(l)\underline{V}_0^{\text{te}}(y_1, y_2) + F_1^{\text{te}}(l)\underline{V}_1^{\text{te}}(y_1, y_2) + \dots \quad (3.17)$$

Terms  $\underline{V}_0^{\text{te}}(y_1, y_2)$  and  $\underline{V}_1^{\text{te}}(y_1, y_2)$  are defined through the matching conditions, as it was explained for the pure mechanical problem,

$$F_0(l)\underline{V}_0^{\text{te}}(y_1, y_2) \approx \underline{U}_0^{\text{te}}(0, 0) \quad \text{when } \rho \rightarrow \infty, \quad (3.18)$$

$$F_1(l)\underline{V}_1^{\text{te}}(y_1, y_2) \approx l \underline{\underline{\varepsilon}}^{\text{in}} [y_1, y_2]^T \quad \text{when } \rho \rightarrow \infty. \quad (3.19)$$

Then  $F_0(l) = 1$  and  $\underline{V}_0^{\text{te}}(y_1, y_2) = \underline{U}_0^{\text{te}}(0, 0)$ , whereas  $F_1(l) = l$  and the term  $\underline{V}_1^{\text{te}}(y_1, y_2)$  is numerically obtained in the same way as it was done for the pure mechanical problem, using FEM on a very large but bounded domain with a traction free condition along the artificial outer boundary, according to (3.15), then

$$\underline{U}_l^{\text{te}}(x_1, x_2) = \underline{U}_0^{\text{te}}(0, 0) + l \underline{V}_1^{\text{te}}(y_1, y_2) + \dots \quad (3.20)$$

The actual stress tensor  $\underline{\underline{\sigma}}_l$  is calculated applying the superposition principle,

$$\underline{\underline{\sigma}}_l(x_1, x_2) = \underline{\underline{\sigma}}_l^{\text{cr}}(x_1, x_2) + \underline{\underline{\sigma}}_l^{\text{te}}(x_1, x_2), \quad (3.21)$$

where terms  $\underline{\underline{\sigma}}_l^{\text{cr}}(x_1, x_2)$  and  $\underline{\underline{\sigma}}_l^{\text{te}}(x_1, x_2)$  are approximated in the vicinity of the reinforcing element by the inner expansion. In the pure mechanical problem that means

$$\underline{\underline{\sigma}}_l^{\text{cr}}(x_1, x_2) = \frac{1}{l} \mathbf{C} : \nabla_y \underline{U}_l^{\text{cr}}(ly_1, ly_2) = \frac{K_I}{\sqrt{l}} \mathbf{C} : \nabla_y \underline{V}_1^{\text{cr}}(y_1, y_2) + \dots \quad (3.22)$$

where  $\nabla_y$  denotes the gradient operator with respect to the space variables  $y_1$  and  $y_2$ . In the thermoelastic problem,

$$\underline{\underline{\sigma}}_l^{\text{te}}(x_1, x_2) = \underline{\underline{\sigma}}_l^{\text{te}}(ly_1, ly_2) = \mathbf{C} : \left( \nabla_y \underline{V}_1^{\text{te}}(y_1, y_2) - \underline{\underline{\epsilon}}^{\text{in}} \right) + \dots \quad (3.23)$$

In addition, notice that the use of the MA approach allows only one calculation to be made regardless the actual size of the reinforcing element. In this regard, the strong refinements in the mesh size, necessary to solve directly the problem on the actual domain, are avoided, which results in a more accurate solution in the neighbourhood of the perturbation, i.e. the reinforcing element at the crack tip.

Notice that the characteristic length used to apply this analytical methodology is the length of the reinforcing element,  $l$ . However, the same procedure could be followed using as a characteristic length of the problem the thickness of the reinforcing element,  $t$ , as it will be shown in Section 3.3.

The estimation of the elastic solution in the vicinity of the reinforcing element is used in the Coupled Criterion.

### 3.1.3 The Coupled Criterion

The well-known theory of Griffith [44] can only be applied in a homogeneous (at least locally around the crack tip) material or along an interface between homogeneous materials. Moreover, it is easily seen, in [88] for instance, that the CC, explained in Section 1.2.1, coincides with Griffith's criterion in these cases and that the stress condition plays no role. In the inner problem, a heterogenous micro-structure is considered. Therefore, the theory of Griffith may not be used in all the possible paths for crack propagation that will be studied in the following sections.

First, when considering the thermomechanical problem, the stress condition (see (1.12)) in the actual domain represented in Fig. 3.1 is written as

$$\bar{\sigma} = \frac{\sigma^{\text{cr}}(s) + \sigma^{\text{te}}(s)}{\sigma_c(s)} \geq 1 \quad \text{for} \quad 0 \leq s \leq \delta l, \quad (3.24)$$

In the energy condition according to (1.16), assuming displacement controlled loading mode, the change in potential energy  $\Delta\Pi_p = \Delta\Psi_{\text{el}}$ , being  $\Psi_{\text{el}}$  the total strain energy in the system defined as

$$\Psi_{\text{el}} = \frac{1}{2} \int_{\Omega} \mathbf{C} : (\nabla \underline{U} - \underline{\underline{\varepsilon}}^{\text{in}}) : (\nabla \underline{U} - \underline{\underline{\varepsilon}}^{\text{in}}) dx_1 dx_2, \quad (3.25)$$

Using the superposition principle of the thermomechanical problem as in (3.2) it comes out,

$$\Psi_{\text{el}} = \frac{1}{2} \int_{\Omega} \mathbf{C} : (\nabla \underline{U}^{\text{cr}} + \nabla \underline{U}^{\text{te}} - \underline{\underline{\varepsilon}}^{\text{in}}) : (\nabla \underline{U}^{\text{cr}} + \nabla \underline{U}^{\text{te}} - \underline{\underline{\varepsilon}}^{\text{in}}) dx_1 dx_2. \quad (3.26)$$

Considering (3.5), the strain energy in the system is rewritten as

$$\begin{aligned} \Psi_{\text{el}} = & \frac{1}{2} \int_{\Omega} \mathbf{C} : \nabla \underline{U}^{\text{cr}} : \nabla \underline{U}^{\text{cr}} dx_1 dx_2 - \frac{1}{2} \int_{\Omega} \mathbf{C} : \nabla \underline{U}^{\text{te}} : \nabla \underline{U}^{\text{te}} dx_1 dx_2 \\ & + \frac{1}{2} \int_{\Omega} \mathbf{C} : \underline{\underline{\varepsilon}}^{\text{in}} : \underline{\underline{\varepsilon}}^{\text{in}} dx_1 dx_2 = \Psi_{\text{el}}^{\text{cr}} - \Psi_{\text{el}}^{\text{te}} + \Psi_{\text{el}}^{\text{in}}. \end{aligned} \quad (3.27)$$

Since we are interested in the increment in strain energy,  $\Delta\Psi_{\text{el}}(\delta l) = \Psi_{\text{el}}^{\delta l} - \Psi_{\text{el}}^0$ , the last term  $\Psi_{\text{el}}^{\text{in}}$  in the previous expression does not play any role in the energy condition, then

$$\bar{G}_{\text{inc}} = -\frac{\Delta\Pi_p}{\delta l} \cdot \frac{1}{G_c(\delta l)} = \left( -\frac{\Delta\Psi_{\text{el}}^{\text{cr}}}{\delta l} + \frac{\Delta\Psi_{\text{el}}^{\text{te}}}{\delta l} \right) \cdot \frac{1}{G_c(\delta l)} \geq 1. \quad (3.28)$$

Note that there is no coupling term in (3.27), this a consequence of the boundary conditions and the variational formulation of the problems (3.3) and (3.5).

The elastic solution considered in these equations is in this case approximated using the MAE. Hence, in the pure mechanical problem the actual strain energy  $\Psi_{\text{el}}^{\text{cr}}$  is defined as

$$\Psi_{\text{el}}^{\text{cr}} = \frac{1}{2} \int_{\Omega_l} \mathbf{C} : \nabla_x \underline{U}_l^{\text{cr}} : \nabla_x \underline{U}_l^{\text{cr}} dx_1 dx_2, \quad (3.29)$$

and therefore the increment  $\Delta\Psi_{\text{el}}^{\text{cr}}$  can be calculated. In this problem,  $\Delta\Psi_{\text{el}}^{\text{cr}}$  is approximated by the inner expansion,  $\Delta\Psi_{\text{el}}^{\text{cr}} = l \Delta\hat{\Psi}_{\text{el}}^{\text{cr}}$ , where

$$\hat{\Psi}_{\text{el}}^{\text{cr}} = \frac{1}{2} \int_{\Omega_{\text{in}}} \mathbf{C} : \nabla_y \underline{V}_1^{\text{cr}} : \nabla_y \underline{V}_1^{\text{cr}} dy_1 dy_2. \quad (3.30)$$

Notice that  $\Delta\hat{\Psi}_{\text{el}}^{\text{cr}}$  depends on  $\delta l_{\text{in}} = \frac{\delta l}{l}$ , the dimensionless newly created crack length in the inner domain  $\Omega_{\text{in}}$ , i.e., the distance from that node to the origin expressed in the dimensionless  $y_i$  variables.

On the other hand, in the thermoelastic problem

$$\Delta \Psi_{\text{el}}^{\text{te}} = l \Delta \hat{\Psi}_{\text{el}}^{\text{te}}. \quad (3.31)$$

The CC is therefore expressed as

$$\bar{\sigma} = \frac{\frac{K_I}{\sqrt{l}} \hat{\sigma}^{\text{cr}}(\hat{s}) + \hat{\sigma}^{\text{te}}(\hat{s})}{\sigma_c(\hat{s})} \geq 1, \quad \text{for } 0 \leq \hat{s} \leq \delta l_{\text{in}} \quad (3.32)$$

$$\bar{G}_{\text{inc}} = \frac{-(K_I)^2 \frac{\Delta \hat{\Psi}_{\text{el}}^{\text{cr}}}{\delta l_{\text{in}}} + l \frac{\Delta \hat{\Psi}_{\text{el}}^{\text{te}}}{\delta l_{\text{in}}}}{G_c(\delta l_{\text{in}})} \geq 1. \quad (3.33)$$

The aim of applying the CC is to calculate the apparent fracture toughness of the composite  $K_{\text{IC}}^{\text{app}}$ , defined as the minimum value of  $K_I$  for which both the stress (3.34) and the energy (3.35) condition are fulfilled. In particular,  $K_{\text{IC}}^{\text{app}}$  is compared to  $K_{\text{IC}}^{\text{m}}$ , the fracture toughness of the matrix, to study how matrix fracture properties are enhanced when a second constituent is added. Moreover, the solution of the thermoelastic problem  $\hat{\sigma}^{\text{te}}(\hat{s})$  and  $\hat{W}^{\text{te}}$  can be expressed for a  $\Delta\theta = 1$  and then with a simple change the solution can be obtained for any value of  $\Delta\theta = 1$ , which gives rise to the following formulation

$$\bar{\sigma} = \frac{\frac{K_I}{\sqrt{l}} \hat{\sigma}^{\text{cr}}(\hat{s}) + \Delta\theta \hat{\sigma}^{\text{te}}(\hat{s})}{\sigma_c(\hat{s})} \geq 1, \quad \text{for } 0 \leq \hat{s} \leq \delta l_{\text{in}} \quad (3.34)$$

$$\bar{G}_{\text{inc}} = \frac{-(K_I)^2 \frac{\Delta \hat{\Psi}_{\text{el}}^{\text{cr}}}{\delta l_{\text{in}}} + l \Delta\theta^2 \frac{\Delta \hat{\Psi}_{\text{el}}^{\text{te}}}{\delta l_{\text{in}}}}{G_c(\delta l_{\text{in}})} \geq 1. \quad (3.35)$$

At this stage, we must point out an important difficulty encountered by the numerical approach of the CC when considering the thermoelastic problem. There is a singularity at the tip of the mother crack impinging the matrix/reinforcing element interface and, despite it is located at the tip of a crack, it differs from the singularity for a crack in the classical theory of Linear Elastic Fracture Mechanics  $\lambda = 0.5$ , because of the heterogeneous conditions [89]. The reinforcing element being stiffer than the matrix, it is a so-called weak singularity with an exponent larger than that of a crack. If the mechanical loading (bending) leads to a positive generalized stress intensity factor (GSIF) of the singularity, on the contrary, the residual stresses tend to close the mother crack and result in a negative GSIF. There is a competition between them, if the GSIF related to a mechanical load is small, then residual stresses take over and the mother crack remains closed.

A way to get rid of this difficulty is to compute the GSIF  $k^{\text{cr}}$ , that can be calculated using the path independent integral described in [86]

$$k^{\text{cr}} = \frac{\Phi(\underline{U}_l^{\text{cr}}, r^{-\lambda} \underline{u}^-(\theta))}{\Phi(r^\lambda \underline{u}(\theta), r^{-\lambda} \underline{u}^-(\theta))}, \quad (3.36)$$

where  $r^\lambda \underline{u}(\theta)$  is the eigenfunction of the heterogeneous problem, being  $r^{-\lambda} \underline{u}^-(\theta)$  the dual eigenfunction. The integral denoted as  $\Psi$  is defined in the Annex 5.2. The inner solution

obtained using MAE can be used in this calculation. Hence, the GSIF  $\kappa^{\text{cr}}$  is extracted from  $\underline{V}_1^{\text{cr}}$ ,

$$\kappa^{\text{cr}} = \frac{\Phi(\underline{V}_1^{\text{cr}}, \rho^{-\lambda} \underline{u}^-(\theta))}{\Phi(\rho^\lambda \underline{u}(\theta), \rho^{-\lambda} \underline{u}^-(\theta))}, \quad (3.37)$$

where  $\underline{V}_1^{\text{te}}$  is the solution considering  $\Delta\theta = 1$ . For the GSIF referred to the thermoelastic problem ( $k^{\text{te}}$ ) the right-hand side member in (3.5) does not vanish in the vicinity of the singular point, and consequently the integral  $\Phi$  is no longer a path-independent integral. A superposition principle might be used to separate the non-homogeneous part of  $\underline{V}_1^{\text{te}}$ , and therefore to calculate  $\kappa^{\text{kte}}$ . The corresponding changes, see (3.13) and (3.20), are applied to obtain the GSIF's of the actual problem,

$$k^{\text{te}} = l^{1-\lambda} \Delta\theta \kappa^{\text{te}} \quad (3.38)$$

$$k^{\text{cr}} = K_{\text{I}} l^{1/2-\lambda} \kappa^{\text{cr}}. \quad (3.39)$$

Then, equality  $k^{\text{cr}} = -k^{\text{te}}$  provides the smaller value  $K_{\text{I}}^{\text{min}}$  of  $K_{\text{I}}$  such that the compressive stress cancels and the mother crack opens.

$$K_{\text{I}}^{\text{min}} = \sqrt{l} \Delta\theta \frac{\kappa^{\text{te}}}{\kappa^{\text{cr}}}. \quad (3.40)$$

It is a lower bound of admissible  $K_{\text{I}}$ .

## 3.2 Application example: borosilicate glass reinforced by alumina platelets

The computational tool presented in the previous section is applied to analyse the borosilicate glass reinforced by alumina ( $\text{Al}_2\text{O}_3$ ) platelets. First, the role of only one platelet is studied in the pure mechanical problem. Then, the effect of residual stresses as well as the effect of the volume fraction are included in the problem. Finally, the numerical tool is verified through a comparison to experiments.

### 3.2.1 Description of the material

In experiments made by [32] and [30] on the borosilicate glass/ $\text{Al}_2\text{O}_3$  platelet composite, the alumina platelets have hexagonal shape with the major axe measuring  $l = 5 - 25 \mu\text{m}$  and the thickness is  $t = 0.2 l$ , which means that the dimensions of the platelets are much much smaller than the tested specimens, whose standard cross-section of  $12\text{mm}^2$  has a rectangular shape. Moreover, the interface between the platelet and the matrix is assumed to be strong as reported in [33].

Table 3.1 lists the mechanical properties of the constituents borosilicate glass and  $\text{Al}_2\text{O}_3$ . It is important to emphasize the high variability of the fracture toughness  $K_{\text{c}}$  and the strength  $\sigma_{\text{c}}$  of a ceramic material, since they are very dependant on the micro-structure [90]. In this case, these parameters were experimentally obtained for glass in [32] and [30]. However, no

experimental data were provided for alumina platelets, being these parameters even more difficult to obtain, since they sometimes differ from the values measured in a bulk material. In [91], a range for  $\sigma_c$  was estimated by the values given in the National Institute of Standards and Technology <sup>1</sup>. Furthermore, in [92] a parametric study is proposed, obtaining a possible value for the fracture toughness based on a comparison with experimental observations, among an initial range taken from the literature [88], [93].

Constituents	$E$ [GPa]	$\nu$	$\alpha_T$ [ $10^{-6}/K$ ]	$\sigma_c$ [MPa]	$K_c$ [MPa m <sup>1/2</sup> ]
Borosilicate glass	60	0.23	3.3	56	0.735
Alumina (Al <sub>2</sub> O <sub>3</sub> )	402	0.22	8.9	300 – 400	2 – 5

Table 3.1: Mechanical properties of the constituents. The extreme values of the tensile strength and toughness of alumina will be called respectively minor and major in the following.

Notice that in Table 3.1 the thermal coefficients are given. They are used to obtain residual stresses generated after manufacture. During the process, the temperature is reduced from the glass transition temperature,  $\theta_0 \approx 550^\circ C$  [37] to the room temperature.

All around the platelet/glass assembly, a homogeneous distribution of platelets is assumed [32] and therefore the composite is represented through an equivalent homogenized material, whose mechanical properties are function of  $V_p$ , the volume fraction of platelets, in Table 3.2. Its Young's modulus  $E^{app}$  was measured in [30] and [32], whereas the Poisson's ratio  $\nu^{app}$  is assumed to be that of glass, since there is not a big difference between Poisson's ratios of alumina  $\nu^a$  and glass  $\nu^g$ , see Table 3.1.

The thermal expansion coefficient  $\alpha_T^{app}$  for the composite was calculated using Voigt's rule of mixtures [94]. The tensile strength and  $\sigma_c^{app}$  was also measured in [30] and [32]. Finally, two experimental sets of data for the apparent fracture toughness  $K_c^{app}$  in the composite were included, denoted as [1] referring to [32] and [2] referring to [30], see Table 3.2.

As mentioned in Section 3.1.1, we focus on the role of the size effect due to the smallness of the inclusion. To that aim, although in the experiments  $l = 5 - 25 \mu m$ , the range selected here is  $l = 2 - 300 \mu m$ .

<sup>1</sup><https://srdata.nist.gov/CeramicDataPortal/Pds/Scdaos>

	$E^{\text{app}}$ [GPa]	$\nu^{\text{app}}$	$\alpha_T^{\text{app}}$ [ $10^{-6}/\text{K}$ ]	$\sigma_c^{\text{app}}$ [MPa]	$K_c^{\text{app}}$ [MPa m <sup>1/2</sup> ]
$V_p = 5\%$	63	0.22	3.58	67	$0.98^1$ $0.9^2$
$V_p = 10\%$	70	0.22	3.86	84	$1.03^1$ $0.95^2$
$V_p = 15\%$	79	0.22	4.14	104	$1.28^1$ $1.1^2$
$V_p = 30\%$	102	0.22	4.98	150	$1.92^1$ $1.5^2$

Table 3.2: Mechanical properties of the equivalent homogenized material for several values of the platelets volume fraction  $V_p$ .

It is important to highlight that the interface glass alumina is considered as strong [30], therefore its fracture properties are those of glass.

**Remark:** In this PhD thesis the CC point is located at a certain point  $s$  in the expected crack path where  $s = \delta l$ , the newly created crack length.

### 3.2.2 The role of a single platelet

A simplified case is studied in this section, when considering only the role of a single platelet embedded in a glass matrix, as shown in Fig. 3.3, and no residual stresses in the problem. Results are compared to the ones obtained considering the effect of the volume fraction, to understand the role of  $V_p$  in the fracture toughness of the composite.

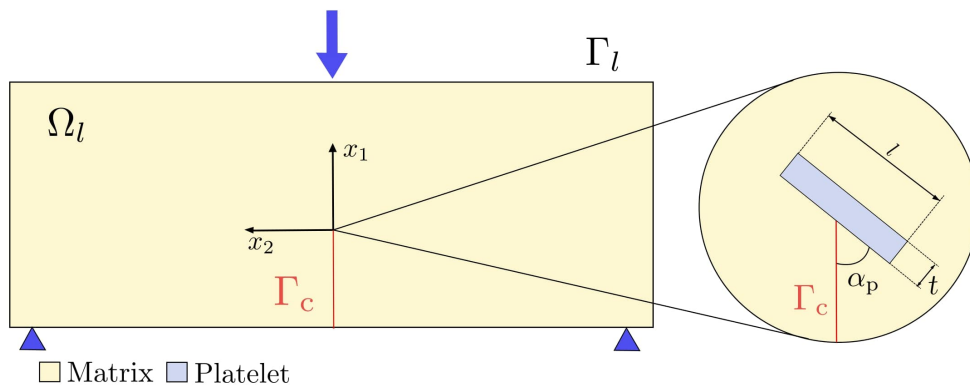


Figure 3.3: Scheme of a symmetric 3-point bending test on a cracked specimen. A platelet (blue) surrounded by its environment (glass in yellow) is located at the tip of the crack.

In the following sub-sections the equivalent 2D model presented in Section 3.1.1 considering the role of a single platelet is applied to numerically determine the apparent fracture toughness  $K_{IC}^{app}$  of the composite, as a function of  $l$  and  $\alpha_p$ . Three different orientations are presented in this section,  $\alpha_p = 0^\circ, 45^\circ, 90^\circ$ . For the sake of simplicity, the subscript  $l$  related to the actual solution in Section 3.1.2, is omitted in the notation. Furthermore,  $K_{IC}^g$  denotes the fracture toughness of glass.

### 3.2.2.1 Results for $\alpha_p = 90^\circ$

A possible relative position of the platelet is given when it is perpendicular to the pre-existing crack,  $\alpha_p = 90^\circ$ . Since a priori the crack path is unknown, different options are investigated, studied in the following subsections: a single deflection, a decohesion, a penetration and a step over.

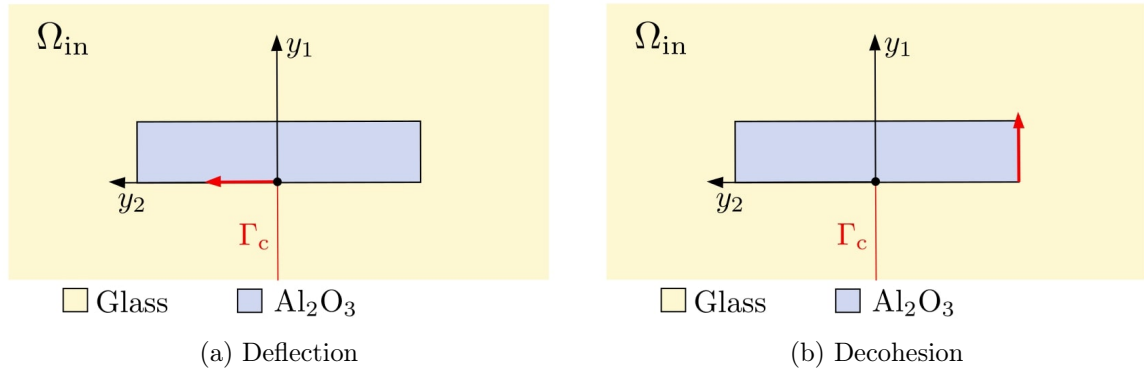


Figure 3.4: Scheme of the inner domain and the supposed crack path (red arrow) for  $\alpha_p = 90^\circ$ , for different toughening mechanisms.

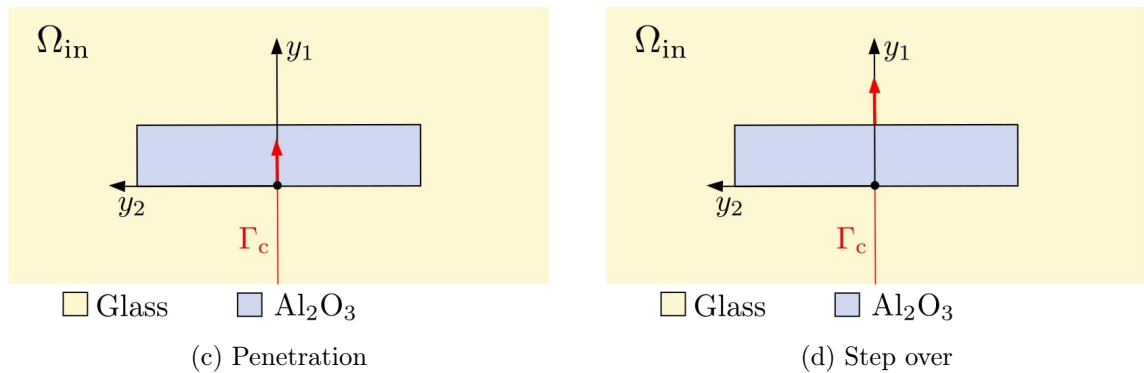


Figure 3.4: Scheme of the inner domain and the supposed crack path (red arrow) for  $\alpha_p = 90^\circ$ , for different toughening mechanisms.

### Single deflection

A first option is given when the crack encounters the platelet and deflects along the interface, as shown in Fig. 3.4a. It is called deflection. The evolution of  $K_{IC}^{app}$  is represented in Fig. 3.5. First, it can be concluded that a deflection of the crack path when considering the role of a single platelet is always a toughening mechanism, since the minimum enhancement of  $K_{IC}^{app}$  is  $1.7K_{IC}^g$  and the maximum is  $\approx 2.14K_{IC}^g$ , for the maximum value of the platelet size considered in this study,  $l = 300 \mu\text{m}$ .

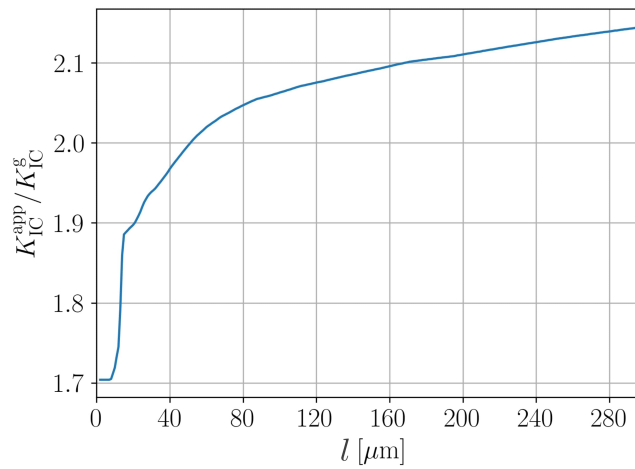


Figure 3.5: Evolution of  $K_{IC}^{app}/K_{IC}^g$  with respect to  $l$ , for  $\alpha_p = 90^\circ$  in the deflection case.

Looking at Fig. 3.5 two changes in the evolution of  $K_{IC}^{app}$  can be distinguished. First, for very short platelets it is observed that  $K_{IC}^{app}$  does not depend on  $l$ , which means that it is the energy condition that governs the failure. An example is shown in Fig. 3.6 for  $l = 4 \mu\text{m}$ , where the CC point (highlighted in the image) is determined by the relative maximum in the energy condition curve  $\bar{G}_{inc}$ . Notice that a peak in the stress condition curve  $\bar{\sigma}$  can be observed at the end of the interface glass alumina, due to the singularity that is generated because of the rectangular shape of the platelet, see Fig. 3.6a. The crack opening after nucleation is represented in Fig. 3.6b, where the adimensional coordinate  $\hat{s} = s/l$  is used to represent the direction of the crack path.

At  $l \approx 8 \mu\text{m}$  the apparent fracture toughness abruptly starts increasing with the platelet size, and therefore the energy condition is no longer governing the failure. An example is given for  $l = 9 \mu\text{m}$  in Fig. 3.7, where it is observed that the newly created crack length is still longer than the length of the interface glass alumina. In this case, the CC point is determined by the crossing point between the stress and the energy curve.

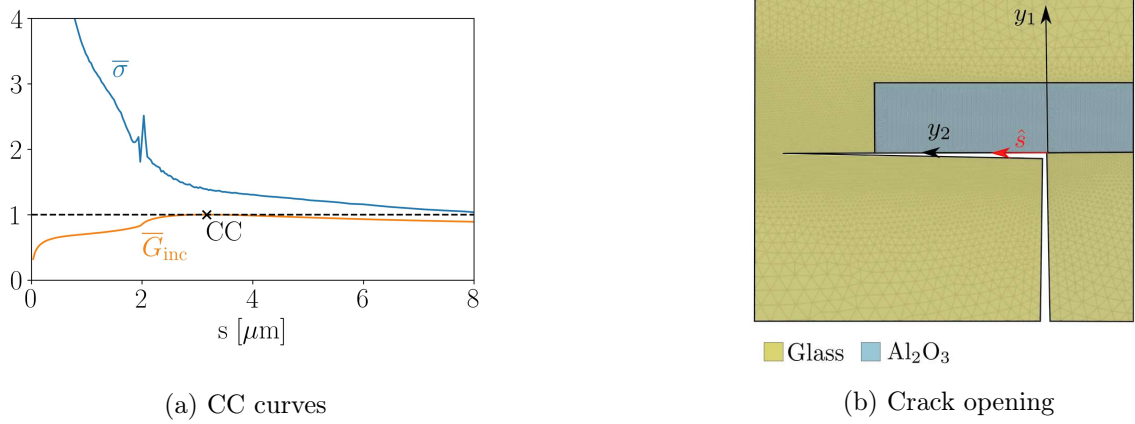


Figure 3.6: Example of the application of the CC for  $\alpha_p = 90^\circ$  and  $l = 4 \mu\text{m}$ , considering the deflection case.

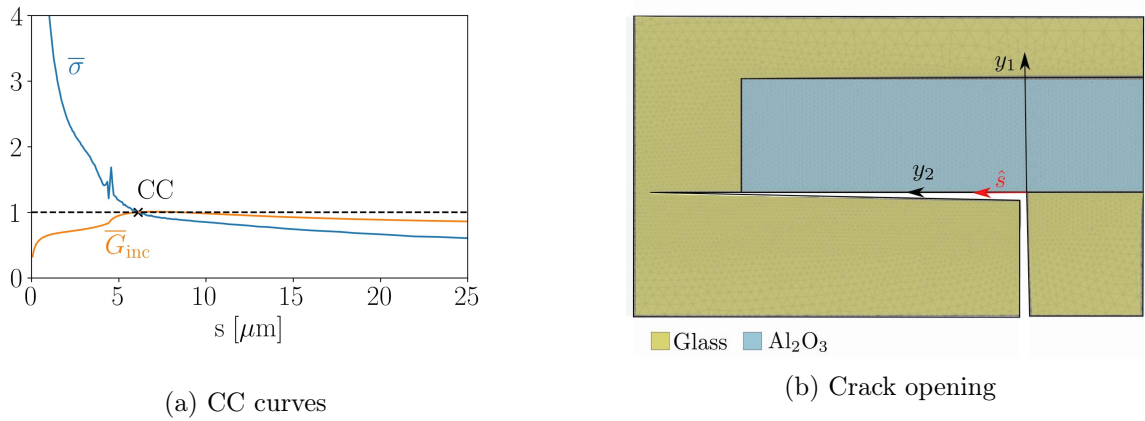


Figure 3.7: Example of the application of the CC for  $\alpha_p = 90^\circ$  and  $l = 9 \mu\text{m}$ , considering the deflection case.

Finally, the evolution of  $K_{IC}^{app}$  changes at  $l \approx 15 \mu\text{m}$ . As shown in the example given in Fig. 3.8 for  $l = 50 \mu\text{m}$ , when long platelets are considered the crack is arrested before reaching the end of the interface glass alumina, at the moment of failure  $K_I = K_{IC}^{app}$ . In particular, for  $l = 50 \mu\text{m}$  the newly created crack length, represented in Fig. 3.8b, is  $\delta l = 15.8 \mu\text{m}$ .

It is important to highlight that the case of a double symmetric deflection, see Fig. 3.9, can also be studied even in a simpler way considering a half of the domain in the problem, and applying the corresponding symmetry conditions, i.e., the horizontal displacement is nulled at  $y_2 = 0, y_1 > 0$ .

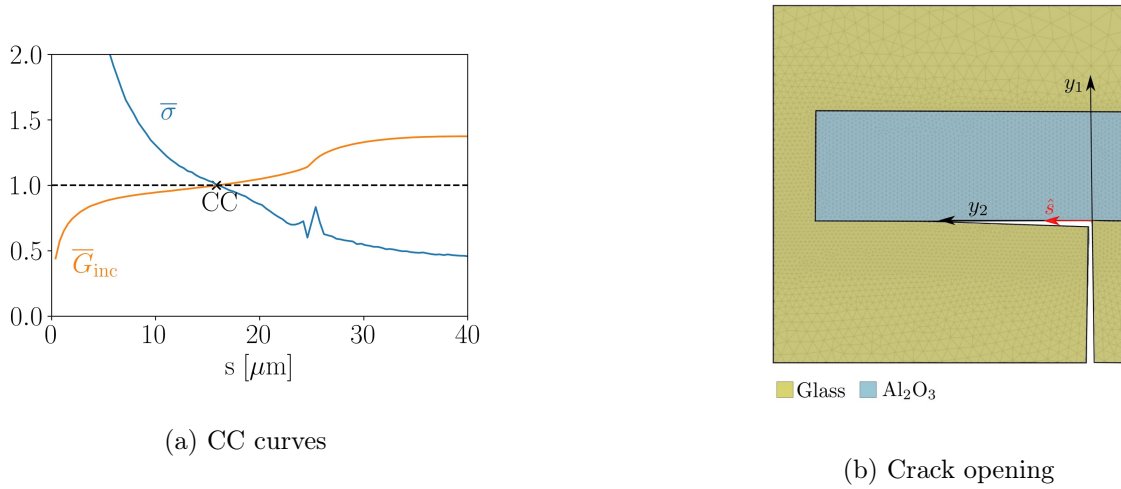


Figure 3.8: Example of the application of the CC for  $\alpha_p = 90^\circ$  and  $l = 50 \mu\text{m}$ , considering the deflection case.

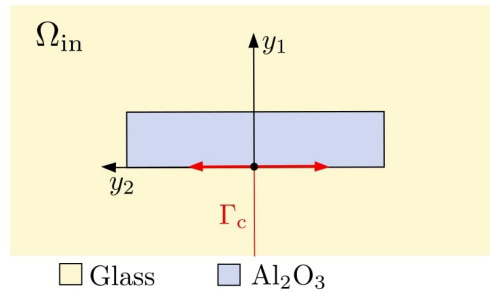


Figure 3.9: Scheme of the inner domain and the supposed crack path (red arrow) for  $\alpha_p = 90^\circ$ , for the symmetric deflection.

Fig. 3.10 shows the comparison between the symmetric and the non-symmetric deflection. No significant differences have been observed between the two cases, since the maximum difference is 6.9%. It is important to highlight that a similar conclusion was obtained in [95] for a single fiber specimen.

### Lateral decohesion

Another possible mechanism is a lateral decohesion of the interface, see Fig. 3.4b. In Fig. 3.11 the evolution of  $K_{IC}^{app}$  in case of decohesion is shown. An enhancement of the apparent fracture toughness with respect to the one of glass is observed over the whole range of the platelet length studied. In fact, the maximum increase in  $K_{IC}^{app}$  occurs when  $l = 300 \mu\text{m}$  and is approximately  $2.26K_{IC}^g$ . Therefore, the lateral decohesion could be a toughening mechanism of the problem, since the apparent fracture toughness is enhanced. This mechanism was already studied in [92].

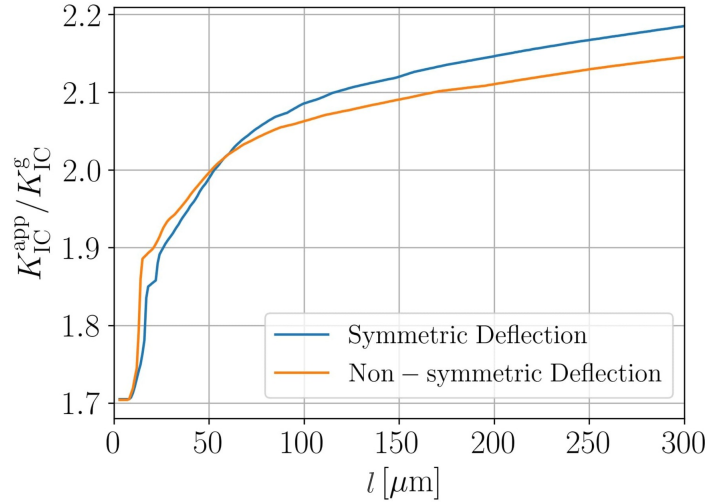


Figure 3.10: Comparison of  $K_{IC}^{\text{app}} / K_{IC}^{\text{g}}$  between the symmetric and the non-symmetric deflection, for  $\alpha_p = 90^\circ$ .

For short platelets, as observed in previous cases,  $K_{IC}^{\text{app}}$  does not depend on the size of the platelet, which indicates that the energy condition governs the propagation of the pre-existing crack. An example is given in Fig. 3.12 for  $l = 4 \mu\text{m}$ . It can be noted that the newly created crack length is in this case much longer than the lateral interface glass alumina, and therefore the crack is arrested inside the glass region at the moment of failure.

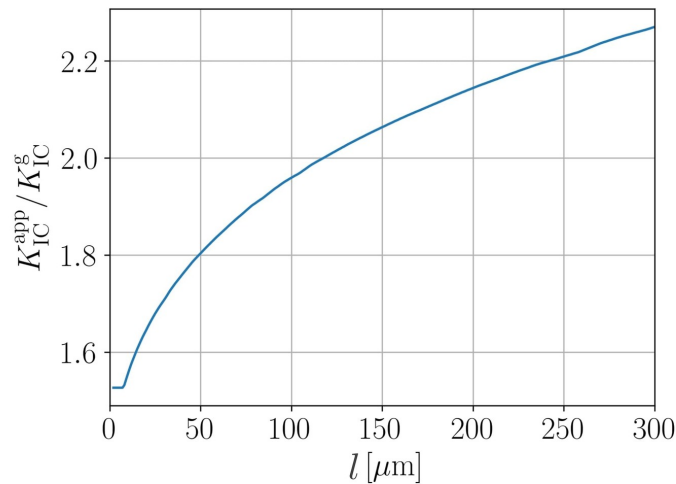


Figure 3.11: Evolution of  $K_{IC}^{\text{app}} / K_{IC}^{\text{g}}$  with respect to  $l$ , for  $\alpha_p = 90^\circ$  in the lateral decohesion case.

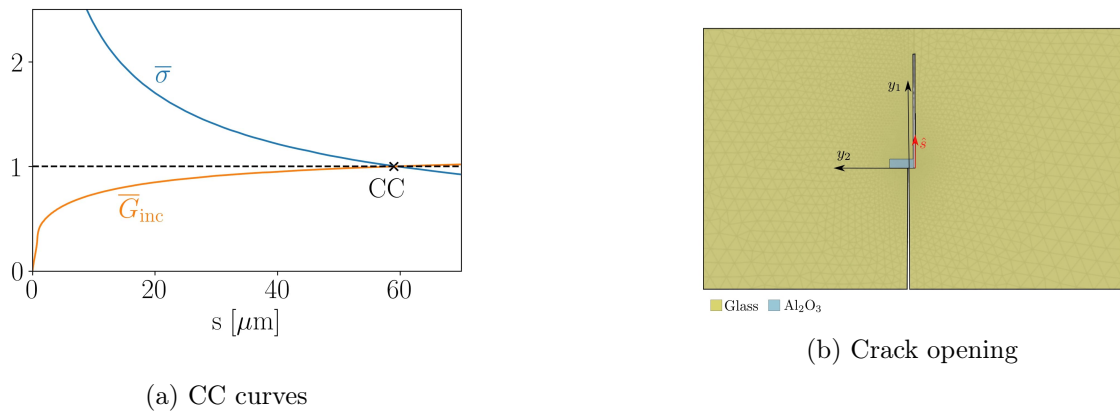


Figure 3.12: Example of the application of the CC for  $\alpha_p = 90^\circ$  and  $l = 4 \mu\text{m}$ , considering the decohesion case.

Another example is represented in Fig. 3.13 for  $l = 200 \mu\text{m}$ . In this case the crack jump is smaller, although the initiation length still ends in the glass region. Notice that in this example a convex stress distribution along the lateral interface glass alumina can be observed.

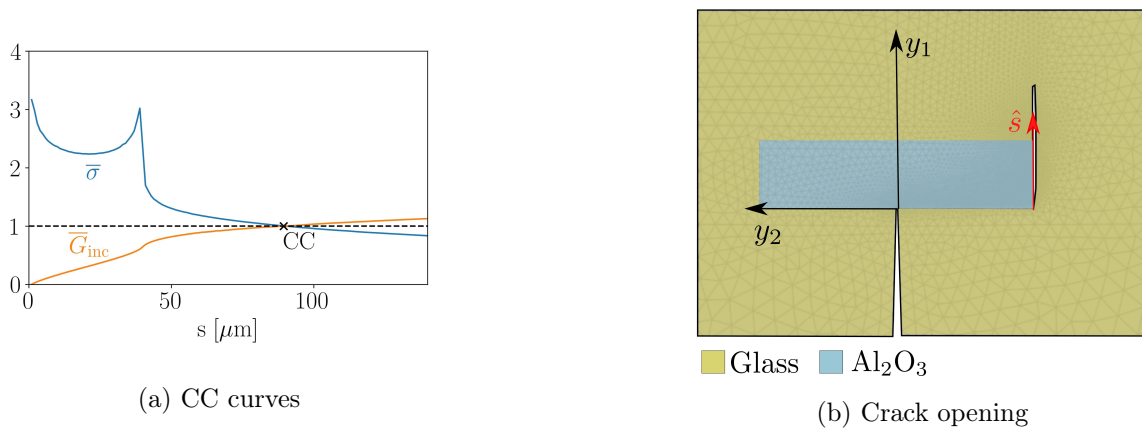


Figure 3.13: Example of the application of the CC for  $\alpha_p = 90^\circ$  and  $l = 200 \mu\text{m}$ , considering the decohesion case.

### Penetration

A separate case in which the crack penetrates in the platelet is presented in Fig. 3.4c, where the fracture properties of  $\text{Al}_2\text{O}_3$ , defined through a range of possible values, determine the evolution of the failure. In Fig. 3.14 the function  $K_{IC}^{\text{app}}(l)$  is studied for the range of  $\sigma_c^a$  given in Table 3.1. It is observed that the apparent fracture toughness is increased with the strength of alumina and the size of the platelet.

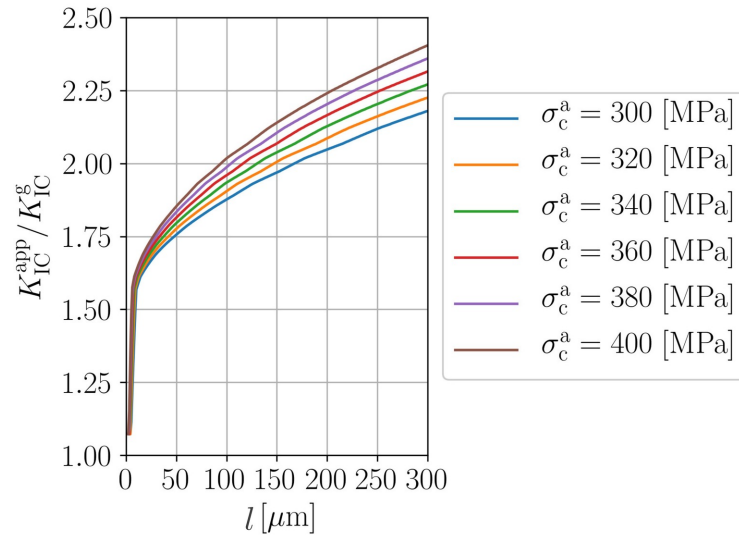


Figure 3.14: Evolution of  $K_{\text{IC}}^{\text{app}}/K_{\text{IC}}^{\text{g}}$  with  $l$  for several values of  $\sigma_c^{\text{a}}$  in the case of a crack penetration, considering an average value of the fracture toughness  $K_{\text{IC}}^{\text{a}} = 3.35 \text{ MPa} \cdot \text{m}^{1/2}$ .

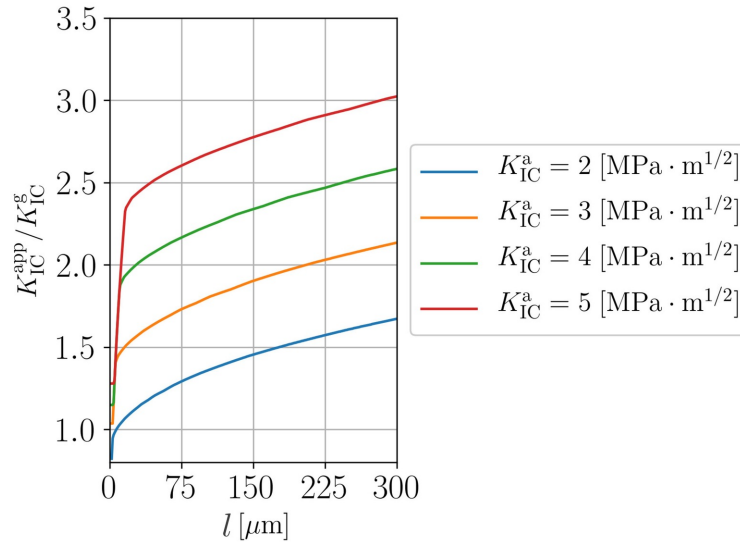


Figure 3.15: Evolution of  $K_{\text{IC}}^{\text{app}}/K_{\text{IC}}^{\text{g}}$  with  $l$  for several values of  $K_{\text{IC}}^{\text{a}}$  in the case of a crack penetration, considering an average value of the strength  $\sigma_c^{\text{a}} = 350 \text{ MPa}$ .

As an example, a description of the CC for  $K_{\text{IC}}^{\text{a}} = 2 \text{ MPa} \cdot \text{m}^{1/2}$  and  $\sigma_c^{\text{a}} = 300 \text{ MPa}$  is given in Fig. 3.16a and 3.17a respectively. In Fig. 3.16a the crack propagates inside the alumina

platelet, whereas in Fig. 3.17a a more standard fulfillment of the CC is represented, for a longer platelet.

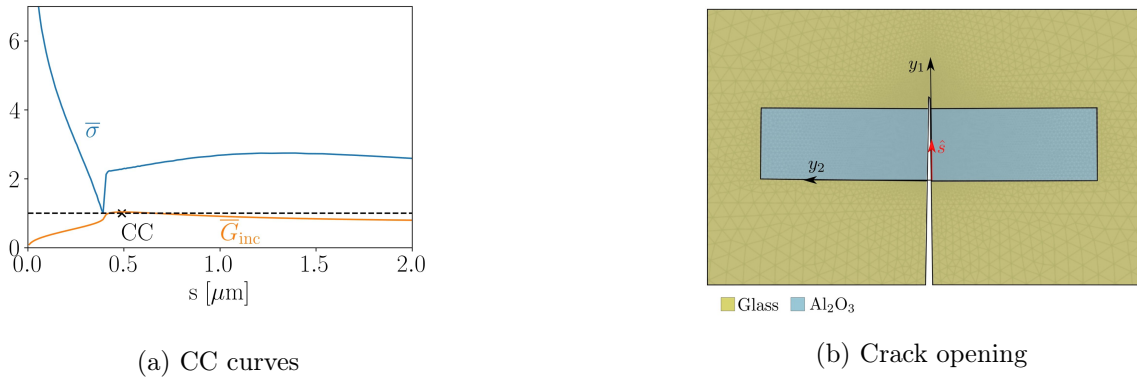


Figure 3.16: Example of the application of the CC for  $\alpha_p = 90^\circ$  and  $l = 2 \mu\text{m}$ , considering the penetration case. In this case  $K_{IC}^a = 2 \text{ MPa} \cdot \text{m}^{1/2}$  and  $\sigma_c^a = 300 \text{ MPa}$ .

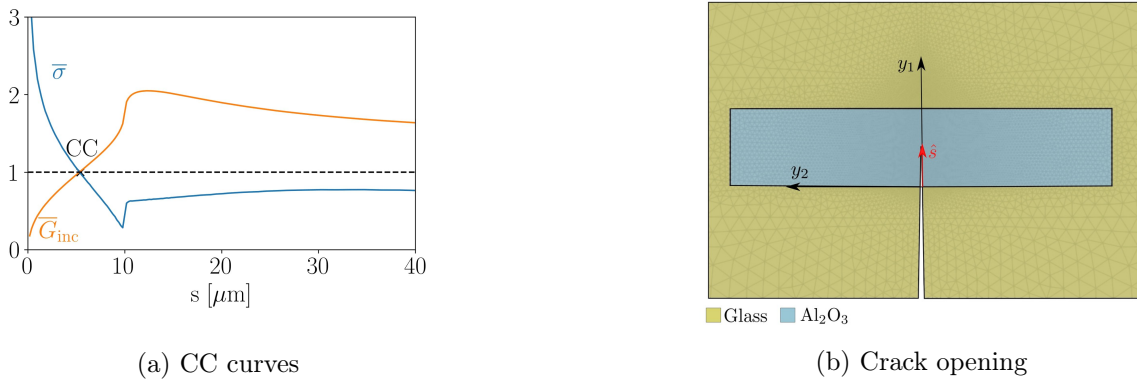


Figure 3.17: Example of the application of the CC for  $\alpha_p = 90^\circ$  and  $l = 50 \mu\text{m}$ , considering the penetration case. In this case  $K_{IC}^a = 2 \text{ MPa} \cdot \text{m}^{1/2}$  and  $\sigma_c^a = 300 \text{ MPa}$ .

### Step over

Finally, the situation in which the crack reinitiates on the opposite face of the platelet, leading to a nucleation in the glass region, has also been studied. It is called the step over case, represented in Fig. 3.4d. This kind of mechanism can be met in rock mechanics for instance [96]. Fig. 3.18 shows an example of the application of the CC for  $l = 25 \mu\text{m}$ . Results show that it is not a relevant mechanism in the present case, since there is a compression at the origin of the new crack that closes the crack so that it would not be a possible mechanism in this case. The same situation has been observed in the whole range studied in this section,  $l = 2 - 300 \mu\text{m}$ .

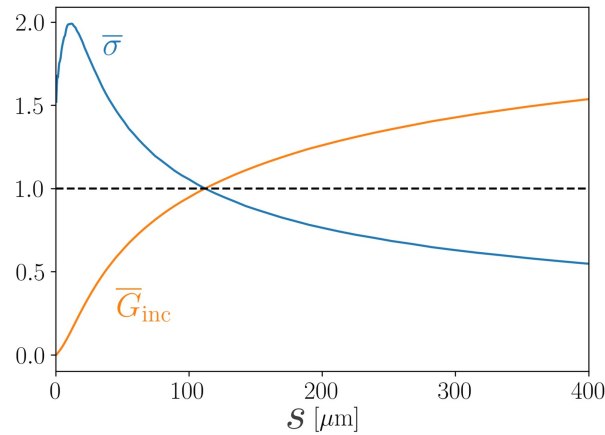


Figure 3.18: Example of the application of the CC for  $\alpha_p = 90^\circ$  and  $l = 25 \mu\text{m}$ , considering the step over case.

### Comparison between mechanisms

Finally, in Fig. 3.19 the expected crack paths presented above are compared to determine the predominant toughening mechanism, which is the one associated with the lowest  $K_{IC}^{\text{app}}$ , i.e. with the lowest critical load.

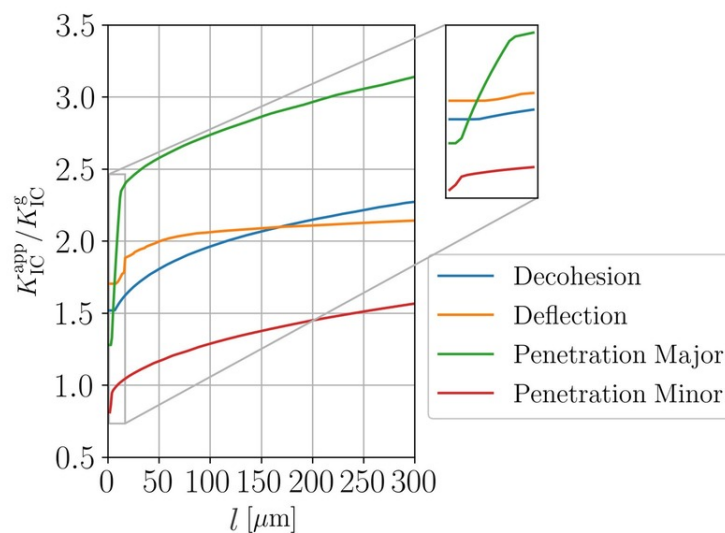


Figure 3.19: Evolution of  $K_{IC}^{\text{app}}/K_{IC}^g$  with respect to the length of the platelet  $l$ , for a single deflection, a decohesion and a penetration, when  $\alpha_p = 90^\circ$ .

For the sake of simplicity, only two cases are chosen for penetration, corresponding to the most extreme values of the  $\text{Al}_2\text{O}_3$  fracture properties, given in Table 3.1. The minor case, in which  $K_{\text{IC}}^{\text{a}} = 2 \text{ MPa} \cdot \text{m}^{1/2}$ ,  $\sigma_{\text{c}}^{\text{a}} = 300 \text{ MPa}$ , and the major case, where  $K_{\text{IC}}^{\text{a}} = 5 \text{ MPa} \cdot \text{m}^{1/2}$ ,  $\sigma_{\text{c}}^{\text{a}} = 400 \text{ MPa}$ . Notice that they constitute an upper and a lower bound in the curves given in Fig. 3.19 for the case of penetration. It is observed that the major case is never predominant. Moreover, for very short platelets the predominant mechanism is the penetration. Then, if  $l > 6 \mu\text{m}$  the predominant mechanism depends on the fracture properties of  $\text{Al}_2\text{O}_3$ , and it can be either a decohesion, either a penetration. Finally, for long platelets  $l > 160 \mu\text{m}$  a deflection through the interface glass/alumina or a penetration can occur, depending, again, on the fracture properties of alumina.

In 1989, He and Hutchinson [97] explained the necessary condition for a crack to either penetrate or deflect through the interface of a semi-infinite domain divided into two phases, in this case, glass and alumina, with a pre-existing crack in glass. For a right angle, H&H's condition for a crack to be deviated is

$$\frac{G_{\text{c}}^{\text{g}}}{G_{\text{c}}^{\text{a}}} < \frac{G_{\text{d}}}{G_{\text{p}}}, \quad (3.41)$$

whereas it penetrates in the reverse situation. The energy release rate related to deflection and penetration are denoted as  $G_{\text{d}}$  and  $G_{\text{p}}$  respectively. In [98] this ratio is expressed in terms of the asymptotic solution as follows

$$\frac{G_{\text{d}}}{G_{\text{p}}} = \frac{A_{\text{d}}}{A_{\text{p}}}, \quad (3.42)$$

where the term  $A_{\text{d}}/A_{\text{p}}$  is a function dependant on the ratio  $E^{\text{a}}/E^{\text{g}}$ , obtained from [98]. In the bi-material case studied this ratio  $E^{\text{a}}/E^{\text{g}} = 1.902$ . Hence,  $G_{\text{d}}/G_{\text{p}} = 0.68$ .

Two different values of  $G_{\text{c}}^{\text{a}}$  are considered, the upper and lower bound of the alumina fracture toughness, see Table 3.1. Hence, according to H&H, for  $K_{\text{IC}}^{\text{a}} = 2 \text{ MPa} \cdot \text{m}^{1/2}$  the ratio  $G_{\text{c}}^{\text{g}}/G_{\text{c}}^{\text{a}} = 0.906$  and the crack will penetrate, whereas for  $K_{\text{IC}}^{\text{a}} = 5 \text{ MPa} \cdot \text{m}^{1/2}$  the ratio  $G_{\text{c}}^{\text{g}}/G_{\text{c}}^{\text{a}} = 0.145$  and it will deflect.

In Fig. 3.19, the numerical toughening mechanisms studied for  $\alpha_{\text{p}} = 90^\circ$  were compared. If  $K_{\text{IC}}^{\text{a}} = 2 \text{ MPa} \cdot \text{m}^{1/2}$ , the penetration clearly predomines. However, if  $K_{\text{IC}}^{\text{a}} = 5 \text{ MPa} \cdot \text{m}^{1/2}$ , the predominant mechanism is deflection for  $l > 160 \mu\text{m}$  and decohesion if  $l < 160 \mu\text{m}$ . This observation agrees with the theoretical results, since they refer to a semi-infinite domain, which would correspond to the case of very large platelets.

### 3.2.2.2 Results for $\alpha_{\text{p}} = 0^\circ$

When  $\alpha_{\text{p}} = 0^\circ$ , the platelet is parallel to the pre-existing crack and we assume the crack to impinge the platelet at its corner. In that case, only one crack path seems likely to occur, it is the one located along the interface between glass and alumina, see Fig. 3.20.

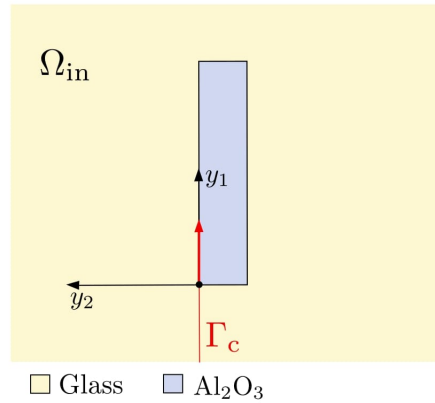


Figure 3.20: Schematic view of the inner domain for  $\alpha_p = 0^\circ$ . The supposed crack path starts from the corner of the platelet (red arrow).

The dependence of  $K_{IC}^{app}$  on the size of the platelet is represented in Fig 3.21, where it is shown that  $K_{IC}^g$  is enhanced only if  $l > 50 \mu\text{m}$ . It can be explained by the stress singularities located at the corners of the platelet. The effect of these singularities, i.e. very high stresses that tend to infinity at the corners, is felt all along the face of the platelet if it is small.

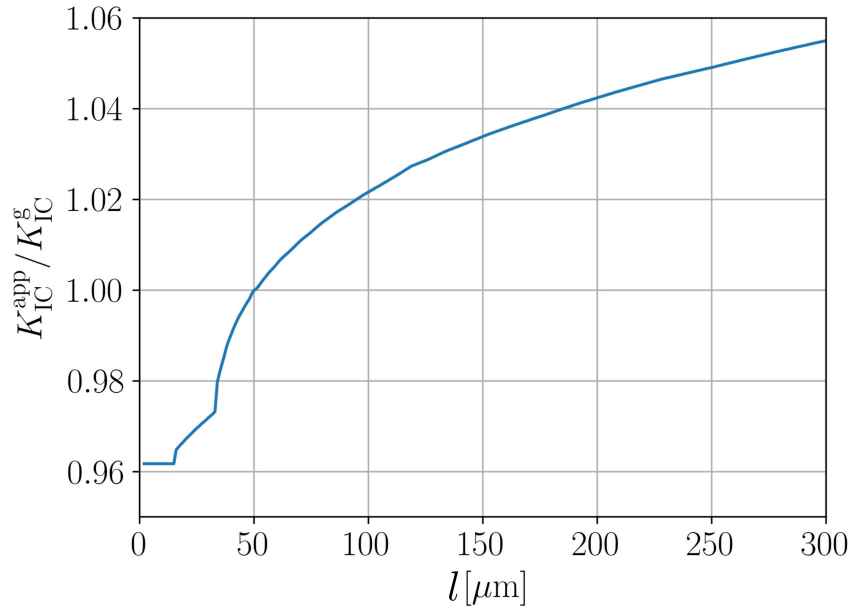


Figure 3.21: Evolution of  $K_{IC}^{app} / K_{IC}^g$  with respect to  $l$ , for  $\alpha_p = 0^\circ$ .

According to the CC, a finite crack increment develops in an unstable manner. For  $l = 16 - 33 \mu\text{m}$  this length is equal to the length of the glass/alumina interface ( $x_1 = l$ ), while for  $l > 33$

$\mu\text{m}$  this finite jump becomes smaller than the interface length, and the presence of the stiff material increasingly diminishes the ability of the crack to open. Moreover, it is observed that if  $l < 16 \mu\text{m}$ , the apparent fracture toughness remains constant, since the evolution of the failure is governed by the energy condition, and  $G_{\text{inc}}$  does not depend on  $l$ , see Section 3.1.3.

As an example, in Fig. 3.22 the CC is analysed for  $l = 10 \mu\text{m}$ . The stress and the energy conditions are represented with respect to  $s$ , the coordinate used to denote the arc length along the expected crack path. It should be noted that there is a small peak in the stress condition at the end of the interface ( $s = 10 \mu\text{m}$ ), due to the singularity at the corner point. Furthermore, notice that this is a non standard result of the CC, which is baptized as negative geometry [99], since the energy curve is not an increasing function in the glass region.

In this case the CC point is located out of the interface glass alumina at  $s \approx 11 \mu\text{m}$ , see Fig. 3.22b for a representative scheme of the crack opening in the inner domain, where the adimensional coordinate  $\hat{s} = s/l$  is used to represent the direction of the crack path. The newly created crack length is determined by the maximum point of the curve  $\tilde{G}_{\text{inc}}$ , that represents the energy condition, as shown in Fig. 3.22a. Noteworthy, in this case the platelet can not be considered a toughening mechanism, since the final value obtained for the apparent fracture toughness of the composite is slightly less than the one in glass,  $K_{\text{IC}}^{\text{app}}/K_{\text{IC}}^{\text{g}} \approx 0.96$ .

Other example of the application of the CC is shown in Fig. 3.23 for  $l = 20 \mu\text{m}$ , where the newly created crack is equal to the length of the interface glass alumina, i.e., the CC point is located at  $s = 20 \mu\text{m}$ , as represented in Fig. 3.23a. The deformed shape and a representative scheme of the crack opening in the inner domain is shown in Fig. 3.23b. It is important to highlight that in this case the platelet can not be considered a toughening mechanism, since  $K_{\text{IC}}^{\text{app}}/K_{\text{IC}}^{\text{g}} \approx 0.97$ . Finally, the CC curves for a long platelet  $l = 100 \mu\text{m}$  are represented in Fig. 3.24a. In this case, the newly created crack length is smaller than the interface glass alumina, as shown in Fig. 3.24b. A small toughening effect can be observed, since  $K_{\text{IC}}^{\text{app}}/K_{\text{IC}}^{\text{g}} \approx 1.02$ .

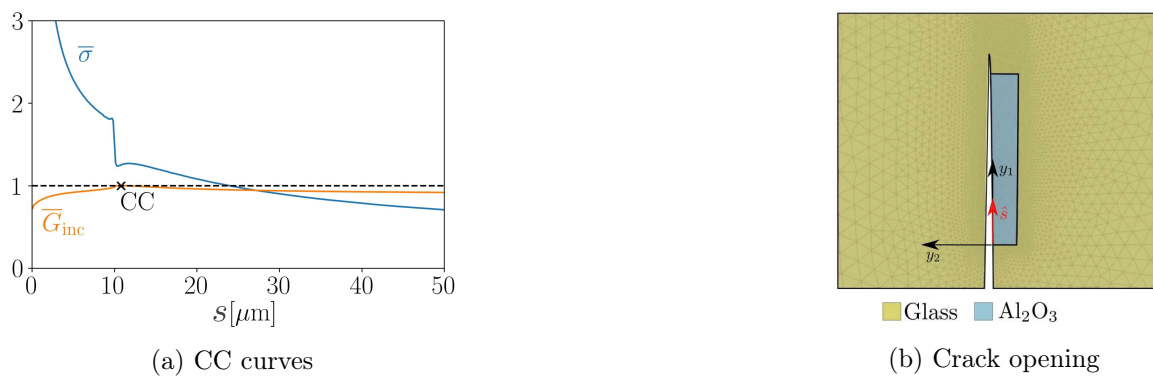
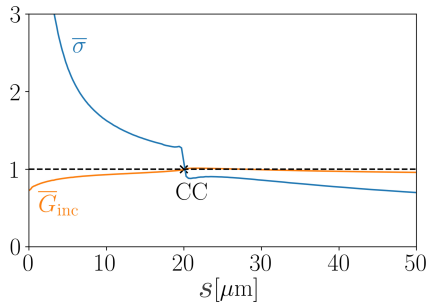
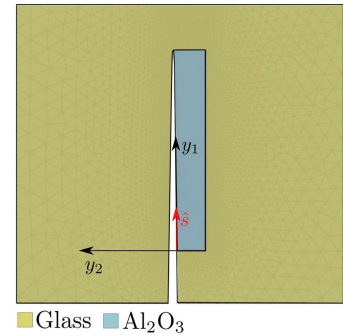


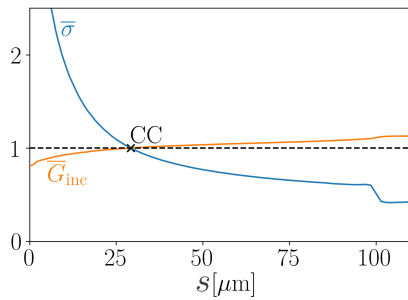
Figure 3.22: Example of the application of the CC for  $\alpha_p = 0^\circ$  and  $l = 10 \mu\text{m}$ .



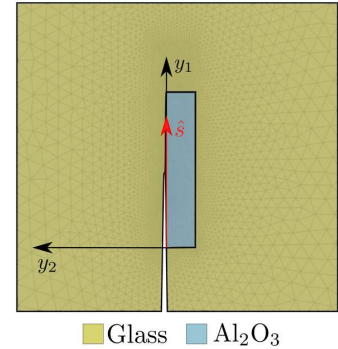
(a) CC curves



(b) Crack opening

Figure 3.23: Example of the application of the CC for  $\alpha_p = 0^\circ$  and  $l = 20 \mu\text{m}$ .

(a) CC curves



(b) Crack opening

Figure 3.24: Example of the application of the CC for  $\alpha_p = 0^\circ$  and  $l = 100 \mu\text{m}$ .

### 3.2.2.3 Results for $\alpha_p = 45^\circ$

In the case  $\alpha_p = 45^\circ$  two more parameters are used to define the expected crack path, as illustrated in Fig. 3.25. The angle  $\beta$ , the first deflection angle of the crack when it penetrates in the alumina platelet, and the angle  $\gamma$ , a secondary deflection when the prescribed crack penetrates from the alumina platelet to the glass matrix. To differentiate the possible toughening mechanisms that can be given in this situation, three possible values for each angle,  $\beta, \gamma = 0^\circ, 45^\circ$  and  $90^\circ$ , are studied.

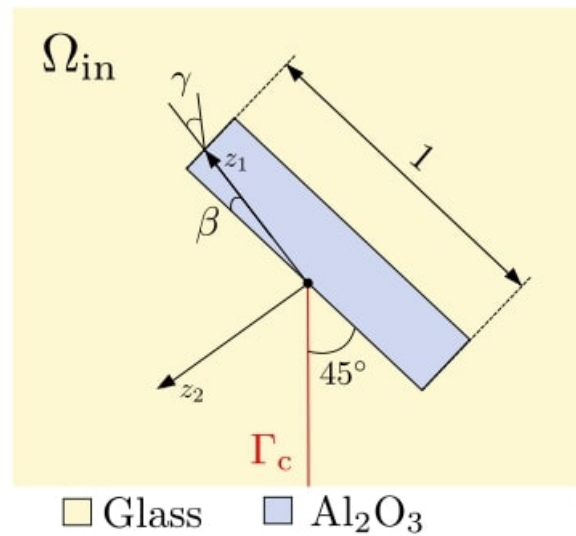


Figure 3.25: Scheme of the expected crack path in the inner problem for  $\alpha_p = 45^\circ$ . A new local coordinates system is defined  $(z_1, z_2)$ , so that  $z_1$  is always oriented with the supposed crack path.

**Toughening mechanisms: case  $\beta = 0^\circ$**

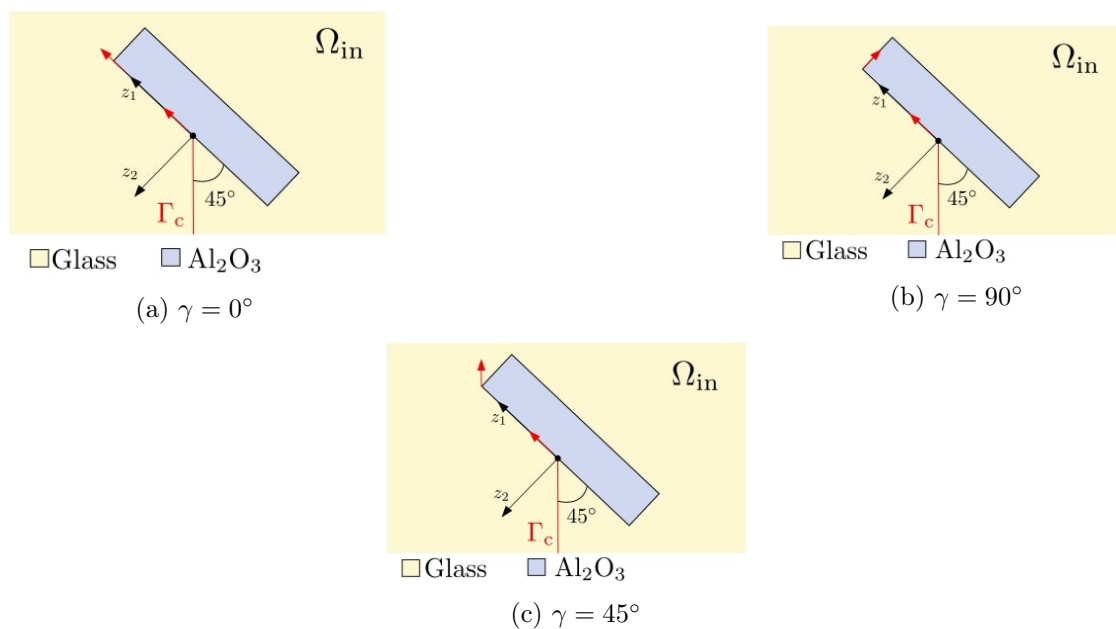


Figure 3.26: Scheme of the inner domain for  $\alpha_p = 45^\circ$  and  $\beta = 0^\circ$  and the supposed crack paths (red arrows).

If  $\beta = 0^\circ$  a deflection of the crack along the interface glass/alumina occurs. A second deflection defined by  $\gamma = 0^\circ, 45^\circ, 90^\circ$ , is shown in Fig. 3.26. The predominant crack path is obtained by comparing the apparent fracture toughness of the three options, see Fig. 3.27.

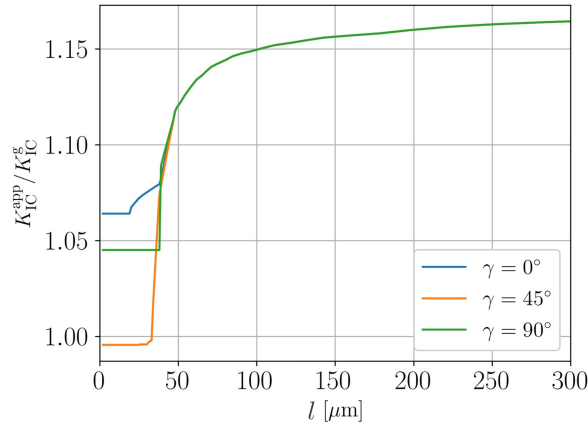
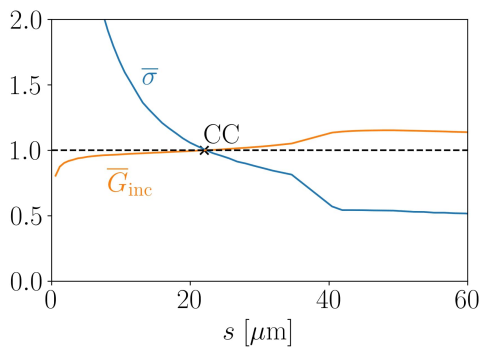
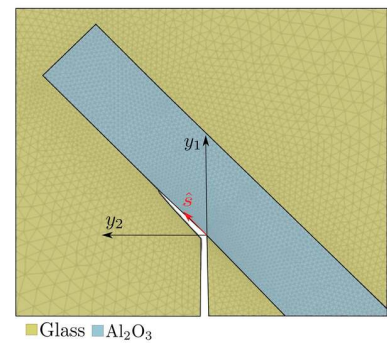


Figure 3.27: Evolution of  $K_{IC}^{\text{app}}/K_{IC}^g$  with  $l$  for several values of  $\gamma$  in the case of  $\beta = 0^\circ$ .

It should be noted that for short platelets  $K_{IC}^{\text{app}}(l)$  remains constant, since it is the energy condition the one that is governing the failure. Moreover, it is observed that for  $l > 47 \mu\text{m}$  there is no difference among the three possibilities, since the crack increment is produced along the glass/alumina interface. As an example, Fig. 3.28 shows the case of  $\gamma = 0^\circ$  and  $l = 75 \mu\text{m}$ . A conventional fulfillment of the CC can be observed in this case, where the CC point is located before the end of the interface glass alumina.



(a) CC curves

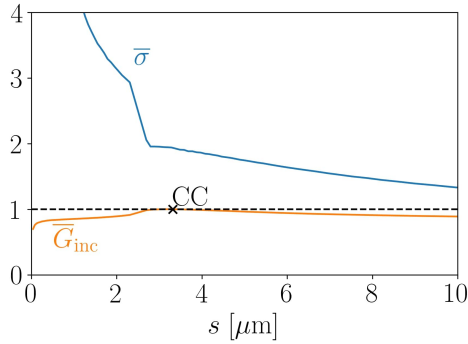


(b) Deformed shape

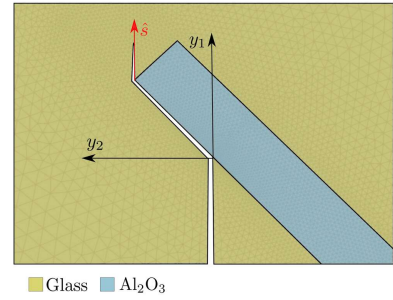
Figure 3.28: Example of the application of the CC for  $\gamma = 0^\circ$  and  $l = 75 \mu\text{m}$ .

Furthermore, below  $l = 47 \mu\text{m}$ ,  $\gamma = 45^\circ$  predominates. It means that the crack would propag-

ate out of the interface with the same orientation it had before impinging into the platelet. As an example, the application of the CC is shown for  $l = 5 \mu\text{m}$  and  $\gamma = 45^\circ$ . It can be observed that CC point corresponds to the maximum point of the energy curve, which means that the failure is completely governed by the energy condition.



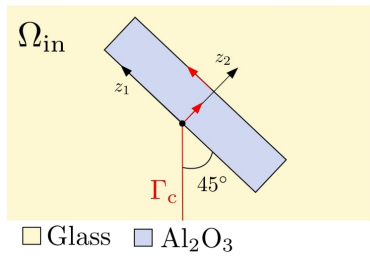
(a) CC curves



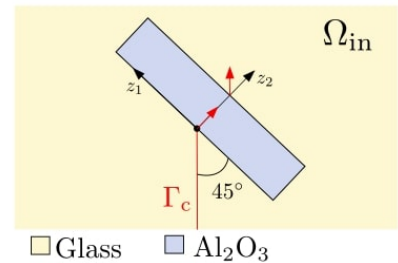
(b) Deformed shape

Figure 3.29: Example of the application of the CC for  $\gamma = 45^\circ$  and  $l = 5 \mu\text{m}$ .

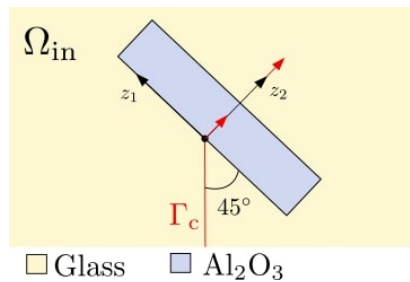
**Toughening mechanisms: case of  $\beta = 90^\circ$  and  $\beta = 45^\circ$**



(a)  $\gamma = 0^\circ$



(b)  $\gamma = 45^\circ$



(c)  $\gamma = 90^\circ$

Figure 3.30: Scheme of the inner domain for  $\alpha_p = 45^\circ$  and  $\beta = 90^\circ$  and the supposed crack paths (red arrows).

In Fig. 3.30 the three expected paths analysed for  $\beta = 90^\circ$  are presented. Once the crack penetrates into the platelet it can be deflected through the interface glass alumina ( $\gamma = 0^\circ$ ), or it can be propagated in the glass region, following the same direction as the pre-existing crack ( $\gamma = 45^\circ$ ) or the same direction as it had when it entered in the alumina ( $\gamma = 90^\circ$ ).

In Fig. 3.31 the three expected crack paths are compared, where the so-called major and minor cases were described in Section 3.2.2.1. As it was observed for other cases, different behaviours can be distinguished. They are related to the different results obtained using the CC analysis. A zoom inside each graph highlights the region of short platelets. Clearly, when the fracture properties of alumina are improving,  $K_{IC}^{app}$  is increasing. In fact, for very short platelets it is observed that the crack deflection for the minor case is not enough to increase  $K_{IC}^{app}$  with respect to  $K_{IC}^g$  for very low values of the alumina fracture properties.

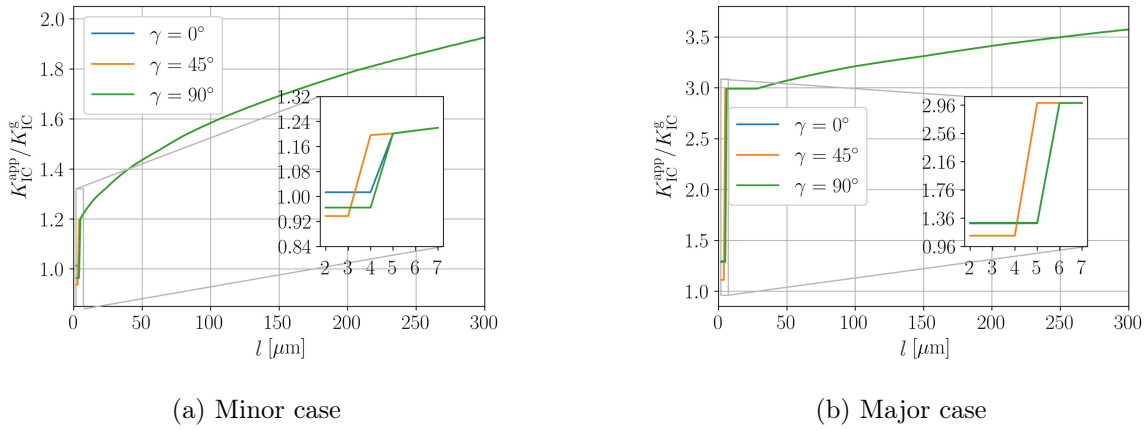


Figure 3.31: Evolution of  $K_{IC}^{app}/K_{IC}^g$  with  $l$  for several values of  $\gamma$  in the case of  $\beta = 90^\circ$ .

On the other hand, Fig. 3.32 shows the three possible crack paths analysed for the case of  $\beta = 45^\circ$ , i.e. when the crack penetrates straight into the platelet.



Figure 3.32: Scheme of the inner domain for  $\alpha_p = 45^\circ$  and  $\beta = 45^\circ$  and the expected crack paths (red arrows).

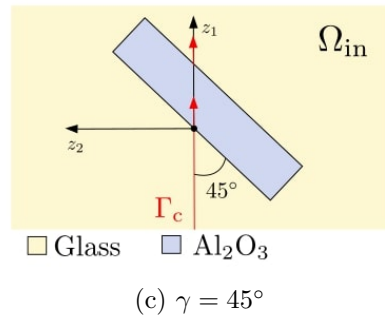
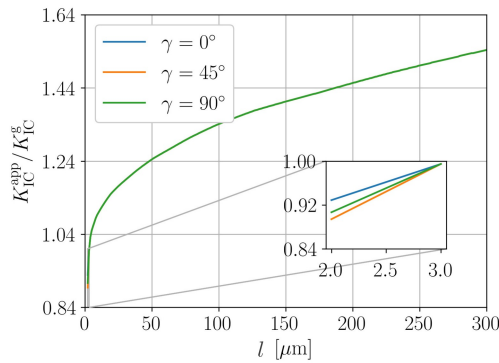
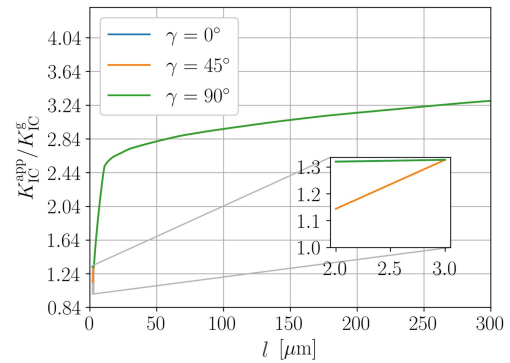


Figure 3.32: Scheme of the inner domain for  $\alpha_p = 45^\circ$  and  $\beta = 45^\circ$  and the expected crack paths (red arrows).

In Fig. 3.33, conclusions are very similar to the two previous cases, where  $\gamma = 45^\circ$  remains the most probable case, i.e. the predominant mechanism, for both the minor and the major examples. Again, there are only differences in the short platelets.



(a) Minor case



(b) Major case

Figure 3.33: Evolution of  $K_{IC}^{app}/K_{IC}^g$  with  $l$  for several values of  $\gamma$  in the case of  $\beta = 45^\circ$ .

Finally, a comparison is made for the minor and major case for the three  $\beta$  angles in Fig. 3.34. As it can be seen, the predominant path depends on the alumina fracture properties. In the major case, in general, it is the deflection  $\beta = 0^\circ$  across the interface glass alumina that predominates, but not for very short platelets, where the crack is expected to penetrate into the platelet, having a deflection with respect to its original orientation, case of  $\beta = 90^\circ$ . On the other hand, in the minor case, the crack penetrates into the platelet without suffering any change in its orientation, i.e.,  $\beta = 45^\circ$ .

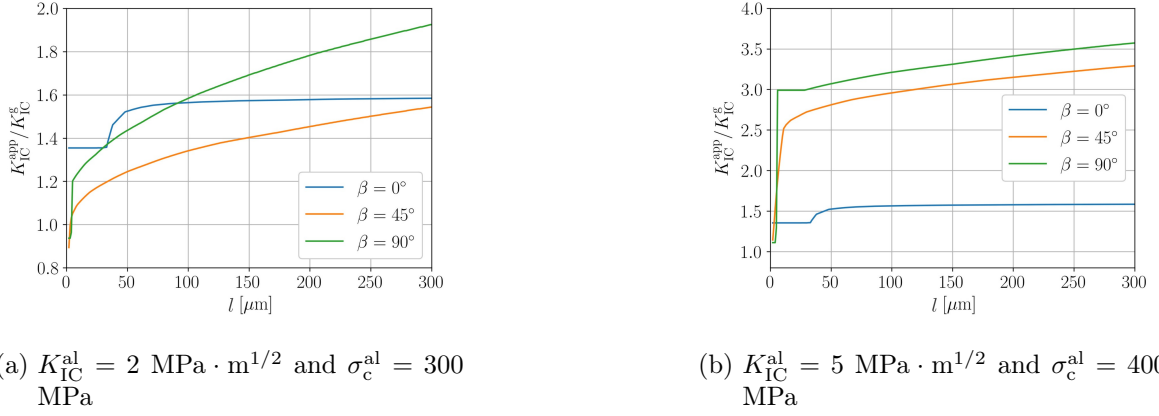


Figure 3.34: Evolution of  $K_{IC}^{app} / K_{IC}^g$  with  $l$  for several values of  $\beta$ .

### 3.2.3 Influence of residual stresses

In this section the influence of residual stresses is included in the problem solved in previous section. Thus, considering the role of a single platelet, we study the complete thermomechanical problem presented in Section 3.1.1, with a cooling down  $\Delta\theta = 500 \text{ K}$ . Notice that here  $\Delta\theta$  is expressed as a positive increment, although it is a negative increment in Section 3.1.1, for the sake of simplicity in the graphics. Results are exhibited for different platelet sizes, at the scale of experiments, i.e.  $l = 5 - 25 \mu\text{m}$  [30] and at an extended scale  $l = 3 - 300 \mu\text{m}$  used to better capture the size effect on the apparent fracture toughness. Moreover, two orientations of the platelet are studied,  $\alpha_p = 90^\circ$  and  $\alpha_p = 0^\circ$ .

Therefore, in this section the influence of  $\Delta\theta$  is investigated in order to determine when it contributes to enhance the apparent fracture toughness of the composite,  $K_{IC}^{app}$ .

Noteworthy, it is important to highlight the difficulty mentioned in Section 3.1.3 when considering the thermomechanical problem. The fact that  $\kappa^{cr}$  outweighs  $\kappa^{te}$ , is tricky to detect, and also difficult to estimate analytically, since in some cases, for example, in  $\alpha_p = 0^\circ$ , the singularity exponent is complex. We have opted for a check of the convexity of  $\bar{\sigma}(s)$  function of  $s$  at the first computation points. Hence, the first and the second derivative of  $\bar{\sigma}(s)$  have been checked in the neighbourhood of the singularity (at  $s = 0$ ). The first derivative must be negative for a decreasing function and the second derivative must be positive to obtain a convex evolution of  $\bar{\sigma}(s)$ . Unfortunately, all this happens in a very small neighborhood of the crack tip, the stress variations are difficult to capture numerically and, due to the singularity, the calculations are very mesh dependent.

#### 3.2.3.1 Results for $\alpha_p = 90^\circ$

When the platelet is perpendicular to the pre-existing crack, the expected crack growth is not known a priori and several possibilities might be analysed: penetration, decohesion and

deflection, see Fig. 3.4.

For penetration (Fig. 3.4c) two scenarios are examined, called minor and major, corresponding to the minor and major values of alumina strength and toughness in Table 3.1. As shown in Fig. 3.35, both converge to the same values of  $K_{IC}^{app}$  for  $l > 150 \mu\text{m}$ , which means that alumina fracture properties play no longer a role in the damage propagation. The reason is that for  $l > 150 \mu\text{m}$  it is the mother crack opening condition which prevails, while, for  $l < 150 \mu\text{m}$  they do play a role, the greater the alumina fracture properties, the higher  $K_{IC}^{app}$ .

Moreover, for  $\alpha_p = 90^\circ$  the singularity exponent in the heterogeneous problem is a real number  $\lambda = 0.638$ , and therefore our numerical calculations can be compared to  $K_I^{min}$ . As expected, both curves are above.

The same comparison is carried out for the deflection mechanism (Fig. 3.4a) with similar conclusions (Fig. 3.36). In the decohesion case (Fig. 3.4b), the situation is slightly different because the crack does not initiate at the mother crack tip but at the corner of the platelet (which undergoes also a singularity), then this mechanism can occur even if the mother crack is closed. The only point to check is the opening or not of the pre-existing crack to be sure that the appropriate boundary conditions prevail along the crack faces. It has been checked that it is either opened or fully closed.

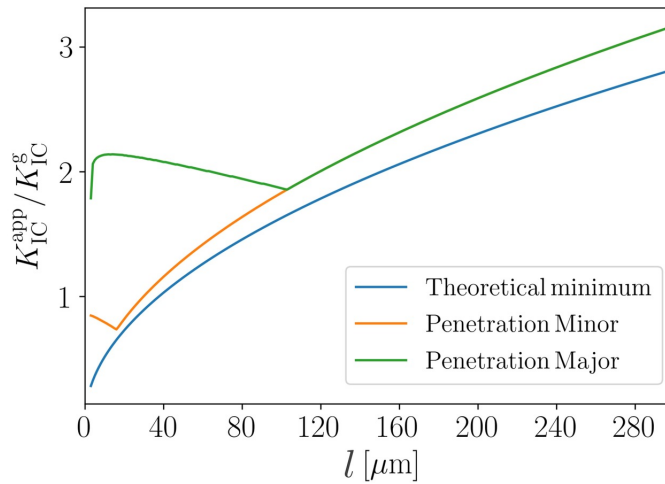


Figure 3.35: Comparison between the theoretical minimum  $K_I^{min}$  and the apparent fracture toughness  $K_{IC}^{app}$  obtained for the major and the minor values of alumina strength and toughness (see Table 3.1), for the penetration case.

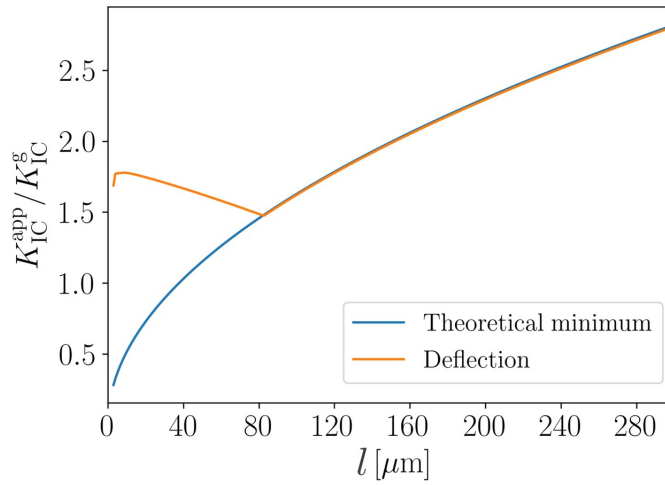


Figure 3.36: Comparison between the theoretical minimum  $K_{\text{I}}^{\text{min}}$  and the apparent fracture toughness  $K_{\text{IC}}^{\text{app}}$  obtained for the deflection case.

The three cases are compared in Fig. 3.37. The actual apparent fracture toughness is the minimum value of  $K_{\text{IC}}^{\text{app}}$  among the three curves which corresponds to the predominant mechanism. It can be pointed out that  $K_{\text{IC}}^{\text{app}}$  is lower than  $K_{\text{IC}}^{\text{g}}$  for long platelets  $l > 98 \mu\text{m}$ . In fact, for  $l > 132 \mu\text{m}$  the CC predicts a breakage by a lateral decohesion during cooling, which agrees with experimental observations [37].

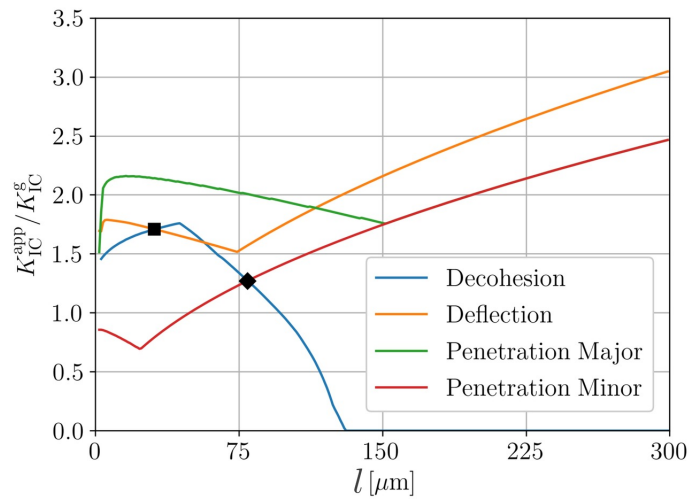


Figure 3.37: Comparison between decohesion, deflection, penetration minor and major, for  $\alpha_{\text{p}} = 90^\circ$  and  $\Delta\theta = 500 \text{ K}$ . The diamond and the square correspond to the optimal points in the minor and the major case respectively.

For short platelets  $l < 98 \mu\text{m}$  the toughening effect depends on alumina fracture properties. In the major case the predominant toughening mechanism is either decohesion or deflection, and  $K_{\text{IC}}^{\text{app}} > K_{\text{IC}}^{\text{g}}$  in the whole range. In the minor case,  $K_{\text{IC}}^{\text{app}} > K_{\text{IC}}^{\text{g}}$  only for  $l = 51 - 98 \mu\text{m}$ , and the governing mechanism is either a penetration or a decohesion. In both the major and the minor cases, there is an optimal platelet size that corresponds to the highest value of the actual  $K_{\text{IC}}^{\text{app}}$  for each case (Fig. 3.37).

The influence of residual stresses at the scale of experiments  $l = 5 - 25 \mu\text{m}$  is studied in Fig. 3.38, where the apparent fracture toughness of the composite is compared for  $\Delta\theta = 0 \text{ K}$  (no residual stresses) and  $\Delta\theta = 500 \text{ K}$ . In the major case a slight enhancement of  $K_{\text{IC}}^{\text{app}}$  with respect to  $K_{\text{IC}}^{\text{g}}$  is observed, whereas in the minor case it is shown that residual stresses do not enhance the toughness, since  $K_{\text{IC}}^{\text{app}} < K_{\text{IC}}^{\text{g}}$  in the whole range. The predominant mechanism does not change with  $\Delta\theta$ , being a lateral decohesion in the major case, which agrees with predictions made in [40], and a penetration for the minor case.

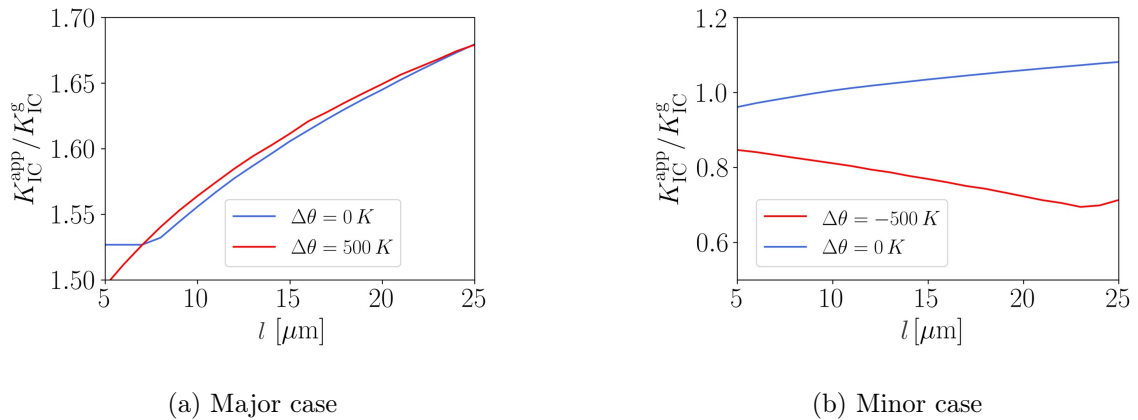


Figure 3.38: Influence of  $\Delta\theta$  on  $K_{\text{IC}}^{\text{app}}$  for  $\alpha_p = 90^\circ$  at the scale of experiments.

Furthermore, the influence of residual stresses is also analysed for an extended range of the platelet size  $l = 3 - 300 \mu\text{m}$  in Fig. 3.39, where it is clearly observed that residual stresses reduce the apparent fracture toughness when considering very long platelets. In both cases residual stresses promote a lateral decohesion as the predominant mechanism, specially for long platelets.

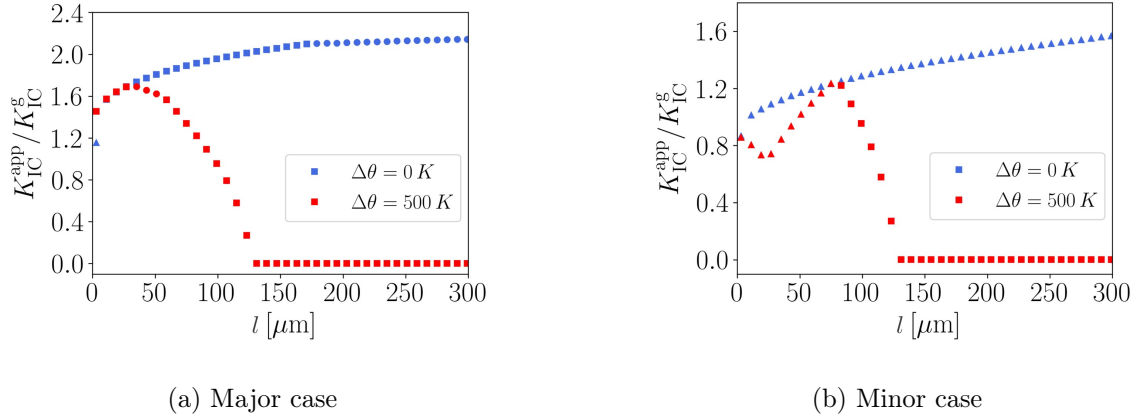


Figure 3.39: Influence of  $\Delta\theta$  on  $K_{IC}^{app}$  for  $\alpha_p = 90^\circ$  in an extended range of  $l$ . The square, circular and triangular symbols represent decohesion, deflection and penetration, respectively.

### 3.2.3.2 Results for $\alpha_p = 0^\circ$

When the platelet is aligned with the pre-existing crack,  $\alpha_p = 0^\circ$ , a crack growth through the interface glass alumina is expected, as shown in Fig. 3.20. The difficulty described in Section 3.1.3 about the negative GSIF in the thermoelastic problem is still present and even worsen than the case of  $\alpha_p = 90^\circ$ , as the exponent of the crack tip singularity impinging the corner of the platelet is a complex number,  $\lambda \pm i\varepsilon = 0.535 \pm i 0.054$ . The same complex character holds for the GSIFs  $\kappa^{te}$  and  $\kappa^{cr}$ , and, contrary to the previous case, it is impossible to compare them to know if the mechanical loading prevails on the residual stresses. However, it can be noted that because of the smallness of the imaginary part  $\varepsilon$  of the singular exponent, the oscillations inherent in this kind of solutions develop on such a small scale that they have no physical significance. Then, (3.40) can be replaced by a condition of decrease and convexity of the tensile stress associated with the singular terms to define  $K_I^{\min}$ .

The effect of residual stresses and the platelet size on  $K_{IC}^{app}$  is studied in Fig. 3.40 for  $\Delta\theta = 0\text{ K}$  and  $\Delta\theta = 500\text{ K}$ , at the two families of scales described in previous section,  $l = 5 - 25\ \mu\text{m}$  and  $l = 3 - 300\ \mu\text{m}$ . Clearly, a toughening effect ( $K_{IC}^{app} > K_{IC}^g$ ) is never observed at the experimental scale, with and without residual stresses, as shown in Fig. 3.40a. In fact, residual stresses reduce the apparent fracture toughness in the composite. Interestingly, when considering an extended scale, see Fig. 3.40b,  $K_{IC}^{app}$  is higher than  $K_{IC}^g$  for  $l > 60\ \mu\text{m}$ , for both  $\Delta\theta = 0\text{ K}$  and  $500\text{ K}$ . In the latter, two different evolution of  $K_{IC}^{app}$  are observed. For  $l < 36\ \mu\text{m}$   $K_{IC}^{app}$  is decreasing and the energy condition is governing the failure, otherwise  $K_{IC}^{app}$  is increasing and the stress condition is governing. In the latter the crack growth is determined by the negative thermal GSIF in the thermoelastic problem.

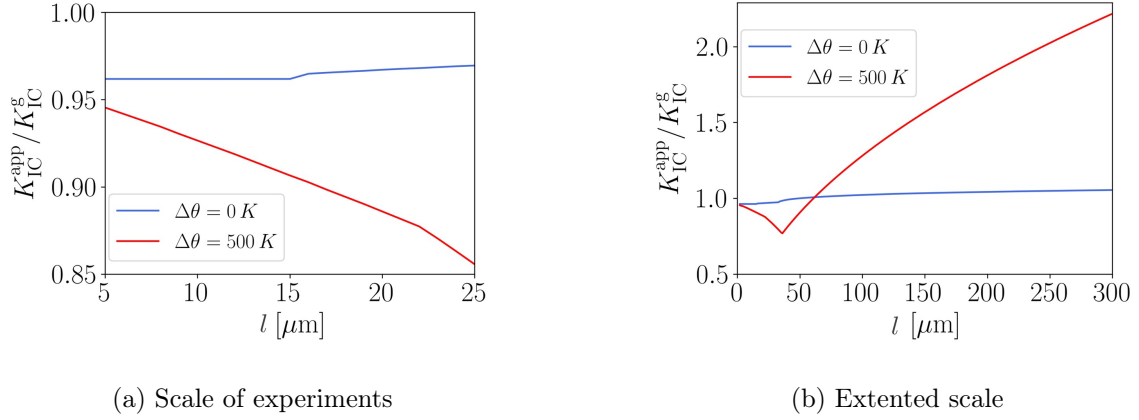


Figure 3.40: Influence of  $\Delta\theta$  and  $l$  on  $K_{IC}^{app}$  for  $\alpha_p = 0^\circ$  and  $V_p = 0\%$ .

### 3.2.4 Influence of the volume fraction

The mechanical properties of the equivalent homogenized material depend on the volume fraction of platelets  $V_p$ . The values chosen for this study correspond to the ones found in the literature [30],  $V_p = 0, 5, 10, 15$  and  $30\%$  (note that  $0\%$  means a single platelet). As in Section 3.2.3, two orientations of the platelet have been studied,  $\alpha = 0^\circ$  and  $\alpha = 90^\circ$ .

#### 3.2.4.1 Results for $\alpha = 90^\circ$

The case of  $\alpha = 90^\circ$  requires the analysis of three different crack paths described in Fig. 3.4: deflection, decohesion and penetration. First, Fig. 3.41 shows the influence of  $V_p$  and  $l$  on  $K_{IC}^{app}$  in the major case at scale of experiments for  $\Delta\theta = 0\text{ K}$  and  $500\text{ K}$ . In general, a great toughening effect is observed when increasing  $V_p$ , whereas little differences related to  $\Delta\theta$  are noticed.

As shown in Fig. 3.41a, for  $\Delta\theta = 0\text{ K}$  and  $V_p = 0\%$  the predominant mechanism is a lateral decohesion, except for  $l = 5\text{ }\mu\text{m}$ , in which it is the penetration. On the other hand, for  $V_p > 0\%$ , the deflection mostly governs the failure. Only in case of  $V_p = 10\%$  and  $l = 5\text{ }\mu\text{m}$  the governing mechanism changes to penetration. Interestingly, intermediate values of the volume fraction  $V_p = 5\%$  and  $10\%$ , show values of  $K_{IC}^{app}$  closer to each other. For instance, for  $l = 5\text{ }\mu\text{m}$  and  $V_p = 10\%$  the predominant mechanism changes to penetration, and  $K_{IC}^{app}$  is very similar to the one for  $V_p = 5\%$ . Moreover, for  $l > 18\text{ }\mu\text{m}$  and  $V_p = 5\%$  there is a jump in  $K_{IC}^{app}$ , and it becomes closer to the one obtained for  $V_p = 10\%$ . The reason why this jump occurs is a change in the crack increment predicted by the CC. For platelets larger than  $18\text{ }\mu\text{m}$  the crack grows outside of the interface glass alumina, otherwise it grows inside. An example is shown in Fig. 3.42, where the CC is applied for  $l = 25\text{ }\mu\text{m}$ . The two adimensional curves  $\bar{\sigma}$  and  $\bar{G}_{inc}$  are represented as well as the crack opening when  $K_I = K_{IC}^{app}$  in the inner domain. It can be observed that in this case the crack grows inside the interface glass alumina until  $s = 11.39\text{ }\mu\text{m}$ . Notice that at the end of the interface glass alumina there is a stress peak due

to the singularity at the corner point.

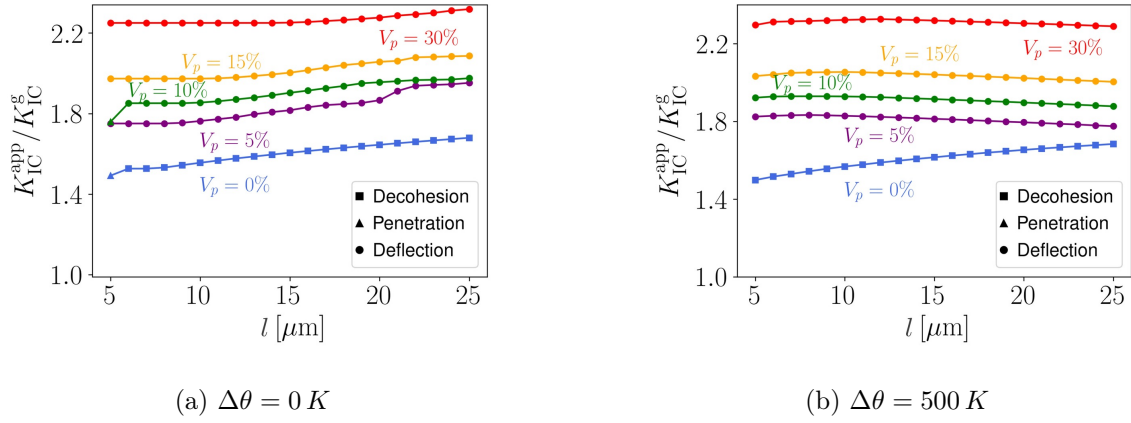


Figure 3.41: Influence of  $V_p$  and  $\Delta\theta$  on  $K_{IC}^{app}$  at the scale of experiments for  $\alpha = 90^\circ$ , considering the major case of alumina fracture properties.

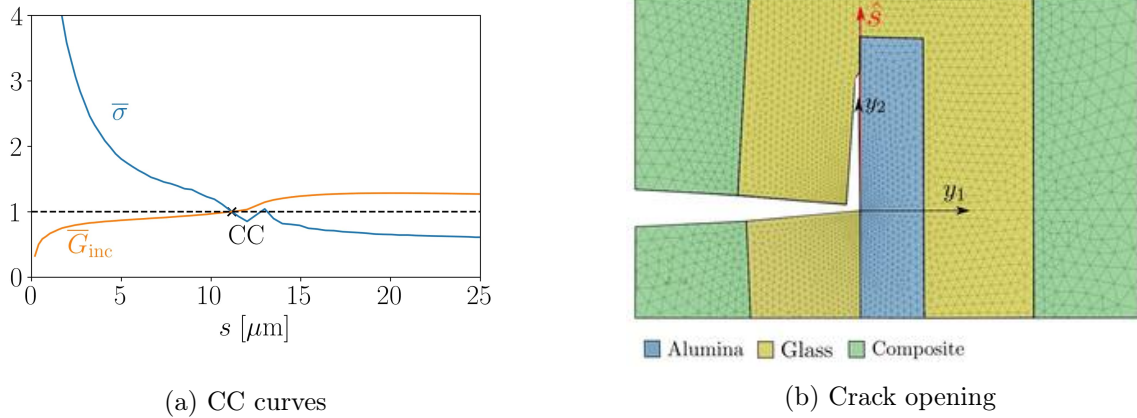


Figure 3.42: Example of the application of the Coupled Criterion for  $l = 25\ \mu\text{m}$ ,  $\Delta\theta = 0\text{ K}$  and  $V_p = 5\%$

Fig. 3.41b shows the case of  $\Delta\theta = 500\text{ K}$ , where it can be observed that penetration is no longer a predominant mechanism at scale of experiments. Instead, the predominant mechanism changes from the decohesion ( $V_p = 0\%$ ) to deflection ( $V_p > 0\%$ ). In this case there is not a jump in  $K_{IC}^{app}$  for  $V_p = 5\%$ . As shown in Fig. 3.43 for  $l = 25\ \mu\text{m}$ , the crack increment is always located at the end of the interface glass alumina ( $s = 12.5\ \mu\text{m}$ ) for the deflection case, where there is a stress drop.

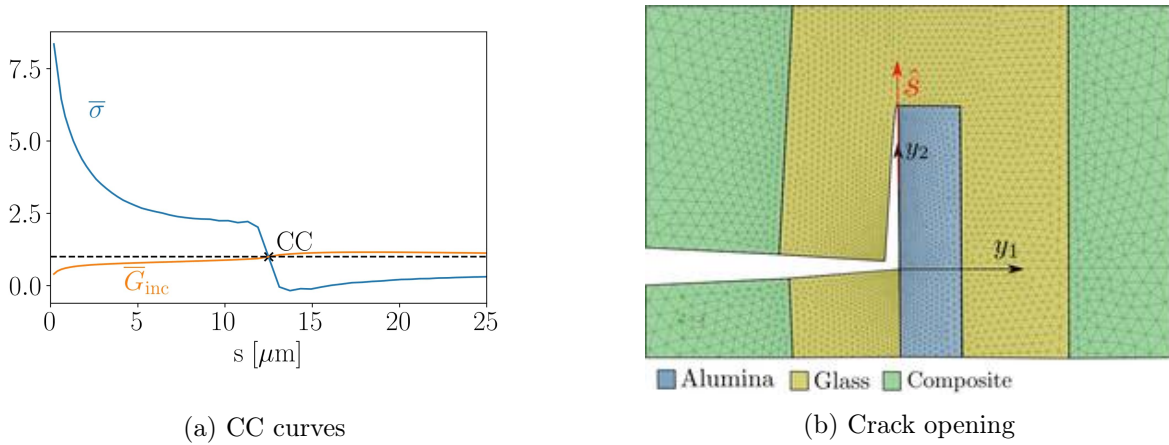


Figure 3.43: Example of the application of the Coupled Criterion for  $l = 25 \mu\text{m}$ ,  $\Delta\theta = 500 \text{ K}$  and  $V_p = 5 \%$

Similar conclusions can be obtained in the minor case represented in Fig. 3.44. The volume fraction has a greater influence on the apparent fracture toughness than residual stresses. Indeed, in this case residual stresses are not a toughening mechanism, since they reduce the value of  $K_{\text{IC}}^{\text{app}}$ . Penetration is the predominant mechanism in both cases, with and without thermal effects, i.e., if the alumina fracture properties are not high enough the pre-existing crack always penetrates the platelet. Moreover,  $K_{\text{IC}}^{\text{app}}$  in the minor case is lower than  $K_{\text{IC}}^{\text{app}}$  in the major case.

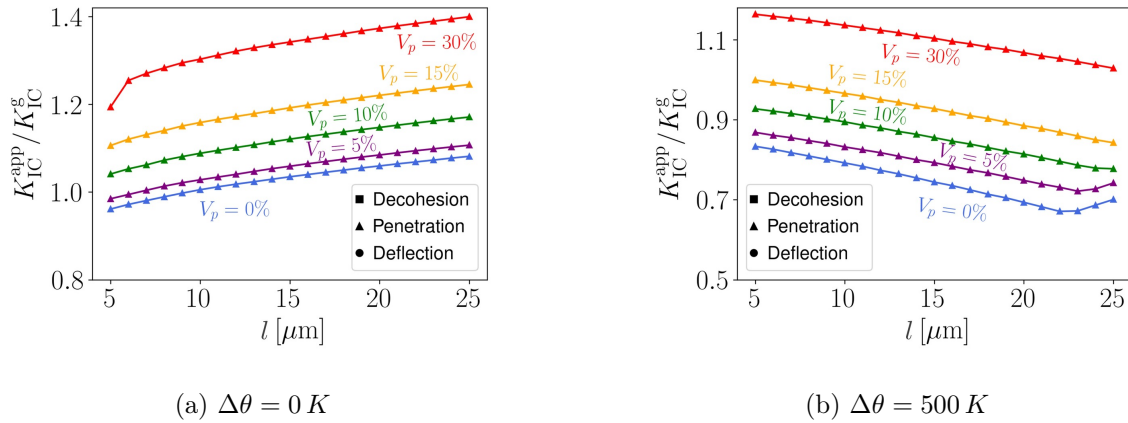


Figure 3.44: Influence of  $V_p$  and  $\Delta\theta$  on  $K_{\text{IC}}^{\text{app}}$  at the scale of experiments for  $\alpha = 90^\circ$ , considering the minor case of alumina fracture properties.

It is worth mentioning the cases  $V_p = 0 \%$  and  $5 \%$  for  $\Delta\theta = 500 \text{ K}$  shown in Fig. 3.44b, where there is a change in the tendency of  $K_{\text{IC}}^{\text{app}}$  at  $l \approx 22.5 \mu\text{m}$ , explained by a change in the crack opening. For platelets smaller than  $l = 22.5 \mu\text{m}$  the crack penetrates into the alumina at the moment of failure until it is arrested when it reaches the glass region, whereas for

$l > 22.5 \mu\text{m}$  the crack growth stops before reaching the end of the platelet, explaining the change in the behaviour of  $K_{IC}^{app}(l)$ . As an example, Fig. 3.45 and 3.46 show the application of the CC for  $\Delta\theta = 500 K$  and  $V_p = 5 \%$ , at  $l = 15$  and  $25 \mu\text{m}$  where the crack increment is given by the CC point. Notice that a drop in the stress function is observed at  $s = 3 \mu\text{m}$ , the end of the platelet. Then, another change in the stress function is noticed at the end of the heterogeneous microstructure,  $s = 8.2 \mu\text{m}$ .

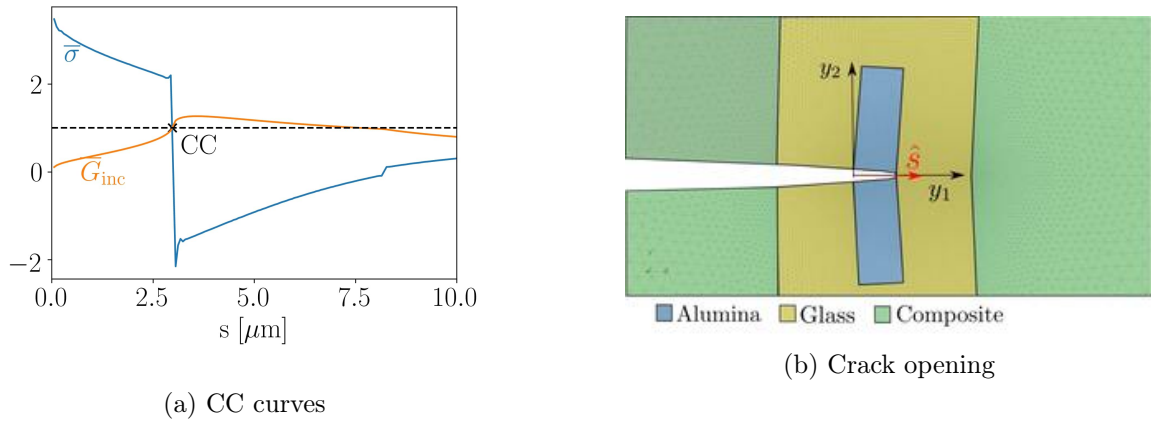


Figure 3.45: Example of the application of the Coupled Criterion for  $l = 15 \mu\text{m}$ ,  $\Delta\theta = 500 K$  and  $V_p = 5 \%$ .

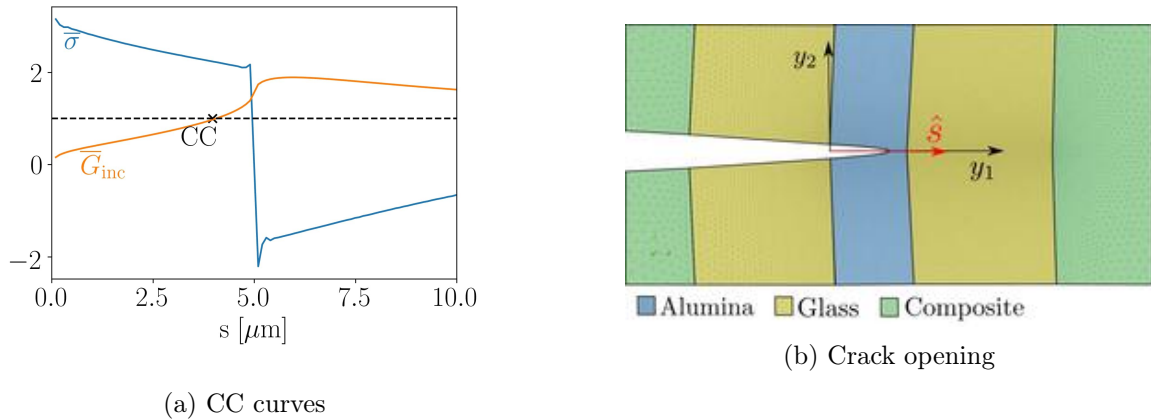


Figure 3.46: Example of the application of the Coupled Criterion for  $l = 25 \mu\text{m}$ ,  $\Delta\theta = 500 K$  and  $V_p = 5 \%$ .

Fig. 3.47 shows the influence of  $V_p$  and the platelet size for an extended range  $l = 3 - 300 \mu\text{m}$  and the major case of alumina fracture properties, omitting the effect of residual stresses ( $\Delta\theta = 0 K$ ). Different shapes can be observed in the behaviour of  $K_{IC}^{app}(l)$ . For high concentrations of alumina  $V_p > 10 \%$ , where the predominant toughening mechanism is always

deflection, the behaviour of the curves is related to a change in the crack opening, depending on the platelet size. For short platelets ( $l < 40 \mu\text{m}$ ) the crack grows until the end of the interface glass alumina at the moment of failure, whereas for longer platelets the crack increment is shorter than the length of the interface. For low concentrations of alumina  $V_p \leq 10\%$  different toughening mechanisms are observed. First, for very short platelets ( $l < 5 \mu\text{m}$ ) the penetration is governing the failure, whereas for very long platelets ( $l > 180 \mu\text{m}$ ) it is always deflection. For an intermediate range ( $l = 5 - 180 \mu\text{m}$ ) of the platelet size the concentration of alumina highly promotes deflection as a toughening mechanism. Hence, for  $V_p = 0\%$  it is a lateral decohesion in the whole range, whereas this range is much smaller when increasing  $V_p$ .

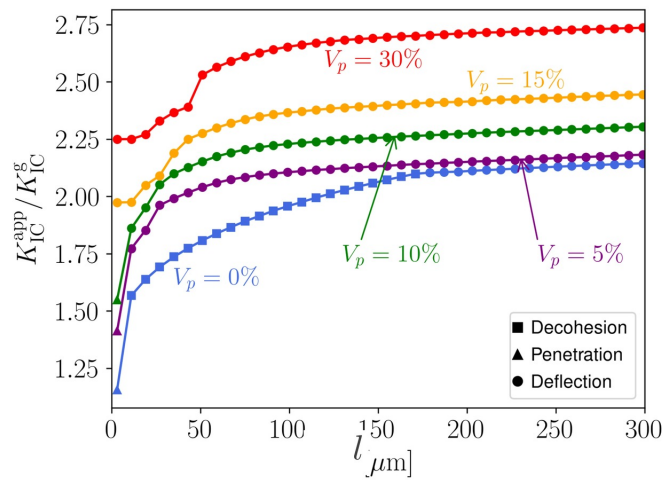


Figure 3.47: Effect of  $V_p$  on  $K_{IC}^{app}$  at the extended scale for  $\Delta\theta = 0^\circ$  and  $\alpha = 90^\circ$ , considering the major case of alumina fracture properties.

The effect of residual stresses is analysed in Fig. 3.48. First, it is observed that for very long platelets the crack grows through lateral decohesion after cooling without mechanical loads, since  $K_{IC}^{app} = 0$ , as shown in Fig. 3.49a for  $l = 250 \mu\text{m}$ . This happens when the platelet size is higher than a certain amount that increases with growing  $V_p$ . Indeed, the phenomenon is no longer observed in the selected range of  $l$  for  $V_p = 30\%$ , although a strong reduction of  $K_{IC}^{app}$  can be noticed.

In general, the combination of two effects is shown in Fig. 3.48. On the one side, the presence of residual stresses promotes decohesion as a predominant mechanism, as it was already mentioned in Section 3.2.3. On the other hand, deflection is more likely to occur for a higher concentration of platelets (i.e. a higher  $V_p$ ). Moreover, for  $V_p \geq 10\%$  a jump in  $K_{IC}^{app}$  is observed, generated by a change in the crack opening. For instance, for  $V_p = 30\%$  and  $l < 202 \mu\text{m}$ , governed by deflection, the crack grows until a point either outside of the interface alumina glass if  $l < 4 \mu\text{m}$ , or located at the end of the interface if  $l = 4 - 147 \mu\text{m}$ , or inside the interface  $l > 147 \mu\text{m}$ .

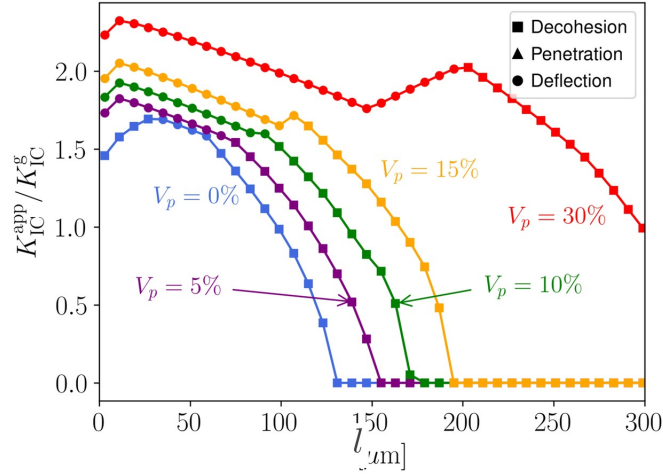
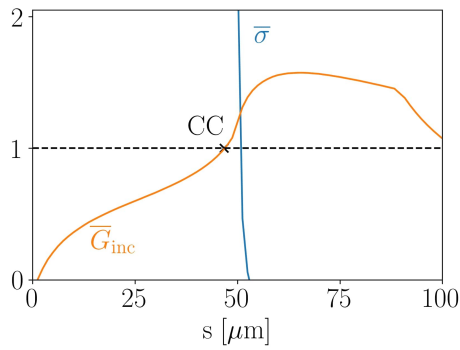
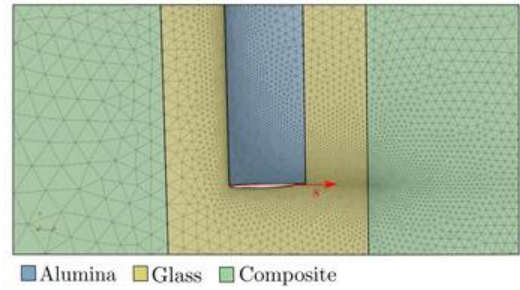


Figure 3.48: Effect of  $V_p$  on  $K_{IC}^{app}$  at the extended scale for  $\Delta\theta = 500 K$  and  $\alpha = 90^\circ$ , considering the major case of alumina fracture properties.



(a) CC curves



(b) Crack opening

Figure 3.49: Example of the application of the Coupled Criterion for  $l = 250 \mu\text{m}$ ,  $\Delta\theta = 500 K$  and  $V_p = 15 \%$ .

Interestingly, when including residual stresses  $K_{IC}^{app}$  is no longer increasing with the platelet size, except for very short platelets or intermediate size and high concentration of alumina ( $V_p = 30 \%$ ). For this reason, an optimal design point for each  $V_p$  can be defined, as it was done in Fig. 3.37. For the sake of simplicity, they have not been highlighted in Fig. 3.48, but an example of the optimal platelet size for  $V_p = 30 \%$  is  $l = 12 \mu\text{m}$ , which gives  $K_{IC}^{app} = 2.32K_{IC}^g$ .

A similar analysis can be made for the minor case. As shown in Fig. 3.50, when residual stresses are not included the crack always penetrates the platelet when considering low values

of the alumina fracture properties. In this case,  $K_{IC}^{app}$  is an increasing with growing  $l$  and  $V_p$ .

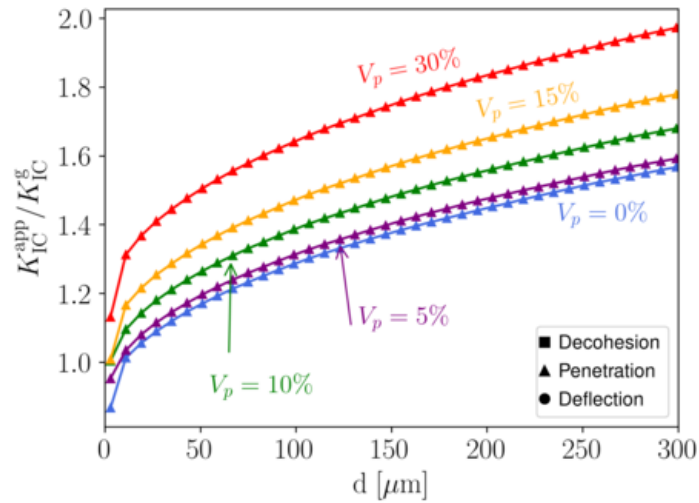


Figure 3.50: Effect of  $V_p$  on  $K_{IC}^{app}$  at the extended scale for  $\Delta\theta = 0 K$  and  $\alpha = 90^\circ$ , considering the minor case of alumina fracture properties.

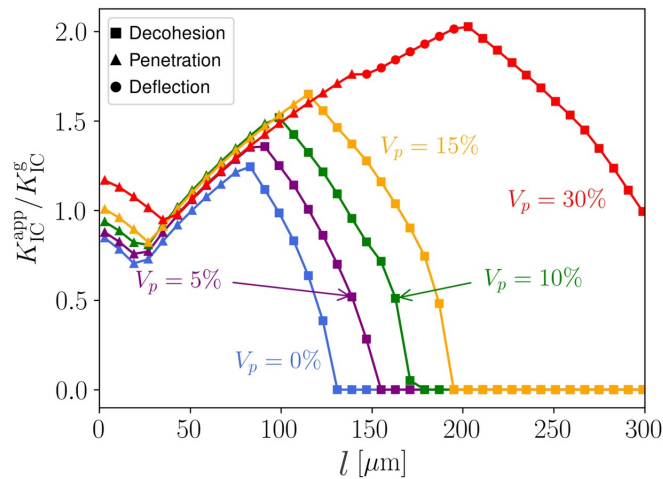


Figure 3.51: Effect of  $V_p$  on  $K_{IC}^{app}$  at the extended scale for  $\Delta\theta = 500 K$  and  $\alpha = 90^\circ$ , considering the minor case of alumina fracture properties.

When including residual stresses in the minor case of alumina fracture properties a lateral decohesion is again promoted for long platelets. Indeed, the phenomenon observed in Fig. 3.48 is exactly the same in Fig. 3.51, since decohesion does not depend on the alumina fracture

properties (the interface is strong and therefore defined by the glass fracture properties). However, the optimal design point mentioned above is in this case noticed for longer platelets. For instance, for  $V_p = 30\%$  the optimal design point is  $l = 200 \mu\text{m}$ , which gives  $K_{\text{IC}}^{\text{app}} = 2.03K_{\text{IC}}^{\text{g}}$ . Notice that the toughening effect in the minor case is lower than in the major case.

### 3.2.4.2 Results for $\alpha = 0^\circ$

Fig. 3.52 shows the influence of  $V_p$  with and without residual stresses, when the platelet is parallel to the pre-existing crack, see Fig. 3.20. It can be observed that  $V_p$  has a scaling effect on  $K_{\text{IC}}^{\text{app}}$ , increasing its value without changing its evolution with  $l$ .

A toughening effect ( $K_{\text{IC}}^{\text{app}} > K_{\text{IC}}^{\text{g}}$ ) is observed only for  $V_p > 5\%$ , although for  $V_p = 10\%$  the apparent fracture toughness is not enhanced when  $l > 16 \mu\text{m}$ . The maximum enhancement of  $K_{\text{IC}}^{\text{app}}$  with respect to  $K_{\text{IC}}^{\text{g}}$  is 1.3. Notice the toughening effect is generated by the improvement of mechanical properties in the composite when increasing  $V_p$ , and not as a consequence of including residual stresses. This conclusion seems to be very difficult to observe through experiments. Moreover, in this case residual stresses always increase the apparent fracture toughness of the composite.

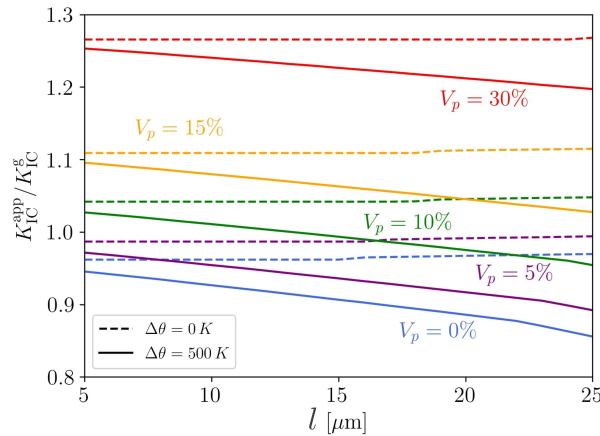


Figure 3.52: Effect of  $V_p$  on  $K_{\text{IC}}^{\text{app}}$  at the scale of experiments for  $\Delta\theta = 0 K$  and  $500 K$  and  $\alpha = 0^\circ$ .

The same analysis can be made considering an extended range of  $l$ , as it is shown in Fig. 3.53. An unpredictable effect of  $V_p$  is observed for large values of  $l$ . An increase of  $V_p$  generates a higher thermal expansion coefficient in the equivalent homogenized material, which reduces the compression residual stresses generated in the glass matrix during cooling, and consequently the negative thermal GSIF in the thermoelastic problem. As explained before, the negative GSIF led to an increase in  $K_{\text{IC}}^{\text{app}}$ , and it would be lower when increasing  $V_p$ . This effect is opposite to the one generated by the enhancement in the mechanical properties of the homogenized material when  $V_p$  is increased, that generally leads to a higher apparent

fracture toughness. As a consequence, results are very difficult to estimate a priori when long platelets are considered, and residual stresses have a greater influence. A particular analysis is necessary to determine an optimal design of the composite in such region.

Furthermore, a toughening effect due to the presence of residual stresses is observed for long platelets, although this effect also strongly depends on  $V_p$ . For such platelets,  $K_{IC}^{app}$  tends to increase, which means that it is the stress condition that is governing the failure. In particular, the value of  $K_{IC}^{app}$  is determined by condition of the opening of the mother crack. Notice that the existence of a decreasing and increasing region in the evolution of  $K_{IC}^{app}$  allows us to determine a certain size of the platelet for which a minimum value of the apparent fracture toughness is obtained.

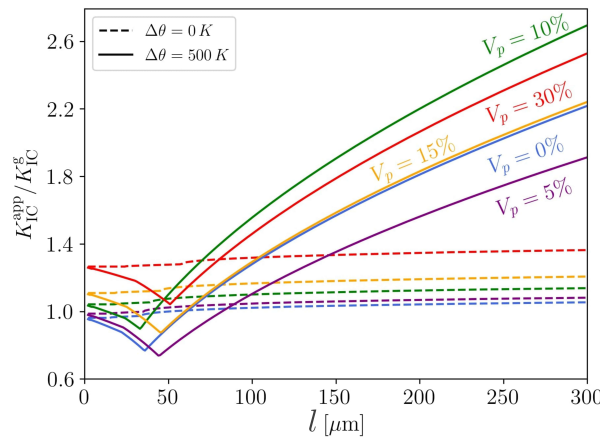


Figure 3.53: Effect of  $V_p$  on  $K_{IC}^{app}$  at the extended scale for  $\Delta\theta = 0 K$  and  $500 K$  and  $\alpha = 0^\circ$ .

### 3.2.5 Comparison to experiments

Cannillo et al. [40] computed the residual stresses in the composite. Todd et al. [37] observed them experimentally and measured the tensile stress in the platelet through electron microscopy, they expressed the results in terms of the mean stress  $\bar{\sigma}_p = (\sigma_{11} + \sigma_{22})/2$ , whereas the compressive residual stress in the matrix  $\bar{\sigma}_m$  was calculated applying the equilibrium condition.

A comparison between these results [37, 40] and the ones obtained using the design tool presented in this work is made in Fig. 3.54. In order to obtain the mean stress, a numerical simulation considering no mechanical loads and no pre-existing crack in the specimen was performed. It is important to highlight that in experiments several measurements were made at different points in the specimen, and that the only ones centered on the platelets were selected to carry out the comparison. Therefore, we calculate the mean stress at the center of the platelet.

The difference between simulations made in this paper and experiments is greater for higher volume fractions. The reason could be that when a high concentration of alumina is con-

sidered, some clusters of platelets appear in the specimen [30], and therefore the theory of homogenization applied to calculate the mechanical properties of the composite in our model could differ from reality. The highest differences between experiments and numerical results are found in the platelet, where residual stresses calculated in this paper seem to be closer to experiments than the numerical data found in [40]. Moreover, using our design tool with one finite element calculation we are able to obtain the apparent fracture toughness for any platelet size, since the calculation is made in the inner domain. This strongly reduce the computational complexity of the analysis.

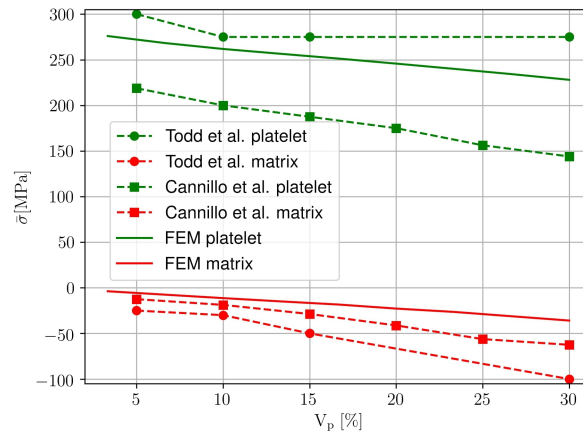


Figure 3.54: Residual stresses found in the literature [40] and [37] and residual stresses obtained in the simulations (FEM platelet and FEM matrix).

As an example, Fig. 3.55 shows the two stress components in the inner domain  $\hat{\sigma}_{11}$  and  $\hat{\sigma}_{22}$  after cooling for  $V_p = 0\%$  and  $\alpha = 0^\circ$ . Notice that according to (3.23) residual stresses do not depend on the platelet size, thus,  $\underline{\underline{\sigma}}(x_1, x_2) = \underline{\underline{\hat{\sigma}}}(y_1, y_2)$ . The thermal coefficient of alumina is higher than the one of glass, and therefore tensile stresses in the platelet and compressive stresses in the matrix appear after cooling. At the horizontal interfaces glass alumina  $y_2 = 0$  and  $y_2 = -t$  (inner domain) the maximum value of  $\sigma_{11}$  is reached, being  $\sigma_{11} = \hat{\sigma}_{11} = 720$  MPa in the platelet and  $\sigma_{11} = \hat{\sigma}_{11} = -280$  MPa in the matrix region. On the other hand, the maximum value of  $\sigma_{22}$  is found at the vertical interfaces glass alumina  $y_2 = 0$  and  $y_1 = 0, l$  (inner domain), being  $\sigma_{22} = \hat{\sigma}_{22} = 350$  MPa in the platelet and  $\sigma_{22} = \hat{\sigma}_{22} = -210$  MPa in the matrix region.

In Fig. 3.56 a validation of the model by comparison of the apparent fracture toughness with simulations is made. For each value of  $V_p$  two experimental measures of  $K_{IC}^{app}$  are considered together with the mean value, see Table 3.2. The two extreme orientations of the platelet analyzed in this paper,  $\alpha = 0^\circ$  and  $\alpha = 90^\circ$  are used for the simulations, including the effect of residual stresses. A good agreement with experiments is observed for low values of  $V_p$ , since the average of the simulated values of  $K_{IC}^{app}$  falls within the error bar of experiments. For high values of  $V_p$  a greater difference is noticed, which can be explained by the inhomogeneities

that appear due to the presence of clusters of platelets for high concentrations of alumina, as it was mentioned above.

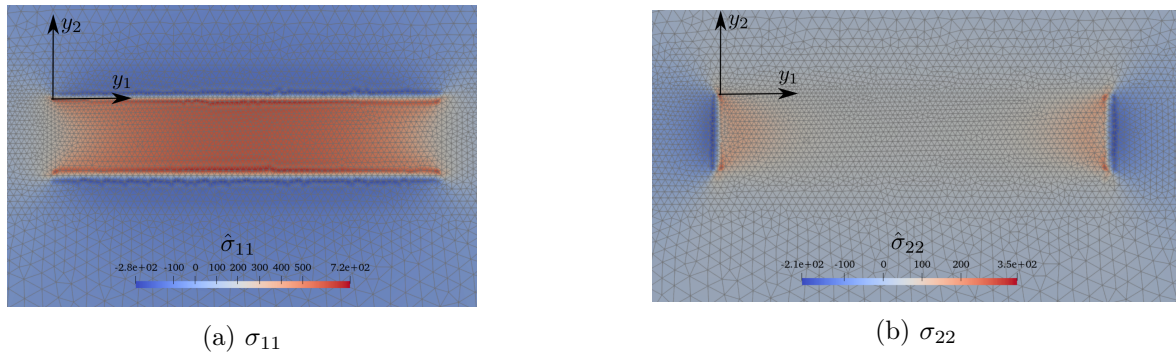


Figure 3.55: Stress component in the thermoelastic problem, with  $\Delta\theta = 500\text{ K}$ .

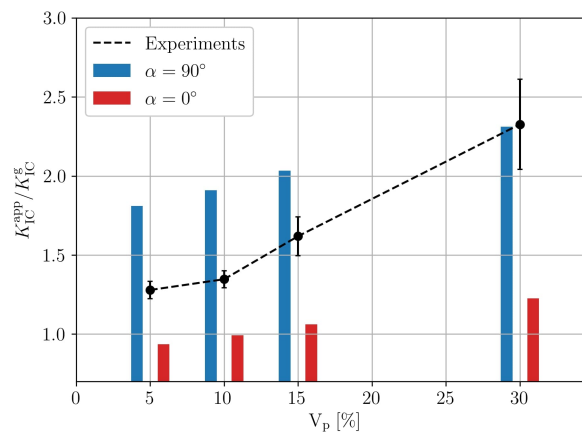


Figure 3.56: Comparison between experiments and simulations

### 3.2.6 Conclusions

As a general conclusion, a size effect is observed. When the length of the platelet is very small, it is the energy condition that is governing the failure, and consequently the apparent fracture toughness remains constant. Notice that similar conclusions were also observed for bending tests on microcantilever beams at the micro-scale in Chapter 2. The size of the platelet plays also a role on the newly created crack length. If the platelet is short, the crack evolves in an unstable manner joining the glass region beyond the platelet, whereas if it is long, the crack increment remains inside the platelet, or along the interface glass/alumina.

Moreover, in some cases with very short platelets, as  $\alpha = 0^\circ$ , a change in the crack path is not enough to enhance the apparent fracture toughness. It means that other toughening

mechanisms, such as the volume fraction of platelets, should be invoked for improving  $K_{IC}^{app}$ .

The influence of the alumina fracture properties on the toughening mechanisms has been analysed. It can be concluded that both  $K_{IC}^a$  and  $\sigma_c^a$  have an impact on the composite fracture properties. However,  $K_{IC}^a$  has a greater influence on  $K_{IC}^{app}$ .

An important conclusion can be obtained from the analysis of residual stresses. It is not a general rule that they are a toughening mechanism. It depends on the size of the platelet and the change in temperature after cooling. The main parameter that explains why an enhancement of the apparent fracture toughness of the composite can be observed is the negative GSIF (or its counterpart in the complex case) related to the thermoelastic problem, since it is related to a compression at the crack-tip, that must be overcome for crack propagation. Moreover, residual stresses promote the lateral decohesion at the end of the platelet as a predominant failure mechanism in the composite. The residual stresses effect is so high that the decohesion mechanism at the end of very long platelets can occur during cooling prior to any mechanical loading.

In general, the volume fraction has a positive scaling effect on the apparent fracture toughness of the composite. When the concentration of alumina is increased the deflection mechanism is promoted as a failure mechanism if the alumina fracture properties are great enough, otherwise penetration is the governing mechanism.

At the scale of experiments the volume fraction has a bigger influence on the apparent fracture toughness than residual stresses, whose effect is very weak. Using that scale, the model proposed was verified by comparison with experimental results found in the literature.

To sum up, a complete design tool for platelets composites is presented, particularized for the case of a glass matrix composite reinforced by alumina platelets. Two key novelties stand out from this methodology. First, it is a design tool in which multiple combinations are possible by modifying the input parameters of the composite, and therefore optimizing the design of platelets composites. Second, it offers the possibility to carry out a separate study of the different factors that are related to the fracture toughness: geometrical factors, such as the volume fraction, the size and the orientation of the platelet, or environmental factors, in particular the effect of residual stresses and the change in the pre-existing crack path. Furthermore, this design tool seems to have an important reduction in the computational complexity with respect to other analysis found in the literature.

Table 3.3 shows a summary of this section. The two main orientations studied,  $\alpha = 0^\circ$  and  $90^\circ$  (Minor and major) have been included, with and without residual stresses. Cells have color orange when  $K_{IC}^{app}$  is not enhanced with respect to  $K_{IC}^g$ , otherwise they have color green. For  $\alpha = 90^\circ$  the predominant mechanism is also written in the Table as a function of the platelet size, whereas for  $\alpha = 0^\circ$  the evolution of  $K_{IC}^{app}$  has been commented. Notice that three sizes have been defined in the table: small, medium and long platelets. However, the ranges of  $l$  for each one are different.

Interestingly, as represented in Table 3.3, when residual stresses are not included only the case of  $\alpha = 0^\circ$  and very small platelets in the minor case of  $\alpha = 90^\circ$  are not increasing the apparent fracture toughness with respect to  $K_{IC}^g$ . On the other hand, when including residual stresses, long platelets are broken after cooling down, and therefore they do not increase  $K_{IC}^g$  when  $\alpha = 90^\circ$ .

It is important to highlight that, for the sake of simplicity, the effect of the volume fraction has been omitted in this table, that only considers the role of a single platelet. As mentioned above, the volume fraction has a positive scaling effect on the apparent fracture toughness, but the main conclusions summarised in the table are not changed by this parameter.

		$\alpha = 0^\circ$	$\alpha = 90^\circ$
		Minor case	
		Major case	
Short platelet	0 K	$l < 16 \mu\text{m}$ Constant $K_{IC}^{\text{app}}(l)$ $l < 36 \mu\text{m}$ Decreasing $K_{IC}^{\text{app}}(l)$	$l < 6 \mu\text{m}$ Penetration $l < 51 \mu\text{m}$ Penetration Decohesion or deflection
	500 K		
Medium platelet	0 K	$l = 16 - 50 \mu\text{m}$ Increasing $K_{IC}^{\text{app}}(l)$ $l = 36 - 60 \mu\text{m}$ Increasing $K_{IC}^{\text{app}}(l)$	$l = 6 - 160 \mu\text{m}$ Penetration $l = 51 - 98 \mu\text{m}$ Penetration Decohesion or deflection
	500 K		
Long platelet	0 K	$l > 50 \mu\text{m}$ Increasing $K_{IC}^{\text{app}}(l)$ $l > 60 \mu\text{m}$ Increasing $K_{IC}^{\text{app}}(l)$	$l > 160 \mu\text{m}$ Penetration Deflection
	500 K		

Table 3.3: Summary of the main states found in the platelets composite considering the role of a single platelet with and without residual stresses, for  $V_p = 0\%$ . Cells are green when  $K_{IC}^{\text{app}} > K_{IC}^{\text{c}}$  otherwise they are orange.

### 3.3 Industrial application: Ceramic matrix composites with short fibers

This section describes the scientific collaboration between Safran Tech research centre and Sorbonne University, to apply the numerical tool developed in this thesis to a material of interest for Safran company. The work presented here was developed during the 4 months that the author spent at Safran, as part of her PhD programme. The work has been supervised by Dr. Hyung-Jun Chang. This collaboration would not have been possible without all the information and help provided by Dr. Yasmin Lergerste Dr. Sébastien Dénneulin, from Safran Ceramics. All the information about the material studied, as well as the objectives and general knowledge of the industrial context and needs presented in this section is based on the thesis of Dr. Yasmin Lergerste [100]. Therefore, the properties included in this document correspond to those published in [100], although some properties are omitted to preserve the confidentiality of the work.

#### 3.3.1 Introduction and general description

In 2019, the European Commission presented the European Green Deal. Among others, one of the challenges proposed is the net-zero greenhouse gas emissions by 2050 [101]. Consequently, the aerospace industry focuses its efforts mainly on reducing aircraft weight and improving engine efficiency. For the latter, it is proposed to increase the current gas temperature from around  $1000^{\circ}\text{C}$  to a target temperature of  $1300^{\circ}\text{C}$ .

In order to achieve this objective, it is necessary to change the metal alloys that are currently used in aircraft engines, which would not be able to work properly at the proposed temperature. The use of ceramic materials is therefore proposed, due to their many advantages, such as their low density and their very good refractory qualities (their mechanical properties do not degrade with temperature). However, the brittleness of classical ceramics due to the presence of internal defects makes the application of advanced ceramics necessary. Among others, a CMC (ceramic matrix composite) structure is proposed as a technological solution to increase fracture toughness. In particular, Safran Ceramics proposes the use of short-fibre CMC for high-pressure turbine blades, as these parts have very complex geometries and a short-fibre material would be more easily adaptable.

A type of CMC with short fibers is numerically and experimentally characterized in [100]. Three batches made of different compositions are studied, although the first one is ultimately discarded due to the high porosity and low Young modulus obtained in the experiments. In the second batch specimens are composed by a matrix made of a composition of  $\text{TiSi}_2$  and  $\text{MoSi}_2$  and silicon carbide (SiC) Hi-Nicalon fibers. The  $\text{MoSi}_2$  has a good advantage for the application, since it changes from a brittle behavior at low temperatures to a ductile behavior at high temperatures (around  $900^{\circ}\text{C}$ ). However, a  $\text{MoSi}_2$ - $\text{TiSi}_2$  composition is proposed to prevent oxidation of  $\text{MoSi}_2$  in the presence of air, which is a common phenomenon in this material referred to as "pest". On the other hand, the fibers are chosen due to their good

properties at high temperatures. Although the SiC fibers have typically problems with oxidation, the family of Nicalon fibers address this deficiency. In the third batch an interphase of Pyrocarbone (PyC) is included.

The material was numerically characterized applying statistical methods and considering experimental results. Hence, the volume fraction of fibers is  $V_f \approx 12\%$ . The fibers have a minimum length of  $l_{\min} = 24.41 \mu\text{m}$  and a maximum of  $l_{\max} = 2271.6 \mu\text{m}$ . The minimum diameter is  $t_{\min} = 8.5 \mu\text{m}$  and the maximum  $t_{\max} = 53.3 \mu\text{m}$ . Average values obtained from statistical distributions are:  $t_{\text{avg}} = 16.67 \mu\text{m}$  and  $l_{\text{avg}} = 152 \mu\text{m}$ . Additionally, in [100] a study of fiber orientation is conducted, revealing that the majority of fibers are contained within the same plane.

As it was done in previous section, a reference problem under the assumption of plane strain elasticity is used to estimate the fracture toughness. This simplification of the problem might not be representative at all of the real model, provided that fibers have a round cross section, and therefore the thickness of the fiber in the perpendicular direction is smaller than the length of the fiber. Consequently, our model is not able to represent some phenomena, such as a crack growing around the fiber. However, a first estimation is expected to obtain using this model, as a summary of the work done during the short industrial secondment (4 months) of the author in the company.

In Table 3.4 the mechanical properties of the constituents obtained from [100] are shown. It is important to highlight that in the case of the interphase  $\sigma_c$  and  $K_c$  are experimentally estimated (and therefore considering the PyC material) but the Young modulus used in the numerical calculations of [100] corresponds to the one of BN, and therefore it is the one used in this analysis.

Constituents	$E$ [GPa]	$\sigma_c$ [MPa]	$K_c$ [MPa m <sup>1/2</sup> ]
Fiber	420	1222	1.74
Interphase	20	107	0.35
Matrix	359	200	2.42

Table 3.4: Mechanical properties of the constituents of the composite material under study

Fracture toughness of the composite was estimated using an analytical approximation based on Linear Elastic Fracture Mechanics (LEFM) [102] and experimentally using Digital Image Correlation (DIC) in [100]. Table 3.5 shows the results.

Although other mechanical properties of the composite, such as the Young modulus, were estimated in [100] there was no numerical method to calculate the fracture toughness. There-

fore, the main objective of this work is to apply our computational tool to give numerical estimations of the apparent fracture toughness of the composite  $K_{IC}^{app}$  and the predominant toughening mechanism, as a function of the length  $l$  and the diameter  $t$  of the fiber, as well as the volume fraction of fibers,  $V_f$ .

Fracture toughness	$K_c^{LEFM}$ [MPa m <sup>1/2</sup> ]	$K_c^{DIC}$ [MPa m <sup>1/2</sup> ]
Without the interphase	2.8 – 3.45	3.5 – 4.40
With the interphase	3.87 – 4.25	5.2 – 6.32

Table 3.5: Fracture toughness obtained in the composite. Results obtained from [100]

### 3.3.2 Considerations in the problem

To properly adapt the application of the computational tool to the objectives of this study, it will be necessary to take into account some considerations, which are discussed in this section, before presenting the results of the study. First, notice that the inner domain shown in Fig. 3.2 should be modified to include the interphase, as shown in Fig. 3.57, where  $\hat{e}$  represents the thickness of the interphase divided by a characteristic dimension of the fiber.

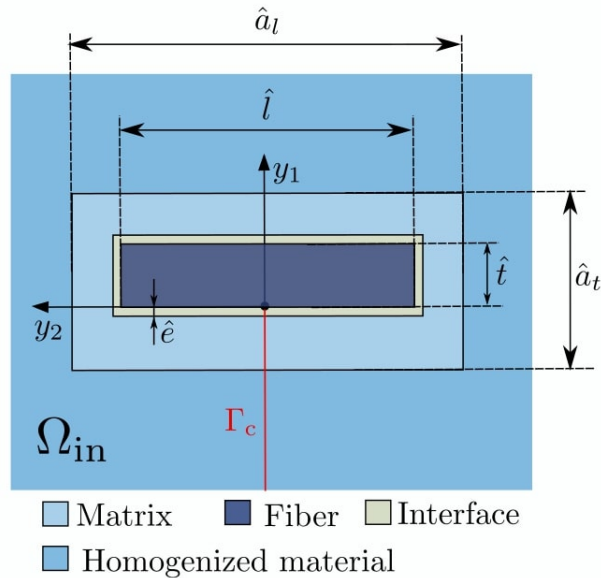


Figure 3.57: Scheme of the inner domain considering a single fiber.

Notice that for the sake of simplicity, only a perpendicular orientation of the fibers with respect to the pre-existing crack is assumed.

When we generate the inner domain, we consider a single fiber located at the crack tip. In previous studies, the effect of the fibers was studied through the homogenized composite material, whose properties were determined through  $V_f$ . With the proposed model, it is assumed that around the reinforcing element (the fiber in this case), there is an area of certain dimensions free of fibers and formed by the matrix. In this section, an additional model is proposed, consisting of multiple fibers, represented in Fig. 3.58. Two new parameters appear,  $h_l$  and  $h_t$ , which define the distance between fibers. This model allow us to consider the effect of fibers close to the one intersecting the crack, which means that we can study possible interactions between fibers modifying the separation distance, and, if the crack length is large enough, study new paths that take into account the action of several fibers. The two models, the single fiber model and the multi-fiber model, will be compared. The geometrical parameters  $\hat{a}_l$  and  $\hat{a}_t$  are defined in the multi-fiber model as

$$\hat{a}_l = 3\hat{l} + 2\hat{h}_l + 6\hat{e}, \quad (3.43)$$

$$\hat{a}_t = 3\hat{t} + 2\hat{h}_t + 6\hat{e}. \quad (3.44)$$

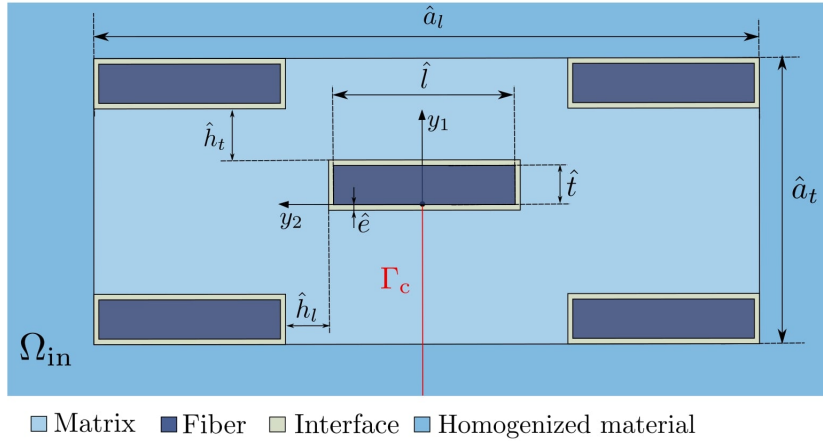


Figure 3.58: Scheme of the inner domain considering multiple fibers.

Some restrictions are naturally deduced from the model

$$\hat{a}_l > 0 \quad \text{and} \quad \hat{a}_t > 0, \quad (3.45)$$

$$\text{if } \hat{h}_l \hat{h}_t > 0 \quad \text{then} \quad \hat{h}_l, \hat{h}_t > 0, \quad (3.46)$$

$$5\hat{t}\hat{l} = V_f \hat{a}_l \hat{a}_t, \quad (3.47)$$

$$\hat{a}_l - 2\hat{l} - 6\hat{e} > 0 \quad \text{and} \quad \hat{a}_t - 2\hat{t} - 6\hat{e} > 0 \quad (3.48)$$

The first restriction refers to the fact that the dimensions  $\hat{a}_l$  and  $\hat{a}_t$  are always positive. The second restriction means that one fiber can not penetrate other fibers in the model. In the third equation we just point out that the definition of the fibers volume fraction must be fulfilled. Finally, the last condition is applied to prevent fibers from overlapping in the geometry. Notice

that these restrictions are not enough to get a unique solution of the geometry of the problem, since  $\hat{t}$  and  $\hat{l}$  are free parameters. For this reason, we choose these two parameters so that they minimize the surface of the multi-fiber model, defined as

$$S(\hat{h}_l, \hat{h}_t) = \hat{a}_l \hat{a}_t = (3\hat{l} + 2\hat{h}_l + 6\hat{e})(3\hat{t} + 2\hat{h}_t + 6\hat{e}). \quad (3.49)$$

Although we use this hypothesis, at the end of this section we will change it to study the influence of  $\hat{h}_l$  and  $\hat{h}_t$ .

Another important comment is that the representation of the Coupled Criterion in this section is slightly different to previous representations. In this case we represent the stress intensity factor  $K_I$  using Eq. (3.34) and Eq. (3.35).

$$K_I(s) \geq \frac{\sqrt{l}\sigma_c(\hat{s})}{\hat{\sigma}^{\text{cr}}(\hat{s})}, \quad (3.50)$$

$$K_I(s) \geq \sqrt{\frac{G_c(\delta l_{\text{in}})}{-\frac{\Delta \hat{W}^{\text{cr}}}{\delta l_{\text{in}}}}}, \quad (3.51)$$

In this section, the thermoelastic problem is not considered and therefore  $\hat{\sigma}^{\text{te}}(\hat{s})$  and  $\hat{W}^{\text{te}}$  have been omitted from the formulation.

### 3.3.3 The influence of the size of the fiber

Safran requested the study of the influence of two variables, the length  $l$  and diameter  $t$  of the fiber. In the analysis carried out in Section 3.2, when varying the length of the platelet, it also proportionally changes the thickness, according to the shape factor,  $f = l/t$ . The big advantage of that calculation is that with one FEM calculation and a postprocess we could obtain  $K_{\text{IC}}^{\text{app}}$  for any value of  $l$ . However, the individual effect of  $l$  and  $t$  are not observed.

The study of influence of  $t$  keeping  $l$  constant, can be done following the procedure explained in Section 3.1.2, i.e., defining

$$\hat{t} = 1/f, \hat{l} = 1, \hat{e} = 1/f/f_e \quad (3.52)$$

in the inner domain. A change in the shape factor  $f$  would change the diameter of the fiber  $t$  and the length of the microstructure  $\hat{a}_t$ , but would not change the length of the fiber  $l$  and the corresponding dimension  $\hat{a}_l$ . On the other hand, influence of  $l$  is analysed using

$$\hat{t} = 1, \hat{l} = f, \hat{e} = f/f_e. \quad (3.53)$$

and therefore keeping constant  $t$  and  $\hat{a}_t$  when changing  $l$ . Moreover, it is important to highlight that in this study the volume fraction is kept constant and the interphase is considered. Only two toughening mechanisms are analysed in this case, penetration and deflection, and, as it was done in Section 3.2, the predominant mechanism would correspond to the one that is related to the lowest value of the apparent fracture toughness.

Fig.3.59 shows the evolution of the apparent fracture toughness  $K_{IC}^{app}$  with respect  $t$ , where chosen range  $t = 3 - 54 \mu\text{m}$  is based on the provided data in Section 3.3.1. In this case, for very thin fibers it can be observed that penetration governs the failure, whereas when the fiber is thicker the predominant mechanism is deflection. It means that if the fiber is thicker the interphase acts as a mechanical fuse, and the crack is deflected through the interphase. The change from penetration to deflection is produced for  $t$  in the range  $[15 - 25] \mu\text{m}$ . Moreover, a higher diameter means a higher fracture toughness in the composite, being the maximum enhancement obtained  $K_{IC}^{app} = 1.38K_{IC}^m$  for  $t = 54 \mu\text{m}$ , and therefore  $K_{IC}^{app} = 3.34 \text{ MPa m}^{0.5}$ . Notice that for intermediate values of  $t$  it would be difficult to determine a predominant mechanism, and both a penetration and deflection could occur more or less randomly relying small defects.

On the other hand, Fig. 3.60 shows the evolution of  $K_{IC}^{app}$  with respect to the length of the fiber,  $l$ , for two different diameters,  $t = t_{avg} = 16.67 \mu\text{m}$  and  $t = 25 \mu\text{m}$ . The range selected for  $l$  is based on the data provided in Section 3.3.1. First, it can be observed that  $l$  does not change the predominant mechanism, which is penetration for  $t = t_{avg} = 16.67 \mu\text{m}$  and deflection for  $t = 25 \mu\text{m}$ . Therefore, it can be concluded that the predominant mechanism mainly depends on the diameter of the fiber. However,  $l$  does play a role in the value of the apparent fracture toughness, being higher when  $l \approx t$ , i.e., for a shape factor  $f = 1$ . Moreover, it can be observed in Fig. 3.60 that for very long fibers the influence of  $l$  on  $K_{IC}^{app}$  is highly reduced. Interestingly, in the case of  $t = 25 \mu\text{m}$  the apparent fracture toughness for penetration and deflection are very similar when considering very short fibers.

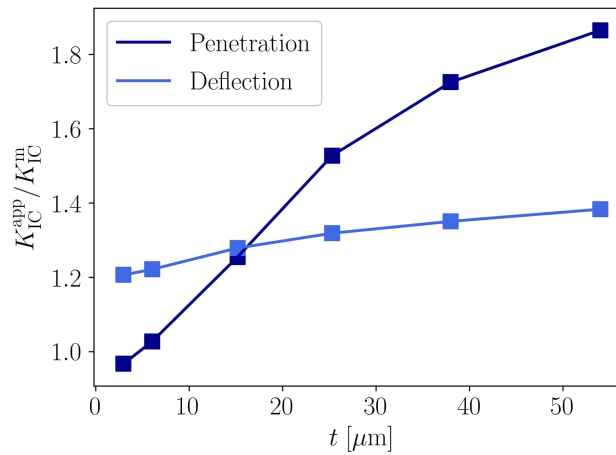


Figure 3.59: Effect of  $t$  on  $K_{IC}^{app}$  for  $V_f = 10\%$  and  $l = 152 \mu\text{m}$ .

As it was mentioned in previous sections, changing  $t$  or  $l$  in this analysis is equivalent to change the shape factor  $f$  in the inner domain. The geometry of the multi-fiber model for a large and a small shape factor ( $f = 50$  and  $f = 1$ ) is shown in Fig. 3.61 and Fig. 3.63b, respectively.

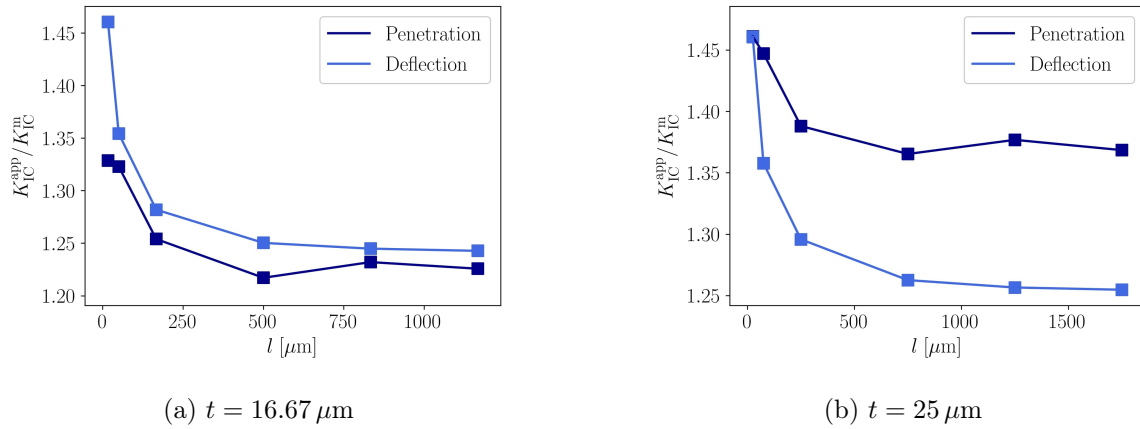


Figure 3.60: Effect of  $l$  on  $K_{IC}^{\text{app}}$  for  $V_f = 10\%$  and two different diameters.

As a conclusion, the diameter plays a major role in the predominant toughening mechanism observed in the composite, although both  $l$  and  $t$  have an influence on  $K_{IC}^{\text{app}}$ , which is increased when  $l$  is close to  $t$ . For this reason, in Fig. 3.62 the evolution of  $K_{IC}^{\text{app}}$  with respect to the size of the fiber for  $f = 1$  ( $t = l$ ) is represented. First, it can be observed that  $K_{IC}^{\text{app}}$  increases with growing  $l$ . Moreover, for small fibers the predominant mechanism is a penetration, whereas for bigger fibers the crack may deflect through the interphase.

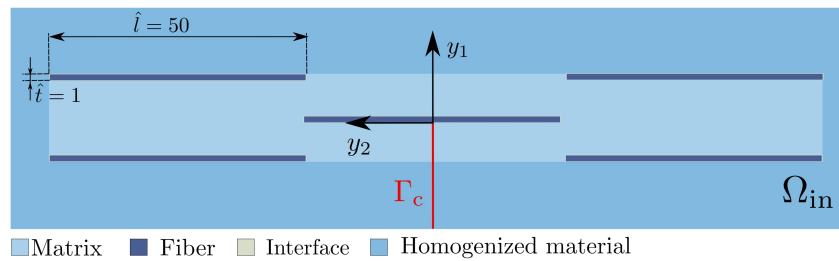


Figure 3.61: Geometry of the inner domain in the multi-fiber model for a great shape factor,  $f = 50$ .

In Fig. 3.62 it can be noted that  $K_{IC}^{\text{app}}$  does not depend on  $t$  for very small fibers, an observation that was also made in Section 3.2. As it was explained before, this is because the energy condition, which does not depend on the size of the fiber, is governing the failure. An example is shown in Fig. 3.63, where the curves of the CC are represented, as well as the deformed shape after the failure. Notice that the crack increment is shorter than the length of the interphase.

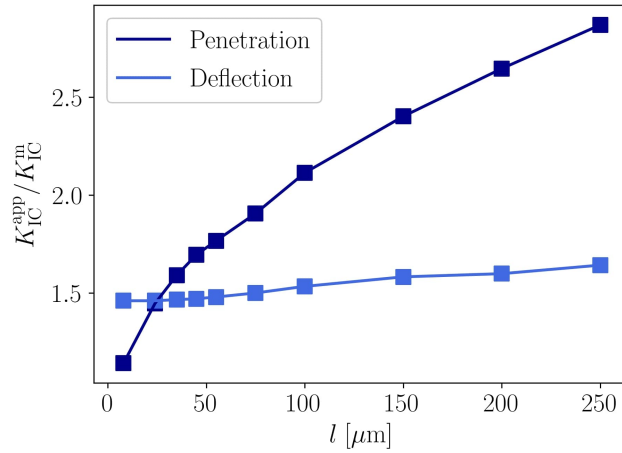
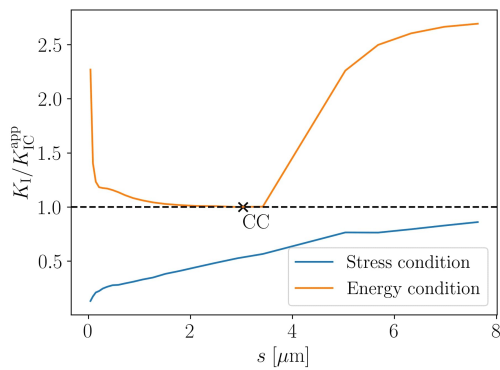
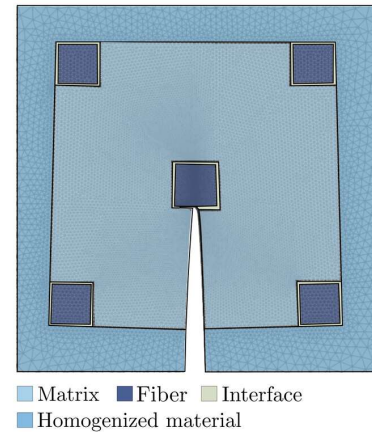


Figure 3.62: Effect of  $l = t$  on  $K_{IC}^{app}$  for  $V_f = 10\%$  and  $f = 1$ .



(a) CC curves



(b) Deformed shape

Figure 3.63: Application of the CC in the case of deflection, for  $V_f = 10\%$ ,  $f = 1$  and  $t = l = 8 \mu\text{m}$ .

When  $t > 25 \mu\text{m}$   $K_{IC}^{app}$  starts increasing with growing  $t$  for deflection, as it can be observed also for penetration. Both situations correspond to conventional cases, where the CC point is the crossing point between the energy condition and the stress condition, as it is shown in Fig. 3.64 and 3.65 for deflection and penetration, respectively. Notice that, due to the small newly created crack length, we have represented only the vicinity of one fiber in the deformed shape, although the multi-fiber model has been applied.

In the following subsections, the shape factor  $f = 1$  will be used to study the influence of other design parameters.

Finally, it is important to highlight that our computational tool assumes plane strain conditions. However, when the shape factor  $f$  is very high the hypothesis might not be true. In this preliminary study we keep the hypothesis of plane strain, understanding that no big differences would be observed if we change to plane stress.

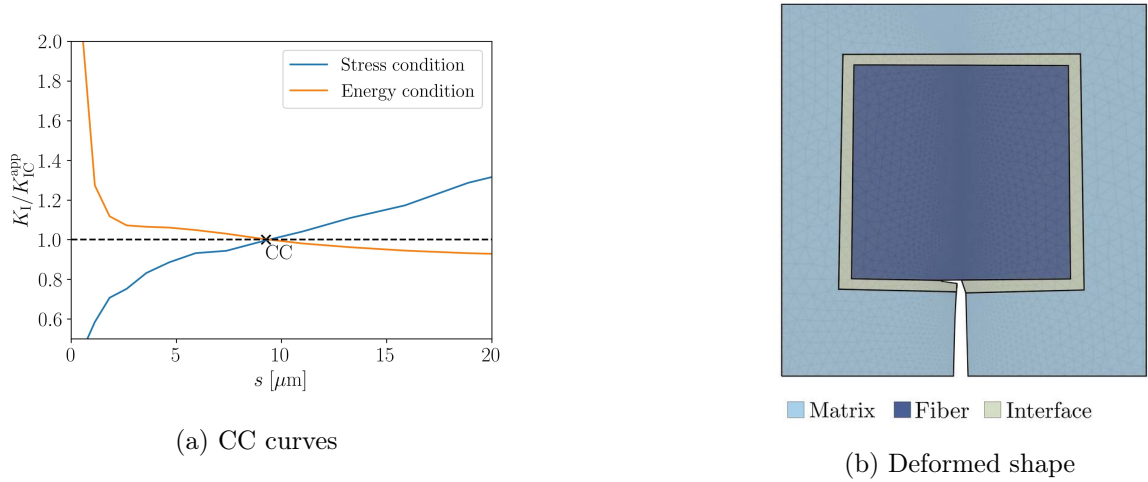


Figure 3.64: Application of the CC in the case of deflection, for  $V_f = 10\%$ ,  $f = 1$  and  $t = l = 100 \mu\text{m}$ . Notice that only the vicinity of one single fiber has been shown for a better representation.

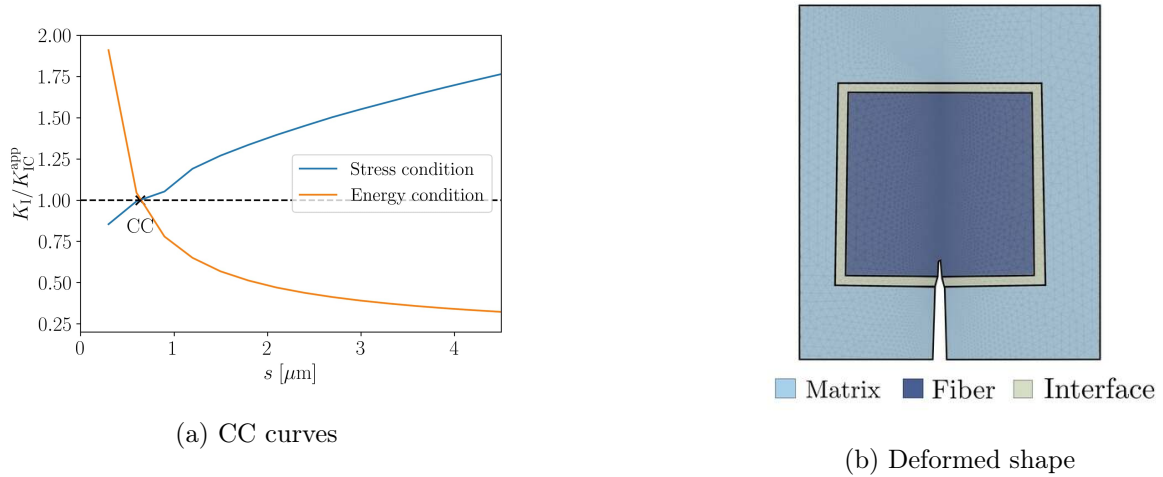


Figure 3.65: Application of the CC in the case of penetration, for  $V_f = 10\%$ ,  $f = 1$  and  $t = l = 100 \mu\text{m}$ . Notice that only the vicinity of one single fiber has been shown for a better representation.

### 3.3.4 Influence of other design parameters

In this section, the influence of other design parameters is studied, such as the fiber volume fraction, the interface effect, and the distance between fibers. Throughout this section, a fiber with  $f = 1$  and  $t = l = 17 \mu\text{m}$  is taken as the object of study. First, Fig. 3.66 shows the influence of  $V_f$  on  $K_{IC}^{\text{app}}$ . The values  $V_f = 5, 10$ , and  $20\%$  correspond to the range obtained statistically in [100]. The value  $V_f = 40\%$  has been proposed to study the effect of saturating the composite with more fibers, although it is purely a numerical model, as it is unknown whether it is feasible to add such a quantity of fibers to the matrix in practice.

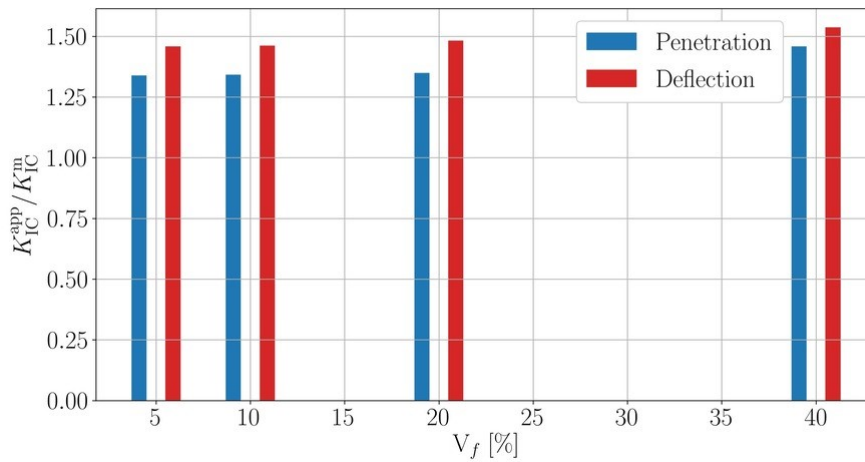


Figure 3.66: Effect of  $V_f$  on  $K_{IC}^{\text{app}}$  for  $t = t_{\text{avg}} = 16.67 \mu\text{m}$  and  $f = 1$ .

For  $V_f = 5 - 20\%$ , there is not much variation in  $K_{IC}^{\text{app}}$ , with a maximum increase of 0.77% for penetration and 1.611% for deflection. However, when considering a higher volume fraction, such as  $V_f = 40\%$ , the fracture toughness of the composite increases 10 times more in penetration and 3 times more in deflection, reaching 8.9% for penetration and 5.37% for deflection. Fig. 3.67 shows the geometry of the multi-fiber model for different values of  $V_f$ . Note that as the volume fraction increases, the distance between fibers decreases.

The influence of the interphase in the composite is studied in Figs. 3.68 and 3.69.  $K_{IC}^{\text{app}}$  is represented as a function of  $t$  for penetration and deflection when there is no interphase in the composite, i.e. a strong interface between the matrix and the fiber is considered. It can be observed that  $K_{IC}^{\text{app}}$  in the case of deflection increases significantly compared to the case where the interphase was included, making penetration the predominant mechanism, regardless of the fiber diameter.

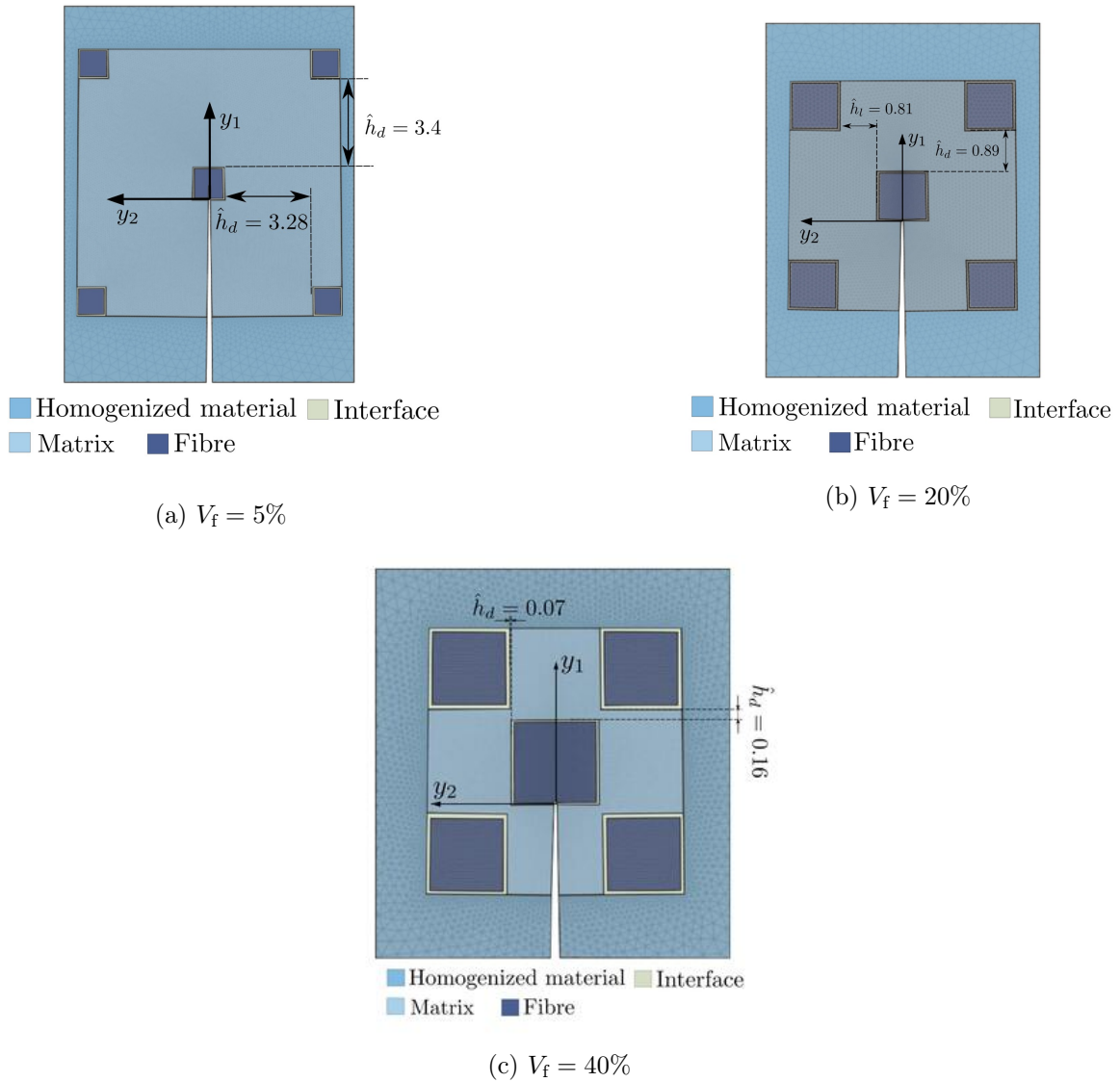


Figure 3.67: Geometries of the multi-fiber model for different volume fraction values.

Therefore, Fig.3.69 represents  $K_{IC}^{app}$  for the cases with and without interphase. For small-diameter fibers, where the predominant mechanism is penetration, there is no difference between the interphase and non-interphase situations. However, for a larger diameter of the fiber,  $K_{IC}^{app}$  is greater in the non-interphase case. This observation seems to be contrary to the ones experimentally measured in [100], as it is shown in Table 3.5. However, the measurement of  $K_{IC}^{app}$  in experiments is based on the total failure of the structure, which is related to the crack propagation until the complete ruin. When the interphase between the fiber and matrix is included, the crack meanders and delays the moment of total failure of the structure, increasing the overall load. This effect can not be captured with our numerical tool, which only measures the interaction between the crack and a single fiber.

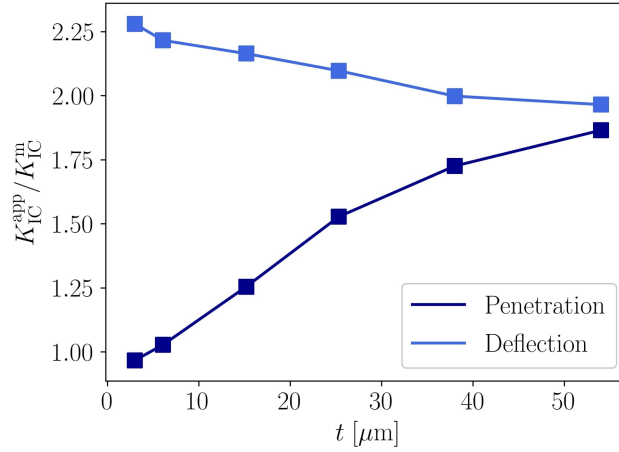


Figure 3.68: Effect of  $t$  on  $K_{\text{IC}}^{\text{app}}$  for  $V_f = 10\%$  and  $l = 152 \mu\text{m}$ , considering no interphase.

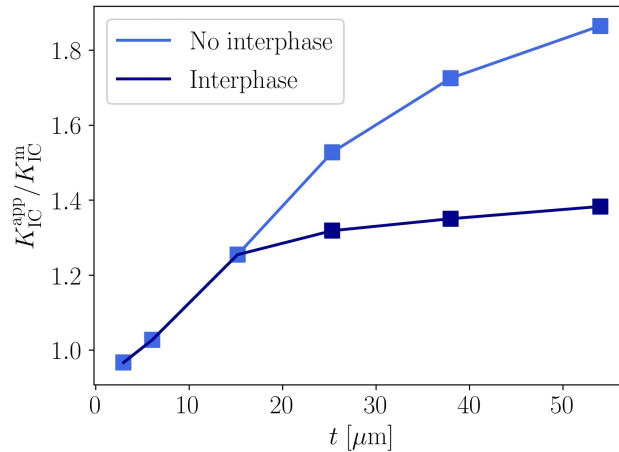


Figure 3.69: Comparison of  $K_{\text{IC}}^{\text{app}}$  with respect to  $t$  with and without the interphase for  $V_f = 10\%$  and  $f = 1$ .

Finally, in Fig. 3.70 the influence of the distance  $h_l$  is analysed. Previously, we have used the minimization of the surface as a criterion to calculate  $h_l$  and  $h_t$  in the heterogeneous microstructure of the inner domain. However, this criterion does not have a physical explanation and may not be representative. For this reason, the influence of the distance between fibers is studied choosing a wide range of  $h_l$  and defining  $h_t$  so that the constraints Eqs. (3.45)-(3.48) are fulfilled. It is observed that for negative values of this distance, which would mean that fibers are interleaved in the microstructure, there is a jump in the fracture toughness.

The fact that an interleaved fiber structure improves the fracture toughness is not a surprising phenomenon. For example, in construction, brick structures often follow a technique called "stretcher bond," where the bricks are interleaved so that the joints do not align, thus improving the strength of the wall.

It is important to note that this effect can only be observed when considering a multi-fiber model and not with the previously presented single fiber model.

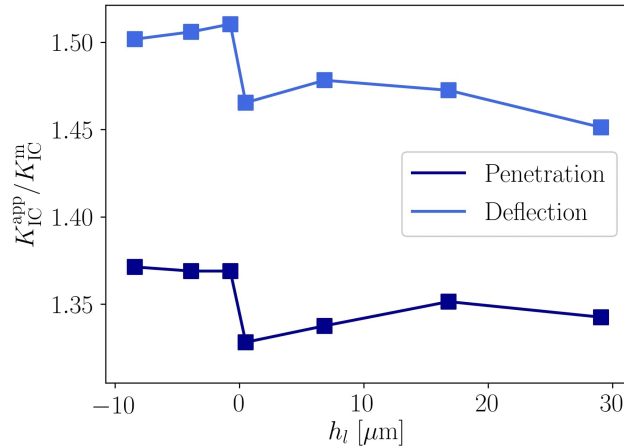


Figure 3.70: Influence of  $h_l$   $K_{IC}^{\text{app}}$  with respect to  $h_l$  for  $V_f = 10\%$ ,  $f = 1$  and  $l = t = 17 \mu\text{m}$ , considering the interphase.

### 3.3.5 Multiple fibers vs single fiber model

In Fig. 3.71,  $K_{IC}^{\text{app}}$  is represented as a function of  $t$  for the multi-fiber model and the single fiber model, for two different values of  $V_f = 10$  and  $40\%$ , considering only the deflection case (similar conclusions are obtained in the penetration case, but have been omitted for the sake of simplicity). For  $V_f = 40\%$ , the maximum difference reaches  $4.15\%$ , greater than for  $V_f = 10\%$ , where the maximum difference is  $1.5\%$ . In other words, the larger the volume fraction, the greater the difference between the two models, although it is not a significant difference.

In general, the difference between the multi-fiber model and the single fiber model will be greater when the neighboring fibers have a greater effect on the central fiber, which is the one directly interacting with the crack. For the same  $V_f$ , a smaller distance between fibers in the multi-fiber model ( $h_l$  and  $h_t$ ) will increase the influence of the neighboring fibers, and therefore the difference between the two models. The latter is clearly exemplified in Fig. 3.71a,  $V_f = 10\%$  and  $l = 152 \mu\text{m}$ , since  $h_l$  and  $h_t$  are reduced for lower values of  $t$ , where the maximum difference between models is found, see Fig. 3.72a.

However, this is not observed in Fig. 3.71b, where it can be seen that the difference between

the two models increases with growing  $t$ . Looking at Fig. 3.72b where  $h_l$  and  $h_t$  are represented, it is observed that although the distance  $h_l$  increases as  $t$  increases, the distance  $h_t$  remains almost constant except for the last point where it is slightly higher. Additionally,  $h_t$  is zero. For this reason, the difference between the two models may be motivated by the diameter of the fibers and their effect on the problem, which will be more pronounced if we consider more fibers.

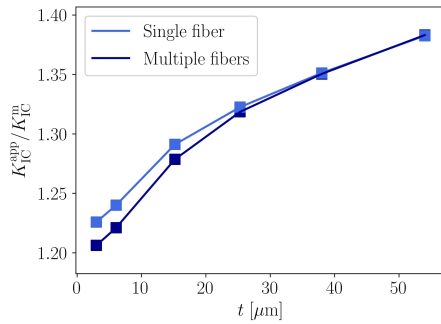
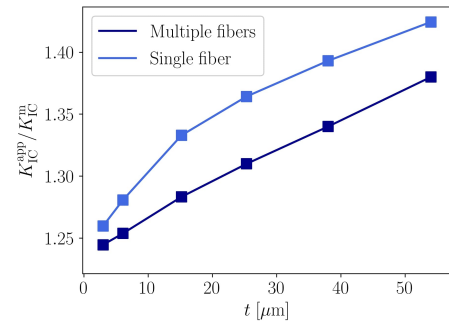
(a)  $V_f = 10\%$ (b)  $V_f = 40\%$ 

Figure 3.71: Comparison between the single fiber and the multi-fiber model in the deflection case, for  $l = l_{avg} = 152 \mu\text{m}$ .

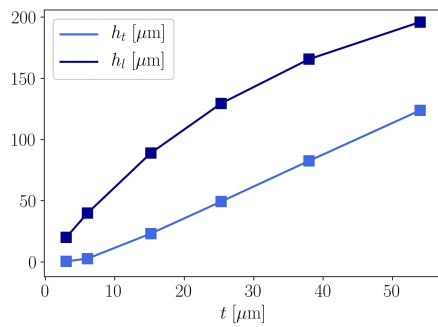
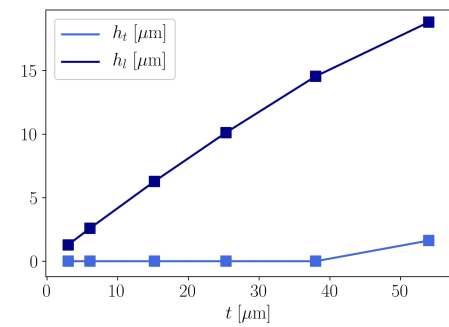
(a)  $V_f = 10\%$ (b)  $V_f = 40\%$ 

Figure 3.72: Evolution of the distances  $h_t$  and  $h_l$  in the multi-fiber model in the deflection case, for  $l = l_{avg} = 152 \mu\text{m}$ .

### 3.3.6 Conclusions

To sum up, the design tool presented in Section 3.1 is applied in this section to an industrial material proposed by Safran. The main objective is to estimate the apparent fracture toughness of the composite and study the influence of various design parameters.

It is difficult to validate this model making a precise comparison with experimental results shown in Table 3.5, because specimens contain fibers of various sizes and aspect ratios. However, looking at Fig. 3.69, the range numerically estimated for  $K_{IC}^{app}$  considering the average  $l_{avg}$ ,  $V_f = 10\%$  and  $t = 3 - 54 \mu\text{m}$ , is

$$K_{IC}^{app} = [2.34 - 4.5] \text{MPa m}^{0.5} \quad \text{with no interphase,} \quad (3.54)$$

$$K_{IC}^{app} = [2.34 - 3.34] \text{MPa m}^{0.5} \quad \text{with interphase,} \quad (3.55)$$

which is similar to the range obtained experimentally without an interphase  $K_{IC}^{app} = [2.8 - 4.4] \text{MPa m}^{0.5}$ , although it is more different to the range obtained in [100] with the interphase,  $K_{IC}^{app} = [3.87 - 6.32] \text{MPa m}^{0.5}$ . The latter might be explained by several reasons, including the fact that dynamic effects of the interface were not considered here, and some of the mechanical properties used in the interphase were the ones of BN instead of PyC, which is the material used in the experiments.

However, qualitative conclusions obtained in experiments are also observed using this computational tool. When considering the interphase, a very small diameter of the fiber results in lower  $K_{IC}^{app}$ , and the failure mechanism is penetration. However, when fibers have larger  $t$ , they are more robust and difficult to penetrate, resulting in higher  $K_{IC}^{app}$ , and the failure mechanism is deflection, allowing the interface to act as a mechanical fuse. This would explain why experimental observations show fiber deflection when an interphase is present, since the diameter used is sufficiently large to favor this mechanism, according to our numerical estimations.

Moreover,  $K_{IC}^{app}$  can be increased when  $l \approx t$ , referred as short fibers. For a square fiber, the highest values of  $K_{IC}^{app}$  is obtained. This type of square fiber structure is found in the Nickel-Based Superalloy, which commonly applied in advanced turbine engines [103].

The volume fraction of fibers does not have a significant influence within the studied range, although it can considerably increase  $K_{IC}^{app}$  when higher values, such as  $V_f = 40\%$ , are considered. On the other hand, when the interphase is removed, penetration becomes the predominant damage mechanism, regardless the fiber size, as observed experimentally. Finally, the intercalation of fibers also has an effect on  $K_{IC}^{app}$ , which increases approximately 4% when  $h_l$  is negative.

There is not a significant difference between the multi-fiber and the single fiber model. That is why, for general estimations, the use of the single fiber model is proposed as it has a lower computational complexity. For the same level of refinement, it requires approximately half of the number of elements. However, this model does not consider the influence of certain phenomena such as the fiber intercalation. Therefore, the multi-fiber model could be used when more specific studies are required.



# Chapter 4

## Conclusions and further studies

In this PhD thesis numerical modelling tools in fracture mechanics have been applied for predicting crack nucleation and growth in advanced ceramics, with a special emphasis in the relationship between the micro and macro-scale characteristics within these materials. Two approaches have been followed: the Coupled Criterion (CC) within the Finite Fracture Mechanics (FFM) framework and the Phase Field (PF) model for fracture.

From the CC perspective there is a nucleation length proportional to the Irwin length. From the point of view of the PF model for brittle fracture, there is a phase field length scale. Both length parameters depend on the Irwin length, an intrinsic mechanical property of the material. At the macro-scale, this length is small compared to any dimension of the structure while at the micro-scale, it is of the same order of magnitude or even larger and can interact with the dimensions of the structure. Throughout Chapter 2, the answer brought by these two methodologies has been analysed and reasonably compared in ceramics at the micro-scale, to determine their similarities and differences.

First, the Coupled Criterion at the micro-scale must be used in its FFE form because the necessary condition of the asymptotic approach is no longer fulfilled. This prevents to use analytical formulas based on Williams' expansion. Moreover, the CC allows to show that the apparent strengthening observed in experiments conducted at the micro-scale is due to a lack of available energy as a consequence of the small size of samples. Accordingly, tests are often weakly or even totally insensitive to the tensile strength whereas they are sensitive to the fracture energy. In addition, in bending tests, the smaller the samples, the larger the stress gradient, leads to a similar apparent strengthening. The size of the specimen also modifies the influence of other parameters, such as the notch blunting or the loading mode (DC or FC).

On the other hand, using the PF model for brittle fracture it is possible to observe a strengthening effect in bending tests of ceramics at the micro-scale, explained by the dissipation of damage when descending the scales. As it was mentioned above, the control parameter in this study is the relation between the Irwin length and the dimensions of the specimen (at the micro-scale they are of the same order). To reinforce this idea, the analysis was conducted

changing the Irwin length and keeping constant the scale of the specimen. When the Irwin length is of the order of the dimensions of the specimen, the PF model no longer defines a Griffith-like crack, but a damage region, and this leads to a strengthening effect.

Differences and similarities were found when comparing the results obtained by the CC and the PF model. When the Irwin length is much smaller than the dimensions of the specimen, there is a good agreement between both methodologies. However, when the Irwin length can interact with the dimensions of the specimen the PF model no longer predicts a Griffith-like fracture, and the dissipation of damage increases the difference between results brought by the CC and the PF model for brittle fracture. Moreover, the same qualitative conclusions about the influence of fracture properties have been found using the CC and the PF model. When the Irwin length is of the order of the dimensions of the specimen, crack nucleation is almost insensitive to the tensile strength.

The analysis made in Chapter 2 would help to better describe ceramic materials at the micro-scale, and therefore to enhance the design of advanced ceramics, which is commonly based on changing the micro-structure of classical ceramics to generate new materials with improved mechanical properties. One type of these new structures was deeply studied in Chapter 3, made of brittle matrices reinforced by short fibers or platelets. They were analysed using numerical techniques that avoid the controversial conclusions obtained about fracture properties when descending the scales in ceramics.

Two examples of application have been presented in Chapter 3, analysing the influence of several design parameters. The study was complemented by a comparison with experiments in each case. The first material considered is the borosilicate glass reinforced by alumina platelets. The following list summarizes the main conclusions obtained:

- **Size of the platelet:** a size effect in the apparent fracture toughness is clearly observed. When residual stresses are not considered, the longer the platelet, the greater its toughness. However, when including the thermoelastic effect, longer platelets leads to a breakage after cooling down.

The size of the platelet plays also a role on the newly created crack length (in the framework of FFM). If the platelet is short, the crack evolves in an unstable manner joining the glass region beyond the platelet, whereas if it is long, the crack increment remains inside the platelet, or along the interface glass alumina.

- **Alumina fracture properties:** It can be concluded that the fracture toughness of alumina has a greater influence on the apparent fracture toughness of the composite than the tensile strength of alumina.
- **Residual stresses:** It is not a general rule that they are a toughening mechanism. It depends on the size of the platelet and the change in temperature after cooling. The

main parameter that explains why an enhancement of the apparent fracture toughness of the composite can be observed is the negative GSIF (or its counterpart in the complex case) related to the thermoelastic problem, since it is related to a compression at the crack-tip, that must be overcome for crack propagation. Moreover, residual stresses promote the lateral decohesion at the end of the platelet as a predominant failure mechanism in the composite. The effect of residual stresses is so high that the decohesion mechanism at the end of very long platelets can occur during cooling prior to any mechanical loading.

- **Volume fraction:** it has a positive scaling effect on the apparent fracture toughness of the composite. When the concentration of alumina is increased the deflection mechanism is promoted as a failure mechanism if the alumina fracture properties are great enough, otherwise penetration is the governing mechanism. At the scale of experiments the volume fraction has a bigger influence on the apparent fracture toughness than residual stresses, whose effect is very weak.

The same design tool was also applied to an industrial material proposed by Safran: a ceramic matrix composite with short fibers. The material was studied with and without an interphase between the fiber and matrix. The effect of geometrical parameters (the length and diameter of the fiber, the distance between fibers...) were analysed using two different models: a multi-fiber and a single-fiber model. As a general conclusion, a configuration with a shape factor close to unity was proposed to optimize the apparent fracture toughness of the composite.

To sum up, a design tool for platelets and short fibers composites is presented in this PhD thesis. Two key novelties stand out from this methodology. First, it is a design tool in which multiple combinations are possible by modifying the input parameters of the composite, and therefore optimizing the design. Second, it offers the possibility to carry out a separate study of the different factors that are related to the fracture toughness: geometrical factors, such as the volume fraction, the size and the orientation of the platelet, or environmental factors, in particular the effect of residual stresses and the change in the pre-existing crack path. Furthermore, this design tool seems to have an important reduction in the computational complexity with respect to other analysis found in the literature.

Some studies are proposed for the future.

First, the CC is a simple formulation to get data. However, throughout this PhD thesis countless cases have been analysed, and for some of them finding the solution can have an excessive computational complexity. The application of some machine learning techniques to reduce this computational complexity is proposed. Moreover, since the CC formulation is easy to implement, this criterion could be used together with artificial intelligence to generate a data base that can be used for virtual certification. The latter has already been proposed by Prof. Pedro Camanho in one of the plenary sessions of the European Conference on Fracture [104], named as "Prediction of fracture of polymer composite materials across different length scales".

In Chapter 2 a reasoned comparison between CC and PF model has been made. For the future, the consideration of more experiments and different problems to reinforce this comparison are proposed. In particular, it could be interesting to study how these models behave when studying heterogeneous structure. This was already started in Chapter 3 with the CC, but it is proposed to apply the PF model. The combination of Phase Field together with the Matched Asymptotics Approach could be an interesting proposal to reduce the computational complexity of the model.

All the models studied in this PhD thesis are limited by 2D elasticity. The correct extension of these methodologies to 3D is also proposed. For example, in Chapter 3, when considering composites with short fibers, the assumption of 2D elasticity might not be appropriated and accuracy might be lost in the numerical estimations, although a first approximation can be given applying our design tool.

# Chapter 5

## Appendices

### Contents

---

5.1	Terms in Williams' expansion . . . . .	136
5.2	Generalized stress intensity factors (GSIFs) . . . . .	136
5.3	Calculation of the dimensionless coefficient $A^*$ . . . . .	137
5.4	Codes developed . . . . .	138

---

In this appendix, additional and complementary information to the previously described results is included. Furthermore, the main codes developed in this thesis are explained in detail.

## 5.1 Terms in Williams' expansion

Assuming that there are no volume forces in the domain, the Beltrami-Michell equation is  $\sigma_{\alpha\alpha,\beta\beta} = 0$ . Consequently, the displacement field  $\underline{U}(r, \theta)$  in the neighborhood of the singularity generated by a re-entrant corner is described through the so-called Williams' expansion [51],

$$\underline{U}(r, \theta) = \underline{U}(0, 0) + Kr^\lambda \underline{u}(\theta) + \dots \quad (5.1)$$

where  $K$  is the Generalized Stress Intensity Factor (GSIF),  $\underline{U}(0, 0)$  is the rigid displacement of the origin set at the tip of the notch,  $(x_1, x_2)$  are the Cartesian coordinates and  $(r, \theta)$  the polar ones, see Fig. 5.1.

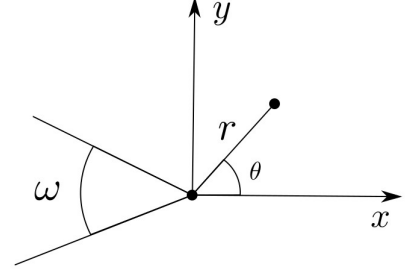


Figure 5.1: V-notch in the MA approach.

The exponent  $\lambda$  and the associated shape function  $\underline{u}(\theta)$  form the par eigenvalue-eigenfunction of a specific problem, and can be numerically obtained [86]. Noteworthy, for an isotropic homogeneous material it is possible calculate the analytical expression of  $\lambda$  and  $\underline{u}(\theta)$  [105] using the following eigenequation in the symmetric mode of the solution,

$$\sin [(2\pi - \omega)\lambda] + \lambda \sin [2\pi - \omega] = 0. \quad (5.2)$$

The symmetric displacement mode  $r^\lambda \underline{u}(\theta) = r^\lambda [u_x(\theta), u_y(\theta)]$  depends on the angle  $\omega$  and material properties. Assuming plane strain conditions, expressions are

$$u_x(\theta) = \frac{1}{2\mu} [(C(3 - 4\nu + \lambda) - (\lambda + 1)) \cos(\lambda\theta) - 2\lambda C \cos\theta \cos[(\lambda - 1)\theta]], \quad (5.3)$$

$$u_y(\theta) = \frac{1}{2\mu} [(C(3 - 4\nu + \lambda) + (\lambda + 1)) \sin(\lambda\theta) - 2\lambda C \sin\theta \cos[(\lambda - 1)\theta]], \quad (5.4)$$

where  $C = -\frac{(\lambda+1) \sin[(\lambda+1)(\pi-\frac{\omega}{2})]}{(\lambda-1) \sin[(\lambda-1)(\pi-\frac{\omega}{2})]}$ . In the same way, symmetric stresses mode  $r^{\lambda-1} \underline{s}(\theta)$  is expressed in polar coordinates

$$s_{rr}(\theta) = -\lambda(\lambda + 1) \cos[(\lambda + 1)\theta] + C\lambda(3 - \lambda) \cos[(\lambda - 1)\theta], \quad (5.5)$$

$$s_{\theta\theta}(\theta) = \lambda(\lambda + 1) [\cos[(\lambda + 1)\theta] + C \cos[(\lambda - 1)\theta]], \quad (5.6)$$

$$s_{r\theta}(\theta) = \lambda [(\lambda + 1) \sin[(\lambda + 1)\theta] + (\lambda - 1)C \sin[(\lambda - 1)\theta]], \quad (5.7)$$

## 5.2 Generalized stress intensity factors (GSIFs)

Generalized stress intensity factors (GSIFs) in the elastic solution of a re-entrant corner with free boundaries are calculated using a non-independent path integral on an arbitrary contour  $\Gamma$  (see Fig. 5.2 for an example), see [86]. Therefore,  $K$  is expressed as

$$K = \frac{\Phi(\underline{U}, r^{-\lambda} \underline{u}^-(\theta))}{\Phi(r^\lambda \underline{u}(\theta), r^{-\lambda} \underline{u}^-(\theta))} \quad (5.8)$$

where  $r^{-\lambda}\underline{u}^-(\theta)$  corresponds to the dual mode of  $r^\lambda\underline{u}(\theta)$  (see appendix 5.1 for expressions), and  $\underline{U}$  is the finite element approximation of the elastic solution. The integral  $\Phi(\underline{A}, \underline{B})$  is defined as

$$\Phi(\underline{A}, \underline{B}) = \frac{1}{2} \int_{\Gamma} [\underline{\sigma}(\underline{A}) \cdot \underline{n} \cdot \underline{B} - \underline{\sigma}(\underline{B}) \cdot \underline{n} \cdot \underline{A}] ds, \quad (5.9)$$

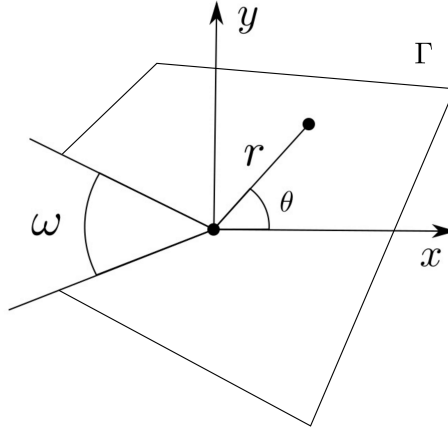


Figure 5.2: Example of a closed path

### 5.3 Calculation of the dimensionless coefficient $A^*$

The coefficient  $A^*$  is used in Section 1.2.1.2 to apply the CC together with the MAE in a V-notched specimen of angle  $\omega$  assuming that  $\delta l$  is small compared to the notch depth. This coefficient is calculated in the inner problem, see Fig. 5.3, in which a huge external radius  $R$  is set to represent an unbounded domain. At  $r = R$  the displacement field  $\rho\underline{u}(\theta)$  defined in Annex 5.1 is prescribed as a displacement boundary condition.

Notice that symmetry conditions have been applied in the V-notched specimen. The numerical solution of this problem is names as  $\underline{V}_1(y_1, y_2)$  Applying the path independent integral defined in (5.9) along a close path  $\Gamma_1$  the coefficient  $A$  is determined.

$$A = 2\Phi(\underline{V}_1(y_1, y_2), r^\lambda\underline{u}(\theta)) \quad (5.10)$$

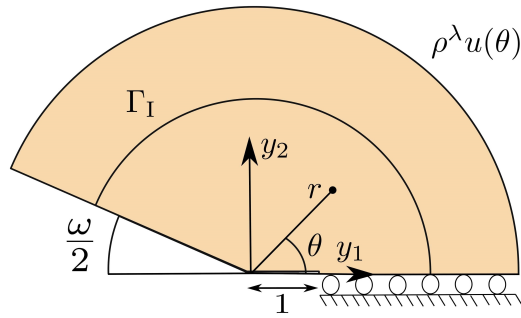


Figure 5.3: Scheme of the inner problem in a V-notched specimen when applying the CC together with MAE. Symmetry conditions have been applied

## 5.4 Codes developed

### 5.4.1 Automatic algorithms for the application of the CC

When applying the CC, the main objective is to find the minimum load for which both the stress (1.9) and the energy conditions (1.8) are fulfilled. In some cases, as the one presented in Chapter 3 where MAE was applied, the result of the CC is not the load, but the apparent fracture toughness of the composite, see (3.34) and (3.35).

Two algorithms are developed and compared in this section. The first algorithm, explained in Section 5.4.1.1, is an iterative process based on the determination of critical points on curves  $\bar{\sigma}$  and  $\bar{G}_{inc}$  that can potentially be the points where the CC is verified: the cross points between the two curves, a relative minimum in  $\bar{\sigma}$  and a relative maximum in  $\bar{G}_{inc}$ .

The main advantage of the first algorithm is the low computational complexity and the high accuracy of results, with 5 – 6 iterations the solution is found accounting for tolerances of the order of  $10^{-6}$ . However, the main drawback is the fact that it is based on the existence of at least one of these specific points. If such points are not identified, a different procedure might be used. For this reason, a second algorithm, explained in Section 5.4.1.2, is developed. It has higher a computational complexity and lower accuracy, but it is valid for any possible case of the CC. We propose the use of both algorithms, the first one would be valid in most of the cases studied, whereas the second one would be used when no critical points are identified or the curves are too complex (several relative extremes or cross points...). It is important to highlight that algorithm 1 is explained in this section for a pure mechanical problem whereas algorithm 2 is prepared for a thermomechanical problem (see Chapter 3).

The inputs needed are:

- The arc length vector that defines the expected crack path  $s$ .
- The vector of tensile stress  $\sigma$ , evaluated at each point along the expected crack path,  $s$ . Notice that if a thermomechanical problem is considered, it is necessary to introduce

$\sigma^{\text{cr}}$  and  $\sigma^{\text{te}}$  for the mechanical and the thermoelastic solution, respectively.

- The vector of incremental energy release rate  $G_{\text{inc}}$ , evaluated at each point of  $s$ . As mentioned above for the stress function, if a thermomechanical problem is considered, it is necessary to introduce  $G_{\text{inc}}^{\text{cr}}$  and  $G_{\text{inc}}^{\text{te}}$ .
- Vector of fracture properties  $\sigma_c$  and  $G_c$  at each point of the expected crack path  $s$ .

In this PhD thesis, vectors  $\sigma$  and  $G_{\text{inc}}$  are obtained using FEM with FEniCS or FEniCSx software [106]. The vectors are calculated for a unitary load under displacement control. Then, if force control is being under study, the correct changes explained in Section 2.2.2 are made before applying the CC algorithm.

Both algorithms are based on the same iterative process. At each iteration  $n + 1$ , two vectors are calculated using previous solution at iteration  $n$

$$\bar{\sigma}^{(n+1)} = \frac{(\Delta^{(n)}\sigma^{\text{cr}} + \sigma^{\text{te}})}{\sigma_c}, \quad \bar{G}_{\text{inc}} = \frac{(\Delta^{(n)2}G_{\text{inc}}^{\text{cr}} + G_{\text{inc}}^{\text{te}})}{G_c} \quad (5.11)$$

where  $\Delta^{(0)} = 1$ . We look for the minimum value of  $\Delta$  for which the CC is fulfilled, named here as  $\Delta_c$ . Thus, the outputs of these codes are  $\Delta_c$  and the newly created crack length  $\delta l$ , highlighted in graphics using the CC point, i.e., when  $s = \delta l$ . Noteworthy, the difference between algorithms 1 and 2 is how  $\Delta^{(n)}$  is calculated in the recursive process.

The codes are updated in the following webpage [https://newfrac.github.io/fenicsx-fracture/notebooks/coupled-criterion/Coupled\\_Criterion.html](https://newfrac.github.io/fenicsx-fracture/notebooks/coupled-criterion/Coupled_Criterion.html).

#### 5.4.1.1 Algorithm 1: based on critical points

As it was mentioned before, this algorithm is an iterative process. At each iteration  $n$  we look for the following critical points in vectors  $\bar{\sigma}^{(n)}$  and  $\bar{G}_{\text{inc}}^{(n)}$ : cross points between the two vectors, a relative minimum point in  $\bar{\sigma}^{(n)}$  or a relative maximum point in  $\bar{G}_{\text{inc}}^{(n)}$ . By analysing these points, a certain scenario is identified, as it is explained in the following subsections, and the fulfillment of the CC is verified under a certain tolerance,  $\text{Tol} = 10^{-6}$ . If the CC conditions are not verified, another iteration is added and the dimensionless vectors  $\bar{\sigma}^{(n+1)}$  and  $\bar{G}_{\text{inc}}^{(n+1)}$  are updated applying (5.12), that can be expressed for as

$$\bar{\sigma}^{(n+1)} = \Delta^{(n)}\sigma \oslash \sigma_c, \quad \bar{G}_{\text{inc}} = \Delta^{(n)2}G_{\text{inc}} \oslash G_c, \quad (5.12)$$

if a pure mechanical problem is considered. Moreover, it is important to highlight that if several cross points or relative extremes are present in the input vectors, only the ones related to the minimum  $s$  are considered.

Below the pseudocode of algorithm 1 is shown. A maximum number of 200 iterations is set to avoid infinite calculations.

**Define**  $N_{\text{iter}}, \text{Tol}$

**Initiate variables**  $\text{Flag} = 0$ ,  $n = 0$ ,  $\bar{\sigma}_0 = \sigma \otimes \sigma_c$ ,  $\bar{G}_{\text{inc}} = G_{\text{inc}0} \otimes G_c$

**While**  $\text{Flag} == 0$  **and**  $n < N_{\text{iter}}$

**Update**  $n = n + 1$

**Update**  $\bar{\sigma} = \Delta \bar{\sigma}_0$ ,  $\bar{G}_{\text{inc}} = \Delta^2 \bar{G}_{\text{inc}0}$

**If** there is a cross point  $s_{\text{cp}}$

**If**  $\bar{\sigma}|_s \geq \bar{\sigma}|_{s_{\text{cp}}}$  **and**  $\bar{G}_{\text{inc}}|_s \leq \bar{G}_{\text{inc}}|_{s_{\text{cp}}}$  **for**  $s \in [0, s_{\text{cp}}]$

(Scenario 1.A)

**If**  $|\bar{G}_{\text{inc}}|_{s_{\text{cp}}} - 1| \leq \text{Tol}$

$\Delta_c = \Delta$ ,  $\text{Flag} = 1$

**Else**

$$\Delta = \frac{1}{\sqrt{|\bar{G}_{\text{inc}}|_{s_{\text{cp}}}|}}$$

**EndIf**

**ElseIf**  $\exists s_{\text{min}} < s_{\text{cp}}$  in  $\bar{\sigma}$  **and**  $\bar{G}_{\text{inc}}|_{s_{\text{min}}} < \bar{\sigma}|_{s_{\text{min}}}$

(Scenario 1.B.1)

**If**  $|\bar{\sigma}|_{s_{\text{min}}} - 1| \leq \text{Tol}$

$\Delta_c = \Delta$ ,  $\text{Flag} = 1$

**Else**

$$\Delta = \frac{1}{|\bar{\sigma}|_{s_{\text{min}}|}},$$

**EndIf**

**ElseIf**  $\exists s_{\text{max}} < s_{\text{cp}}$  in  $\bar{G}_{\text{inc}}$  **and**  $\bar{\sigma}|_{s_{\text{max}}} > \bar{G}_{\text{inc}}|_{s_{\text{max}}}$

(Scenario 1.B.2)

**If**  $|\bar{G}_{\text{inc}}|_{s_{\text{max}}} - 1| \leq \text{Tol}$

$\Delta_c = \Delta$ ,  $\text{Flag} = 1$

**Else**

$$\Delta = \frac{1}{\sqrt{|\bar{G}_{\text{inc}}|_{s_{\text{max}}|}}$$

**EndIf**

**EndIf**

**ElseIf**  $\exists s_{\text{min}}$  in  $\bar{\sigma}$  **and**  $\bar{G}_{\text{inc}}|_{s_{\text{min}}} < \bar{\sigma}|_{s_{\text{min}}}$

(Scenario 2.A)

**If**  $|\bar{\sigma}|_{s_{\text{min}}} - 1| \leq \text{Tol}$

$\Delta_c = \Delta$ ,  $\text{Flag} = 1$

**Else**

$$\Delta = \frac{1}{|\bar{\sigma}|_{s_{\text{min}}|}},$$

**EndIf**

**ElseIf**  $\exists s_{\max}$  in  $\bar{G}_{\text{inc}}$  **and**  $\bar{\sigma}|_{s_{\max}} > \bar{G}_{\text{inc}}|_{s_{\max}}$   
 (Scenario 2.B)

**If**  $|\bar{G}_{\text{inc}}|_{s_{\max}} - 1| \leq \text{Tol}$   
 $\Delta_c = \Delta, \quad \text{Flag} = 1$

**Else**  
 $\Delta = \frac{1}{\sqrt{|\bar{G}_{\text{inc}}|_{s_{\max}}|}}$

**EndIf**

**EndIf**

**EndWhile**

### Scenario 1: There is a cross point

The cross point  $s_{\text{cp}}$  between the two curves  $\bar{\sigma}^{(n)}$  and  $\bar{G}_{\text{inc}}^{(n)}$  is a critical point that might governs crack nucleation. Different scenarios can be analysed if there is a cross point.

#### Scenario 1.A. : The cross point might governs crack nucleation

This is the simplest scenario of the CC, and is applied when

$$\bar{\sigma}^{(n)}|_s \geq \bar{\sigma}^{(n)}|_{s_{\text{cp}}}, \quad \text{and} \quad \bar{G}_{\text{inc}}^{(n)}|_s \leq \bar{G}_{\text{inc}}^{(n)}|_{s_{\text{cp}}} \quad \text{for } 0 \leq s \leq s_{\text{cp}}, \quad (5.13)$$

If this case is found at iteration  $n$ , a residual is compared to a certain tolerance

$$|\bar{G}_{\text{inc}}^{(n)}|_{s_{\text{cp}}} - 1| \leq \text{Tol}, \quad (5.14)$$

to verify if the CC is fulfilled. If not, a new iteration  $n+1$  is needed, and  $\Delta^{(n+1)}$  is calculated as

$$\Delta^{(n+1)} = \frac{1}{\sqrt{|\bar{G}_{\text{inc}}^{(n)}|_{s_{\text{cp}}|}}, \quad (5.15)$$

Since  $\bar{\sigma}^{(n)}$  and  $\bar{G}_{\text{inc}}^{(n)}$  are a set of discrete values that depends on the mesh used, it is more than common that the cross point does not coincide with one of the elements in these vectors. In that case, it is possible to find the interval  $[s_i, s_{i+1}]$  in which  $s_{\text{cp}}$  is located, and then to determine through interpolation  $s_{\text{cp}}$  and the corresponding  $\bar{\sigma}^{(n)}|_{s_{\text{cp}}}$  and  $\bar{G}_{\text{inc}}^{(n)}|_{s_{\text{cp}}}$ . Hence, an accurate solution to the algorithm in this scenario is obtained.

An example can be observed in Fig. 5.4. One of the problems solved in Chapter 3 has been selected, the case of  $\alpha = 0^\circ$ ,  $l = 100 \mu\text{m}$ ,  $\Delta\theta = 0^\circ$  and  $V_p = 0\%$ , where it is indicated the number of iterations needed in the algorithm,  $n = 7$ . In this example, the CC is fulfilled with a tolerance lower than  $10^{-16}$ . Notice that the CC point denotes the newly created crack length, and in this case it is equal to the cross point.

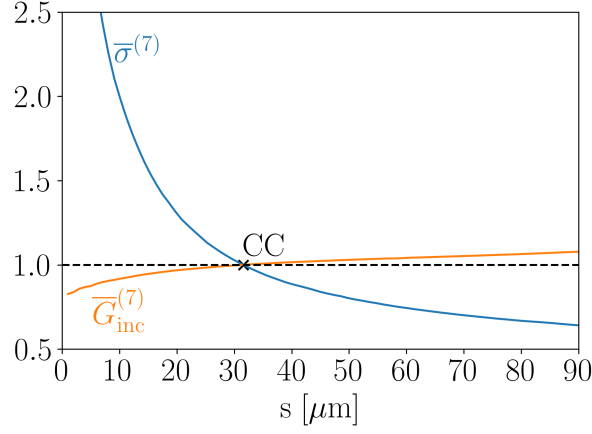


Figure 5.4: Example of the application of the algorithm 1, in the scenario 1.A. Case  $\alpha = 0^\circ$ ,  $l = 100 \mu\text{m}$ ,  $\Delta\theta = 0 K$  and  $V_p = 0\%$ .

### Scenario 1.B. : The cross point might not governs crack nucleation

If the cross point is not governing crack nucleation ((5.13) is not fulfilled), a relative minimum in  $\bar{\sigma}^{(n)}$  and maximum in  $\bar{G}_{\text{inc}}^{(n)}$  must be analysed. Notice that here we are not considering relative maximum points in  $\bar{\sigma}^{(n)}$  or minimum points in  $\bar{G}_{\text{inc}}^{(n)}$ . This is a simplification, based on the idea that normally there is only one relative extreme in these vectors, and the global tendency of  $\bar{\sigma}^{(n)}$  and  $\bar{G}_{\text{inc}}^{(n)}$  is generally decreasing and increasing, respectively. Moreover, if there are several relative extremes in  $\bar{\sigma}^{(n)}$  or  $\bar{G}_{\text{inc}}^{(n)}$  we take the one related to the lowest value of  $s$ .

#### Scenario 1.B.1. : There is a local minimum in $\bar{\sigma}^{(n)}$ and it might governs crack nucleation

If the condition over  $\bar{\sigma}^{(n)}$  in (5.13) is not fulfilled we look for the existence of relative minimum points in  $\bar{\sigma}^{(n)}$  along the interval  $[0, s_{\text{cp}}]$ , by checking if there is a point denoted as  $s_{\text{min}}$  where the derivative of  $\bar{\sigma}^{(n)}$  changes its sign from negative to positive. If so, the condition

$$\bar{G}_{\text{inc}}^{(n)}|_{s_{\text{min}}} < \bar{\sigma}^{(n)}|_{s_{\text{min}}} \quad (5.16)$$

is studied to assume that  $s_{\text{min}}$  might be governing the CC. Remember that if several relative extremes are present, only the one related to the smallest  $s$  is considered. In that case, the following residual is compared to a certain tolerance to verify the CC conditions.

$$|\bar{\sigma}^{(n)}|_{s_{\text{min}}} - 1| \leq \text{Tol}. \quad (5.17)$$

If this is not verified, a new iteration  $n + 1$  is needed, and  $\Delta^{(n+1)}$  is calculated as

$$\Delta^{(n+1)} = \frac{1}{|\bar{\sigma}^{(n)}|_{s_{\text{min}}}|}, \quad (5.18)$$

A more accurate calculation of  $s_{\min}$  would imply the interpolation in the interval where this minimum point is located in the discrete vector  $s$ , as it was explained for the cross point. However, for the calculation of  $s_{\min}$ , the interpolation is not necessary since the curves are normally smooth, and the value estimated from the discrete vector provided as an input is a good approximation. The same happens with the following scenario 1.B.2., and the maximum point in the energy condition curve.

**Scenario 1.B.2. : There is a local maximum in  $\bar{G}_{\text{inc}}^{(n)}$  and it might governs crack nucleation**

If the condition over  $\bar{G}_{\text{inc}}^{(n)}$  in (5.13) is not fulfilled we look for the existence of a relative maximum point in  $\bar{G}_{\text{inc}}^{(n)}$  along the interval  $[0, s_{\text{cp}}]$ , by checking if there is a point denoted as  $s_{\text{max}}$  where the derivative of  $\bar{G}_{\text{inc}}^{(n)}$  changes its sign from positive to negative. If so, the condition

$$\bar{\sigma}^{(n)}|_{s_{\text{max}}} > \bar{G}_{\text{inc}}^{(n)}|_{s_{\text{max}}} \quad (5.19)$$

is necessary to consider that  $s_{\text{max}}$  might be the CC point. In that case, the following residual is compared to a certain tolerance to verify the CC conditions.

$$|\bar{G}_{\text{inc}}^{(n)}|_{s_{\text{max}}} - 1| \leq \text{Tol}. \quad (5.20)$$

If this is verified, the CC is fulfilled. If not, a new iteration  $n + 1$  is needed, and  $\Delta^{(n+1)}$  is calculated using (5.15).

An example can be observed in Fig. 5.5. The problem is selected from Chapter 3, the case of  $\alpha = 0^\circ$ ,  $d = 10 \mu\text{m}$ ,  $\Delta\theta = 0^\circ$  and  $V_p = 0\%$ . In the graphic it is indicated the number of iterations needed in the algorithm,  $n = 4$ . In this example, the CC is fulfilled with a tolerance lower than  $3 \cdot 10^{-16}$ .

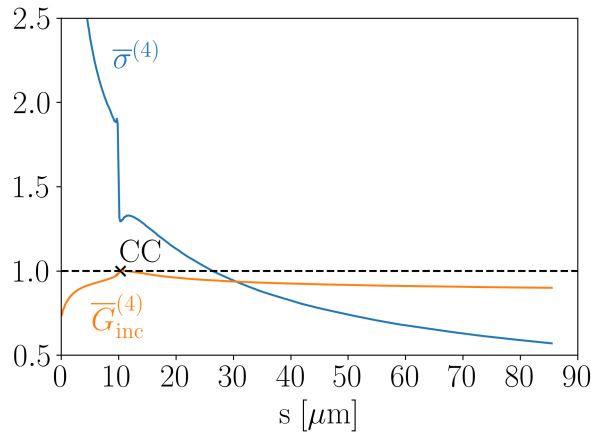


Figure 5.5: Example of the application of the algorithm 1, in the scenario 1.B.2: the maximum point in  $\bar{G}_{\text{inc}}^{(n)}$  is the CC point. Case  $\alpha = 0^\circ$ ,  $d = 10 \mu\text{m}$ ,  $\Delta\theta = 0 K$  and  $V_p = 0\%$

**Scenario 2: There is not a cross point**

If there is not a cross point, we look for a relative minimum point in  $\bar{\sigma}^{(n)}$  or a relative maximum point in  $\bar{G}_{\text{inc}}^{(n)}$ , and we apply the same reasoning studied in scenarios 1.B.1.

One example is shown in Fig. 5.6. The CC analysis corresponds to a traction test on a double-notched nano-tablet (see Section 2.2.3.2 for more details). In particular, the CC is governing by a relative minimum of  $\bar{\sigma}^{(n)}$  when  $\sigma_c = 5.5$  GPa and  $G_c = 2.091$  J m<sup>-2</sup>. Only 4 iterations are needed to find the solution. Notice that in this case, although  $s_{\text{min}}$  is the point that governs the failure, it does not correspond to the CC point, defined as the point where  $s = \delta l$ , the newly created crack length. In this case,  $s_{\text{min}} < \delta l \approx W - a$ .

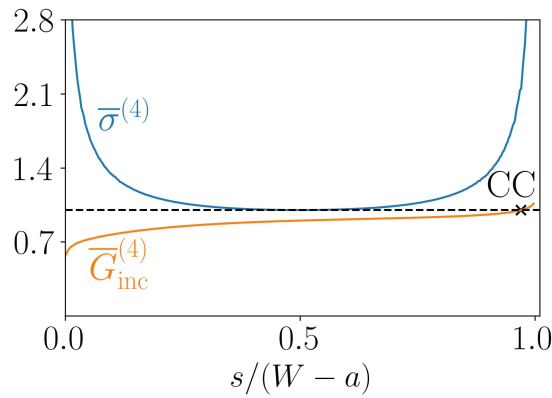


Figure 5.6: Example of the application of the algorithm 1, in the scenario 1.B.1: the minimum point in  $\bar{\sigma}^{(4)}$  is governing the failure. Case studied in Section 2.2.3.2, for  $\sigma_c = 5.5$  GPa and  $G_c = 2.091$  J m<sup>-2</sup>

**Final remark:** this algorithm is not optimized. First, notice that we only consider relative minimum points in  $\bar{\sigma}^{(n)}$  and maximum points in  $\bar{G}_{\text{inc}}^{(n)}$ . A better performance is expected if machine learning techniques are introduced and several relative extreme points are studied. Moreover, under simplifications made in this code, only one maximum point in  $\bar{G}_{\text{inc}}^{(n)}$  and one minimum point in  $\bar{\sigma}^{(n)}$  are considered in the algorithm.

**5.4.1.2 Algorithm 2: based on load steps**

In algorithm 2 the parameter  $\Delta$  is evaluated in a certain range. We look for the minimum value of  $\Delta$  for which the stress and the energy condition is verified, as described in the following pseudocode. Notice that this code is prepared for a thermomechanical problem. If a pure mechanical problem is considered, the thermoelastic variables must be set to 0.

As mentioned above, the main disadvantage of algorithm 1 is that there are some cases that it can not solve, because the CC point does not correspond to a critical point of the curves representing the stress and the energy condition, or other effects (for example, thermoelasticity) are included. When algorithm 1 works, both procedures give the same results, as shown in Fig. 5.7, where  $K_{IC}^{app}/K_{IC}^g$  with respect to 1 is represented for  $\alpha = 0^\circ$ ,  $V_p = 0\%$  and  $\Delta\theta = 0 K$  (case studied in Chapter 3).

The main disadvantage of algorithm 2 is the number of iterations, that depends on the value of  $\delta\Delta$ . If a high accuracy is required, the number of iterations can be much more than in case of using algorithm 1. For example, in the situation represented in Fig. 5.6. With algorithm 1 it was solved using 4 iterations, whereas with algorithm 2 a total of 439 iterations were required. The high computational complexity of this code with respect to the other one suggests us to combine the use of both codes when applying the CC.

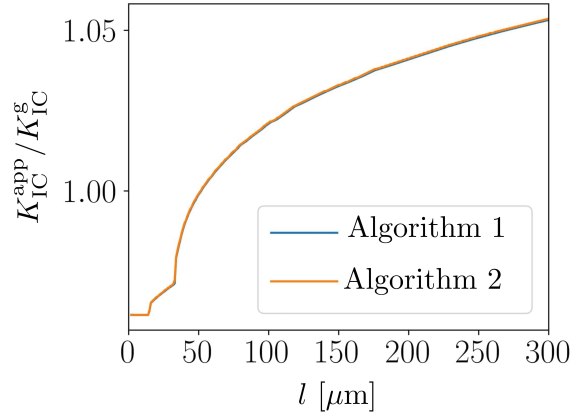


Figure 5.7: Comparison between the algorithm 1 and the algorithm 2. Evolution of  $K_{IC}^{app}/K_{IC}^g$  with respect to  $l$ , for  $\alpha = 0^\circ$  and  $V_p = 0\%$  (The two curves are superimposed).

**Define**  $\Delta^{\max}, \delta\Delta$

**Initiate variables**  $\Delta = 0$

**While**  $\Delta < \Delta^{\max}$

**Update**  $\Delta = \Delta + \delta\Delta$

**Update**  $\bar{\sigma} = (\Delta\sigma^{cr} + \sigma^{te}) \otimes \sigma_c$  **and**  $\bar{G}_{inc} = (\Delta^2 G_{inc}^{cr} + G_{inc}^{te}) \otimes G_c$

**If**  $\bar{\sigma} > 1$  **and**  $\bar{G}_{inc} > 1$ , **Then**

$\Delta^{\max} = \Delta$

**EndIf**

**If** There is a point ( $s_{cc1}$ ) where  $\bar{G}_{inc} = 1$  **Then**

```

If  $\bar{\sigma}(s) > 1$  for  $0 \geq s \geq s_{cc1}$  and  $\left. \frac{\partial \bar{\sigma}}{\partial s} \right|_{s[0]} < \left. \frac{\partial \bar{\sigma}}{\partial s} \right|_{s[1]}$ 
    Update  $\Delta^{\max} = \Delta$  and  $\Delta_c = \Delta$ 
EndIf
EndIf
EndWhile
Initiate variables  $\Delta = 0$ 
While  $\Delta < \Delta^{\max}$ 
    Update  $\Delta = \Delta + \delta\Delta$ 
    Update  $\bar{\sigma} = (\Delta \sigma^{\text{cr}} + \sigma^{\text{te}}) \otimes \sigma_c$  and  $\bar{G}_{\text{inc}} = (\Delta^2 G_{\text{inc}}^{\text{cr}} + G_{\text{inc}}^{\text{te}}) \otimes G_c$ 
    If  $\bar{\sigma} > 1$  and  $\bar{G}_{\text{inc}} > 1$ , Then
         $\Delta^{\max} = \Delta$ 
    EndIf
    If There is a point ( $s_{cc2}$ ) where  $\bar{\sigma} = 1$  Then
        If  $\bar{\sigma}(s) > 1$  for  $0 \geq s \geq s_{cc1}$  and  $\left. \frac{\partial \bar{\sigma}}{\partial s} \right|_{s[0]} < \left. \frac{\partial \bar{\sigma}}{\partial s} \right|_{s[1]}$  and  $\bar{G}_{\text{inc}}|_{s_{cc2}} \geq 1$ 
            Update  $\Delta^{\max} = \Delta$  and  $\Delta_c = \Delta$ 
        EndIf
    EndIf
EndWhile

```

### 5.4.2 A code for the application of the PF model for brittle fracture

In this section we explain the PF code used in Section 2.3, which is summarized in Fig. 5.8. It is important to highlight that the code developed in this PhD thesis is based on the online tutorial<sup>1</sup>. We follow a staggered scheme of the problem, and therefore the displacement and damage are separately calculated.

At each time step  $\tau$ , an iterative process is initiated. The inputs of each iteration  $n$  are  $\underline{u}_\tau^{n-1}, \alpha_\tau^{n-1}$ , the solution of iteration  $n - 1$ . Notice that for the first iteration  $n = 1$  the inputs correspond to the solution of the previous time step  $\underline{u}_{\tau-1}, \alpha_{\tau-1}$ . Applying a specific solver described in Section 5.4.2.2, the displacement vector at iteration  $n$  is obtained, keeping constant the damage variable  $\alpha_\tau^{n-1}$ , and then the damage variable at iteration  $n$  is calculated keeping constant the displacement vector  $\underline{u}_\tau^n$ . The outputs  $\underline{u}_\tau^n, \alpha_\tau^n$  are checked using a function  $E(\alpha_\tau^n)$ , based on the L2 norm,

$$E(\alpha_\tau^n) = \frac{\int_\Omega \|\alpha_\tau^n - \alpha_\tau^{n-1}\| dx}{\text{Vol}} \quad (5.21)$$

<sup>1</sup><https://newfrac.gitlab.io/newfrac-fenicsx-training/04-phase-field/phase-field.html>

where Vol is the total volume of the specimen (area if we refer to 2D elasticity). The convergence at time step  $\tau$  is achieved when  $E(\alpha_\tau^n) < \text{Tol}$ , being Tol a certain tolerance that is normally set as  $10^{-4}$ .

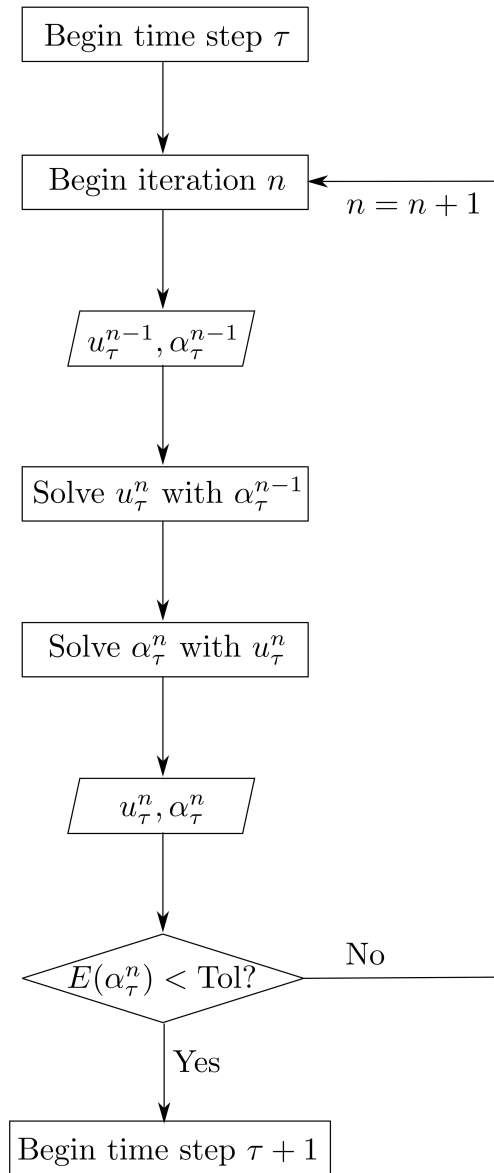


Figure 5.8: Flow chart for the Phase Field code used in this PhD thesis.

The irreversibility condition in this code is imposed by setting the lower bound of the damage function  $\alpha_\tau$  at time step  $\tau$ , as  $\alpha_{\tau-1}$ . The upper bound of this function is equal to 1,

which means completely damage. The library Dolfinx <sup>2</sup> is used to apply this methodology. Moreover, to enhance its performance, the code is prepared for parallel operation, using the MPI library <sup>3</sup>.

#### 5.4.2.1 Description of the code

Since the phase field code is not updated in the website<sup>4</sup>, it is explained in this appendix. First, we import the required libraries in this code.

```
import dolfinx
import numpy as np
from mpi4py import MPI
import ufl
```

Then, we define a function that receives several inputs: `name_input`, `mesh`, `facets` and `Parameters_data`. In the input `name_input` we include a key name for the outputs of the code. In the inputs (`mesh` and `facets`) we include the nodes generated in the mesh (in this case it has been generated by the mesh tool Gmsh <sup>5</sup>) of the domain and the boundaries, respectively. Finally, in `Parameters_data` we include additional parameters of the problem (mechanical and geometrical parameters). The parameter `comm` is used to define the communicator for parallel computation.

```
def phasefield_solver(name_input, mesh, facets, Parameters_data):
    # Parallel computation: multiprocessors
    comm = MPI.COMM_WORLD
```

In the following, all the lines described are locate inside the function described above. First, the vector `Parameters_data` is decomposed. The parameters that will be included in the formulation are scattered in the mesh: the Lamé constants (`lmbda` and `mu`), the residual parameter (`kres`) for avoiding zero stiffness in the structure, the phase field length scale (named as `l0` in this code and defined using the AT1 model), the critical energy release rate (`Gc`), the bulk modulus (`Kn`) and the imposed displacement (`Uimp`). Moreover, the function (`w`) and the coefficient (`cw`) defined in the following lines will be used in the damaged energy density, following the AT1 model.

```
# Parameters in the problem
E, nu = Parameters_data.get('E'), Parameters_data.get('nu')
Umax = Parameters_data.get('Umax')
Nincr = Parameters_data.get('Nincr')
L = Parameters_data.get('L') + Parameters_data.get('n')
W, av = Parameters_data.get('W'), Parameters_data.get('a')
Sc, Gc = Parameters_data.get('Sc'), Parameters_data.get('Gc')
```

<sup>2</sup><https://docs.fenicsproject.org/dolfinx/main/python/>

<sup>3</sup><https://www.open-mpi.org/>

<sup>4</sup><https://newfrac.gitlab.io/newfrac-fenicsx-training/04-phase-field/phase-field.html>

<sup>5</sup><https://gmsh.info/>

```

10      = 3/8 * E * Gc / ((1-nu**2)*Sc**2)

# Parameters sparsed in the mesh
lmbda = dolfinx.fem.Constant(mesh, E*nu/(1+nu)/(1-2*nu))
mu     = dolfinx.fem.Constant(mesh, E / 2 / (1 + nu))
kres   = dolfinx.fem.Constant(mesh, 1e-6)
l0     = dolfinx.fem.Constant(mesh, 10)
Gc     = dolfinx.fem.Constant(mesh, Gc)
Kn     = dolfinx.fem.Constant(mesh, E*nu/(1+nu)/(1-2*nu)+E/2/(1+nu))
Uimp   = dolfinx.fem.Constant(mesh, 0.)

cw = dolfinx.fem.Constant(mesh, 8 / 3.0)
w = lambda d: d

```

Then, the strain and stress tensor are defined, using a function. Noticed that the stress tensor considering damage ( $\sigma$ ) is defined using the stress tensor with no damage, previously calculated ( $\sigma_{\text{undamaged}}$ ). In each function,  $v$  represents the displacement vector and  $d$  the damage variable.

```

# Elastic variable: stress and strains
def eps(v):
    return ufl.sym(ufl.grad(v))

def sigma_undamaged(v):
    return lmbda * ufl.tr(eps(v)) * ufl.Identity(2) + 2*mu*eps(v)

def sigma(v, d):
    return ((1 - d) ** 2 + kres) * sigma_undamaged(v)

```

In Dolfinx we need to define the function spaces of the variables that we want to calculate: displacements, damage and stresses in our code. The following lines are used.

```

# Function spaces
# function space for the displacement
V_u = dolfinx.fem.VectorFunctionSpace(mesh, ("CG", 1))
# function space for the damage
V_a = dolfinx.fem.FunctionSpace(mesh, ("CG", 1))
# function space for the stress
V_s = dolfinx.fem.TensorFunctionSpace(mesh, ("CG", 1))

```

Dirichlet boundary conditions for displacements are defined in two different steps. First, we define the degrees of freedom on which these conditions will be applied. Second, we define the dirichlet boundary conditions, that are stored in a vector ( $\text{bcs}$ ). These conditions depend on the problem we want to solve. As an example, we apply our code to a bending test of a 2D beam (see Section 2.3.4). The displacements of the beam are restricted by a fixed boundary condition on the left face, while a vertical distributed displacement is imposed on

the right face. That is why we define the degrees of freedom for both faces (Ldofs, Rdofs). Since we are under 2D elasticity, there will be 2 degrees of freedom per node. On the left face both are restricted, whereas on the right face only the degrees of freedom related to a vertical displacement are changed by the Dirichlet boundary condition. The left and the right boundaries were designated in the input facets (named at the beginning of the function). In this problem there are not Neumann boundary conditions.

```
# Dirichlet boundary conditions for displacements
dim = facets.dim
Lnods = facets.indices[facets.values == 1]
Rnods = facets.indices[facets.values == 2]
Ldofs = dolfinx.fem.locate_dofs_topological(V_u, dim, Lnods)
Rdofs = dolfinx.fem.locate_dofs_topological(V_u.sub(1), dim, Rnods)
bcl = dolfinx.fem.dirichletbc(np.zeros((2,)), Ldofs, V_u)
bcr = dolfinx.fem.dirichletbc(Uimp, Rdofs, V_u.sub(1))
bes = [ bcl , bcr]
# Neumann boundary conditions
q = dolfinx.fem.Constant( mesh, np.zeros((2,)) )
f = dolfinx.fem.Constant( mesh, np.zeros((2,)) )
```

Dirichlet boundary condition for the damage variable might also be imposed. In that case, we need to repeat the process. For example, in this case we impose  $\alpha = 0$  (no damage) on the left and the right faces to avoid damage nucleation in those sides of the beam. Notice that the degrees of freedom must be redefined, since they refer in this case to the function space of the damage variable.

```
Ldofs_a = dolfinx.fem.locate_dofs_topological(V_a, dim, Lnods)
Rdofs_a = dolfinx.fem.locate_dofs_topological(V_a, dim, Rnods)
bcl_a = dolfinx.fem.dirichletbc(0.0, Ldofs_a, V_a)
bcr_a = dolfinx.fem.dirichletbc(0.0, Rdofs_a, V_a)
bca = [bcl_a, bcr_a]
```

We define now the functions of the code. Additional functions are defined for the damage variable: aold, that stores the damage state at the previous time step, aupp and allow, that defines the upper and the lower limits of the damage variable. As mentioned above, the lower limit is updated at each time step, so that the irreversibility condition is always directly imposed. The upper limit is equal to 1.

```
u = dolfinx.fem.Function(V_u, name = 'Displacement')
alpha = dolfinx.fem.Function(V_a, name = 'Damage')
sig = dolfinx.fem.Function(V_s, name = 'Stress')

aold = dolfinx.fem.Function(V_a, name='Previous_damage')
aupp = dolfinx.fem.Function(V_a, name='Upper_bound_damage')
allow = dolfinx.fem.Function(V_a, name='Lower_bound_damage')

# ..... Defining the maximum upper bound
```

```

with aupp.vector.localForm() as bc_local:
    bc_local.set(1.0)

dolfinx.fem.set_bc(aupp.vector, bca)

```

Once the functions are defined, the energy densities are introduced. We need to include the elastic and the fracture energy density (`psi_el` and `psi_fr`, respectively). In the elastic energy density we apply a decomposition to separate compression and tension. In this example this is important since crack nucleation is only affected by tension. The decomposition was already explained in Section 1.2.3

```

def psi_el(v,d):
    trace, dev = ufl.tr(eps(v)), ufl.dev(eps(v))
    cond = ufl.conditional(trace > 0, trace, -trace)
    eps_po, eps_ng = 1/2*(trace + cond), 1/2*(trace - cond)
    psi0_p = Kn/2*eps_po**2 + mu*ufl.inner(dev,dev)
    psi0_m = Kn/2*eps_ng**2
    return (((1-d)**2 + kres) * psi0_p + psi0_m)

def psi_fr(d):
    grad = ufl.grad(d)
    return Gc/cw * (w(d)/10 + 10*ufl.dot(grad,grad))

```

At this point, the solver must be created. To see how this solver is defined, have a look at Section 5.4.2.2. After generating the solver, a vector is created to include the different values of the load at each time step (using the maximum load and the number of increments). They will be used to update the parameter `Uimp` defined at the beginning. Moreover, in the processor 0 (if parallel computing) the results will be stored in a matrix. The output will be also plot in a `.xdmf` file. Moreover, to calculate the function  $E(\alpha_\tau^n)$  the total volume (or area) in the solid is obtained (`vol_total`). The command `allreduce` is used in parallel computing for a correct integration.

```

# Load steps vector
load_steps = np.linspace(0, Umax, Nincr + 1)
t = 0

# Results stored in a matrix
if comm.rank==0:
    results = np.zeros(Nincr + 1, 4)

# Output plots in a xdmf file
ffile = dolfinx.io.XDMFFile(comm, str(name_input+".xdmf"), "w")
ffile.write_mesh(mesh)

# Volume definition
vol_unit = dolfinx.fem.Constant(mesh, 1.0)

```

```

vol_form = dolfinx.fem.form(vol_unit * ufl.dx)
vol_rank = dolfinx.fem.assemble_scalar(vol_form)
vol_total = MPI.COMM_WORLD.allreduce(vol_rank, op=MPI.SUM)

```

The iterative process described in Fig. 5.8 starts. For each time step the imposed load is updated and the iterative process is initiated.

```

insertmode = PETSc.InsertMode.INSERT
scattermode = PETSc.ScatterMode.FORWARD
for (i,t) in enumerate(load_steps[1:]):

    if comm.rank == 0:
        print("Increment {:3d}".format(i + 1))
        print("Load {:3f}".format(t))

    # .. Update the load value
    Uimp.value = -0.1

    niter = 0

    for niter in range(Parameters_data.get('Nitermax')):

        # Staggered model: displacement
        solver_u_snes.solve(None,u.vector)
        solver_u_snes.destroy, b_u.destroy(), J_u.destroy()

        # Staggered model: damage SNES solver
        solver_a_tao.solve(alpha.vector)
        solver_a_tao.destroy, b_a.destroy(), J_a.destroy()

        # Expand the vectors in the multiprocessors
        alpha.x.scatter_forward()
        u.x.scatter_forward()

        # Check convergence condition
        e_L2 = ufl.inner(alpha-aold, alpha-aold)
        E_L2 = dolfinx.fem.form(e_L2*ufl.dx)
        E_rank = dolfinx.fem.assemble_scalar(error)
        E_total = MPI.COMM_WORLD.allreduce(error_rank, op=MPI.SUM)
        ErrorL2 = np.sqrt(E_total)/vol_total
        # Update damage aold for the next iteration
        alpha.vector.copy(aold.vector)
        aold.vector.ghostUpdate(addv=insertmode, mode=scattermode)

    if comm.rank == 0:

```

```

        print("Iter  {:3d}: ||Res||={:5e}".format(niter, ErrorL2))

    if ErrorL2 < Parameters_data.get('tol'):
        break
    else:
        warnings.warn("Too many iterations")

# Check irreversibility: update the lower bound
alpha.vector.copy(alow.vector)
alow.vector.ghostUpdate(adv=insertmode, mode=scattermode)

# Compute energies
en_el_form = dolfinx.fem.form(psi_el(u, alpha))
en_el_rank = dolfinx.fem.assemble_scalar(en_el_form*ufl.dx)
en_el = comm.allreduce(en_el_rank)
en_fr_form = dolfinx.fem.form(psi_fr(alpha))
en_fr_rank = dolfinx.fem.assemble_scalar(en_fr_form*ufl.dx)
en_fr = comm.allreduce(en_fr_rank)
force = en_el*2/t

if comm.rank==0:
    results[i + 1, :] = (t, en_el, en_fr, force)

# Expand the vectors in the multiprocessors
ffile.write_function(u, t)
ffile.write_function(alpha, t)
ffile.write_function(sig, t)

return results

```

#### 5.4.2.2 Description of the solvers

In this section we explain the solver used in the code. We have used two different solvers that use the Newton-Raphson methodology: SNES solver and TAO solver. The first one (SNES) is a minimization solver, and it works better with parallel computing, but it fails when the phase field length scale is too close to the dimensions of the specimen. The second one (TAO) is an optimization solver. It is used because it compiles when the phase field length scale is of the order of the dimensions of the specimen, but it is much more difficult to compute using parallel computing. It has been verified that in cases where both solvers can be used they give the same results. In the code, both have been defined and applied according to the situation analysed. Two problems are defined, one for displacements and the other one for damage. As an example, we show the code used to define the displacement problem using SNES and the damage problem using TAO. For the first one,

```

func_psi = psi_el(u, aold) + psi_fr(aold) - ufl.dot(f, u)
func_u    = (func_psi)*ufl.dx - ufl.dot(q, u)*ufl.ds
dfunc_u   = ufl.derivative(functional_u, u, ufl.TestFunction(V_u))
ddfunc_u  = ufl.derivative(dfunctional_u, u, ufl.TrialFunction(V_u))

# Definition of the problem
u_problem = SNES_problem( dfunc_u, ddfunc_u, u, bcs )

# b = xk (degrees of freedom)
dofs_domain_u, = V_u.dofmap.index_map
dofs_borders_u = V_u.dofmap.index_map_bs
b_u = dolfinx.la.create_petsc_vector(dofs_domain_u, dofs_borders_u)
J_u = dolfinx.fem.petsc.create_matrix(u_problem.a)

# Create Newton solver and solve
solver_u_snes = petsc4py.PETSc.SNES().create()
solver_u_snes.setType("vinewtonrsls")
solver_u_snes.setFunction(u_problem.F, b_u)
solver_u_snes.setJacobian(u_problem.J, J_u)
solver_u_snes.setTolerances(rtol=1.0e-9, max_it=50)
solver_u_snes.getKSP().setType("preonly")
solver_u_snes.getKSP().setTolerances(rtol=1.0e-9)
solver_u_snes.getKSP().getPC().setType("lu")

```

whereas for the second one it is necessary to define the upper and the lower limits of the variable. These lines work with a complementary function that has been omitted for the sake of simplicity, where variables `b_a`, `b_u` and `J_a`, `J_u` are created. For a deeper information the author invites the reader to ask for the codes by email or look at the NewFrac project website, where similar methodologies will be uploaded.

```

# Definition of the damage solver
func_a    = psi_el(u, alpha) * ufl.dx + psi_fr(alpha) * ufl.dx
dfunc_a   = ufl.derivative(func_a, alpha, ufl.TestFunction(V_a))
ddfunc_a  = ufl.derivative(dfunc_a, alpha, ufl.TrialFunction(V_a))

# Definition of the problem (TAO solver)
a_problem = TAOProblem(func_a, dfunc_a, ddfunctional_a, alpha, bca)

# b = xk (degrees of freedom)
dofs_domain_a = V_a.dofmap.index_map
dofs_borders_a = V_a.dofmap.index_map_bs
b_a = dolfinx.la.create_petsc_vector(dofs_domain_a, dofs_borders_a)
J_a = dolfinx.fem.petsc.create_matrix(a_problem.a)

# Create PETSc TAO

```

```

solver_a_tao = petsc4py.PETSc.TAO().create(comm=comm)
solver_a_tao.setType("tron")
solver_a_tao.setObjective(a_problem.f)
solver_a_tao.setGradient(a_problem.F, b_a)
solver_a_tao.setHessian(a_problem.J, J_a)
solver_a_tao.setTolerances(grtol=1e-6, gttol=1e-6)
solver_a_tao.getKSP().setType("preonly")
solver_a_tao.getKSP().setTolerances(rtol=1.0e-6)
solver_a_tao.getKSP().getPC().setType("lu")

# We set the bound (Note: they are passed as reference)
solver_a_tao.setVariableBounds(alow.vector, aupp.vector)

```

#### 5.4.2.3 Additional comments about the PF code

The mesh size in the PF model for brittle fracture is a critical decision in the problem, and it is related to the phase field length scale. In this PhD thesis we follow the rule: 5 elements must define the phase field length scale. Therefore, the maximum mesh size allowed in the damage region would be:  $l_{\text{mesh}} = l_{\text{PF}}/5$  [70]. For example, for the bending test of an unnotched beam (see Section 2.2.2.1) we have analysed the mesh sensitivity for  $l_{\text{PF}} = 1 \mu\text{m}$ . According to our rule, the mesh size chosen is  $l_{\text{mesh}} = 0.2 \mu\text{m}$ . In Fig. 5.9 the Force-Displacement curve is represented for several values of  $l_{\text{mesh}}$  to study the verify that the critical displacement (the parameter we are interested in) does not change when a lower value than  $l_{\text{mesh}} = l_{\text{PF}}/5 = 0.2 \mu\text{m}$  is considered. Notice that the computational complexity is highly reduced when  $l_{\text{mesh}} = 0.2 \mu\text{m}$ , from 309 elements to 25000 elements for  $l_{\text{mesh}} = 0.01 \mu\text{m}$ .

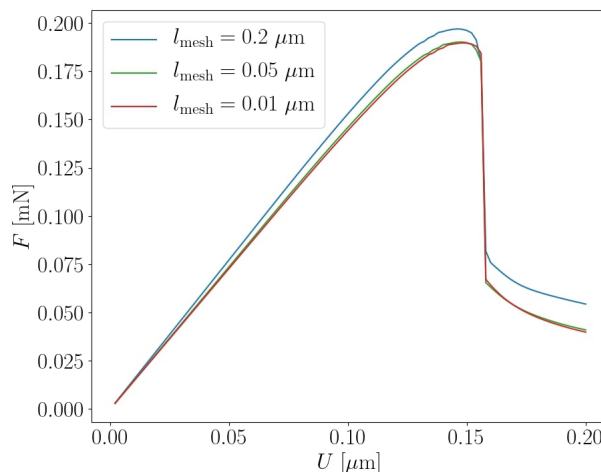


Figure 5.9: Influence of the mesh size used in the application of the phase field model for  $l_{\text{PF}} = 1 \mu\text{m}$ .

The convergence of the solution is also analysed when applying the PF model. To that aim, we reduce the load step until little variations are noticed in the critical displacement, as shown in Fig. 5.10 for the bending test of a microcantilever beam, studied in Section 2.3.4. It is important to highlight that a similar convergence analysis was done in the unnotched and v-notched specimen. When  $1/\Delta U \approx 10^4 \text{ 1}/\mu\text{m}$  little variations are noticed and reliable results can be obtained from the simulation.

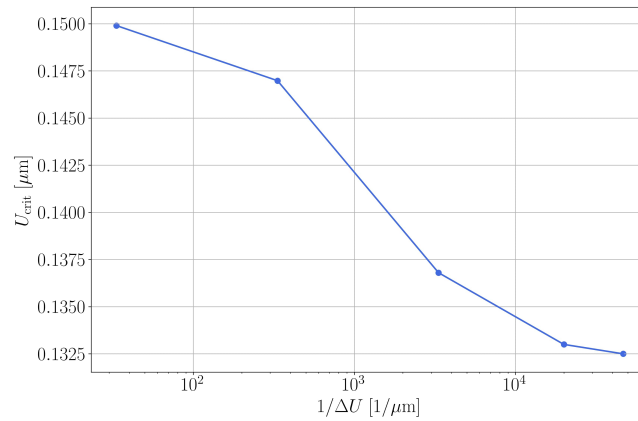


Figure 5.10: Evolution of the critical displacement  $U_{\text{crit}}$  with respect to the load step in the numerical simulation.

# Bibliography

- [1] S. Somiya, Handbook of advanced ceramics: materials, applications, processing, and properties, Academic press, 2013. doi:<https://doi.org/10.1016/C2010-0-66261-4>.
- [2] J. Montes, J. Cintas, F. Gómez, Ciencia e Ingeniería de los Materiales, Ediciones Paraninfo, SA, 2014.
- [3] S. Singh, P. Kumar, D. Mondal, Advanced Ceramics for versatile interdisciplinary applications, Elsevier, 2022.
- [4] R. Heimann, Classic and advanced ceramics: from fundamentals to applications, John Wiley & Sons, 2010. doi:[10.1002/9783527630172](https://doi.org/10.1002/9783527630172).
- [5] M. Ashby, Overview no. 80: On the engineering properties of materials, Acta metallurgica 37 (5) (1989) 1273–1293. doi:[https://doi.org/10.1016/0001-6160\(89\)90158-2](https://doi.org/10.1016/0001-6160(89)90158-2).
- [6] W. Matizanhuka, Advanced ceramics - the new frontier in modern-day technology: Part I, Journal of the Southern African Institute of Mining and Metallurgy 118 (7) (2018) 757–764. doi:<http://dx.doi.org/10.17159/2411-9717/2018/v118n7a9>.
- [7] M. Boniecki, T. Sadowski, P. Gołębiewski, H. Węglarz, A. Piątkowska, M. Romaniec, K. Krzyżak, K. Łosiewicz, Mechanical properties of alumina/zirconia composites, Ceramics International 46 (1) (2020) 1033–1039. doi:<https://doi.org/10.1016/j.ceramint.2019.09.068>.
- [8] P. Gallo, A. Sapura, Brittle failure of nanoscale notched silicon cantilevers: a finite fracture mechanics approach, Applied Sciences 10 (5) (2020) 1640. doi:<https://doi.org/10.3390/app10051640>.
- [9] K. Matoy, H. Schönherr, T. Detzel, T. Schöberl, R. Pippan, C. Motz, G. Dehm, A comparative micro-cantilever study of the mechanical behavior of silicon based passivation films, Thin Solid Films 518 (1) (2009) 247–256. doi:<https://doi.org/10.1016/j.tsf.2009.07.143>.

- [10] R. Henry, I. Zacharie-Aubrun, T. Blay, S. Chalal, J. Gatt, C. Langlois, S. Meille, Fracture properties of an irradiated PWR UO<sub>2</sub> fuel evaluated by micro-cantilever bending tests, *Journal of Nuclear Materials* 538 (2020) 152209. doi:<https://doi.org/10.1016/j.jnucmat.2020.152209>.
- [11] A. Doitrand, R. Henry, I. Zacharie-Aubrun, J. Gatt, S. Meille, UO<sub>2</sub> micron scale specimen fracture: Parameter identification and influence of porosities, *Theoretical and Applied Fracture Mechanics* 108 (2020) 102665. doi:<https://doi.org/10.1016/j.tafmec.2020.102665>.
- [12] A. Doitrand, R. Henry, H. Saad, S. Deville, S. Meille, Determination of interface fracture properties by micro-and macro-scale experiments in nacre-like alumina, *Journal of the Mechanics and Physics of Solids* 145 (2020) 104143. doi:<https://doi.org/10.1016/j.jmps.2020.104143>.
- [13] A. Doitrand, R. Henry, J. Chevalier, S. Meille, Revisiting the strength of micron-scale ceramic platelets, *Journal of the American Ceramic Society* 103 (12) (2020) 6991–7000. doi:<https://doi.org/10.1111/jace.17148>.
- [14] M. Von Ardenne, On the history of scanning electron microscopy, of the electron microprobe, and of early contributions to transmission electron microscopy, in: *The beginnings of electron microscopy*, Vol. 16, Academic Press Orlando, 1985, pp. 1–21. doi:<https://doi.org/10.1016/bs.aiep.2021.08.002>.
- [15] G. Binnig, H. Rohrer, C. Gerber, E. Weibel, Surface studies by scanning tunneling microscopy, *Physical review letters* 49 (1) (1982) 57. doi:<https://doi.org/10.1103/PhysRevLett.49.57>.
- [16] W. Croft, *Under the microscope: a brief history of microscopy*, Vol. 5, World Scientific, 2006. doi:<https://doi.org/10.5860/choice.44-6203>.
- [17] C. Schuh, Nanoindentation studies of materials, *Materials today* 9 (5) (2006) 32–40. doi:[https://doi.org/10.1016/S1369-7021\(06\)71495-X](https://doi.org/10.1016/S1369-7021(06)71495-X).
- [18] G. Dehm, B. Jaya, R. Raghavan, C. Kirchlechner, Overview on micro- and nanomechanical testing: New insights in interface plasticity and fracture at small length scales, *Acta Materialia* 142 (2018) 248–282. doi:<https://doi.org/10.1016/j.actamat.2017.06.019>.
- [19] H. Espinosa, B. Peng, A new methodology to investigate fracture toughness of freestanding mems and advanced materials in thin film form, *Journal of microelectromechanical systems* 14 (1) (2005) 153–159. doi:<https://doi.org/10.1109/JMEMS.2004.839013>.
- [20] H. Kahn, N. Tayebi, R. Ballarini, R. Mullen, A. Heuer, Fracture toughness of polysilicon mems devices, *Sensors and Actuators A: Physical* 82 (1-3) (2000) 274–280. doi:[https://doi.org/10.1016/S0924-4247\(99\)00366-0](https://doi.org/10.1016/S0924-4247(99)00366-0).

- [21] R. Ballarini, R. Mullen, Y. Yin, H. Kahn, S. Stemmer, A. Heuer, The fracture toughness of polysilicon microdevices: a first report, *Journal of Materials Research* 12 (4) (1997) 915–922.
- [22] T. Pardoën, M. Colla, H. Idrissi, B. Amin-Ahmadi, B. Wang, D. Schryvers, U. Bhaskar, J. Raskin, A versatile lab-on-chip test platform to characterize elementary deformation mechanisms and electromechanical couplings in nanoscopic objects, *Comptes Rendus Physique* 17 (3-4) (2016) 485–495. doi:<https://doi.org/10.1016/j.crhy.2015.11.005>.
- [23] D. Di Maio, S. Roberts, Measuring fracture toughness of coatings using focused-ion-beam-machined microbeams, *Journal of materials research* 20 (2) (2005) 299–302. doi:<https://doi.org/10.1557/JMR.2005.0048>.
- [24] M. Uchic, D. Dimiduk, J. Florando, W. Nix, Sample dimensions influence strength and crystal plasticity, *Science* 305 (5686) (2004) 986–989. doi:<https://doi.org/10.1126/science.1098993>.
- [25] A. Norton, S. Falco, N. Young, J. Severs, R. Todd, Microcantilever investigation of fracture toughness and subcritical crack growth on the scale of the microstructure in  $\text{Al}_2\text{O}_3$ , *Journal of the European Ceramic Society* 35 (16) (2015) 4521–4533. doi:<https://doi.org/10.1016/j.jeurceramsoc.2015.08.023>.
- [26] G. Žagar, V. Pejchal, M. Mueller, L. Michelet, A. Mortensen, Fracture toughness measurement in fused quartz using triangular chevron-notched micro-cantilevers, *Scripta Materialia* 112 (2016) 132–135. doi:<https://doi.org/10.1016/j.scriptamat.2015.09.032>.
- [27] M. Mueller, V. Pejchal, G. Žagar, A. Singh, M. Cantoni, A. Mortensen, Fracture toughness testing of nanocrystalline alumina and fused quartz using chevron-notched microbeams, *Acta Materialia* 86 (2015) 385–395.
- [28] H. Zhang, B. Schuster, Q. Wei, K. Ramesh, The design of accurate micro-compression experiments, *Scripta Materialia* 54 (2) (2006) 181–186. doi:<https://doi.org/10.1016/j.scriptamat.2005.06.043>.
- [29] J. Schneider, S. Schula, W. Weinhold, Characterisation of the scratch resistance of annealed and tempered architectural glass, *Thin solid Film* 520 (2012) 4190–4198. doi:<http://dx.doi.org/10.1016/j.tsf.2011.04.104>.
- [30] M. Kotoul, J. Pokluda, P. Šandera, I. Dlouhý, Z. Chlup, A. Boccaccini, Toughening effects quantification in glass matrix composite reinforced by alumina platelets, *Acta materialia* 56 (12) (2008) 2908–2918. doi:<https://doi.org/10.1016/j.actamat.2008.02.024>.
- [31] A. Winn, A. Boccaccini, N. Imam, P. Trusty, Examination of microhardness indentation-induced subsurface damage in alumina platelet reinforced borosilicate glass using confocal scanning laser microscopy, *Journal of Microscopy* 186 (1) (1997) 35–40. doi:<https://doi.org/10.1046/j.1365-2818.1997.1880751.x>.

- [32] A. R. Boccaccini, P. A. Trusty, Toughening and strengthening of glass by  $\text{Al}_2\text{O}_3$  platelets, *Journal of materials science letters* 15 (1) (1996) 60–63. doi:<https://doi.org/10.1007/BF01855614>.
- [33] A. Boccaccini, V. Winkler, Fracture surface roughness and toughness of  $\text{Al}_2\text{O}_3$ -platelet reinforced glass matrix composites, *Composites Part A: Applied Science and Manufacturing* 33 (1) (2002) 125–131. doi:[https://doi.org/10.1016/S1359-835X\(01\)00080-X](https://doi.org/10.1016/S1359-835X(01)00080-X).
- [34] A. R. Boccaccini, E. A. Olevsky, Processing of platelet-reinforced glass matrix composites: effect of inclusions on sintering anisotropy, *Journal of Materials Processing Technology* 96 (1-3) (1999) 92–101. doi:[https://doi.org/10.1016/S0924-0136\(99\)00272-1](https://doi.org/10.1016/S0924-0136(99)00272-1).
- [35] E. Bernardo, G. Scarinci, Sintering behaviour and mechanical properties of  $\text{Al}_2\text{O}_3$  platelet-reinforced glass matrix composites obtained by powder technology, *Ceramics international* 30 (5) (2004) 785–791. doi:<http://dx.doi.org/10.1016/j.ceramint.2003.09.013>.
- [36] E. Bernardo, R. Castellan, S. Hreglich,  $\text{Al}_2\text{O}_3$ -platelet reinforced glass matrix composites from a mixture of wastes, *Journal of materials science* 42 (8) (2007) 2706–2711. doi:<https://doi.org/10.1007/s10853-006-1378-8>.
- [37] R. Todd, A. Boccaccini, R. Sinclair, R. Yallee, R. Young, Thermal residual stresses and their toughening effect in  $\text{Al}_2\text{O}_3$  platelet reinforced glass, *Acta materialia* 47 (11) (1999) 3233–3240. doi:[https://doi.org/10.1016/S1359-6454\(99\)00177-9](https://doi.org/10.1016/S1359-6454(99)00177-9).
- [38] C.-H. Hsueh, Sintering behaviour of powder compacts with multiheterogeneities, *Journal of materials science* 21 (6) (1986) 2067–2072. doi:<http://dx.doi.org/10.1007/BF00547948>.
- [39] M. Taya, S. Hayashi, A. S. Kobayashi, H. Yoon, Toughening of a particulate-reinforced ceramic-matrix composite by thermal residual stress, *Journal of the American Ceramic Society* 73 (5) (1990) 1382–1391. doi:<https://doi.org/10.1111/j.1151-2916.1990.tb05209.x>.
- [40] V. Cannillo, C. Leonelli, A. R. Boccaccini, Numerical models for thermal residual stresses in  $\text{Al}_2\text{O}_3$  platelets/borosilicate glass matrix composites, *Materials Science and Engineering: A* 323 (1-2) (2002) 246–250. doi:[https://doi.org/10.1016/S0921-5093\(01\)01345-4](https://doi.org/10.1016/S0921-5093(01)01345-4).
- [41] P. Weißgraeber, D. Leguillon, W. Becker, A review of finite fracture mechanics: crack initiation at singular and non-singular stress raisers, *Archive of Applied Mechanics* 86 (1) (2016) 375–401. doi:<https://link.springer.com/article/10.1007/s00419-015-1091-7>.
- [42] A. Parvizi, K. Garrett, J. Bailey, Constrained cracking in glass fibre-reinforced epoxy cross-ply laminates, *Journal of Materials Science* 13 (1) (1978) 195–201. doi:[https://doi.org/10.1016/0010-4361\(87\)90006-1](https://doi.org/10.1016/0010-4361(87)90006-1).

- [43] D. Leguillon, Strength or toughness? A criterion for crack onset at a notch, *European Journal of Mechanics - A/Solids* 21 (1) (2002) 61–72. doi:[https://doi.org/10.1016/S0997-7538\(01\)01184-6](https://doi.org/10.1016/S0997-7538(01)01184-6).
- [44] A. A. Griffith, VI. The phenomena of rupture and flow in solids, *Philosophical transactions of the royal society of London. Series A, containing papers of a mathematical or physical character* 221 (582-593) (1921) 163–198. doi:<https://doi.org/10.1098/rsta.1921.0006>.
- [45] Z. Hashin, Finite thermoelastic fracture criterion with application to laminate cracking analysis, *Journal of the Mechanics and Physics of Solids* 44 (7) (1996) 1129–1145. doi:[https://doi.org/10.1016/0022-5096\(95\)00080-1](https://doi.org/10.1016/0022-5096(95)00080-1).
- [46] D. Taylor, The theory of critical distances, *Engineering Fracture Mechanics* 75 (7) (2008) 1696–1705. doi:<https://doi.org/10.1016/j.engfracmech.2007.04.007>.
- [47] D. Taylor, Applications of the theory of critical distances to the prediction of brittle fracture in metals and non-metals, in: *15th European Conference of Fracture-ECF15*, Stockholm, Citeseer, 2004. doi:<http://dx.doi.org/10.1016/j.engfailanal.2010.07.002>.
- [48] E. Martin, D. Leguillon, N. Carrère, A coupled strength and toughness criterion for the prediction of the open hole tensile strength of a composite plate, *International journal of Solids and Structures* 49 (26) (2012) 3915–3922. doi:<https://doi.org/10.1016/j.ijsolstr.2012.08.020>.
- [49] P. Cornetti, N. Pugno, A. Carpinteri, D. Taylor, Finite fracture mechanics: a coupled stress and energy failure criterion, *Engineering Fracture Mechanics* 73 (14) (2006) 2021–2033. doi:<https://doi.org/10.1016/j.engfracmech.2006.03.010>.
- [50] T. Laschuetza, T. Seelig, Remarks on dynamic cohesive fracture under static pre-stress—with a comparison to finite fracture mechanics, *Engineering Fracture Mechanics* 242 (2021) 107466. doi:<https://doi.org/10.1016/j.engfracmech.2020.107466>.
- [51] M. Williams, Stress singularities resulting from various boundary conditions in angular corners of plates in extension.
- [52] G. R. Irwin, Analysis of stresses and strains near the end of a crack traversing a plate doi:<https://doi.org/10.1115/1.4011547>.
- [53] A.-K. Hofer, R. Walton, O. Ševeček, G. L. Messing, R. Bermejo, Design of damage tolerant and crack-free layered ceramics with textured microstructure, *Journal of the European Ceramic Society* 40 (2) (2020) 427–435. doi:<https://doi.org/10.1016/j.jeurceramsoc.2019.09.004>.
- [54] A. Doitrand, E. Martin, D. Leguillon, Numerical implementation of the coupled criterion: Matched asymptotic and full finite element approaches, *Finite Elements in Analysis and Design* 168 (2020) 103344. doi:<https://doi.org/10.1016/j.finel.2019.103344>.

- [55] M. Elices, G. Guinea, J. Gomez, J. Planas, The cohesive zone model: advantages, limitations and challenges, *Engineering fracture mechanics* 69 (2) (2002) 137–163. doi:[https://doi.org/10.1016/S0013-7944\(01\)00083-2](https://doi.org/10.1016/S0013-7944(01)00083-2).
- [56] G. A. Francfort, J.-J. Marigo, Revisiting brittle fracture as an energy minimization problem, *Journal of the Mechanics and Physics of Solids* 46 (8) (1998) 1319–1342. doi:[https://doi.org/10.1016/S0022-5096\(98\)00034-9](https://doi.org/10.1016/S0022-5096(98)00034-9).
- [57] C. Miehe, F. Welschinger, M. Hofacker, Thermodynamically consistent phase-field models of fracture: Variational principles and multi-field fe implementations, *International journal for numerical methods in engineering* 83 (10) (2010) 1273–1311.
- [58] A. Sapora, P. Cornetti, Crack onset and propagation stability from a circular hole under biaxial loading, *International Journal of Fracture* 214 (1) (2018) 97–104. doi:<https://link.springer.com/article/10.1007/s10704-018-0315-6>.
- [59] J. Kevorkian, J. Cole, Perturbation methods in applied mathematics. series, *Applied Mathematical Sciences* 43. doi:<https://doi.org/10.1109/TSMC.1973.4309322>.
- [60] J.-J. Marigo, C. Maurini, K. Pham, An overview of the modelling of fracture by gradient damage models, *Meccanica* 51 (2016) 3107–3128. doi:<http://dx.doi.org/10.1007/s11012-016-0538-4>.
- [61] K. Pham, H. Amor, J.-J. Marigo, C. Maurini, Gradient damage models and their use to approximate brittle fracture, *International Journal of Damage Mechanics* 20 (4) (2011) 618–652.
- [62] K. Pham, J.-J. Marigo, Approche variationnelle de l’endommagement: I. les concepts fondamentaux, *Comptes Rendus Mécanique* 338 (4) (2010) 191–198.
- [63] B. Bourdin, G. A. Francfort, J.-J. Marigo, Numerical experiments in revisited brittle fracture, *Journal of the Mechanics and Physics of Solids* 48 (4) (2000) 797–826. doi:[https://doi.org/10.1016/S0022-5096\(99\)00028-9](https://doi.org/10.1016/S0022-5096(99)00028-9).
- [64] D. B. Mumford, J. Shah, Optimal approximations by piecewise smooth functions and associated variational problems, *Communications on pure and applied mathematics* doi:<https://doi.org/10.1002/cpa.3160420503>.
- [65] L. Ambrosio, V. M. Tortorelli, Approximation of functional depending on jumps by elliptic functional via t-convergence, *Communications on Pure and Applied Mathematics* 43 (8) (1990) 999–1036. doi:<https://doi.org/10.1002/cpa.3160430805>.
- [66] P. Sicsic, J.-J. Marigo, From gradient damage laws to griffith’s theory of crack propagation, *Journal of Elasticity* 113 (2013) 55–74. doi:<http://dx.doi.org/10.1007/s10659-012-9410-5>.
- [67] H. Amor, J.-J. Marigo, C. Maurini, Regularized formulation of the variational brittle fracture with unilateral contact: Numerical experiments, *Journal of the Mechanics and Physics of Solids* 57 (8) (2009) 1209–1229. doi:<https://doi.org/10.1016/j.jmps.2009.04.011>.

- [68] M. Ambati, T. Gerasimov, L. De Lorenzis, Phase-field modeling of ductile fracture, *Computational Mechanics* 55 (2015) 1017–1040.
- [69] C. Miehe, M. Hofacker, F. Welschinger, A phase field model for rate-independent crack propagation: Robust algorithmic implementation based on operator splits, *Computer Methods in Applied Mechanics and Engineering* 199 (45-48) (2010) 2765–2778.
- [70] Y. Navidtehrani, C. Betegón, E. Martínez-Pañeda, A simple and robust abaqus implementation of the phase field fracture method, *Applications in Engineering Science* 6 (2021) 100050. doi:<https://doi.org/10.1016/j.apples.2021.100050>.
- [71] E. Tanné, T. Li, B. Bourdin, J.-J. Marigo, C. Maurini, Crack nucleation in variational phase-field models of brittle fracture, *Journal of the Mechanics and Physics of Solids* 110 (2018) 80–99. doi:<https://doi.org/10.1016/j.jmps.2017.09.006>.
- [72] S. Jiménez-Alfaro, D. Leguillon, Finite fracture mechanics at the micro-scale. application to bending tests of micro cantilever beams, *Engineering Fracture Mechanics* 258 (2021) 108012. doi:<https://doi.org/10.1016/j.engfracmech.2021.108012>.
- [73] S. Jiménez-Alfaro, J. Reinoso, D. Leguillon, C. Maurini, Finite fracture mechanics from the macro-to the micro-scale. comparison with the phase field model, *Procedia Structural Integrity* 42 (2022) 553–560. doi:<https://doi.org/10.1016/j.prostr.2022.12.070>.
- [74] A. Kumar, B. Bourdin, G. A. Francfort, O. Lopez-Pamies, Revisiting nucleation in the phase-field approach to brittle fracture, *Journal of the Mechanics and Physics of Solids* 142 (2020) 104027. doi:<https://doi.org/10.1016/j.jmps.2020.104027>.
- [75] C. Cui, R. Ma, E. Martínez-Pañeda, A phase field formulation for dissolution-driven stress corrosion cracking, *Journal of the Mechanics and Physics of Solids* 147 (2021) 104254. doi:<https://doi.org/10.1016/j.jmps.2020.104254>.
- [76] W. Weibull, A statistical distribution function of wide applicability, *Journal of applied mechanics* doi:<https://doi.org/10.1115/1.4010337>.
- [77] H. Gao, B. Ji, I. L. Jäger, E. Arzt, P. Fratzl, Materials become insensitive to flaws at nanoscale: lessons from nature, *Proceedings of the national Academy of Sciences* 100 (10) (2003) 5597–5600. doi:<https://doi.org/10.1073/pnas.0631609100>.
- [78] H. Tata, P. Paris, G. Irwin, *The stress analysis of crack handbook* (2000). doi:<https://doi.org/10.1115/1.801535>.
- [79] R. Henry, T. Blay, T. Douillard, A. Descamps-Mandine, I. Zacharie-Aubrun, J. Gatt, C. Langlois, S. Meille, Local fracture toughness measurements in polycrystalline cubic zirconia using micro-cantilever bending tests, *Mechanics of Materials* 136 (2019) 103086. doi:<https://doi.org/10.1016/j.mechmat.2019.103086>.

- [80] W. Luo, C. Kirchlechner, X. Fang, S. Brinckmann, G. Dehm, F. Stein, Influence of composition and crystal structure on the fracture toughness of nbco2 laves phase studied by micro-cantilever bending tests, *Materials & Design* 145 (2018) 116–121. doi:<https://doi.org/10.1016/j.matdes.2018.02.045>.
- [81] S. P. Patil, Y. Heider, C. A. H. Padilla, E. R. Cruz-Chú, B. Markert, A comparative molecular dynamics-phase-field modeling approach to brittle fracture, *Computer Methods in Applied Mechanics and Engineering* 312 (2016) 117–129. doi:<https://doi.org/10.1016/j.cma.2016.04.005>.
- [82] J. Andersons, J. Modniks, Y. Leterrier, G. Tornare, P. Dumont, J.-A. Manson, Evaluation of toughness by finite fracture mechanics from crack onset strain of brittle coatings on polymers, *Theoretical and Applied Fracture Mechanics* 49 (2) (2008) 151–157. doi:<https://doi.org/10.1016/j.tafmec.2007.11.002>.
- [83] D. Leguillon, E. Martin, Prediction of multi-cracking in sub-micron films using the coupled criterion, *International Journal of Fracture* 209 (1) (2018) 187–202. doi:<https://link.springer.com/article/10.1007/s10704-017-0255-6>.
- [84] S. Jiménez-Alfaro, D. Leguillon, Modelling of glass matrix composites by the coupled criterion and the matched asymptotics approach. the role of a single platelet, *Theoretical and Applied Fracture Mechanics* 122 (2022) 103650. doi:<https://doi.org/10.1016/j.tafmec.2022.103650>.
- [85] S. Jiménez-Alfaro, D. Leguillon, Modelling of glass matrix composites by the coupled criterion and the matched asymptotics approach. the role of residual stresses and the volume fraction (minor revision)., *Theoretical and Applied Fracture Mechanics*.
- [86] D. Leguillon, E. Sanchez-Palencia, Computation of singular solutions in elliptic problems and elasticity, 1987. doi:<https://doi.org/10.1002/zamm.19880681137>.
- [87] H. P. Langtangen, A. Logg, *Solving PDEs in Python*, Springer, 2017. doi:[10.1007/978-3-319-52462-7](https://doi.org/10.1007/978-3-319-52462-7).
- [88] A. G. Evans, E. A. Charles, Fracture toughness determinations by indentation, *Journal of the American Ceramic Society* 59 (7-8) (1979) 371–372. doi:<https://doi.org/10.1111/j.1151-2916.1976.tb10991.x>.
- [89] D. Leguillon, E. Sanchez-Palencia, Fracture in heterogeneous materials, weak and strong singularities, in: P. Ladeveze, O. Zienkiewicz (Eds.), *New Advances in Computational Structural Mechanics*, Studies in applied mechanics, 32, Elsevier, Amsterdam, 1992, pp. 423–434.
- [90] R. Danzer, On the relationship between ceramic strength and the requirements for mechanical design, *Journal of the European Ceramic Society* 34 (15) (2014) 3435–3460. doi:<http://dx.doi.org/10.1016/j.jeurceramsoc.2014.04.026>.

- [91] V. Cannillo, G. Pellacani, C. Leonelli, A. Boccaccini, Numerical modelling of the fracture behaviour of a glass matrix composite reinforced with alumina platelets, *Composites Part A: Applied Science and Manufacturing* 34 (1) (2003) 43–51. doi:[https://doi.org/10.1016/S1359-835X\(02\)00230-0](https://doi.org/10.1016/S1359-835X(02)00230-0).
- [92] V. Cannillo, A. Corradi, C. Leonelli, A. Boccaccini, A simple approach for determining the in situ fracture toughness of ceramic platelets used in composite materials by numerical simulations, *Journal of materials science letters* 20 (20) (2001) 1889–1891. doi:<https://doi.org/10.1023/A:1012870110675>.
- [93] G. Anstis, P. Chantikul, B. R. Lawn, D. Marshall, A critical evaluation of indentation techniques for measuring fracture toughness: I, direct crack measurements, *Journal of the American Ceramic Society* 64 (9) (1981) 533–538. doi:<https://doi.org/10.1111/j.1151-2916.1981.tb10320.x>.
- [94] W. Voigt, Ueber die beziehung zwischen den beiden elasticitätsconstanten isotroper körper, *Annalen der physik* 274 (12) (1889) 573–587. doi:<https://doi.org/10.1002/andp.18892741206>.
- [95] I. García, V. Mantič, E. Graciani, Debonding at the fibre–matrix interface under remote transverse tension. one debond or two symmetric debonds?, *European Journal of Mechanics-A/Solids* 53 (2015) 75–88. doi:<https://doi.org/10.1016/j.euromechsol.2015.02.007>.
- [96] D. Quesada, D. Picard, C. Putot, D. Leguillon, The role of the interbed thickness on the step-over fracture under overburden pressure, *International Journal of Rock Mechanics and Mining Sciences* 46 (2) (2009) 281–288. doi:<https://doi.org/10.1016/j.ijrmmms.2008.04.006>.
- [97] H. Ming-Yuan, J. W. Hutchinson, Crack deflection at an interface between dissimilar elastic materials, *International journal of solids and structures* 25 (9) (1989) 1053–1067. doi:[https://doi.org/10.1016/0020-7683\(89\)90021-8](https://doi.org/10.1016/0020-7683(89)90021-8).
- [98] D. Leguillon, E. Martin, Crack nucleation at stress concentration points in composite materials—application to crack deflection by an interface, in: *European Journal of Mechanics - A/Solids*, 2014, pp. 401–424. doi:[https://doi.org/10.1142/9781848167858\\_0010](https://doi.org/10.1142/9781848167858_0010).
- [99] P. Weißgraeber, S. Hell, W. Becker, Crack nucleation in negative geometries, *Engineering Fracture Mechanics* 168 (2016) 93–104, modeling of fracture and damage in composite materials. doi:<https://doi.org/10.1016/j.engfracmech.2016.02.045>.
- [100] Y. Legerstee, Caractérisation et modélisation du comportement thermomécanique de composites à matrice céramique renforcés par des fibres courtes, Ph.D. thesis, École doctorale des sciences physiques et de l'ingénieur (2022).
- [101] 2050 long-term strategy by the European Commission, [https://climate.ec.europa.eu/eu-action/climate-strategies-targets/2050-long-term-strategy\\_en](https://climate.ec.europa.eu/eu-action/climate-strategies-targets/2050-long-term-strategy_en), [Online; accessed 17-May-2023].

- 
- [102] D. Munz, T. Fett, *Ceramics: mechanical properties, failure behaviour, materials selection*, Vol. 36, Springer Science & Business Media, 1999.
- [103] T. M. Pollock, S. Tin, Nickel-based superalloys for advanced turbine engines: chemistry, microstructure and properties, *Journal of propulsion and power* 22 (2) (2006) 361–374. doi:<https://doi.org/10.2514/1.18239>.
- [104] P. Camanho, Prediction of fracture of polymer composite materials across different length scales, ECF23 book of abstracts. European Structural Integrity Society.
- [105] D. Vasilopoulos, On the determination of higher order terms of singular elastic stress fields near corners, *Numerische Mathematik* 53 (1988) 51–95.
- [106] M. Alnæs, J. Blechta, J. Hake, A. Johansson, B. Kehlet, A. Logg, C. Richardson, J. Ring, M. E. Rognes, G. N. Wells, The fenics project version 1.5, *Archive of numerical software* 3 (100). doi:<http://dx.doi.org/10.11588/ans.2015.100.20553>.

# List of symbols

## Latin symbols

### A

$a$  Notch depth

$a_h$  Notch width

$a_l, a_t$  Dimensions of the heterogeneous structure in the actual domain

$\hat{a}_l, \hat{a}_t$  Dimensions of the heterogeneous structure in the inner domain

$A$  Scaling coefficient

$A^*$  Dimensionless scaling coefficient

$A_0$  Stiffness tensor of the pristine material

$A(\alpha)$  Stiffness tensor

### B

$B$  Bulk modulus

### C

$C$  Elastic matrix

### D

$d$  Density

### E

$e, \hat{e}$  Thickness of the interphase in the actual and the inner domain, respectively

$E$  Young's modulus

$E^{\text{app}}$  Homogenized Young's modulus

**F**

$f$	Shape factor
$\underline{f}$	Vector of volumetric forces
$\underline{f}_\tau$	Vector of volumetric forces at time $\tau$
$F^{\text{DC}}$	Force under displacement control
$F^{\text{FC}}$	Force under force control
$F_{\text{crit}}$	Critical force
$\underline{F}_\tau$	Vector of surface forces at time $\tau$
$F_{0/1}(l)$	Terms in the inner expansion
$F_{0/1}^{\text{cr/te}}(l)$	Terms in the outer expansion in the mechanical (cr) or the thermoelastic (te) problem

**G**

$G_c$	Critical energy release rate
$G_{\text{inc}}$	Incremental energy release rate
$\bar{G}_{\text{inc}}$	Dimensionless incremental energy release rate
$G$	Energy release rate

**H**

$h_l, h_t$	Distances between fibers in the actual domain
$\hat{h}_l, \hat{h}_t$	Distances between fibers in the inner domain
$\underline{h}$	Imposed distributed force
$H$	History variable
$H^1(\Omega_l)$	First Sobolev space defined in the domain $\Omega_l$

**I**

$\underline{\underline{I}}$	Identity matrix
-----------------------------	-----------------

**K**

- $k^{\text{cr/te}}$  GSIF of actual problem in the mechanical (cr) and thermoelastic (te) problem
- $k_{\text{res}}$  Residual parameter
- $K$  Generalized stress intensity factor
- $K_c$  Fracture toughness
- $K_{\text{I}}$  Stress intensity factor for a crack under Mode I
- $K_{\text{I}}^{\text{min}}$  Minimum GSIF in the thermomechanical problem
- $K_c^{\text{app}}$  Homogenized fracture toughness

**L**

- $l$  Length
- $l_{\text{Irwin}}$  Irwin length
- $l_{\text{mesh}}$  Maximum mesh size allowed in the nucleation damage region
- $l_{\text{PF}}$  Phase Field length scale
- $\hat{l}$  Length in the inner domain
- $L$  Length of the specimen
- $L_c$  Critical length of the specimen

**P**

- $P_\tau$  Total energy in the system at instant  $\tau$

**Q**

- $\underline{q}$  Damage vector flux

**S**

- $s$  Coordinate along the expected crack path
- $s_d$  Damage variable
- $S$  Cross surface

**T**

- $t$  Thickness
- $\hat{t}$  Thickness in the inner domain
- Tol Tolerance

**U**

- $u_d$  Distributed displacement
- $u_{dc}$  Critical distributed displacement
- $\underline{u}_\tau$  Displacement vector at instant  $\tau$
- $\underline{u}(\theta)$  Opening shape function in Williams' expansion
- $U$  Load
- $U^{DC}$  Displacement under displacement control
- $U^{FC}$  Displacement under force control
- $\underline{U}_0$  Leading term in the outer expansion
- $U_{crit}$  Critical load
- $\underline{U}$  Displacement vector
- $\underline{U}^{cr/te}$  Displacement vector in the mechanical (cr) / thermoelastic (te) problem
- $\underline{U}_l$  Actual displacement vector
- $\bar{\underline{U}}$  Imposed displacement

$\underline{U}_0^{\text{cr/te}}$  Leading term in the outer expansion in the mechanical (cr) / thermoelastic (te) problem

$\underline{U}_l^{\text{cr/te}}$  Actual displacement vector in the mechanical (cr) / the thermoelastic (te) problem

## V

$V_r$  Volume fraction of the reinforcing element

$V_p$  Volume fraction of platelets

$V_f$  Volume fraction of fibers

$\underline{V}_{0/1}(y_1, y_2)$  Terms in the inner expansion

$\underline{V}_{0/1}^{\text{cr/te}}(y_1, y_2)$  Terms in the outer expansion in the mechanical (cr) or the thermoelastic (te) problem

## W

$w_1$  Total energy dissipated in a damage process

$w(\alpha)$  Local term in the regularized energy density

$W$  Width of the specimen

## Y

$Y$  Energy release rate density

## Coordinates systems

$r, \theta$  Polar coordinates

$x_1, x_2$  Cartesian coordinates

$y_1, y_2$  Cartesian coordinates in the inner domain

## Greek symbols

$\alpha$  Damage variable

$\alpha_r$  Orientation of the reinforcing element

---

$\alpha_T$	Thermal expansion coefficient
$\alpha_\tau$	Damage variable at instant $\tau$
$\alpha_T^{\text{app}}$	Homogenized thermal expansion coefficient
$\delta l$	Newly created crack length
$\delta l_c$	Crack initiation length
$\delta l_{\text{in}}$	Newly created crack length in the inner domain
$\delta S$	Newly created crack surface
$\kappa^{\text{cr/te}}$	GSIF in the inner expansion in the mechanical (cr) and thermoelastic (te) problem
$\lambda$	Singularity exponent in Williams' expansion
$\nu$	Poisson's ratio
$\nu^{\text{a/g}}$	Alumina/Glass Poisson's ratio
$\nu^{\text{app}}$	Homogenized Poisson's ratio
$\omega$	Opening angle
$\phi$	Test function
$\psi$	Energy density
$\psi_{\text{el}}$	Elastic energy density
$\psi_{\text{d}}$	Fracture energy density
$\psi_{\text{lPF}}$	Regularized energy density
$\Psi_{\text{el}}$	Elastic energy
$\hat{\Psi}_{\text{el}}$	Elastic energy in the inner domain
$\rho$	Notch blunting
$\bar{\sigma}$	Dimensionless tensile stress
$\sigma_c$	Tensile strength
$\sigma_f$	Equivalent flexural stress

---

$\sigma_{\text{fcrit}}$	Equivalent flexural stress at failure
$\sigma_{\text{fail}}$	Failure stress
$\sigma_{\text{c}}^{\text{app}}$	Homogenized tensile strength
$\underline{\underline{\sigma}}$	Stress tensor
$\underline{\underline{\sigma}}_l$	Actual stress tensor
$\underline{\underline{\sigma}}_0$	Outer stress tensor
$\sigma(s)$	Tensile stress along the expected crack path
$\sigma^{\text{DC/FC}}(s)$	Tensile stress along the expected crack path under DC or FC
$\tau$	Time
$\theta_0$	Initial temperature
$\theta_f$	Final temperature
$\underline{\underline{\varepsilon}}$	Strain tensor
$\underline{\underline{\varepsilon}}^{\text{in}}$	Inelastic strain tensor
$\Delta\theta$	Cooling change in temperature
$\Gamma$	Crack region
$\Gamma_{\text{c}}$	Pre-existing crack region
$\Gamma_l$	Actual perturbed boundary
$\Gamma_{\text{N}}$	Neumann boundary
$\Gamma_{\text{D}}$	Dirichlet boundary
$\Gamma_{\text{V}}$	V-notch outer boundaries
$\Omega$	Domain
$\Omega_0$	Outer domain
$\Omega_{\text{in}}$	Inner domain
$\Omega_l$	Actual perturbed domain
$\Pi_{\text{k}}$	Kinetic energy

---

$\Pi_p$	Potential energy
$\Pi_p^{\text{DC/FC}}$	Potential energy under displacement (DC) or force (FC) control
$\Psi_f$	Total work of external forces at instant $\tau$
$\Psi_{\text{el}}$	Total elastic energy
$\mathcal{W}^{\text{cr/te}}$	Functional space for trial functions in the mechanical (cr) or thermoelastic (te) problem
$\mathcal{W}_0^{\text{cr}}$	Functional space for test functions in the mechanical (cr) problem

## Abbreviations

CC	Coupled Criterion
CMC	Ceramic Matrix Composites
DC	Displacement control
ERR	Energy Release Rate
FC	Force control
FEM	Finite Element Method
FFM	Full Finite Element
FFM	Finite Fracture Mechanics
FIB	Focused Ion Beam
F-U	Force-displacement
GSIF	Generalized Stress Intensity Factor
IERR	Incremental Energy Release Rate
K-U	Stiffness-displacement

---

MAE	Matched Asymptotics Expansion
MEMS	Micro-Electro-Mechanical System
PF	Phase Field
SEM	Scanning Electron Microscope
SENB	Single-edge notched beam
SIF	Stress Intensity Factor
SPM	Scanning Probe Microscope
STM	Scanning Tunneling Microscope

